HAL
open science

Dynamics and global stability analysis of three-dimensional flows

Jean-Christophe Loiseau

To cite this version:

Jean-Christophe Loiseau. Dynamics and global stability analysis of three-dimensional flows. Mechanics [physics.med-ph]. Ecole nationale supérieure d'arts et métiers - ENSAM, 2014. English. NNT : 2014ENAM0016 . tel-01177042

HAL Id: tel-01177042

https://pastel.hal.science/tel-01177042v1

Submitted on 16 Jul 2015

HAL is a multi-disciplinary open access archive for the deposit and dissemination of scientific research documents, whether they are published or not. The documents may come from teaching and research institutions in France or abroad, or from public or private research centers.

L'archive ouverte pluridisciplinaire **HAL**, est destinée au dépôt et à la diffusion de documents scientifiques de niveau recherche, publiés ou non, émanant des établissements d'enseignement et de recherche français ou étrangers, des laboratoires publics ou privés.

2014-ENAM-0016

École doctorale n° 432 : Science des Métiers de l'ingénieur

Doctorat ParisTech

T H È S E

pour obtenir le grade de docteur délivré par

l'École Nationale Supérieure d'Arts et Métiers

Spécialité " Mécanique "

présentée et soutenue publiquement par

Jean-Christophe LOISEAU

le 26 Mai 2014

Dynamics and global stability analyses of three-dimensional flows

Directeur de thèse : **Jean-Christophe ROBINET**
Co-encadrement de la thèse : **Emmanuel LERICHE**

Jury

M. Denis SIPP, Maître de Recherche, DAFE, ONERA	Président
M. Luca BRANDT, Professeur, KTH Mechanics, Royal Institute of Technology (KTH)	Rapporteur
M. Uwe EHRENSTEIN, Professeur, IRPHE, Aix-Marseille Université	Rapporteur
M. Dwight BARKLEY, Professeur, Mathematics Institute, University of Warwick	Examinateur
M. François LUSSEYRAN, Chargé de Recherche, LIMSI, CNRS	Examinateur
Mme Stefania CHERUBINI, Maître de Conférence, DynFluid, Arts et Métiers ParisTech	Examinateur
M. Jean-Christophe ROBINET, Professeur, DynFluid, Arts et Métiers ParisTech	Examinateur
M. Emmanuel LERICHE, Professeur, Laboratoire de Mécanique de Lille, Université Lille-1	Examinateur

T H È S E

Arts et Métiers ParisTech - Centre de Paris
Laboratoire DynFluid

Remerciements

Les remerciements sont un exercice de style dans lequel certains excellent. Pas moi. J'essayerai malgré tout d'être aussi expansif que possible. Je suis en premier lieu particulièrement reconnaissant envers Jean-Christophe Robinet et Emmanuel Leriche de m'avoir offert l'occasion de faire cette thèse. Celle-ci n'aurait sans doute pas été la même sans leur gentillesse et la liberté quasiment totale qu'ils m'ont laissée. J'ai beaucoup appris d'eux et souhaite sincèrement avoir l'occasion de continuer à collaborer avec eux deux pendant de nombreuses années encore.

Je tiens aussi à remercier l'ensemble des doctorants du laboratoire grâce à qui j'ai beaucoup rigolé pendant ces quatre années, notamment Gégoire (et ses blagues pourries), Matthieu (mon bizu et sa faculté à me laisser lui taxer des cigarettes), Renan (et sa gentillesse innée), Florian (et les nombreuses bières bues ensemble) ainsi que Karim et Pierre-Yves (compagnons de galère depuis le tout début). Je suis aussi très reconnaissant envers mes camarades de bureau, Frédéric, Xavier M. et Elie qui ont eu à supporter mes improbables goûts musicaux et crises de démence pendant ces quatre années. J'aimerai aussi remercier chaleureusement Stefania pour les (trop?) nombreuses discussions aussi bien scientifiques que personnelles qui m'ont aidé à grandir et je suis très touché qu'elle ait accepté de faire partie du jury de thèse. Enfin, je n'oublie pas l'ensemble des autres membres du laboratoire: Simon, Xavier G., Paola, Virginie, Grégory, Jérémie, Guillaume, Cédric, Antoine, Damien, et tout ceux que j'ai oublié.

Concernant mon jury de thèse, je suis en premier lieu particulièrement reconnaissant envers Luca Brandt, pour qui j'ai beaucoup d'estime, qui a accepté d'être rapporteur de mon manuscrit et qui m'offre une occasion incroyable d'aller travailler avec lui au KTH. J'aimerai aussi remercier Uwe Ehrenstein, rapporteur de mon travail mais aussi porteur du projet ANR dans lequel s'est incrit cette thèse, qui a eu l'occasion de suivre mon travail et de le questionner tout au long de ces quatre années. Enfin, je n'oublie pas Denis Sipp, François Lusseyran, Dwight Barkley et Stefania Cherubini (que j'ai déjà eu l'occasion de remercier) qui ont accepté de prendre part à cette aventure.

Avant de terminer, j'aimerai remercier ma famille: mon père, mes frères et ma soeur, ainsi que ma grand-mère qui m'ont tous poussés à commencer cette thèse. Enfin, je tiens à remercier mes amis: Joséphine, JR, Gaëlle, Marielle, Stéphanie, Angéla, mes colocataires Jérémy et Caroline, Emine, Christophe, Nicolas et Juliette ainsi que tout ceux que je ne cite pas par manque de place mais que je n'oublie pas pour autant.

Merci.

Contents

I Introduction . . . 1
I.1 Hydrodynamic instabilities . . . 2
I.1.1 Local stability theory . . . 5
I.1.1.1 Temporal stability analysis . . . 7
I.1.1.2 Spatial stability analysis . . . 8
I.1.1.3 Absolute and convective instabilities . . . 9
I.1.1.4 2D local stability theory . . . 11
I.1.1.5 Global stability theory . . . 13
I.2 Context and Objectives . . . 16
II Numerical methods . . . 19
II.1 Introduction to the spectral elements code Nek5000 . . . 19
II.1.1 Spatial discretisation . . . 20
II.1.1.1 Variational formulation of the equations . . . 20
II.1.1.2 Legendre polynomials and Legendre spectral elements discretisation 21
II.1.2 Time discretisation . . . 25
II.2 Steady states computation . . . 27
II.3 Modal decomposition . . . 30
II.3.1 Global linear stability, time-stepping and Arnoldi algorithm . . . 30
II.3.1.1 Time-stepper approach . . . 31
II.3.1.2 Arnoldi algorithm . . . 32
II.3.2 Koopman modes decomposition . . . 36
II.4 Optimal perturbations and Transient growth analysis . . . 40
II.4.1 Adjoint linearised Navier-Stokes equations . . . 42
II.4.2 Optimal perturbation and eigenvalue analysis of $\mathbf{M}^*\mathbf{M}$ . . . 43
III Three-dimensional lid-driven cavity flow . . . 47
III.1 Problem formulation . . . 47
III.2 State of the art . . . 49
III.3 Results . . . 52
III.3.1 Steady state solutions . . . 52
III.3.2 Linear stability analysis . . . 56
III.3.3 Non-linear evolution . . . 66
III.3.3.1 Unstable limit cycle at Re=1930 . . . 69
III.3.3.2 Fully chaotic dynamics at Re=2000 . . . 73
III.4 Conclusion . . . 77

IV Stenotic pipe flow . . . 83
IV.1 Introduction . . . 83
IV.1.1 Axisymmetric stenotic pipe flows . . . 84
IV.1.2 Asymmetric stenotic pipe flows . . . 86
IV.2 Problem formulation . . . 87
IV.3 Reference case: the axisymmetric stenotic pipe flow . . . 88
IV.3.1 Steady state solutions . . . 88
IV.3.2 Linear stability analysis . . . 89
IV.3.3 Non-linear saturation and transition to turbulence . . . 93
IV.4 Asymmetric stenotic pipe flows . . . 94
IV.4.1 Influence of the eccentricity at fixed Reynolds number . . . 94
IV.4.1.1 Linear stability analysis . . . 97
IV.4.1.2 Kinetic energy budget analysis . . . 99
IV.4.2 Influence of the Reynolds number at fixed eccentricity . . . 100
IV.5 Discussion . . . 108
IV.6 Conclusion . . . 111
V Roughness-induced transition . . . 115
V.1 Introduction . . . 115
V.2 Problem formulation . . . 119
V.3 The Fransson experiment . . . 122
V.3.1 Base flow . . . 122
V.3.2 Global stability . . . 124
V.4 Parametric investigation . . . 126
V.4.1 Base flow . . . 127
V.4.1.1 Influence of the Reynolds number . . . 127
V.4.1.2 Influence of the aspect ratio . . . 128
V.4.2 Global stability . . . 129
V.4.2.1 Analysis of the modes . . . 133
V.4.3 Perturbation kinetic energy budget . . . 136
V.4.3.1 Sinuous instability . . . 137
V.4.3.2 Varicose instability . . . 138
V.4.4 Wavemaker . . . 139
V.5 Non-linear evolution . . . 142
V.5.1 Varicose global instability . . . 142
V.5.2 Sinuous global instability . . . 144
V.5.2.1 Criticality of the bifurcation . . . 144
V.5.2.2 Mean flow characteristics . . . 145
V.5.2.3 Dynamics . . . 147
V.5.3 Comparison with von Doenhoff-Braslow transition diagram . . . 149
V.6 Summary and conclusions . . . 149
VI Overall conclusion . . . 157

Appendices **167**
A Very large aspect ratio lid-driven cavity flow . . . 167
A.1 Primary base flow . . . 167

A.2 Non-linear evolution . . . 168
A.3 Conclusion . . . 168
B Influence of the shape on the roughness-induced transition . . . 173
B.1 Introduction . . . 174
B.2 Problem formulation . . . 174
B.3 Results and discussion . . . 175
B.4 Conclusion . . . 177

References **177**

Chapter I

Introduction

Fluid mechanics is a branch of Physics concerned with the study of fluids (liquid, gases or plasmas). It can be divided into fluid statics and fluid dynamics. The study of fluid mechanics goes back at least to the days of ancient Greece, when Archimedes investigated fluid statics and buoyancy and formulated his famous law known as the Archimedes' principle. Rapid advancement in fluid mechanics began with Leonardo da Vinci (observations and experiments), Evangelista Torricelli (invented the barometer), Isaac Newton (investigation of viscosity) and Blaise Pascal (Pascal's law), and was continued by Daniel Bernoulli. During the course of the nineteenth century, two mathematicians, Claude-Louis Navier and Georges Gabriel Stokes have derived the equations governing the motion of a fluid. These equations, now known as the Navier-Stokes equations, are non-linear partial differential equations. Assuming the flow is incompressible and Newtonian, these equations read:

$$\begin{cases} \dfrac{\partial \mathbf{U}}{\partial t} = -(\mathbf{U}\cdot\nabla)\mathbf{U} - \nabla P + \dfrac{1}{Re}\Delta\mathbf{U} \\ \nabla\cdot\mathbf{U} = 0 \end{cases} \tag{I.1}$$

where $\mathbf{U}$ is the velocity field, P the pressure and Re a non-dimensional number characterising the flow and known as the Reynolds number. Up to now, very few analytical solutions are known. Moreover, there is no general proof so far that the solutions are smooth and bounded in energy[1]. Yet, despite this lack of mathematical foundations, these equations are widely used nowadays in Computational Fluid Dynamics (CFD) and have greatly helped scientists to unravel the basic mechanisms responsible for transition of flows to unsteadiness and eventually turbulence. Among these mechanisms, the keyrole of hydrodynamic linear instabilities in the transition, already identified as early as the nineteenth century, has been observed in a vast variety of flows.

[1]Since 2000, proving the Navier-Stokes smoothness and boundedness in $\mathbb{R}^3$ has been made one of the seven Millenium Prize problems. In 1934, the French mathematician Jean Leray [101] proved the existence of so-called weak solutions to the Navier–Stokes equations, satisfying the equations in mean value, not pointwise. In the 1960's, proof has been given about the smoothness and boundedness of the solutions of the two-dimensional Navier-Stokes equations [95]. Early 2014, a Kazakh mathematician, Mukhtarbay Otelbayev, claimed he had solved this problem in three dimensions. Very recently, Terence Tao has shown that Otelbayev's proof was wrong. Shortly after, Tao has published a paper [150] proving that the three-dimensional incompressible Navier-Stokes equations admit solutions blowing up in a finite time.

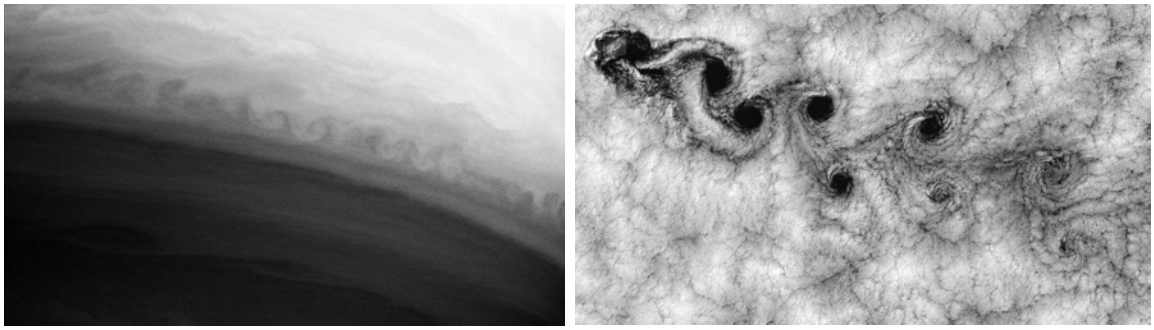

(a) (b)

Figure I.1: (a) A Kelvin-Helmholtz instability on Saturn, caused by the interaction between two bands of the planet's atmosphere. Image from the Cassini probe. (b) This Landsat 7 image of clouds off the Chilean coast near the Juan Fernandez Islands on September 15, 1999, shows a unique pattern called a *von Karman vortex street*.

I.1 Hydrodynamic instabilities

As underlined by its name, hydrodynamic stability theory is a branch of fluid mechanics concerned with the stability and the onset of instability in fluid flows. The concept of stability of the state of a physical system was understood as early as the eighteenth century. According to P. G. Drazin [54], Clerk Maxwell was the first to qualitatively expressed this concept in the nineteenth century:

> "When ... an infinitely small variation of the present state will alter only by an infinitely small quantity the state at some future time, the condition of the system, whether at rest or in motion, is said to be stable; but when an infinitely small variation in the present state may bring about a finite difference in the state of the system in a finite time, the condition of the system is said to be unstable."

Hydrodynamic instabilities have been investigated for over a hundred years. Lot of famous names have been attached to various instabilities. One can cite for instance the Kelvin-Helmholtz instability, illustrated on figure I.1(a), studied in the nineteenth century by Lord Kelvin and Hermann Ludwig von Helmholtz, or the Bénard-von Karman vortex street depicted on figure I.1(b), a wake instability named after Henri Bénard and Theodore von Karman.

Osborne Reynolds and the pipe flow transition

An introduction to hydrodynamic instabilities would not be worthwhile without a word said about Osborne Reynolds and his famous experimental investigation of pipe flow transition in 1883 yielding him to introduce for the first time what is now known as the *Reynolds number* [128]. We now know that the pipe flow transition to turbulence results from mechanisms more complex than simple hydrodynamic linear instabilities, the scope of the present thesis. Nonetheless, it is believed by the author that describing the experiment O. Reynolds had conducted might help new comers to better understand what hydrodynamic instabilities are and how important it might be to study them.

> The experiments were made on three tubes. The diameters of these were nearly 1 inch, $\frac{1}{2}$ inch and $\frac{1}{4}$ inch. They were all fitted with trumpet mouthpieces, so that the water might enter without disturbance. The water was drawn through the tubes out of a large glass tank, in which the tubes were immersed, arrangements being made so that a streak or streaks of highly coloured water entered the tubes with the clear water. The general results were as follows:
>
> (1) When the velocities were sufficiently low, the streak of colour extended in a beautiful straigth line through the tube (see figure I.2, top).
>
> (2) If the water in the tank had not quite settled to rest, at sufficiently low velocities, the streak would shift about the tube, but there was no appearance of sinuosity.
>
> (3) As the velocity was increased by small stages, at some point in the tube, always at considerable distance from the trumpet or intake, the colour band would all at once mix up with the surrounding water, and fill the rest of the tube with a mass of coloured water (see figure I.2, middle).
>
> Any increase of the velocity caused the point of break down to approach the trumpet but with no velocities that were tried did it reach this. On viewing the tube by the light of an electric spark, the mass of colour resolved itself into a mass of more or less distinct curls, showing eddies (see figure I.2, bottom).

O. Reynolds' experimental work, by introducing what is now known as the Reynolds number Re, clearly higlights that beyond a critical value of Re, the laminar flow in a pipe breaks down and transition to what is called a *turbulent state*. His pionnering experimental work clearly illustrates what are the aims of someone investigating hydrodynamics stability theory: to find if a given laminar flow is stable or unstable, and if so, what are the physical mechanisms responsible for transition to unsteadiness and eventually turbulence.

Mathematical background

The theoretical and numerical study of hydrodynamic instabilities are inherently linked to the concept of base flow and to the spectral properties of the associated linearised Navier-Stokes operator. The concept of base flow can be defined in several different ways. To the author's knowledge, one of the most comprehensive definition is the following:

> **Base flow:** A base flow is a peculiar solution of the Navier-Stokes equations. In the context of linear stability theory, this solution is either stationnary or periodic in time.

From a mathematical point of view, the concept of base flow is similar to that of fixed point (stationnary solution) or limit cycle (time-periodic solution) in the dynamical system framework. As already said, very few analytical solutions of the Navier-Stokes equations are known. However, with the progress made in CFD over the last decades, such peculiar solutions can be computed numerically even in relatively complex setups. In order to do so, one can use various tools ranging from the Newton method and its variants to the more recent selective frequency damping approach introduced by Akervik *et al.* [6]. Once

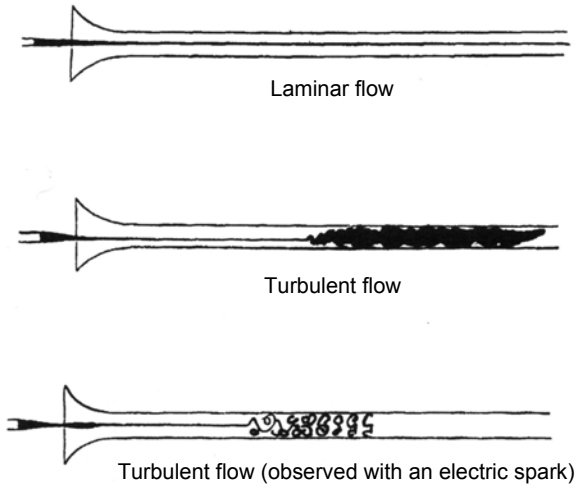

Figure I.2: Water flow observed in a pipe, as drawn by Osborne Reynolds in his famous experiment on pipe flow transition. Water flows from left to right in a transparent tube, and dye (represented in black) flows in the middle. The nature of the flow (laminar or turbulent) can easily be observed. These drawings were originally Reynolds' influential 1883 paper [128].

such solution has been computed, one can then investigate the dynamics of infinitesimal perturbations evolving onto this given base flow by linearising the non-linear Navier-Stokes equation around this peculiar solution. In the most general framework treated here, i.e. three-dimensional incompressible flows of Newtonian fluids, these linearised equations are linear three-dimensional partial differential equations:

$$\begin{cases} \dfrac{\partial u}{\partial t} = -U_b\dfrac{\partial u}{\partial x} - V_b\dfrac{\partial u}{\partial y} - W_b\dfrac{\partial u}{\partial z} - u\dfrac{\partial U_b}{\partial x} - v\dfrac{\partial U_b}{\partial y} - w\dfrac{\partial U_b}{\partial z} - \dfrac{\partial p}{\partial x} + \dfrac{1}{Re}\Delta u \\ \dfrac{\partial v}{\partial t} = -U_b\dfrac{\partial v}{\partial x} - V_b\dfrac{\partial v}{\partial y} - W_b\dfrac{\partial v}{\partial z} - u\dfrac{\partial V_b}{\partial x} - v\dfrac{\partial V_b}{\partial y} - w\dfrac{\partial V_b}{\partial z} - \dfrac{\partial p}{\partial y} + \dfrac{1}{Re}\Delta v \\ \dfrac{\partial w}{\partial t} = -U_b\dfrac{\partial w}{\partial x} - V_b\dfrac{\partial w}{\partial y} - W_b\dfrac{\partial w}{\partial z} - u\dfrac{\partial W_b}{\partial x} - v\dfrac{\partial W_b}{\partial y} - w\dfrac{\partial W_b}{\partial z} - \dfrac{\partial p}{\partial z} + \dfrac{1}{Re}\Delta w \\ \dfrac{\partial u}{\partial x} + \dfrac{\partial v}{\partial y} + \dfrac{\partial w}{\partial z} = 0 \end{cases} \tag{I.2}$$

with $\mathbf{u} = (u, v, w)^T$ and p the velocity and pressure fields characterising the perturbation, respectively, and $\mathbf{U}_b = (U_b, V_b, W_b)$ a stationnary solution of the non-linear Navier-Stokes equations (I.1) either known analytically or computed numerically. In the linear dynamical system framework, this set of equations can be recast into the following matrix equation:

$$\mathbf{B}\frac{\partial \mathbf{q}}{\partial t} = \mathbf{J}\mathbf{q} \tag{I.3}$$

where $\mathbf{q} = (\mathbf{u}, p)^T$ is the state vector characterising the perturbation, $\mathbf{B}$ a mass matrix and $\mathbf{J}$ the Jacobian of the Navier-Stokes equations. The linear stability of the base flow $\mathbf{U}_b$ is then fully determined by the spectrum of eigenvalues of the linearised Navier-Stokes operator $\mathbf{J}$, whereas the associated leading eigenvectors then provide the spatial

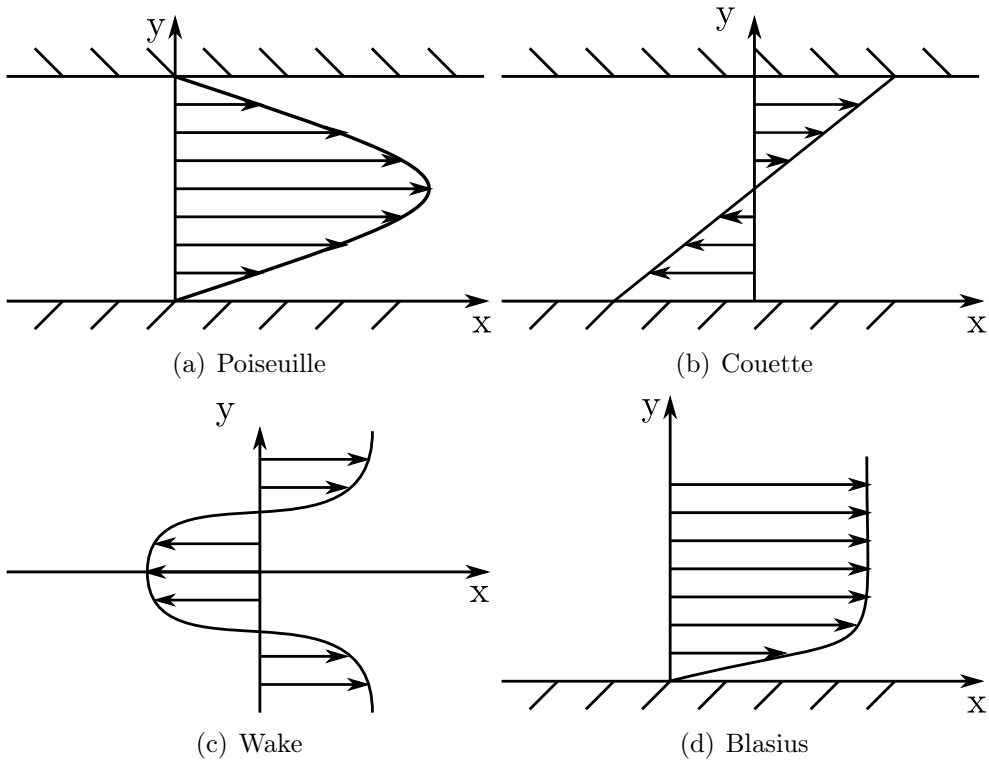

Figure I.3: (a) and (b): Examples of parallel flows. (c) and (d): Examples of quasi-parallel flows.

distribution of the unstable perturbations. Depending on the nature of the base flow (parallel, two- or three-dimensional flow), different tools can be used:

- Local stability theory for parallel flows,
- Global stability theory[2] when it comes to two- and three-dimensional flows.

In the following sections, a brief introduction to local stability theory for parallel flows and global stability theory applied to two-dimensional base flows will be given. On the other hand, the case of global stability theory applied to fully three-dimensional base flows being the scope of the present thesis, it will be discussed later.

I.1.1 Local stability theory

Because of limited analytical tools and limited computational ressources in the past, the instability of flows has traditionally been investigated assuming that the wavelength of

[2]To differentiate between global stability applied to two- or three-dimensional flows, some authors refer to bi- and tri-global stability analyses. The author however believes that such distinction should not be. Moreover, the stability analysis of flows having two inhomogeneous directions but for which a streamiwse independence (or almost independence) assumption still holds is sometime refered to bi-global stability [48, 122] as well. Such name can unfortunately be misleading since such analysis remains within the framework of local stability analysis. From the author's point of view, the term global stability should thus be strictly restricted to the stability of flows being strongly non-parallel for which a local stability approach would make no sense.

the underlying instability mechanism is short compared to the typical scale over which the flow develops along the streamwise direction. Under such assumption, one can use the parallel flow hypothesis such that the base flow has the form $\mathbf{U}_b = (U_b(y), 0, 0)^T$ as those depicted on figure I.3. As a consequence, the complexity of the linearised Navier-Stokes equations (I.2) is reduced:

$$\begin{cases} \dfrac{\partial u}{\partial t} = -v\dfrac{\partial U}{\partial y} - U_b\dfrac{\partial u}{\partial x} - \dfrac{\partial p}{\partial x} + \dfrac{1}{Re}\Delta u \\ \dfrac{\partial v}{\partial t} = -U_b\dfrac{\partial v}{\partial x} - \dfrac{\partial p}{\partial y} + \dfrac{1}{Re}\Delta v \\ \dfrac{\partial w}{\partial t} = -U_b\dfrac{\partial w}{\partial x} - \dfrac{\partial p}{\partial z} + \dfrac{1}{Re}\Delta w \\ \dfrac{\partial u}{\partial x} + \dfrac{\partial v}{\partial y} + \dfrac{\partial w}{\partial z} = 0 \end{cases} \tag{I.4}$$

Moreover, because these equations are homogeneous in x, z and t, they can be solved using *normal modes expansion* of the perturbation both in the streamwise and spanwise directions as well as in time. Only the cross-stream (also called wall-normal) direction then remains unchanged. Assuming the infinitesimal perturbation $\mathbf{q}(x, y, z) = (\mathbf{u}, p)^T$ has the form:

$$\mathbf{q}(x, y, z) = \int_{L_\lambda}\int_{F_\alpha}\int_{F_\beta} \hat{\mathbf{q}}(y)e^{i(\alpha x+\beta z)+\lambda t}\, \mathrm{d}\beta\mathrm{d}\alpha\mathrm{d}\lambda + c.c \tag{I.5}$$

where, $c.c$ the complex conjugate, α is the streamwise wavenumber, β the spanwise wavenumber and $\lambda = \sigma + i\omega$ the (possibly complex) frequency of the normal mode considered. Since the equations considered are linear, one can then solve them for each of these normal modes involved in the decomposition. As a consequence, the linearised Navier-Stokes equations (I.4) can be rewritten as:

$$\begin{cases} \lambda\hat{u} = -\hat{v}\dfrac{\partial U_b}{\partial y} - i\alpha\hat{u}U_b - i\alpha\hat{p} + \dfrac{1}{Re}\left(\dfrac{\partial^2}{\partial y^2} - \alpha^2 - \beta^2\right)\hat{u} \\ \lambda\hat{v} = -i\alpha\hat{v}U_b - \dfrac{\partial\hat{p}}{\partial y} + \dfrac{1}{Re}\left(\dfrac{\partial^2}{\partial y^2} - \alpha^2 - \beta^2\right)\hat{v} \\ \lambda\hat{w} = -i\alpha\hat{w}U_b - i\beta\hat{p} + \dfrac{1}{Re}\left(\dfrac{\partial^2}{\partial y^2} - \alpha^2 - \beta^2\right)\hat{w} \\ i\alpha\hat{u} + \dfrac{\partial\hat{v}}{\partial y} + i\beta\hat{w} = 0 \end{cases} \tag{I.6}$$

Thanks to the parallel flow assumption and the normal modes expansion, the resulting system (I.6) falls into the framework of *local stability theory*. Since only the wall-normal direction needs to be discretised, the system of equations (I.6) involves only up to a few hundreds degrees of freedom such that it has been extensively investigated numerically since the early 1960's for a wide variety of parallel flows. Several different types of analyses can be conducted to investigate the properties of this system:

- Temporal stability analysis: investigation of the asymptotic time behaviour of perturbations having real wavenumbers (see Michalke [114]).

- Spatial stability analysis (also known as the Signaling problem): investigation of the flow's response to time-harmonic localised forcing. In such analysis, the prescribed frequency of the forcing is real whereas the wavenumbers characterising the perturbation can be complex (see Michalke [115]).

- Absolute and convective instabilities: investigation of the flow's response to a spatially and temporally localised impulse. Such analysis allows one to distinguish between convectively and absolutely unstable flows (see Huerre & Monkewitz [81]).

- Transient growth analysis: investigation of the short-time dynamics and amplification of perturbations (see Reddy & Henningson [127]).

All of these analyses are based on the same set of equations (I.6) but look at different aspects and thus require different mathematical tools. In the following, a brief introduction will be given to each of these analyses. For extensive details, the reader is however refered to the books by Drazin [54], Drazin & Reid [55], Schmid & Henningson [138] as well as Charru [39].

I.1.1.1 Temporal stability analysis

Within the framework of temporal linear stability, the asymptotic time evolution of infinitesimal perturbations having a prescribed real wavevector $\mathbf{k} = \alpha\mathbf{x} + \beta\mathbf{z}$ (where $\mathbf{x}$ and $\mathbf{z}$ are the unit-vectors along the streamwise and spanwise directions, respectively) is investigated. This investigation can be further simplified using the Squire theorem[3] [146]. Based on this theorem, the local stability equations (I.6) can be reduced to:

$$\begin{cases} \lambda\hat{u} = -\hat{v}\dfrac{\partial U_b}{\partial y} - i\alpha\hat{u}U_b - i\alpha\hat{p} + \dfrac{1}{Re}\left(\dfrac{\partial^2}{\partial y^2} - \alpha^2\right)\hat{u} \\ \lambda\hat{v} = -i\alpha\hat{v}U_b - \dfrac{\partial\hat{p}}{\partial y} + \dfrac{1}{Re}\left(\dfrac{\partial^2}{\partial y^2} - \alpha^2\right)\hat{v} \\ i\alpha\hat{u} + \dfrac{\partial\hat{v}}{\partial y} = 0 \end{cases} \tag{I.7}$$

This set of linear coupled partial differential equations can be further simplified by introducing the stream function ψ of the perturbation. One then obtains the well-known Orr-Sommerfeld equation[4] [118, 145]. However, to ease the comparison for the reader be-

[3]**Squire theorem:** To any three-dimensional unstable mode $(\mathbf{k}, \lambda)$ can be associated a two-dimensional mode $(\bar{\mathbf{k}}, \bar{\lambda})$ more unstable with $\Re(\bar{\lambda}) = \Re(\lambda)\sqrt{\alpha^2 + \beta^2}/\alpha$

[4]Introducing the streamfunction ψ such that $\hat{u} = -\partial_y\hat{\psi}$ and $\hat{v} = i\alpha\hat{\psi}$ and eliminating the pressure from the equations (I.7) yields to:

$$(U_b - c)\left(\frac{\partial^2}{\partial y^2} - \alpha^2\right)\hat{\psi} - \frac{\partial^2 U_b}{\partial y^2}\hat{\psi} = \frac{1}{i\alpha Re}\left(\frac{\partial^2}{\partial y^2} - \alpha^2\right)^2\hat{\psi}$$

where $c = \lambda/\alpha$ is the complex phase velocity of the disturbance. This equation, independently derived by Orr [118] and Sommerfeld [145] in the early twenteeh century, is commonly used in local stability theory instead of its primitive variable counterpart. Though it involves fewer degrees of freedom than system (I.7), it can still be quite computationally hard on the numerical method used to discretise it since it involves the square of the second derivative of the streamfunction ψ.

tween the local and global approaches, the choice has been made to stick to the primitive variables formulation of the problem. Within the framework of temporal stability, the linear system (I.7) can be recast into a linear generalised eigenvalue problem in λ:

$$\lambda \mathbf{B}\hat{\mathbf{q}} = \mathbf{J}\hat{\mathbf{q}} \tag{I.8}$$

where the mass matrix $\mathbf{B}$ and the Jacobian matrix $\mathbf{J}$ are given by:

$$\mathbf{B} = \begin{pmatrix} 1 & 0 & 0 \\ 0 & 1 & 0 \\ 0 & 0 & 0 \end{pmatrix} \tag{I.9}$$

and

$$\mathbf{J} = \begin{pmatrix} \frac{1}{Re}\left(\frac{\partial^2}{\partial y^2} - \alpha^2\right) - i\alpha U_b & -\frac{\partial U_b}{\partial y} & -i\alpha \\ 0 & \frac{1}{Re}\left(\frac{\partial^2}{\partial y^2} - \alpha^2\right) - i\alpha U_b & -\frac{\partial}{\partial y} \\ -i\alpha & -\frac{\partial}{\partial y} & 0 \end{pmatrix} \tag{I.10}$$

The asymptotic time evolution of the infinitesimal perturbation $\hat{\mathbf{q}} = (\hat{\mathbf{u}}, \hat{p})^T$ is then solely governed by the sign of $\Re(\lambda)$ (i.e. the real part of the complex frequency λ):

- if $\Re(\lambda) < 0$, the perturbation decays exponentially in time and the base flow $\mathbf{U}_b$ is then denoted as linearly stable.
- if $\Re(\lambda) > 0$, the perturbation grows exponentially in time and the base flow $\mathbf{U}_b$ is then denoted as linearly unstable.
- if $\Re(\lambda) = 0$, the system is said to be neutral and one has to use weakly non-linear analysis to determine whether it is stable or unstable. Such analysis is however beyond the scope of this rapid introduction.

Investigation of the properties of the linearised Navier-Stokes operator then allows one to determine whether the flow considered is linearly stable (and thus physically observable) or linearly unstable and might thus transition to another state. Thanks to the small number of degrees of freedom involved, the generalised eigenvalue problem (I.8) can be solved nowadays using direct eigenvalue solvers on a simple laptop.

I.1.1.2 Spatial stability analysis

Investigating the temporal stability of a certain class of problems, such as the response of the boundary layer flow to a localised vibrating ribbon, might lead to an ill-posed problems. Indeed, for such problem, the frequency of the perturbation is fixed by the ribbon's oscillations and one is thus more interested in the spatial evolution of the perturbation rather than its temporal evolution. Such problems fall into the framework of *spatial stability analysis*. Within this framework, the response of the flow to a time-harmonic

forcing having a prescribed real frequency ω is investigated. The linearised Navier-Stokes equations (I.7) can be recast into a non-linear generalised eigenvalue problem in α:

$$\mathbf{C}_0\hat{\mathbf{q}} + \alpha\mathbf{C}_1\hat{\mathbf{q}} + \alpha^2\mathbf{C}_2\hat{\mathbf{q}} = 0 \tag{I.11}$$

where the $\mathbf{C}_0$, $\mathbf{C}_1$ and $\mathbf{C}_2$ matrices are given by:

$$\begin{aligned}
\mathbf{C}_0 &= \begin{pmatrix} \omega - \dfrac{1}{Re}\dfrac{\partial^2}{\partial y^2} & \dfrac{\partial U_b}{\partial y} & 0 \\ 0 & \omega - \dfrac{1}{Re}\dfrac{\partial^2}{\partial y^2} & -\dfrac{\partial}{\partial_y} \\ 0 & \dfrac{\partial}{\partial y} & 0 \end{pmatrix} \\
\mathbf{C}_1 &= \begin{pmatrix} iU_b & 0 & i \\ 0 & iU_b & 0 \\ i & 0 & 0 \end{pmatrix} \\
\mathbf{C}_2 &= \begin{pmatrix} \dfrac{1}{Re} & 0 & 0 \\ 0 & \dfrac{1}{Re} & 0 \\ 0 & 0 & 0 \end{pmatrix}
\end{aligned} \tag{I.12}$$

One must be aware that the spatial stability of incompressible parallel flows is often investigated based on the Orr-Sommerfeld equation. In this framework, since the equation involves the fourth derivative of the perturbation streamfunction ψ, the non-linear generalised eigenvalue problem is no longer quadratic in α but quartic. Solving such non-linear generalised eigenvalue problem might be relatively computationally expensive and require sophisticated eigenvalue algorithms. However, this eigenvalue problem (I.11) can be rewritten as:

$$\begin{pmatrix} \mathbf{C}_0 & \mathbf{C}_1 \\ 0 & 1 \end{pmatrix} \begin{pmatrix} \hat{\mathbf{q}} \\ \alpha\hat{\mathbf{q}} \end{pmatrix} = \alpha \begin{pmatrix} 0 & -\mathbf{C}_2 \\ 1 & 0 \end{pmatrix} \begin{pmatrix} \hat{\mathbf{q}} \\ \alpha\hat{\mathbf{q}} \end{pmatrix} \tag{I.13}$$

Based on this formulation of the problem, the resulting eigenvalue problem is now linear and can be solved relatively easily. The spatial linear stability of the flow is then solely defined by the sign of $\Im(i\alpha)$:

- if $\Im(i\alpha) < 0$ then the flow is spatially stable. Perturbations shed from the forcing sources consist in a spatially decaying wavepacket.
- if $\Im(i\alpha) > 0$ then the flow is spatially stable. Perturbations shed from the forcing sources consist in a spatially growing wavepacket.

whereas the eigenvectors provide the shape of spatially growing (decaying) perturbation. Among the parallel flows prone to spatial instabilities, one might cite for instance the Blasius boundary layer flow or the co-flowing mixing layer.

I.1.1.3 Absolute and convective instabilities

In the previous sections, the stability of the flow was solely defined by the growth either in time or space of infinitesimal perturbations. However, inifinitesimal perturbations can

also grow both in time AND space. The investigation of such perturbations requires further mathematical developments beyond the scope of the present introduction. Such investigation however falls within the framework of *absolute-convective linear stability analysis*. This concept is only defined for *open* shear flows (i.e. situations where fluid particles enter and leave the domain of interest in finite time without being recycled, in contrast to close flows in a finite box such as the lid-driven cavity flow) that break the Galilean invariance. Investigating the absolute-convective instability of such a flow allows to determine whether the considered flow behave as a *noise amplifier* sensitive to external noise (e.g. co-flowing mixing layers, flat plate boundary layer, ...) or as a *flow oscillator* with a well-defined frequency relatively insensitive to external noise (e.g. wakes at Reynolds numbers above the onset of the Karman vortex street).

Introducing the stream function ψ of the infinitesimal perturbation $\mathbf{q}(x, y)$ and following the notation introduced in [80], the linearised stability equations can be written as:

$$D\left(-\frac{\partial}{\partial x}, i\frac{\partial}{\partial t}, Re\right)\psi(x,t) = S(x,t) \tag{I.14}$$

where the term $D(\cdot)$ is the dispersion relation of the equations and $S(x,t)$ a source term specifiying the forcing imposed on the system in some localised interval both in time and space, and where the dependence in y has been dropped for the sake of simplicity. In the absence of forcing $S(x,t) = 0$ and one has to solve the spatial or temporal eigenvalue problems introduced previously. Introducing the Green function $G(x,t)$, i.e. the impulse response of the system, one can then write:

$$D\left(-\frac{\partial}{\partial x}, i\frac{\partial}{\partial t}, Re\right)G(x,t) = \delta(x)\delta(t) \tag{I.15}$$

where δ denotes the Dirac delta function. The Green function contains all the information regarding the spatio-temporal dynamics of the system. Depending on the value of the Reynolds number, several different impulse reponse of the system are possible. The concept of temporal and spatial instability are then defined as:

- if the flow is linearly stable then:

$$\lim_{t\to\infty} G(x,t) = 0 \text{ along all rays } x/t = const. \tag{I.16}$$

- if the flow is linearly unstable (temporal or spatial instability) then:

$$\lim_{t\to\infty} G(x,t) = 0 \text{ along at least one ray } x/t = const. \tag{I.17}$$

If unstable, the impulse response of the flow then consists of an unstable wavepacket confined in a wedge in the (x,t) plane growing either in time or space. Among linearly unstable flows, one can then make the distinction between absolute and convective instability:

- An unstable flow is said to be convectively unstable if:

$$\lim_{t\to\infty} G(x,t) = 0 \text{ along the ray } x/t = 0 \tag{I.18}$$

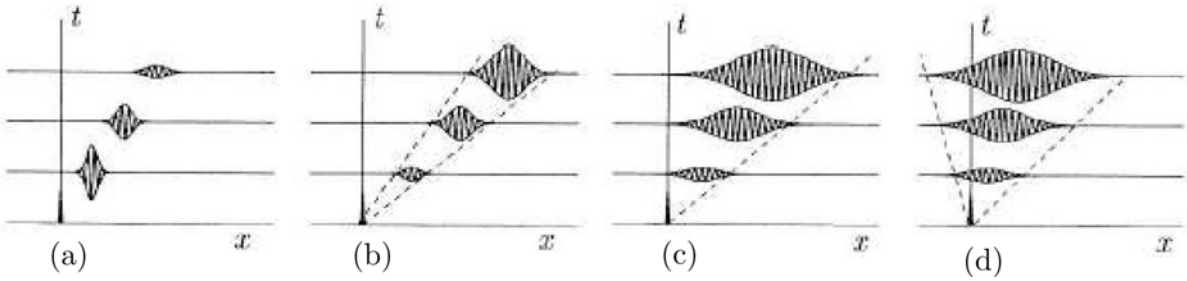

Figure I.4: Linear impulse response $G(x,t)$. (a) Linearly stable flow; (b) linearly convectively unstable flow; (c) marginally convectively/absolutely unstable flow; (d) absolutely unstable flow. Figure from [80].

- It said to be absolutely unstable if:

$$\lim_{t\to\infty} G(x,t) = \infty \text{ along the ray } x/t = 0 \tag{I.19}$$

These different impulse response of the system are summarised on figure I.4. If the flow is convectively unstable, a spatially unstable wavepacket is typically advected away from the source and let it eventually undisturbed. On the other hand, if the flow is absolutely unstable, the unstable wavepacket surround the source and eventually contaminates the whole medium. Extensive details about these concepts and the associated mathematical framework can be found in [80, 81].

I.1.1.4 2D local stability theory

So far, the different local stability theories introduced have assumed that the flow investigated has the form $\mathbf{U}_b = (U_b(y), 0, 0)^T$. One can however consider a flow slowly evolving in the streamwise direction and yet inhomogeneous both in the wall-normal and spanwise direction. The base flow then has the form $\mathbf{U}_b = (U_b(y,z), 0, 0)^T$. Such definition of the base flow allows one to investigate the stability of streaky boundary layer flows [34, 46] or Poiseuille flow in a rectangular duct [151] for instance. Based on the form of the base flow, the linearised Navier-Stokes equations (I.2) can be simplified as:

$$\begin{cases} \dfrac{\partial u}{\partial t} = -v\dfrac{\partial U_b}{\partial y} - w\dfrac{\partial U_b}{\partial z} - U_b\dfrac{\partial u}{\partial x} - \dfrac{\partial p}{\partial x} + \dfrac{1}{Re}\Delta u \\ \dfrac{\partial v}{\partial t} = -U_b\dfrac{\partial v}{\partial x} - \dfrac{\partial p}{\partial y} + \dfrac{1}{Re}\Delta v \\ \dfrac{\partial w}{\partial t} = -U_b\dfrac{\partial w}{\partial x} - \dfrac{\partial p}{\partial z} + \dfrac{1}{Re}\Delta w \\ \dfrac{\partial u}{\partial x} + \dfrac{\partial v}{\partial y} + \dfrac{\partial w}{\partial z} = 0 \end{cases} \tag{I.20}$$

As one can see, whereas the u velocity component of perturbation is only coupled with the v component in the local stability theory, in the case of bi-local stability theory it is now coupled both with v and w. Since these equations are no longer homogeneous in the

z direction, the solution to this set of equations can only be sought as:

$$\mathbf{q}(x,y,z) = \int_{L_\lambda}\int_{L_\alpha} \hat{\mathbf{q}}(y,z)e^{i\alpha x+\lambda t}\,\mathrm{d}\alpha\mathrm{d}\lambda + c.c \tag{I.21}$$

Introducing such normal mode expansion in (I.20) yields to:

$$\begin{cases} \lambda\hat{u} = -\hat{v}\dfrac{\partial U_b}{\partial y} - \hat{w}\dfrac{\partial U_b}{\partial z} - i\alpha U_b\hat{u} - i\alpha\hat{p} + \dfrac{1}{Re}\Delta_\alpha\hat{u} \\ \lambda\hat{v} = -i\alpha U_b\hat{v} - \dfrac{\partial\hat{p}}{\partial y} + \dfrac{1}{Re}\Delta_\alpha\hat{v} \\ \lambda\hat{w} = -i\alpha U_b\hat{w} - \dfrac{\partial\hat{p}}{\partial z} + \dfrac{1}{Re}\Delta_\alpha\hat{w} \\ i\alpha\hat{u} + \dfrac{\partial\hat{v}}{\partial y} + \dfrac{\partial\hat{w}}{\partial z} = 0 \end{cases} \tag{I.22}$$

where $\Delta_\alpha = \dfrac{\partial^2}{\partial y^2} + \dfrac{\partial^2}{\partial z^2} - \alpha^2$. As previously, one can investigate either the temporal, spatial or spatio-temporal linear stability of this system. For the temporal stability, one would then have to solve the linear generalised eigenvalue problem in λ:

$$\lambda\mathbf{B}\hat{\mathbf{q}} = \mathbf{J}\hat{\mathbf{q}} \tag{I.23}$$

with $\hat{\mathbf{q}} = (\hat{u},\hat{v},\hat{w},\hat{p})^T$ and where the matrices $\mathbf{J}$ and $\mathbf{B}$ are given by:

$$\mathbf{B} = \begin{pmatrix} 1 & 0 & 0 & 0 \\ 0 & 1 & 0 & 0 \\ 0 & 0 & 1 & 0 \\ 0 & 0 & 0 & 0 \end{pmatrix} \tag{I.24}$$

and:

$$\mathbf{J} = \begin{pmatrix} -i\alpha U_b + \dfrac{1}{Re}\Delta_\alpha & -\dfrac{\partial U_b}{\partial y} & -\dfrac{\partial U_b}{\partial z} & -i\alpha \\ 0 & -i\alpha U_b + \dfrac{1}{Re}\Delta_\alpha & 0 & -\dfrac{\partial}{\partial y} \\ 0 & 0 & -i\alpha U_b + \dfrac{1}{Re}\Delta_\alpha & -\dfrac{\partial}{\partial z} \\ i\alpha & \dfrac{\partial}{\partial y} & \dfrac{\partial}{\partial z} & 0 \end{pmatrix} \tag{I.25}$$

As previously, the linear temporal stability of $\mathbf{U_b} = (U_b(y,z),0,0)^T$ is solely governed by the sign of the real part of λ:

- if $\Re(\lambda) < 0$, the perturbation decays exponentially in time and the base flow $\mathbf{U}_b$ is then denoted as linearly stable.
- if $\Re(\lambda) > 0$, the perturbation grows exponentially in time and the base flow $\mathbf{U}_b$ is then denoted as linearly unstable.

Figure I.5 provides an example of a flow inhomogeneous in both the wall-normal and spanwise directions and yet slowly evolving in the streamwise direction. It depicts slices of a streaky boundary layer flow for which a parallel flow assumption is valid far enough from the roughness element. Such problem, treated in the fully three-dimensional global stability framework in the present thesis, has been investigated by Cossu & Brandt [46], Brandt [34] or Piot *et al.* [122] based on bi-local approach.

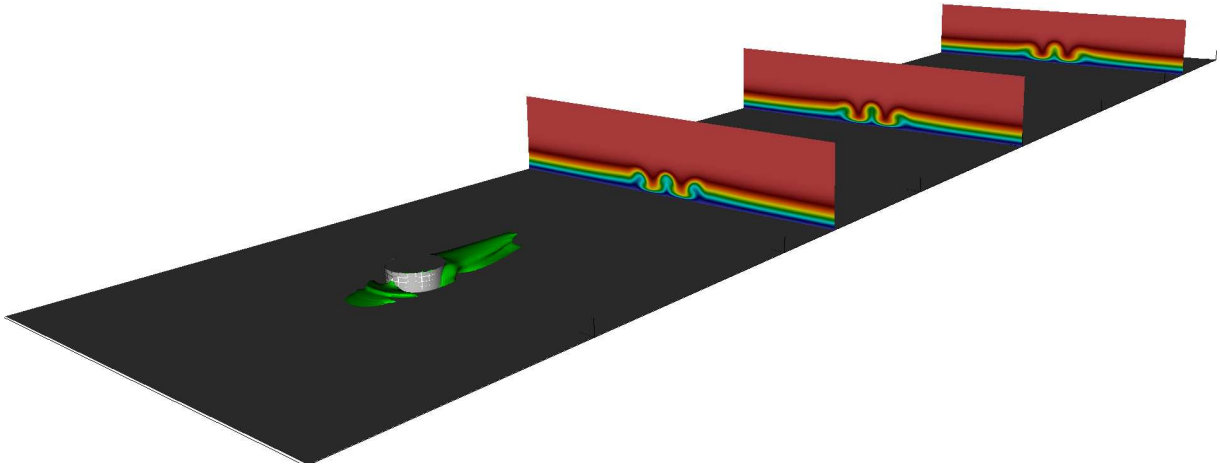

Figure I.5: Visualisation of the streamwise velocity component of the roughness-induced boundary layer flow in several cross-streamwise planes. The green isosurface highlights the spatial extent of the reversed flow region developing right downstream the cylindrical roughness element.

I.1.1.5 Global stability theory

Though they allow one to have a deep understanding of the instability mechanisms, all the analyses introduced so far are greatly limited by the parallel flow assumption they rely on. Unfortunately, in most applications such assumption of the velocity profile does not hold. To circumvent this problem, improvements have been brought to the local stability theory in the form of the weakly non-parallel flow assumption or the parabolised stability equations. Such approachs, based on a length scale separation hypothesis, allow the investigation of weakly non-parallel flows as the flat plate boundary layer [30] or the corner flow [10] for instance. However, due to the length scale separation hypothesis they rely on, such approach still is enable to allow the investigation of strongly non-parallel flows where separation can occur. Since the early 2000's, with the increase of computational ressources available, some light has been shed on the linear instability mechanisms responsible for transition in two-dimensional strongly non-parallel flows $\mathbf{U}_b = (U_b(x,y), V_b(x,y), 0)^T$. Investigating the stability of such two-dimensional flow toward infinitesimal perturbations now falls within the framework of so-called *global stability theory*.

In order to derive the global stability equations governing the evolution of infinitesimal perturbations evolving on strongly non-parallel two-dimensional flows, let us start from the three-dimensional linearised Navier-Stokes equations (I.2). Assuming the base flow considered is of the form $\mathbf{U}_b = (U_b(x,y), V_b(x,y), 0)^T$, the linearised Navier-Stokes

equations (I.2) can be simplified as:

$$\begin{cases} \dfrac{\partial u}{\partial t} = -u\dfrac{\partial U_b}{\partial x} - v\dfrac{\partial U_b}{\partial y} - U_b\dfrac{\partial u}{\partial x} - V_b\dfrac{\partial u}{\partial y} - \dfrac{\partial p}{\partial x} + \dfrac{1}{Re}\Delta u \\ \dfrac{\partial v}{\partial t} = -u\dfrac{\partial V_b}{\partial x} - v\dfrac{\partial V_b}{\partial y} - U_b\dfrac{\partial v}{\partial x} - V_b\dfrac{\partial v}{\partial y} - \dfrac{\partial p}{\partial y} + \dfrac{1}{Re}\Delta v \\ \dfrac{\partial w}{\partial t} = -U_b\dfrac{\partial w}{\partial x} - V_b\dfrac{\partial w}{\partial y} - \dfrac{\partial p}{\partial z} + \dfrac{1}{Re}\Delta w \\ \dfrac{\partial u}{\partial x} + \dfrac{\partial v}{\partial y} + \dfrac{\partial w}{\partial z} = 0 \end{cases} \tag{I.26}$$

Whereas the local stability equations (I.4) are homogeneous both in the x and z directions, this set of equations is only homogeneous in the z direction. Nonetheless, the solution to these equations can still be sought in the form of normal modes:

$$\mathbf{q}(x, y, z) = \int_{L_\lambda}\int_{F_\beta} \hat{\mathbf{q}}(x, y)e^{i\beta z+\lambda t}\ \mathrm{d}\beta\mathrm{d}\lambda + c.c \tag{I.27}$$

with $\hat{\mathbf{q}}(x, y) = (\hat{\mathbf{u}}, \hat{p})^T$ being now a normal mode depending on both the x and y spatial directions, β the spanwise wavenumber of the normal mode considered and λ its complex frequency. As previously, since the equations considered are linear, one can solve them for each of the normal mode. The global stability equations then read:

$$\begin{cases} \lambda\hat{u} = -\hat{u}\dfrac{\partial U_b}{\partial x} - \hat{v}\dfrac{\partial U_b}{\partial y} - U_b\dfrac{\partial \hat{u}}{\partial x} - V_b\dfrac{\partial \hat{u}}{\partial y} - \dfrac{\partial \hat{p}}{\partial x} + \dfrac{1}{Re}\left(\dfrac{\partial^2}{\partial x^2} + \dfrac{\partial^2}{\partial y^2} - \beta^2\right)\hat{u} \\ \lambda\hat{v} = -\hat{u}\dfrac{\partial V_b}{\partial x} - \hat{v}\dfrac{\partial V_b}{\partial y} - U_b\dfrac{\partial \hat{v}}{\partial x} - V_b\dfrac{\partial \hat{v}}{\partial y} - \dfrac{\partial \hat{p}}{\partial y} + \dfrac{1}{Re}\left(\dfrac{\partial^2}{\partial x^2} + \dfrac{\partial^2}{\partial y^2} - \beta^2\right)\hat{v} \\ \lambda\hat{w} = -U_b\dfrac{\partial \hat{w}}{\partial x} - V_b\dfrac{\partial \hat{w}}{\partial y} - i\beta\hat{p} + \dfrac{1}{Re}\left(\dfrac{\partial^2}{\partial x^2} + \dfrac{\partial^2}{\partial y^2} - \beta^2\right)\hat{w} \\ \dfrac{\partial \hat{u}}{\partial x} + \dfrac{\partial \hat{v}}{\partial y} + i\beta\hat{w} = 0 \end{cases} \tag{I.28}$$

It is worthy to note that when a strictly two-dimensional perturbation is considered, these equations can be further simplified using a stream function Ψ formulation of the equations. However, there exists no equivalent form of the Squire theorem for the global stability problem. More importantly, numerous studies have highlighted that spanwise periodic perturbations behave very differently from strictly two-dimensional ones. Nonetheless, depending on the problem of interest, the global stability of the flow can be investigated using different tools:

- Temporal stability: investigation of the asymptotic time evolution of infinitesimal perturbations.
- Resolvent analysis: investigation of the response of the flow to harmonic forcing.
- Transient growth analysis: investigation of the short-time dynamics and transient amplification of infinitesimal perturbations.

Whereas the wavenumber of the normal mode in the local stability framework could be complex, one must be aware that in the global stability framework, the wavenumber characterising the perturbation is only allowed to be a real number. Since the scope of the present thesis focuses on global stability analysis of fully three-dimensional flows, only a very brief illustration of the global stability of two-dimensional flows will be given. For the sake of conciseness, the transient growth analysis in the global stability framework is only treated in chapter II. Moreover, since the signaling problem in the global stability framework is beyond the scope of the present work, it will not be presented. For details, the reader is however referred to Monokroussos *et al.* [116] for an illustration on a fully three-dimensional flow configuration.

Stability analysis

As for the temporal local stability of parallel flows, the global stability of two-dimensional flow is governed by the spectrum of eigenvalues of the linearised Navier-Stokes operator. The global stability equations (I.28) can be recast into a linear generalised eigenvalue problem in λ:

$$\lambda \mathbf{B}\hat{\mathbf{q}} = \mathbf{J}\hat{\mathbf{q}} \tag{I.29}$$

where the mass matrix $\mathbf{B}$ and the Jacobian matrix $\mathbf{J}$ are given by:

$$\mathbf{B} = \begin{pmatrix} 1 & 0 & 0 & 0 \\ 0 & 1 & 0 & 0 \\ 0 & 0 & 1 & 0 \\ 0 & 0 & 0 & 0 \end{pmatrix} \tag{I.30}$$

and

$$\mathbf{J} = \begin{pmatrix} -\frac{\partial U_b}{\partial x} - (\mathbf{U_b} \cdot \nabla) + \frac{1}{Re}\Delta_\beta & -\frac{\partial U_b}{\partial y} & 0 & -\frac{\partial}{\partial x} \\ -\frac{\partial V_b}{\partial x} & -\frac{\partial V_b}{\partial y} - (\mathbf{U_b} \cdot \nabla) + \frac{1}{Re}\Delta_\beta & 0 & -\frac{\partial}{\partial y} \\ 0 & 0 & -(\mathbf{U_b} \cdot \nabla) + \frac{1}{Re}\Delta_\beta & -i\beta \\ \frac{\partial}{\partial x} & \frac{\partial}{\partial y} & i\beta & 0 \end{pmatrix} \tag{I.31}$$

with $\Delta_\beta = \partial_x^2 + \partial_y^2 - \beta^2$. The asymptotic time evolution of the infinitesimal perturbation $\hat{\mathbf{q}}(x, y)$ is then governed by the sign of $\Re(\lambda)$:

- if $\Re(\lambda) < 0$, the perturbation decays exponentially in time and the base flow $\mathbf{U}_b$ is then labelled as being globally stable.
- if $\Re(\lambda) > 0$, the perturbation grows exponentially in time and the base flow $\mathbf{U}_b$ is then labelled as being globally unstable.
- if $\Re(\lambda) = 0$, the system is said to be neutral. As for the local stability, one can then use global weakly non-linear analysis to determine the actual stability of the flow.

Illustration of a two-dimensional globaly unstable lid-driven cavity flow is given in chapter II, whereas figure I.6 depicts the two-dimensional base flow and the two-dimensional global mode obtained from the global stability of a detached boundary layer flow. It

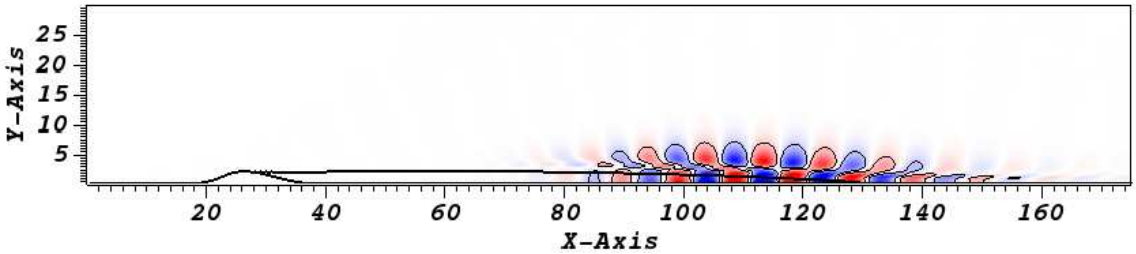

Figure I.6: Leading unstable two-dimensional global mode of the detached boundary layer flow at $Re = 700$. The geometry considered is the same as in [58]. Solid black line depicts the spatial extent of the base flow's recirculation bubble.

is worthy to note that global instability and local absolute instability might be closely related. Indeed, it has been shown by Hammond & Redekopp [77] for two-dimensional separated flows that local absolute instability of the flow within the reversed flow region could be a sufficient condition for a global instability of the whole flow. On the other hand, from the work of Marquillie & Ehrenstein [113] on the global instability of a detached boundary layer flow, it appears that local absolute instability of the flow is not a necessary condition for global instability. This point is however still an open question receiving a lot of attention.

Finally, from a purely practical point of view, since global stability analysis requires two spatial directions to be discretised, a larger number of degrees of freedom are necessary to characterise the perturbation compared to local stability analysis, typically $O(50\ 000)$ degrees of freedom. As a consequence, the matrices involved in the computation are much more computationally expensive to construct and solving the generalised eigenvalue problem with direct solvers might not be the most efficient way. To circumvent this problem, one might then use iterative eigenvalue solvers. Among these eigenvalue solvers, the most famous is the Arnoldi method introduced in 1951 by W. E. Arnoldi [16] and some of its variants as the Implicitely Restarted Arnoldi Method (IRAM) introduced by Lehoucq & Sorensen [100] in 1996. Nowadays, iterative eigenvalue solvers based on the exponential propagator $e^{\mathbf{J}t}$ are more and more popular (see Edwards *et al.* [57] and Bagheri *et al.* [20]). For details about these eigenvalue sovlers, the reader is referred to the book by Antoulas [14] as well as to the numerical aspects regarding this part of the present thesis.

I.2 Context and Objectives

Context

The present PhD thesis is part of a broader project entitled SICOGIF (SImulation and COntrol of Geometry Induced Flows) under the supervision of Uwe Ehrenstein and funded by the French National Agency for Research (ANR). Started in 2009 and finished in August 2013, this project involved several different parties among which:

- IRPHE, Aix-Marseille Université: Uwe Ehrenstein, Thomas Leweke, Pierre-Yves Passaggia
- Laboratatoire Jean Dieudonné, Université de Nice Sophia Antipolis: François Gallaire and Edouard Boujo
- DynFluid, Arts et Métiers ParisTech: Jean-Christophe Robinet
- LMFA@Université Jean Monnet, Saint-Etienne (2009-2011) and LML, Université de Lille 1 (2011-2014): Emmanuel Leriche, Alexandre Delache

Its aim was to improve our understanding of instability and transition in complex separated flows as well as try to control them. Two configurations were originally part of it: *i*) the flow over a two-dimensional bump (IRPHE, EPFL) and *ii*) the stenotic pipe flow (IRPHE, DynFluid, LML). These two flow configurations have been both investigated numerically and experimentally.

Objectives

Recently, Bagheri *et al.* [21] and Ilak *et al.* [82] have performed the first ever global stability analyses of fully three-dimensional flows. Such breakthrough has been made possible by the constant increase of computational ressources available as well as to the development of new iterative eigenvalue solvers [20, 57]. Following their footsteps, the major aim of the present thesis is to develop the tools necessary to perform similar investigations. As to illustrate how fully three-dimensional global stability analyses can improve our understanding of flow instability and transition as well as its connection to two-dimensional global stability analyses and its limitations, three different cases have been considered:

- the lid-driven cavity flow with spanwise end-walls,
- the asymmetric stenotic pipe flow,
- the roughness-induced boundary layer transition

Each of these cases has very different applications and properties. On the one hand, the lid-driven cavity (LDC) flow is a fully three-dimensional confined flow with applications essentially in the paper coating industry. Nonetheless, despite its apparent simplicity, the flow in a lid-driven cavity exhibits some of the major features of fluid dynamics: boundary layers, shear layers, vortices and velocity streaks. These properties thus make the LDC flow a perfect candidate for three-dimensional global stability analysis and it is believed that improving our understanding of its transition mechanisms might eventually help as well our understanding of the transition of various others flows exhibiting the same features. On the other hand, the flow in a stenotic pipe with rigid walls is an open shear flow having applications in the bio-medical area. It exhibits a three-dimensional reversed flow region and shear layers as well as a confined jet. For small asymmetry of the stenosis, one might think that the flow can be considered at the first order as being almost axisymmetric. Yet, as explained in chapter IV, the global stability properties of the strictly axisymmetric stenotic pipe flow and that of the very slightly asymmetric one are very different. Finally, the boundary layer flow over a three-dimensional roughness

element is an open shear flow having applications mostly in aerodynamics. The associated roughness-induced transition has been extensively investigated since the 1950's and still is nowadays quite a challenging fundamental problem with yet practical applications. Until very recently, this problem has enssentially been addressed by direct numerical simulations and local stability theory [35]. Though it is the most computationally challenging problem treated in this PhD thesis, results presented in chapter V stunningly highlight the improved understanding one might gain from fully three-dimensional global stability anlysis.

Outlines

This manuscript is organised as follows. First, the different numerical methods and tools used during this PhD are presented in chapter II. It includes a short presentation of the spectral elements code Nek 5000 [63], the fully three-dimensional global stability equations and the Arnoldi method employed to solve the resulting eigenvalue problem, as well as an introduction to the Koopman mode decomposition and to the optimal perturbation theory. In chapter III, the instability and transition taking place in three-dimensional lid-driven cavity flows are investigated. More particularly, the influence of the spanwise extent of the cavity on the stability properties of the flow is studied along with some insights given about the chaotic dynamics observed in a cubical lid-driven cavity at a moderate Reynolds number. Chapter IV summarises results obtained regarding the global stability of the flow within an asymmetric stenotic pipe. Focus is given about the influence of the stenosis eccentricity on the stability of the flow. Then, chapter V details the investigation conducted on the roughness-induced transition to turbulence in boundary layer flows. This transition has been investigated using the joint application of fully three-dimensional analyses and direct numerical simulations. Finally, conclusions are drawn in the last chapter along with perspectives.

Chapter II

Numerical methods

Contents

II.1 Introduction to the spectral elements code Nek5000 ..... **19**
II.1.1 Spatial discretisation 20
II.1.2 Time discretisation 25
II.2 Steady states computation **27**
II.3 Modal decomposition **30**
II.3.1 Global linear stability, time-stepping and Arnoldi algorithm 30
II.3.2 Koopman modes decomposition 36
II.4 Optimal perturbations and Transient growth analysis **40**
II.4.1 Adjoint linearised Navier-Stokes equations 42
II.4.2 Optimal perturbation and eigenvalue analysis of $\mathbf{M}^*\mathbf{M}$ 43

II.1 Introduction to the spectral elements code Nek5000

"In the mid-eighties Paul Fischer, Lee Ho, and Einar Rønquist (M.I.T) developed the incompressible fluid flow solver NEKTON, with technical input from A. Patera and Y. Maday. A commercial version was brought to market by Fluent, Inc, as NEKTON 2.0, in 1996. Paul Fischer branched off a research version of the code known as Nek5000. This code was recognized with the Gordon Bell prize for algorithmic quality and sustained parallel performance in 1999. Today, Fischer's code is released as an open source project covering a broad range of applications including thermal hydraulics of reactor cores, transition in vascular flows, ocean current modeling and combustion. More than two dozen research institutions and more than 100 users worldwide are using the code. Leading edge scalability has been demonstrated up to 262'144 processors producing more than 170TFlops (Extreme Scaling Workshop 2010 Report)."

from https://nek5000.mcs.anl.gov/index.php/Main_Page

II.1.1 Spatial discretisation

The non-linear Navier-Stokes equations as well as their linearised counterparts are partial differential equations (PDE) and as such require to be spatially discretised in order to be solved numerically. The code Nek 5000 [62] used for this PhD thesis is based on the Legendre spectral elements method. This method, introduced in 1984 by A. Patera [119], shares close connections with the well-known finite elements discretisation and, as such, is part of the family of approximation schemes based on the Galerkin method. Only a brief introduction to this discretisation method will be given in the present manuscript. For further details, the reader is referred to the books by Deville *et al.* [52] and Karniadakis & Sherwin [87]. For the sake of simplicity, the notation used in this section will be the same as the one in [52].

To gain clarity, the spectral elements spatial discretisation will be applied to a one-dimensional non-linear advection-diffusion problem: the Burgers equation. Named after Johannes Martinus Burgers (1895-1981), this non-linear partial differential equation shares some connections with the Navier-Stokes equations. Introducing the velocity u and the viscous coefficient ν, the one-dimensional Burgers equation reads:

$$\begin{cases} \dfrac{\partial u}{\partial t} + u\dfrac{\partial u}{\partial x} = \nu\dfrac{\partial^2 u}{\partial x^2}, \\ u(t=0,x) = u^0 \\ u(t,x=-1) = 1;\ u(t,x=1) = -1 \end{cases} \tag{II.1}$$

The computational domain considered is $\Omega := \{x \in [-1,1]\}$. Equation (II.1) is moreover subject to dirichlet boundary conditions at each end of the computational domain Ω. Though equation (II.1) appears to share close connections with the Navier-Stokes equations, Hopf [79] and Cole [45] have shown that it lacks the most important property attributed to turbulence: its solutions do not exhibit chaotic features like sensitivity to initial conditions. Despite this major difference with the Navier-Stokes equations, equation (II.1) exhibits a similar non-linearity and often serves as a benchmark for numerical methods, hence it is used in the present introduction to the spectral element method.

II.1.1.1 Variational formulation of the equations

As mentionned, the spectral elements method is part of the approximation schemes based on the Galerkin method. Partial differential equations discretised using such technique need to be solved in what is known as the *weak form*. Introducing a set of test functions $v(x)$ belonging to a Sobolov space $\mathcal{H}_0^1(\Omega)$, one can recast equation (II.1) into its weak counterpart:

$$\int_\Omega v\frac{\partial u}{\partial t}\mathrm{d}x + \int_\Omega vu\frac{\partial u}{\partial x}\mathrm{d}x = -\nu\int_\Omega \frac{\partial v}{\partial x}\frac{\partial u}{\partial x}\mathrm{d}x \tag{II.2}$$

where the right-hand side has been treated using integration by parts and the dependence on the variables x and t has been dropped for the sake of clarity. Let us now consider a set of $N+1$ basis functions $\phi_i(x)$ such that:

$$\begin{cases} u(x,t) = \sum_{i=0}^{N} \phi_i(x) u_i(t) \\ v(x) = \phi_j(x) \ 0 \leq j \leq N \end{cases} \tag{II.3}$$

Introducing such expansion of $u(x,t)$ and $v(x)$ into the weak formulation of the Burgers equation (II.2) yields to:

$$\left(\int_\Omega \phi_j \phi_i \mathrm{d}x \right) \frac{\mathrm{d}u_i}{\mathrm{d}t} + \left(\int_\Omega \phi_j \phi_i u_i \frac{\mathrm{d}\phi_i}{\mathrm{d}x} \mathrm{d}x \right) u_i = - \left(\nu \int_\Omega \frac{\mathrm{d}\phi_j}{\mathrm{d}x} \frac{\mathrm{d}\phi_i}{\mathrm{d}x} \mathrm{d}x \right) u_i \tag{II.4}$$

Equation (II.4) can be recast in matrix-vector form:

$$\mathcal{M} \frac{\mathrm{d}}{\mathrm{d}t} \mathbf{u} + \mathcal{C}(\mathbf{u}) \mathbf{u} + \mathcal{K} \mathbf{u} = 0 \tag{II.5}$$

with $\mathbf{u} = (u_0, \cdots, u_N)^T$ and where $\mathcal{M}$ is the mass matrix, $\mathcal{C}(\mathbf{u})$ the convective operator and $\mathcal{K}$ the stiffness matrix. The ij^{th} entries of these matrices are given by:

$$\begin{aligned} \mathcal{M}_{i,j} &= \int_\Omega \phi_i \phi_j \mathrm{d}x, \\ \mathcal{C}_{i,j}(\mathbf{u}) &= \int_\Omega \phi_i \phi_j \frac{\mathrm{d}\phi_i}{\mathrm{d}x} \mathrm{d}x, \\ \mathcal{K}_{i,j} &= \nu \int_\Omega \frac{\mathrm{d}\phi_j}{\mathrm{d}x} \frac{\mathrm{d}\phi_i}{\mathrm{d}x} \mathrm{d}x \end{aligned} \tag{II.6}$$

To this point, derivation of the variational form of the Burgers equation is similar to any Galerkin-like discretisation method. Differences between the different discretisation schemes result from the choice of the test and trial functions.

II.1.1.2 Legendre polynomials and Legendre spectral elements discretisation

Equation (II.5) resulting from the weak formulation of the Burgers equation (II.1) is a common feature to all approximation schemes based on the Galerkin method. The determination of the particular approximation scheme used is then determined by the choice of the set of test and trial functions $\phi_i(x)$. In the code Nek 5000 [62], these functions are based on the Legendre polynomials. This specific choice of function basis is where the spectral element method greatly differs from the finite elements method: orthogonality of the functions is related to the topological (local extension) and analytical nature of the function basis chosen in the SEM framework. Moreover, the Legendre polynomials provide the best approximation in the H^1 norm.

Let us consider the partition Δ_E of the segment (a,b) with E elements such that:

$$\Delta_E : a = x_0 < x_1 < x_2 < \cdots < x_{E-1} < x_E = b \tag{II.7}$$

Each element of this partition is defined as $\Omega^e := \{x \ ; \ x_{e-1} < x < x_e\}, \ 1 \leq e \leq E$, and let $\hat{\Omega} := \{\xi \ ; \ -1 \leq \xi \leq 1\}$ be the reference (or parent) element onto which each element

Ω^e will be mapped using an affine transformation. For the sake of simplicity, an equi-repartition of the elements is considered such that they are all of length $h_e = (b-a)/E$. Only the discretisation of the problem within the reference element will be presented, for further details readers are referred to [52]. Let $\Xi_{N+1} = \{\xi_0, \xi_1, \ldots, \xi_N\}$ be the ordered set of $N+1$ Gauss-Lobatto-Legendre (GLL) quadrature points on $\hat{\Omega}$. These points are the roots of the following equation:

$$(1-\xi^2)L'_N(\xi) = 0 \tag{II.8}$$

where L'_N is the first derivative of the Legendre polynomial of degree N. The Lagrange interpolation polynomial of any function $u(\xi)$ on the GLL quadrature points is given by:

$$I_N u(\xi) = \sum_{j=0}^{N} u(\xi_j)\pi_j(\xi) \tag{II.9}$$

with $\{\pi_j(\xi)\}_{j=0}^{N}$ being the associated interpolation basis of degree N. Elements of this basis are related to the set of basis functions $\phi_i(x)$ by an affine transformation such that:

$$\phi_i(x)|_{\Omega_e} = \pi_i(\xi^e(x)) \tag{II.10}$$

with the functions π_i given by:

$$\pi_j(\xi) = \frac{-1}{N(N+1)}\frac{(1-\xi^2)L'_N(\xi)}{(\xi-\xi_j)L_N(\xi_j)},\ 0 \leq j \leq N \tag{II.11}$$

As to further illustrate the difference between the Legendre spectral element and the finite element methods, figure II.1 depicts the first five functions of (a) the Legendre-SEM function basis and (b) the classical FEM, respectively.

Based on this Legendre spectral element basis, the spectral elements approximation of $u_N^e(x)$ of degree N in the element Ω^e mapped onto the reference element $\hat{\Omega}$ is:

$$u_N^e(x) = \sum_{j=0}^{N} u_j^e \pi_j(\xi^e(x)) \tag{II.12}$$

with $\left\{u_j^e\right\}_{j=0}^{N}$ the nodal values of the unknown vector field u in Ω^e. Replacing $\phi(x)$ in (II.4) by the Legendre basis functions $\pi_j(\xi)$ and applying Gaussian quadrature rule based on the GLL nodes to evaluate numerically the different integrals yields:

$$\mathbf{M}_{ij}^e = \frac{h_e}{2}\rho_i\delta_{ij} \tag{II.13}$$

for the discretised elemental mass matrix, where ρ_i denote the GLL quadrature weight at the ith GLL node. The discretised elemental stiffness matrix and the non-linear convection operator are given by:

$$\begin{aligned} \mathbf{K}_{ij}^e &= \nu\frac{2}{h_e}\sum_{m=0}^{N}\rho_m D_{N,mi}^{(1)} D_{N,mj}^{(1)} \\ \mathbf{C}(\mathbf{u})_{ij} &= \rho_i u_i D_{N,ij}^{(1)} \end{aligned} \tag{II.14}$$

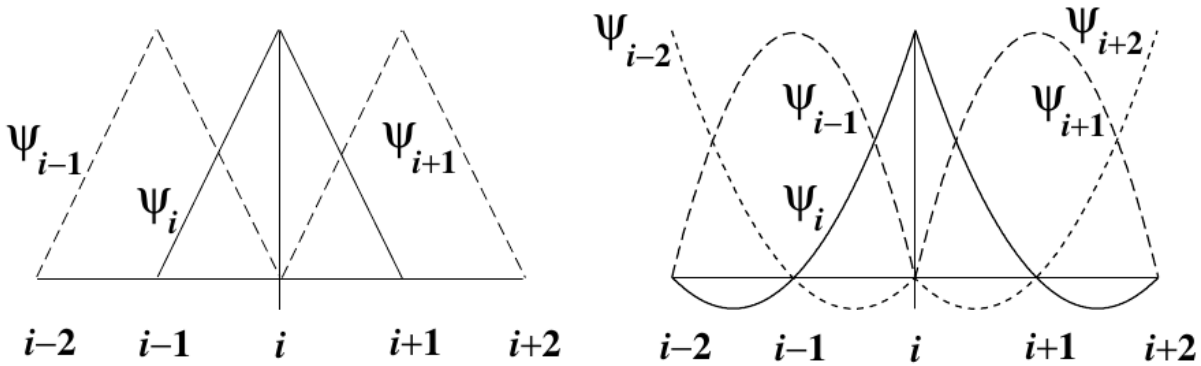

(a)

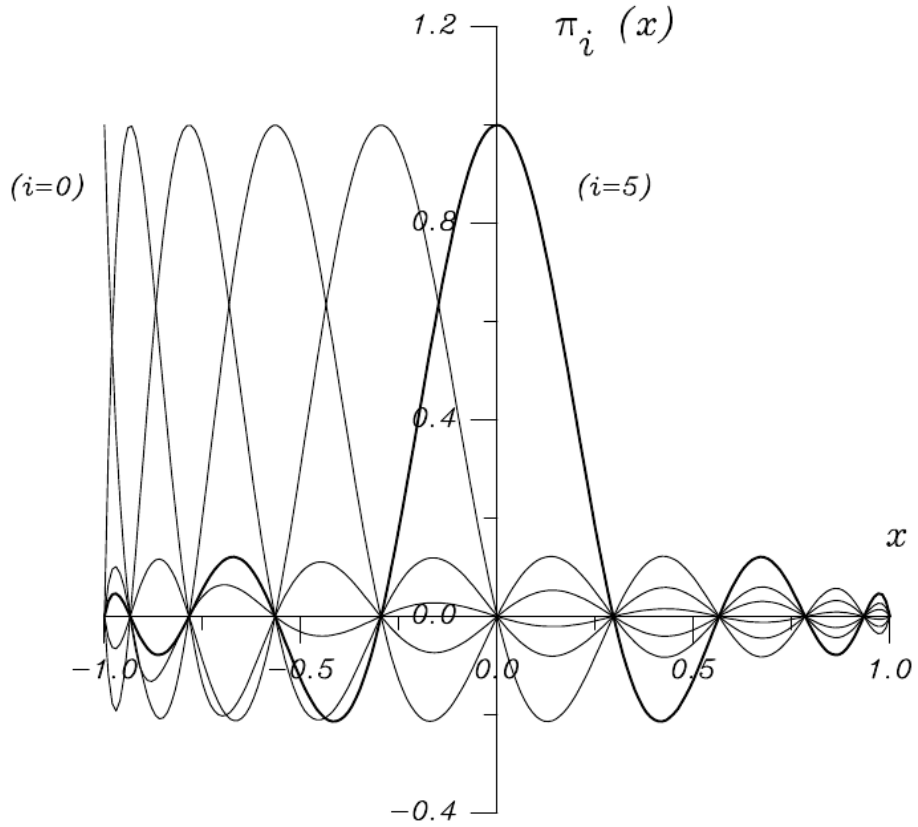

(b)

Figure II.1: Example of (a) the finite element basis and (b) the Legendre spectral element basis for $N = 10$. Figures from [52].

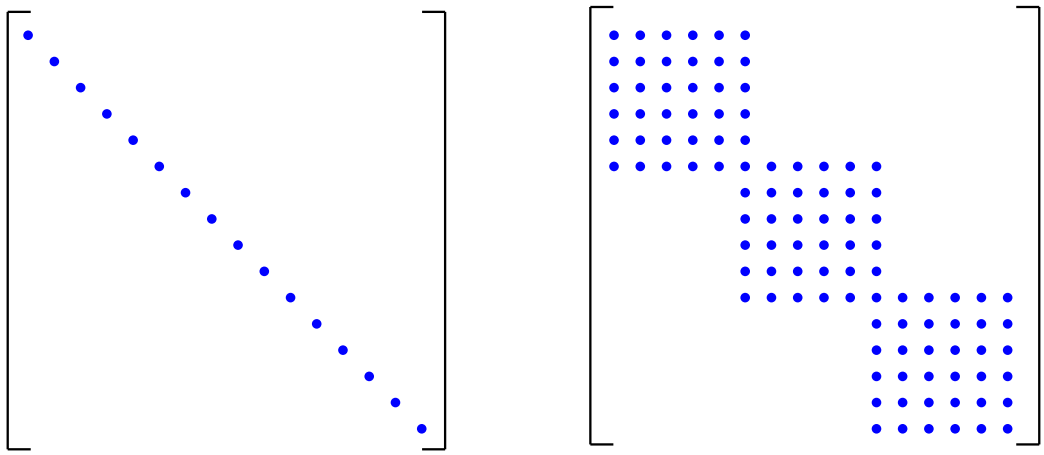

(a) Global mass matrix $\mathbf{M}$ (b) Global stiffness matrix $\mathbf{K}$

Figure II.2: Structure of the global mass and stiffness matrices for $E = 3$ and $N = 5$.

where the differentiation matrix $D_N^{(1)}$ is given by:

$$D_{N,ij}^{(1)} = \frac{\mathrm{d}\pi_j}{\mathrm{d}\xi}(\xi = \xi_i) = \begin{cases} \dfrac{L_N(\xi_i)}{L_n(\xi_j)} \dfrac{1}{\xi_i - \xi_j}, & i \neq j, \\ -\dfrac{(N+1)N}{4}, & i = j = 0, \\ \dfrac{(N+1)N}{4}, & i = j = N, \\ 0 \text{ otherwise} \end{cases} \tag{II.15}$$

In order to assemble the contribution of all elements Ω^e to the global matrices, one has to use direct stiffness summation which is beyond the scope of this rapid introduction to spectral elements. The semi-discretised equation however finally reads:

$$\mathbf{M}\frac{d}{dt}\mathbf{u} + \mathbf{C}(\mathbf{u})\mathbf{u} + \mathbf{K}\mathbf{u} = 0 \tag{II.16}$$

Figure II.2 displays the structure of the global stiffness $\mathbf{K}$ and mass $\mathbf{M}$ matrices resulting from the direct stiffness summation. As one can see, the mass matrix $\mathbf{M}$ exhibits a diagonal structure (it usually is tri- or penta-diagonal in the finite elements method), whereas the stiffness matrix $\mathbf{K}$ exhibits a block-diagonal structure, another major difference with the finite element method where the matrices are sparse. The stiffness matrix is moreover symmetric and positive-definite.

On boundary conditions

So far, nothing has been said about the implementation of boundary conditions. In the spectral elements method, these conditions can be imposed by several different ways.

Though the use of Lagrange multipliers is not the way boundary conditions are implemented within NEK 5000, this method will be presented here due to the resemblance of the resulting system with the Navier-Stokes equations. Introducing the Lagrange multiplier p, equation (II.16) along with its constraints can be rewritten as:

$$\begin{cases} \mathbf{M}\frac{d}{dt}\mathbf{u} + \mathbf{C}(\mathbf{u})\mathbf{u} = -\mathbf{K}\mathbf{u} - \mathbf{D}^T p \\ \mathbf{D}\mathbf{u} = 0 \end{cases} \tag{II.17}$$

Assuming the constraint $\mathbf{D}\mathbf{u} = 0$ is similar to the divergence-free constraint $\nabla \cdot \mathbf{u} = 0$ and $\mathbf{D}^T p$ similar to the pressure gradient term ∇p, then the resemblance to the Navier-Stokes equations is striking. From this point of view, the pressure p in the incompressible Navier-Stokes equations can actually be seen to play the role of a Lagrange multiplier in order to impose the divergence-free constraint. One major difference remains however the way this pressure p is treated in the spectral elements discretisation of the Navier-Stokes equations. Further details about this can be found in [52].

Remarks about the meshing process

As for any discretisation of partial differential equations, a mesh is a pre-requisite. Meshing a geometry using spectral elements is not as straightforward as in finite differences for instance. Indeed, as it has just be shown, one has to bear in mind that spectral elements mesh relies on two different grid levels: the spectral elements distribution itself and the polynomial approximation within each element. Figures II.3(a) and (b) depict a typical elemental mesh for a square lid-driven cavity problem along with the resulting mesh when polynomial approximation of order 7 is used, respectively. In order to refine the mesh, two different types of refinements can be used:

- One can add more spectral elements to the spectral elements distribution, a refinement known as h-type.
- Or keeping the spectral elements distribution unchanged and increases the polynamial order within each of the spectral element. This is known as p-type refinement.

In all the different studies presented in this manuscript, p-type refinement has been prefered to h-type refinement. Indeed, p-type refinement only requires an increase of the number of Legendre polynomials used while h-type requires the construction of a new mesh.

II.1.2 Time discretisation

Let us consider the semi-discretised formulation (II.17) of the Burgers equation just established. As we have just seen, this problem is equivalent to the semi-discretised formulation of the Navier-Stokes equations. In order to avoid the algorithmic difficulties resulting from an implicit treatment of the non-symmetric non-linear terms $\mathbf{C}(\mathbf{u})\mathbf{u}$, the remaining possibility is to treat them explicitly. The temporal discretisation scheme used in NEK 5000 is the semi-implicit scheme BDF_k/EXT_k: the viscous terms are discretised implicitly using

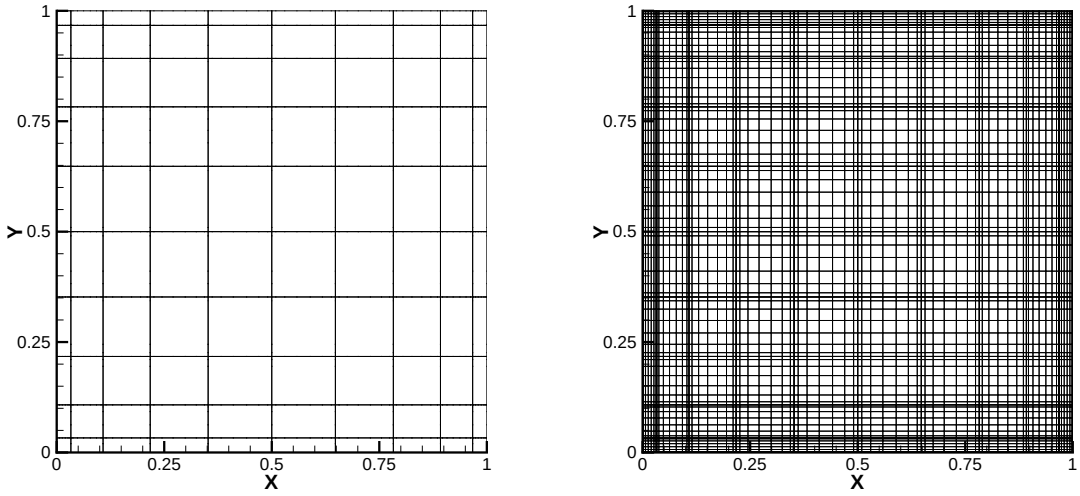

(a) (b)

Figure II.3: (a) Elemental mesh for the lid-driven cavity flow problem. 10 elements are used in each direction and located along a GLL grid. (b) Resulting mesh using a polynomial approximation of order 7 within each element.

a backward differentiation scheme of order k whereas the non-linear terms are treated explicitly by an extrapolation of order k, with $k = 2$ or 3. For $k = 3$, the fully discretised Burgers (Navier-Stokes) problem then reads:

$$\left(\frac{11}{6\Delta t}\mathbf{M} + \mathbf{K}\right)\underline{u}_i^{n+1} - \mathbf{D}_i^T\underline{p}^{n+1} = \frac{\mathbf{M}}{\Delta t}\left(3\underline{u}_i^n - \frac{3}{2}\underline{u}_i^{n-1} + \frac{1}{3}\underline{u}_i^{n-2}\right) - \left(3\mathbf{C}\underline{u}_i^n - 3\mathbf{C}\underline{u}_i^{n-1} + \mathbf{C}\underline{u}_i^{n-2}\right) \tag{II.18}$$

Adding $\mathbf{D}_i^T\underline{p}^n$ to both sides and rewritting the right-hand side as a simple forcing vector $\mathbf{M}\underline{\mathbf{F}}_i^n$, equation (II.18) along with the divergence-free condition can be recast into the following matrix form of the unsteady forced Stokes problem:

$$\begin{pmatrix} \mathbf{H} & -\mathbf{D}^T \\ -\mathbf{D} & 0 \end{pmatrix} \begin{pmatrix} \underline{\mathbf{u}}^{n+1} \\ \underline{\delta p}^{n+1} \end{pmatrix} = \begin{pmatrix} \mathbf{M}\underline{\mathbf{F}}^n + \mathbf{D}^T\underline{p}^n \\ 0 \end{pmatrix} \tag{II.19}$$

where $\mathbf{H}$ is known as the Helmholtz operator. This matrix problem can be solved using a LU decomposition. Introducing a matrix $\mathbf{Q}$ for the sake of projection onto a divergence-free space, the solution to such LU decomposition is a two-step procedure:

$$\begin{pmatrix} \mathbf{H} & 0 \\ -\mathbf{D} & -\mathbf{D}\mathbf{Q}\mathbf{D}^T \end{pmatrix} \begin{pmatrix} \underline{\mathbf{u}}^{*} \\ \underline{\delta p}^{n+1} \end{pmatrix} = \begin{pmatrix} \mathbf{M}\underline{\mathbf{F}}_i^n + \mathbf{D}^T\underline{p}^n \\ 0 \end{pmatrix} \tag{II.20}$$

and

$$\begin{pmatrix} \mathbf{I} & -\mathbf{Q}\mathbf{D}^T \\ 0 & \mathbf{I} \end{pmatrix} \begin{pmatrix} \underline{\mathbf{u}}^{n+1} \\ \underline{\delta p}^{n+1} \end{pmatrix} = \begin{pmatrix} \underline{\mathbf{u}}^{*} \\ \underline{\delta p}^{n+1} \end{pmatrix} \tag{II.21}$$

The choice of the matrix $\mathbf{Q}$ then determines which projection method is used. In the present code, the matrix $\mathbf{Q}$ is set to be:

$$\mathbf{Q} = \mathbf{H}^{-1} \tag{II.22}$$

resulting in the Uzawa algorithm. From a practical point of view, evaluations of the inverse of the Helmholtz operator is computationnally intensive. In order to overcome this problem, instead of the exact Uzawa algorithm, the Blair-Perot algorithm is implemented within Nek 5000. The projection matrix then is $\mathbf{Q} = \gamma \mathbf{M}^{-1}/\Delta t$ (with $\gamma = 11\Delta t/6$ for the BDF3/EXT3 scheme). Since the mass matrix $\mathbf{M}$ is diagonal, computing its inverse is a straightforward task. Extensive details on the resolution of this Helmholtz problem and the choice of both the temporal discretisation and the projection method can be found in [52].

II.2 Steady states computation

Computing steady equilibriums of the non-linear Navier-Stokes equations is a pre-requisite to any linear stability calculation. Several procedures exist to compute such solutions, also called fixed points of the equations in the applied mathematics community or base flows in the fluid dynamics one, among which all the techniques derived from the Newton algorithm. Though extremely efficient, the major drawback of these techniques is that they rely on the computation of a Jacobian matrix[1]. Unfortunately, when dealing with fully three-dimensional Navier-Stokes equations, the number of degrees of freedom involved is far too large to enable the computation and storage of such matrices. This problem has been overcome in 2006 by Akervik *et al.* [6] introducing a method known as *selective frequency damping*. This technique enables a damping of the oscillations of the unsteady part of the solution using a temporal low-pass filter. From a practical point of view, this is achieved by adding a forcing term to the right-hand side of the Navier-Stokes equations and extending the Navier-Stokes equations (I.1) with an equation for the filtered state $\bar{\mathbf{U}}$. The extended system is then governed by the following set of equations:

$$\begin{cases} \dot{\mathbf{U}} + (\mathbf{U}\cdot\nabla)\mathbf{U} = -\nabla P + \dfrac{1}{Re}\Delta\mathbf{U} - \chi(\mathbf{U} - \bar{\mathbf{U}}) \\ \dot{\bar{\mathbf{U}}} = \omega_c(\mathbf{U} - \bar{\mathbf{U}}) \\ \nabla\cdot\mathbf{U} = 0 \end{cases} \tag{II.23}$$

with χ being the gain of the filter and ω_c its cutting circular frequency. The choice of these two parameters is crucial for the computation: χ has to be positive and larger than the growth rate of the instability one aims to kill, whereas ω_c has to be lower than the eigenfrequency ω_I of the instability (usually $\omega_c = \omega_I/2$). Provided the filtered state $\bar{\mathbf{U}}$ equals the Navier-Stokes state $\mathbf{U}$, system (II.23) reduces to the steady Navier-Stokes equations highlighting that this extended system indeed enables the computation of fixed points of the original non-linear Navier-Stokes equations (I.1). One major limitation of this technique remains however the computation of steady solutions when an eigenvalue of the associated linearised system turns out to be a real eigenvalue. Indeed, in such cases

[1]The reader must be aware nonetheless that some Jacobian-free Newton methods exist. Such method however requires important modifications of the one's code and have thus not been considered as potential steady state computation tool in the present thesis for the sake of time limitations.

the low-pass filter applied to the non-linear Navier-Stokes equations is unable to kill such non-oscillating unstable mode and consequently to stabilise the fully non-linear system. One possibility to overcome this problem is to use existing symmetries of the base flow solution whenever possible though this is not always sufficient.

Numerical implementation : Two different time discretisation schemes can be used to implement the filtered state's evolution equation within a direct numerical simulation code: implicit or explicit schemes. For the sake of simplicity, it has been decided in the present work to make use of explicit Euler schemes since they do not need any intrusive modifications of the code and are pretty straigthforward to implement. For a simple explicit Euler scheme of order 1, the resulting discretised filtered state's equation would then reads:

$$\bar{\mathbf{U}}^{n+1} = \bar{\mathbf{U}}^{n} + \Delta t \left(\omega_c \left(\mathbf{U}^{n} - \bar{\mathbf{U}}^{n}\right)\right)$$

In the meantime, the stabilising forcing term in the right-hand side of the Navier-Stokes equations has been treated explicitly as well: $-\chi(\mathbf{U}^n - \bar{\mathbf{U}}^n)$.

Illustration : To illustrate the use of selective frequency damping to compute unstable steady equilibrium of the Navier-Stokes, the flow over a two-dimensional cylinder is taken as an example. Numerous studies have shown that such flow becomes globally unstable for $Re \geq 48$. Hence, the Reynolds number will be set to $Re = 60$ as to compute an unstable steady equilibrium. Previous global stability analyses have predicted that the leading eigenvalue for this given Reynolds number is $\lambda \simeq 0.02 + i0.8$. As a consequence, in order for the selective frequency damping to work, one must have $\chi \geq 0.02$ and $\omega_c \leq 0.4$.

In order to highlight the influence of the parameters χ and ω_c on how fast the computation converges toward the unstable steady equilibrium solution, several differents cases have been considered. Table II.1 provides the values of χ and ω_c for these different cases as well as the number of iterations that have been needed to reach a steady state converged down to $\|\mathbf{u}^{n+1} - \mathbf{u}^n\|_{L_2}/\mathrm{dt} \leq 10^{-8}$, whereas figures II.4(a) and (b) provide the time-evolution of the residual for fixed ω_c and fixed χ, respectively, along with the unfiltered case. As one can see, the choice of the couple (χ, ω_c) is crucial for how fast the solution converges toward the unstable equilibrium. Indeed, though only the values of χ and ω_c have been changed, the computational time needed for convergence between Case 1 and Case 5 has almost been reduced by a factor 3. Mathematical details about the influence of χ and ω_c on the convergence rate can be found in the paper by Akervik *et al.* [6]. Despite the dependance of the convergence rate on the values of χ and ω, provided $\chi \geq 0.02$ and $\omega_c \leq 0.4$, this procedure will always converges toward the same unstable equilibrium. As shown on figure II.5, the streamwise velocity contours of the solution computed for $(\chi, \omega_c) = (0.5, 0.05)$ (solid lines) and $(\chi, \omega_c) = (0.125, 0.2)$ (dashed lines) are superimposed.

	Case 1	Case 2	Case 3	Case 4	Case 5
χ	0.5	0.25	0.125	0.125	0.125
ω_c	0.05	0.05	0.05	0.1	0.2
Number of iterations	276'636	188'662	141'974	105'650	87'796

Table II.1: Values of the different couples (χ, ω_c) for selective frequency damping as well as the number of iterations needed to reach a steady state converge down to $\|\mathbf{u}^{n+1} - \mathbf{u}^n\|_{L_2}/\mathrm{dt} \leq 10^{-8}$ for all the cases considered. A two-dimensional cylinder flow at $Re = 60$ has been considered.

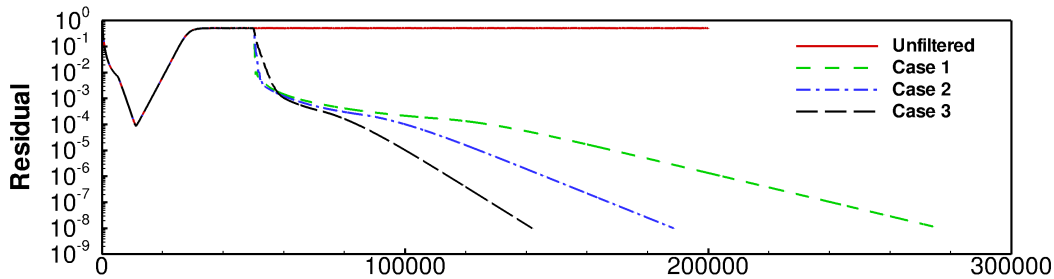

(a) Fixed $\omega_c = 0.05$

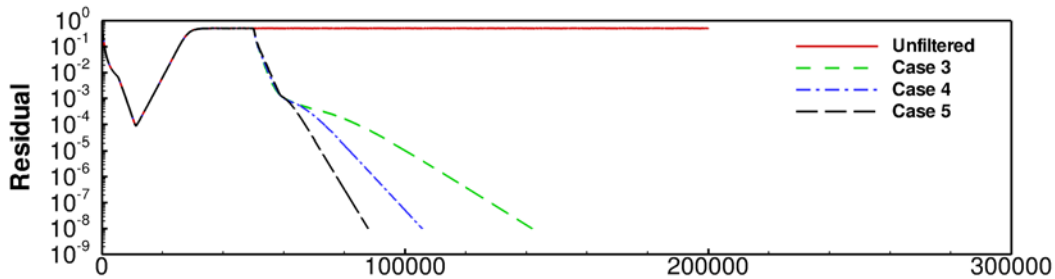

(b) Fixed $\chi = 0.125$

Figure II.4: Time-evolution of the residual for the different set of parameters (χ, ω_c) considered in table II.1. Convergence threshold is set to 10^{-8}.

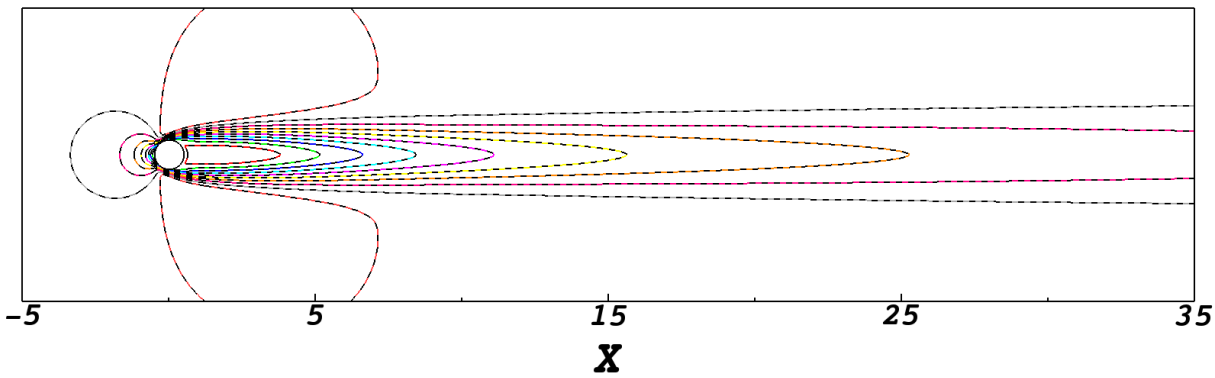

Figure II.5: Streamwise velocity contours of the 2D cylinder unstable equilibrium solution at $Re = 60$ computed for $(\chi, \omega_c) = (0.5, 0.05)$ (solid lines) and $(\chi, \omega_c) = (0.125, 0.2)$ (dashed lines).

II.3 Modal decomposition

II.3.1 Global linear stability, time-stepping and Arnoldi algorithm

Various types of stability may be discussed for the solutions of differential equations describing dynamical systems. As such, before continuing with the stability analysis of fluid systems, one needs to properly define what is meant by *linear stability*. In the present section, we base our definition of linear stability on the one initially given by Lyapunov. Given a fixed point $\mathbf{Q}_b = (\mathbf{U}_b, P_b)^T$ of the Navier-Stokes equations, one then infinitesimally perturbs the fluid system in the vicinity of this particular equilibrium. If the perturbation decays exponentially so that the system eventually relaxes toward the fixed point $\mathbf{Q}_b$, this particular fixed point is said to be linearly stable, otherwise it is said to be linearly unstable. It is important to note that, given this definition of linear stability, one only is interested in the asymptotic time evolution of a given infinitesimal perturbation $\mathbf{q} = (\mathbf{u}, p)^T$. In the present framework, this time-evolution is governed by the linearised three-dimensional incompressible Navier-Stokes equations:

$$\begin{cases} \dot{\mathbf{u}} + (\mathbf{u}\cdot\nabla)\mathbf{U}_b + (\mathbf{U}_b\cdot\nabla)\mathbf{u} = -\nabla p + \dfrac{1}{Re}\Delta\mathbf{u} \\ \nabla\cdot\mathbf{u} = 0 \end{cases} \tag{II.24}$$

Introducing the Jacobian matrix $\mathbf{J}$ and the mass matrix $\mathbf{B}$, one can recast system (II.24) into the following linear dynamical system form:

$$\mathbf{B}\frac{\partial\mathbf{q}}{\partial t} = \mathbf{J}\mathbf{q} \tag{II.25}$$

where the Jacobian and mass matrices are given by:

$$\begin{aligned} \mathbf{J} &= \begin{pmatrix} -\nabla\mathbf{U}_b - \mathbf{U}_b\cdot\nabla + Re^{-1}\Delta & -\nabla \\ \nabla\cdot & 0 \end{pmatrix} \\ \mathbf{B} &= \begin{pmatrix} \mathbf{I} & 0 \\ 0 & 0 \end{pmatrix} \end{aligned} \tag{II.26}$$

Since the system under consideration is a time-autonomous linear dynamical system, one can expend the perturbation $\mathbf{q}$ into normal modes such that $\mathbf{q}(\mathbf{x}, t) = \hat{\mathbf{q}}(\mathbf{x})e^{\lambda t}$. Introducing such expansion for $\mathbf{q}$, system (II.25) can then be transformed into the following generalised eigenvalue problem:

$$\lambda\mathbf{B}\hat{\mathbf{q}} = \mathbf{J}\hat{\mathbf{q}} \tag{II.27}$$

where $\lambda = \sigma + i\omega$ is the eigenvalue and $\hat{\mathbf{q}}$ is the eigenvector one seeks for. The sign of the leading eigenvalue's real part σ then determines whether the fixed point $\mathbf{Q}_b$ is linearly stable or unstable, whereas its imaginary part ω characterises the stationnary or oscillatory nature of the associated eigenvector. Moreover, the imaginary part of the first eigenvalue to step within the upper-half complex plane also determines whether the fixed point experiences a pitchfork ($\omega = 0$) or a Hopf bifurcation ($\omega \neq 0$).

	Base Flow	Inhomo. direction(s)	Dim. of u(t)	Storage of $\mathbf{J}$
Poiseuille	$U(y)$	1D	10^2	∼1Mo
2D LDC	$U(x,y)$	2D	10^5	∼25Mo
Roughness element	$U(x,y,z)$	3D	10^7	∼10To

Table II.2: Estimates of the memory footprint required for explicit construction of the matrices involved in generalised eigenvalue problems.

II.3.1.1 Time-stepper approach

Numerous algorithms exist to compute the eigenpairs $(\lambda, \hat{\mathbf{q}})$ solution to the generalised eigenvalue problem (II.27). However, most of these algorithms require the explicit construction of the matrices $\mathbf{B}$ and $\mathbf{J}$. Unfortunately, generalised eigenvalue problems resulting from the discretisation of the fully three-dimensional linearised Navier-Stokes equations (II.24) involve a very large number of degrees of freedom resulting in mass and Jacobian matrices of extremely large dimensions. Table II.2 provides some estimates of the memory requirements one would typically need to explicitly construct the generalised eigenvalue problem (II.27) depending on the spatial dimension of the initial problem under investigation. Though the actual memory footprint highly depends on the size of the problem and the choice of dicretisation used, these rough estimates clearly highlight how costly and unpractical it would be to explicitly construct these matrices in the fully three-dimensional global stability framework. As to circumvent this problem, quite a few algorithms have been proposed over the past decades. The one chosen for the present PhD thesis is based on a time-stepper formulation of the eigenvalue problem as proposed initally by Marcus & Tuckerman [111] in 1987 and used by few other authors [12, 24, 57, 70, 86, 110, 134] until it has been greatly popularised in 2008 by Bagheri *et al.* [20]. This technique relies on the projection of the linear dynamical system (II.25) onto a divergence-free vector space such that it can simply be rewritten as:

$$\frac{\partial \mathbf{u}}{\partial t} = \mathbf{A}\mathbf{u} \tag{II.28}$$

where $\mathbf{A}$ is the projected Jacobian matrix. Equation (II.28) now accepts the following expression:

$$\mathbf{u}(\Delta t) = e^{\mathbf{A}\Delta t}\mathbf{u}_0 \tag{II.29}$$

as a formal solution. The operator $e^{\mathbf{A}\Delta t}$, also denoted $\mathbf{M}(\Delta t)$, is called the time or exponential propagator of the system (II.28). It appears at first sight that this so-called *time stepper* approach does not really simplify the initial problem of memory footprint. Indeed, not only does $e^{\mathbf{A}\Delta t}$ is a matrix of very large dimensions as well, but it is well-known that computing a matrix exponential can be quite a challenging computational task. The most interesting feature of such a time-stepper approach however is that, though $e^{\mathbf{A}\Delta t}$ is at least as computationally challenging to construct explicitly as the Jacobian $\mathbf{A}$, the action of this exponential propagator onto a vector $\mathbf{u}_0$ can easily be approximated by simply time-marching the linearised Navier-Stokes equations (II.24) with $\mathbf{u}_0$ as the initial condition. Moreover, it is worthy to note that the eigenpairs $(\mathbf{V}, \Lambda)$ of the Jacobian matrix $\mathbf{A}$ and those $(\mathbf{V}_e, \Sigma)$ of the associated exponential propagator $e^{\mathbf{A}\Delta t}$ are related as follows:

$$\Lambda = \frac{\log(\Sigma)}{\Delta t}, \ \mathbf{V} = \mathbf{V}_e \tag{II.30}$$

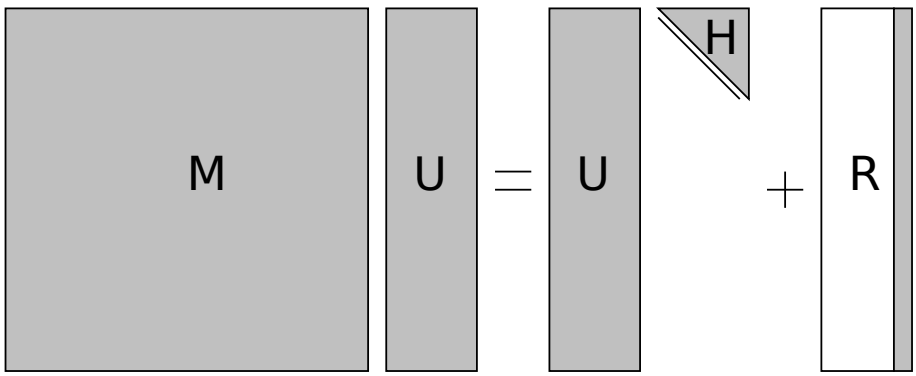

Figure II.6: *The Arnoldi process:* given $\mathbf{M} \in \mathbb{R}^{n\times n}$, construct $\mathbf{U} \in \mathbb{R}^{n\times k}$ with orthonormal columns such that $\mathbf{H} \in \mathbb{R}^{k\times k}$ is an upper Hessenberg matrix and only the last column of the residual $\mathbf{R} \in \mathbb{R}^{n\times k}$ is nonzero. Figure has been adapted from [14].

Due to this fairly simple relationship linking the eigenpairs of the Jacobian matrix to those of the exponential propagator, and because the action of the latter operator onto a given vector can be approximated relatively easily, the technique proposed in [20, 57] aims at computing the exponential propagator's eigenpairs instead of the Jacobian matrix ones.

II.3.1.2 Arnoldi algorithm

To compute the eigenpairs of the exponential propagator $\mathbf{M}$, the time-stepper approach then relies on the Arnoldi factorisation. Introduced in 1951 by W.E. Arnoldi [16] and derived from the Lanczos iteration, the Arnoldi algorithm is an iterative eigenvalue solver enabling one to compute the eigenpairs of a general - possibly non-Hermitian - matrix. Whereas regular direct eigenvalue solvers work out the eigenvalues directly from the elements of the matrices (hence the label *direct methods*), the Arnoldi algorithm rather make the matrices map vectors and makes its conclusions from their images. As a consequence, this Arnoldi factorisation is based on the use of Krylov subspaces. Consequently, this iterative eigenvalue algorithm aims at computing approximations of the leading subsets of eigenpairs instead of the eigenpairs themselves. For extensive details on the Arnoldi algorithm and other eigenvalue algorithms, the reader is refered to the book by Antoulas [14].

Given the exponential propagator $\mathbf{M}$ and an initial vector $\mathbf{u}_0$ such that $\|\mathbf{u}_0\| = 1$, one can build-up the following Krylov sequence $\mathbf{K}_n$ of dimension n:

$$\mathbf{K}_n(\mathbf{M}, \mathbf{u}_0) = \left\{\mathbf{u}_0, \mathbf{M}\mathbf{u}_0, \cdots, \mathbf{M}^{n-1}\mathbf{u}_0\right\} \tag{II.31}$$

This Krylov sequence $\mathbf{K}_n$ converges towards the eigenvector corresponding to the largest eigenvalue (in modulus) of $\mathbf{M}$. Unfortunately, as the dimension n is increased, the sequence $\mathbf{K}_n$ becomes increasingly badly conditionned. This simple iteration is known as the *power iteration*. Though such method is extremely simple to implement within a given code, it is unfortunately relatively slowly converging and only enables the recovery of the leading eigenpair discarding in the meantime all of the information contained in the $n-1$ previous vectors of the sequence. As to overcome this loss of information, the Arnoldi factorisation combines the power iteration with a Gram-Schmidt orthogonalistion

process. The basic Arnoldi iteration then reads:

$$\mathbf{M}\mathbf{U}_k = \mathbf{U}_k\mathbf{H}_k + \mathbf{r}_k\mathbf{e}_k^T \tag{II.32}$$

where $\mathbf{U}_k$ is an orthonormal set of vectors, $\mathbf{H}_k$ a $k \times k$ upper Hessenberg matrix, and $\mathbf{r}_k\mathbf{e}_k^T$ is the residual vector indicating how far from an invariant subspace of $\mathbf{M}$ is $\mathbf{U}_k$. Figure II.6 depicts the structure of the matrices involved in the process. Because of its relatively small dimension, the eigenpairs $(\Sigma_H, \mathbf{X})$ of the Hessenberg matrix, also known as Ritz pairs, can be directly computed and are a good approximation of those of $\mathbf{M}$. Since this Hessenberg matrix is a low-dimensional approximation of the exponential propagator $\mathbf{M} = e^{\mathbf{A}\Delta t}$, these Ritz pairs are linked to the eigenpairs of the Jacobian matrix $\mathbf{A}$ by:

$$\begin{cases} \Lambda \simeq \dfrac{\log(\Sigma_H)}{\Delta t}, \\ \mathbf{V} \simeq \mathbf{U}\mathbf{X} \end{cases} \tag{II.33}$$

Though extremely efficient at computing the leading subsets of eigenvalues of the matrix $\mathbf{M}$, one has to bear in mind that this technique actually relies on a sophisticated signal processing treatment. As a consequence, in order to capture an eigenvector oscillating at a given circular frequency ω, one has to obey to the Nyquist criterion and needs at least four snapshots to appropriately discretise the associated time period. Hence, for a given sampling period Δt one would then be able to compute only eigenvalues of the linearised Navier-Stokes operator such that their imaginary parts are smaller than $2\pi/4\Delta t$. The actual Arnoldi algorithm used during this thesis is presented on algorithm 1 and displayed on figure II.7 in its block-diagram representation as well. One must remember that every time one has to compute the matrix-vector product $\mathbf{M}\mathbf{u}_j$, this is actually performed numerically by time-marching the linearised Navier-Stokes equations as explained in the previous subsection. More elaborate versions of this algorithm, though harder to implement, are the explicitly restarted Arnoldi method, the implicitly restarted one introduced by Lehoucq & Sorensen [100] or the one proposed more recently by Barkley *et al.* [25].

Validation and performances

To illustrate the algorithm just introduced, the unregularised square lid-driven cavity flow at $Re = 10\,000$ is used as a benchmark. The Legendre spectral element mesh is composed of 10 elements within each spatial direction and polynomial reconstructions of order 8 within each element are used in the two directions as well. The resulting linearised Navier-Stokes operator thus involves 18 700 degrees of freedom. The four leading eigenvalues for Krylov subspaces of dimension 250, 500 and 750 are presented in tables II.4, II.5 and II.6, respectively, and compared with those obtained by Robinet *et al.* [130] in table II.3. As one can see, even for dimension of the Krylov subspace as low as 250, these four leading eigenvalues are correctly computed by the algorithm. The converged subsets of the spectra computed for each case are depicted on figure II.8. It is obvious from this figure that, for all Krylov subspaces considered, the leading part of the eigenspectrum is converged quite easily. It is noteworthy moreover that the higher the Krylov subspace's dimension the more eigenvalues are converged within the lower-half complex plane.

Algorithm 1 The k-step *Arnoldi* factorisation.

Require: $\mathbf{M} \in \mathbb{R}^{n \times n}$, starting vector $\mathbf{u} \in \mathbb{R}^n$.

$\mathbf{u}_1 = \mathbf{u}/\|\mathbf{u}\|$;
$\mathbf{w} = \mathbf{M}\mathbf{u}_1$;
$\alpha_1 = \mathbf{u}_1^T \mathbf{w}$;
$\mathbf{f}_1 \leftarrow \mathbf{w} - \alpha_1 \mathbf{u}_1$;
$\mathbf{U}_1 \leftarrow (\mathbf{u}_1)$;
$\mathbf{H}_1 \leftarrow (\alpha_1)$;
for $j = 1, 2, \cdots, k-1$ **do**
  $\beta_j = \|\mathbf{f}_j\|$;
  $\mathbf{u}_{j+1} \leftarrow \mathbf{f}_j/\beta_j$;
  $\mathbf{U}_{j+1} \leftarrow (\mathbf{U}_j, \mathbf{u}_{j+1})$;
  $\hat{\mathbf{H}}_j \leftarrow \begin{pmatrix} \mathbf{H}_j \\ \beta_j \mathbf{e}_j^T \end{pmatrix}$
  $\mathbf{w} \leftarrow \mathbf{M}\mathbf{u}_{j+1}$;
  $\mathbf{h} \leftarrow \mathbf{U}_{j+1}^T \mathbf{w}$;
  $\mathbf{f}_{j+1} \leftarrow \mathbf{w} - \mathbf{U}_{j+1}\mathbf{h}$;
  $\mathbf{H}_{j+1} \leftarrow (\hat{\mathbf{H}}_j, \mathbf{h})$;
end for

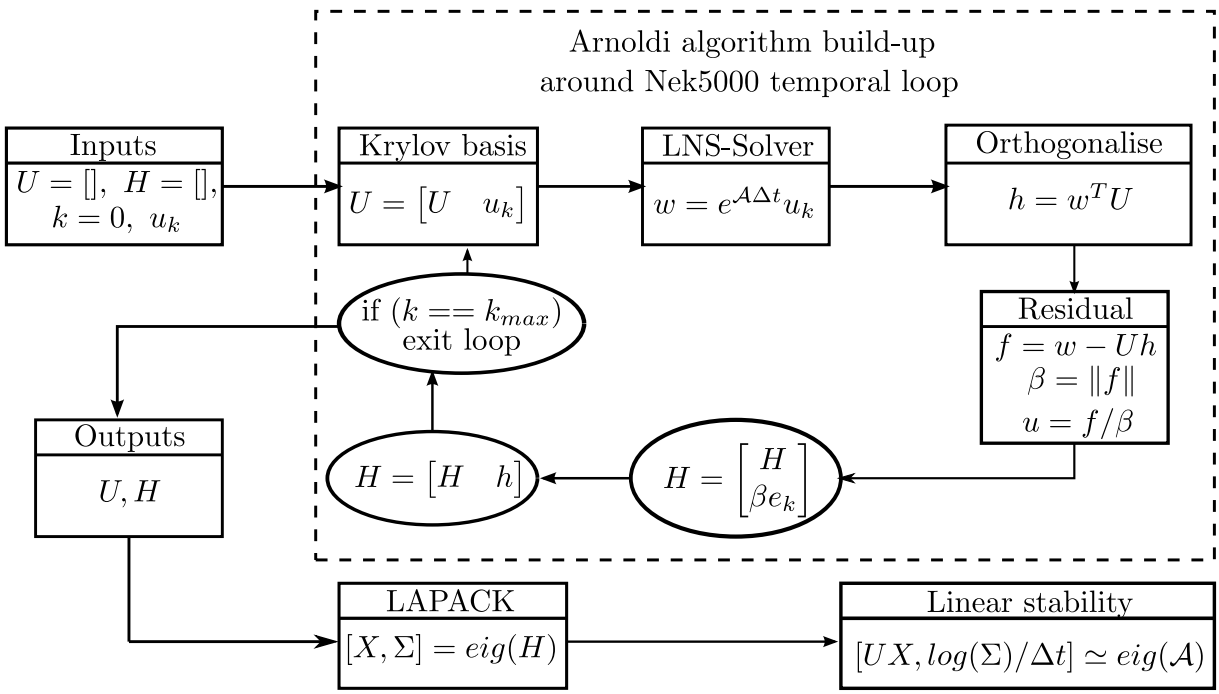

Figure II.7: Block diagram of the time-stepping Arnoldi algorithm implemented around the Nek5000 temporal loop.

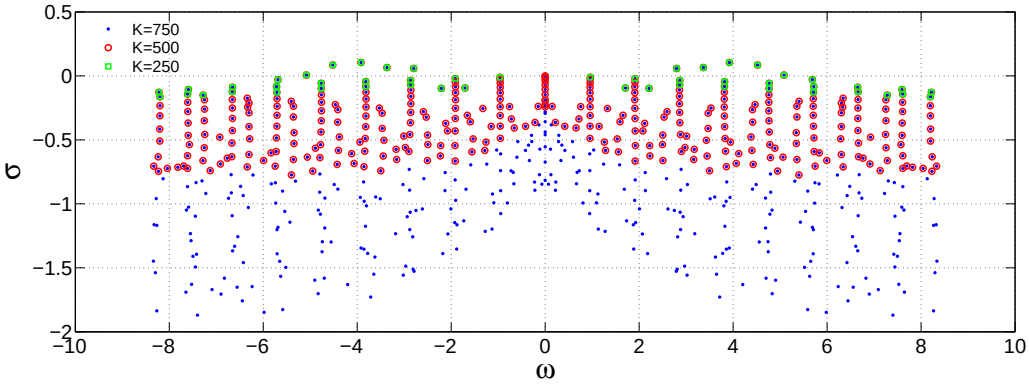

Figure II.8: Spectra of the lid-driven cavity flow at $Re = 10\ 000$ for Krylov subspace's dimensions $k = 250$ (green squares), $k = 500$ (red circles) and $k = 750$ (blue dots).

σ	0.093	0.070	0.055	0.051
$\omega/2\pi$	0.61	0.71	0.43	0.53

Table II.3: Leading eigenvalues reported by Robinet *et al.* [130]

σ	0.1046	0.0848	0.0653	0.0583
$\omega/2\pi$	0.6239	0.7193	0.5361	0.4453

Table II.4: Leading eigenvalues obtained for a Krylov subspace of dimension $k = 250$.

σ	0.1046	0.0848	0.0653	0.0583
$\omega/2\pi$	0.6239	0.7193	0.5361	0.4453

Table II.5: Leading eigenvalues obtained for a Krylov subspace of dimension $k = 500$.

σ	0.1046	0.0848	0.0653	0.0583
$\omega/2\pi$	0.6239	0.7193	0.5361	0.4453

Table II.6: Leading eigenvalues obtained for a Krylov subspace of dimension $k = 750$.

II.3.2 Koopman modes decomposition

Fluid flows often exhibit complex phenomena involving a substantially large range of both spatial and time scales. Because of this complexity, analysing and inferring conclusions regarding the behaviour of a given flow directly from raw measurements data is more than often quite unpractical. As to unravel some order hidden behind the apparent complexity, one often resort to *modal decomposition* of these data to identify the flow structures and investigate their spatio-temporal dynamics. The global modes decomposition just presented is one of these modal decomposition applied to a linear system, however other exist and can be applied to non-linear systems such as the famous *Fourier transform* or the *Proper Orthogonal Decomposition* (POD) [78].

Over the past twenty years, modal decomposition of non-linear systems has essentially been relying on the Proper Orthogonal Decomposition. Such decomposition is based on a singular value decomposition (SVD) of a sequence of the flow's observables. Singular value decomposition can be seen as a generalisation of the eigenvalue decomposition concept applied to not-necessarilly square matrices. Given a matrix $\mathbf{X} \in \mathbb{R}^{n \times k}$ into which the n flow's observables have been stacked in k columns, performing SVD would decompose this matrix into three parts:

- $\mathbf{U}$: a matrix whose columns are orthonormal one to another. Each of these columns then contains one of the so-called POD modes.
- $\mathbf{\Sigma}$: a real-valued diagonal matrix containing the singular values. The ith singular value indicates the importance of the ith POD mode from $\mathbf{U}$ in the initial sequence of data.
- $\mathbf{V}$: the dynamics matrix. Its ith row provides the temporal evolution of the ith POD mode.

Such decomposition thus identifies flow structures and their associated dynamics accordingly to their relative energetic importance within the initial sequence. Moreover, because the matrix of POD modes $\mathbf{U}$ is constrained to be an orthonormal matrix, the flow structures are orthonormal one to another. Figure II.9 summarizes this decomposition. Though extremely efficient when it comes to the identification of some specific patterns within a given flow field, one major drawback of such Proper Orthogonal Decomposition relies in the dynamics matrix $\mathbf{V}$: several different frequencies can be involved in the time evolution of a single POD mode. As a consequence, identifiying the spatial structure associated to a given frequency of the flow might be quite complicated using POD. In order to overcome this problem, a new modal decomposition as been introduced in 2008 by Schmid & Sesterhenn [139] known as *Dynamic Modes Decomposition* (DMD) and a year later by Rowley *et al.* [131] known as *Koopman Modes Decomposition.* Despite having different names, these two modal decompositions essentially are the same and only differ in the actual algorithm used to compute these modes. The major difference with the Proper Orthogonal Decomposition is that the orthonormality constraint is no more applied to the modes matrix $\mathbf{U}$ but to the dynamics matrix $\mathbf{V}$ instead. As a result, though the spatial modes are no more orthogonal one to another, each dynamics within the $\mathbf{V}$ matrix now involves only one single frequency.

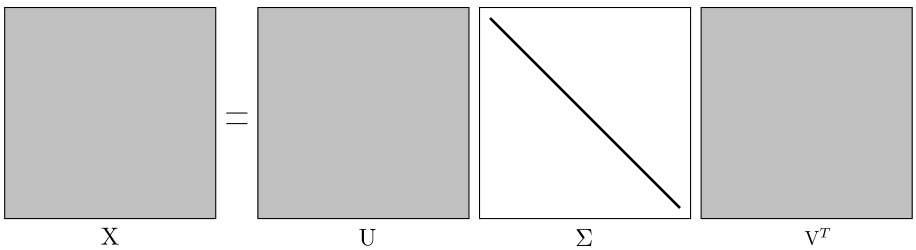

Figure II.9: Structure of the matrices resulting from singular value decomposition.

The algorithm to be presented is the one originally introduced by Rowley *et al.* [131]. Assume one has a given discrete set of flow observables $\mathbf{x}_j = \mathbf{x}(j\Delta t)$ at k different time steps such that:

$$\mathbf{K} = [\mathbf{x}_0, \mathbf{x}_1, \cdots, \mathbf{x}_{k-1}] \tag{II.34}$$

Koopman modes decomposition relies on the strong assumption that the $(k+1)^{th}$ vector of this sequence can be given by a linear operator $\mathbf{A}$ such that we actually have the following time-discrete linear dynamical system:

$$\mathbf{x}_{i+1} = \mathbf{A}\mathbf{x}_i \tag{II.35}$$

One must be aware that, as for global stability analysis, the operator $\mathbf{A}$ might not be directly accessible. Moreover, the observables $\mathbf{x}_i$ might even actually be those of a non-linear flow in which this operator is actually unknown. However, assuming this time-discrete linear dynamical system form is at the heart of the Koopman modes decomposition. Indeed, stemming from this strong assumption, the sequence $\mathbf{K}$ can be seen as a Krylov sequence resulting from repeated application of the linear operator $\mathbf{A}$ onto the initial vector $\mathbf{x}_0$. Hence, as for the global modes decomposition, given this Krylov sequence one can construct a low-dimensional approximation of the operator $\mathbf{A}$ and compute reasonnable approximations of its eigenvalues and eigenvectors. Difference with the global modes decomposition however relies in the fact that, for Koopman modes decomposition, the matrix resulting from the low-dimensional approximation is no more an upper Hessenberg matrix but a Companion one. Let us assume that the kth vector of the Krylov sequence can be expressed as a linear combination of the previous iterates:

$$\begin{aligned} \mathbf{x}_k &\simeq c_0\mathbf{x}_0 + c_1\mathbf{x}_1 + \cdots + c_{k-1}\mathbf{x}_{k-1} \\ \mathbf{x}_k &\simeq \mathbf{K}\mathbf{c} \end{aligned} \tag{II.36}$$

where $\mathbf{c}$ is a column vector containing the k coefficients c_i needed for the linear combination. These coefficients can either be computed by a least-square best fit or by solving a linear system. This linear problem can be recast into the following equivalent matrix form:

$$\mathbf{A}\mathbf{K} \simeq \mathbf{K}\mathbf{C} \tag{II.37}$$

where $\mathbf{C}$ is a $k \times k$ Companion matrix given by:

$$\mathbf{C} = \begin{bmatrix} 0 & 0 & \dots & 0 & c_0 \\ 1 & 0 & & 0 & c_1 \\ 0 & 1 & & 0 & c_2 \\ \vdots & & \ddots & & \vdots \\ 0 & 0 & \dots & 1 & c_{k-1} \end{bmatrix} \tag{II.38}$$

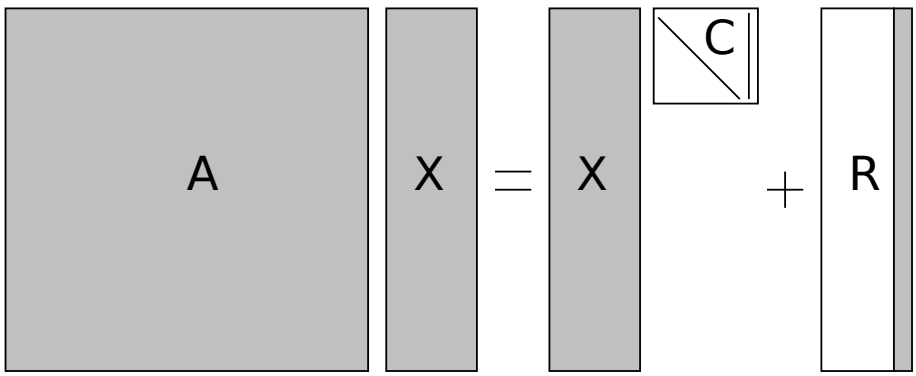

Figure II.10: Representation of the basic Koopman iteration along with the involved matrices structures. Gray denotes full matrices.

It is clear from the structure of expression (II.37) that, apart from the specific structure of $\mathbf{C}$, a striking resemblence exists between the Koopman modes decomposition and the global modes one as underlined by the representation of this basic Koopman iteration depicted on figure II.10. In fact, the Koopman modes decomposition can be seen as a generalisation of global stability analysis applied to non-linear system. As a consequence, the eigenpairs $(\Sigma_c, \mathbf{X})$ of the Companion matrix $\mathbf{C}$ are a reasonnably good approximation of the eigenpairs $(\Sigma, \mathbf{U})$ of the operator $\mathbf{A}$ since:

$$\begin{cases} \Sigma \simeq \Sigma_c \\ \mathbf{U} \simeq \mathbf{KX} \end{cases} \tag{II.39}$$

As for global stability analysis, the growth rate and circular frequency of the Koopman modes can be recovered by:

$$\sigma + i\omega = \frac{\log(\Sigma)}{\Delta t} \tag{II.40}$$

Δt being the sampling period between two snapshots of the observables. For further details on the algorithm, the reader is referred to Rowley *et al.* [131] as well as Schmid [136]. One question however remains unanswered. Whereas in the Proper Orthogonal Decomposition, modes are classified accordingly to their energy in the initial sequence, sorting the Koopman modes might be slightly less well defined. Yet, most studies have however sorted these Koopman modes accordingly to their norm: the larger the mode's norm, the more important its contribution in the vector sequence analysed.

Illustration

The following illustration of the Koopman modes decomposition is based on a collaboration with Antoine Ducoin and Jean-Christophe Robinet. The Koopman modes decomposition has been recently used by Ducoin *et al.* [56] to investigate the structures to be found in the flow past an airfoil at a Reynolds number $Re = 20\ 000$ based on the chord length c, the incoming velocity U_∞ and the kinematic viscosity ν. Though much more complicated than the rest of the flow configurations investigated during this thesis, this particular study greatly underlines the strong interest one could have in using Koopman modes decomposition when analysing high Reynolds numbers flows.

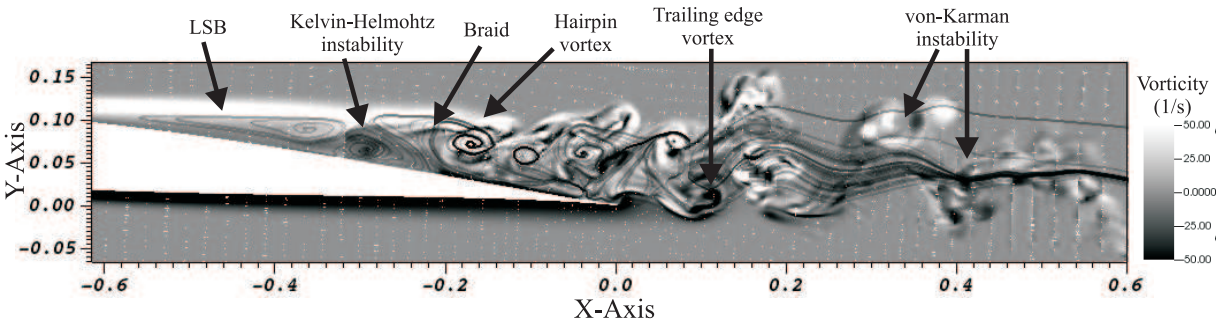

(a)

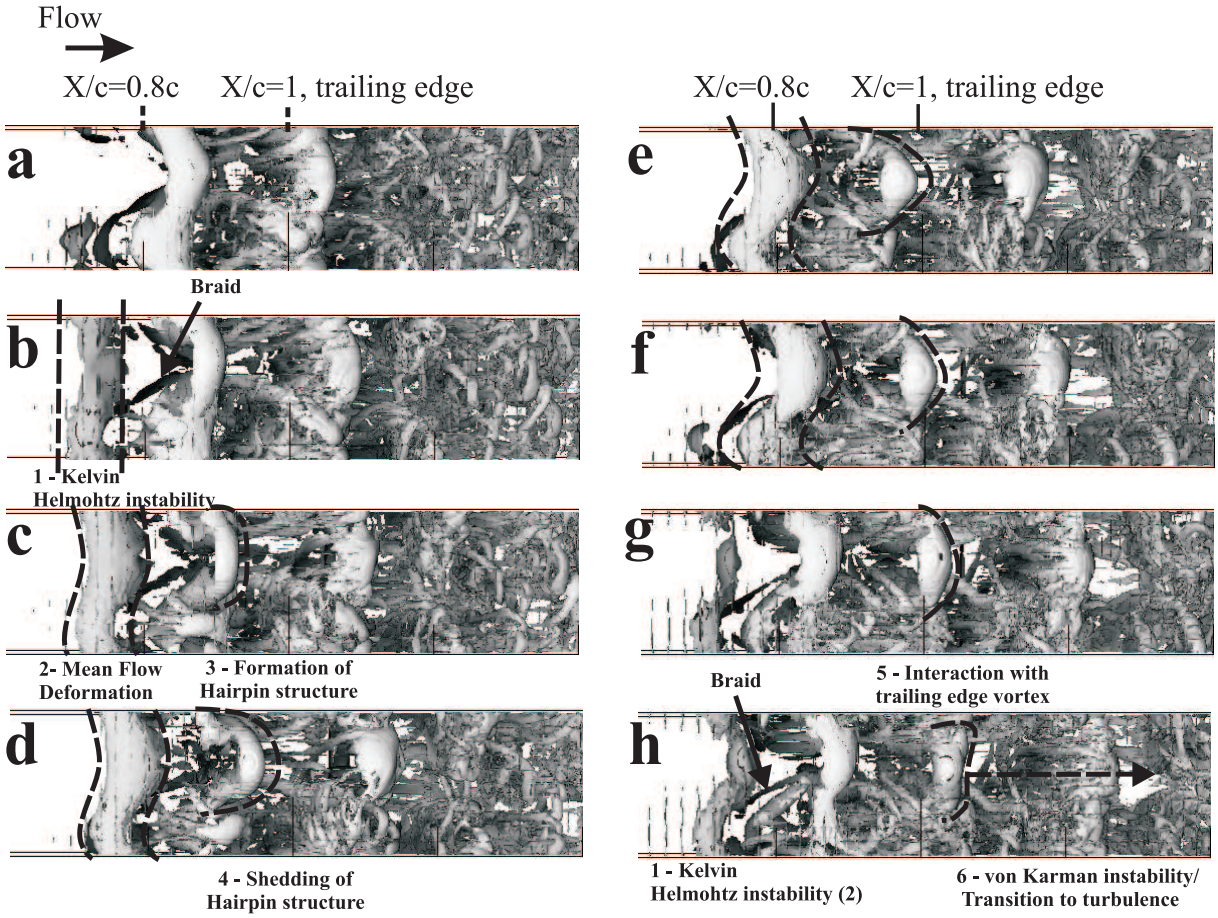

(b)

Figure II.11: (a) Instantaneous vorticity field and velocity streamlines along the laminar to turbulent transition region. (b) Isosurfaces of λ_2 criterion and velocity contours downstream of the Laminar Separation bubble. Figure from [56]

Figure II.11(a) depicts the instantaneous vorticity contours and velocity streamlines in the vicinity of the trailing edge of the wing section considered whereas figure II.11(b) depicts λ_2 criterion isosurfaces near the trailing edge as well (top view). It is clear from the numerous physical mechanisms at play identified by Ducoin *et al.* [56] that the flow is characterised by rather complicated space-time dynamics. A sequence of 600 velocity snapshots taken from the direct numerical simulation has then been analysed using the Koopman modes decomposition just presented. Figures II.12(a) and (b) depict the eigenpsectum of the Koopman operator as well as the evolution of the norm of the Koopman modes with respect to their circular frequency. Whereas the figure II.12(a) shows that most of the eigenvalues computed are indeed converged (i.e. almost all along the unit circle), figure II.12(b) clearly highlights that three families of modes dominate the dynamics. Three of these modes are represented on figure II.12(c) displaying the norm of the velocity vector. It is clear from these figures that Koopman analysis has indeed been able to identify some specific flow structures linked to periodic shedding toward the wake of spanwise-oriented vortices from the laminar separation bubble located in the vicinity of the trailing edge. For extensive details on the physical analysis of this quite complicated flow, the reader is again referred to the paper by Ducoin *et al.* [56] to be published soon.

II.4 Optimal perturbations and Transient growth analysis

As already explained, the term *linear stability* can recover several different definitions. In the previous section, *linear stability* was based on the definition enonced by Lyapunov: given a fixed point $\mathbf{Q}_b = (\mathbf{U}_b, P_b)^T$ of the Navier-Stokes equations, one then infinitesimally perturbs the fluid system in the vicinity of this particular equilibrium. If the perturbation decays exponentially so that the system eventually relaxes toward the fixed point $\mathbf{Q}_b$, this particular fixed point is said to be *linearly stable*, otherwise it is said to be *linearly unstable*. The linear stability or instability of the fixed point $\mathbf{Q}_b$ is then governed by the spectrum of eigenvalues of the linearised Navier-Stokes operator. Perturbations governed by such eigenvalues often turn out to have relatively small growth rates. As a consequence, it would take quite a large amount of time for such perturbations to grow up to only a few orders of magnitude higher than their initial amplitude. However, numerous experimental investigations have reported instabilities and transition scenarios occuring on substantially smaller timescales revealing how poor of a proxy the eigenspectrum of the linearised Navier-Stokes operator can be when inferring the short-time evolution of infinitesimal perturbations. These scenarios are closely related to the concepts of subcritical bifurcations and linear transient growth. Hence, defining the stability of a given fixed point based on an asymptotic time-evolution of the perturbations seems to be rather limiting. As a consequence, one can redefine the concept of *linear instability* as the ability for an initial perturbation to exhibit transient energy amplification over a given time interval [135, 137, 138].

Mathematical details about the relationship between eigenspectrum of the linearised Navier-Stokes operator and transient growth analysis can be found in the book by Schmid & Henningson [138] as well as in the recent review paper by Schmid & Brandt [137]. The

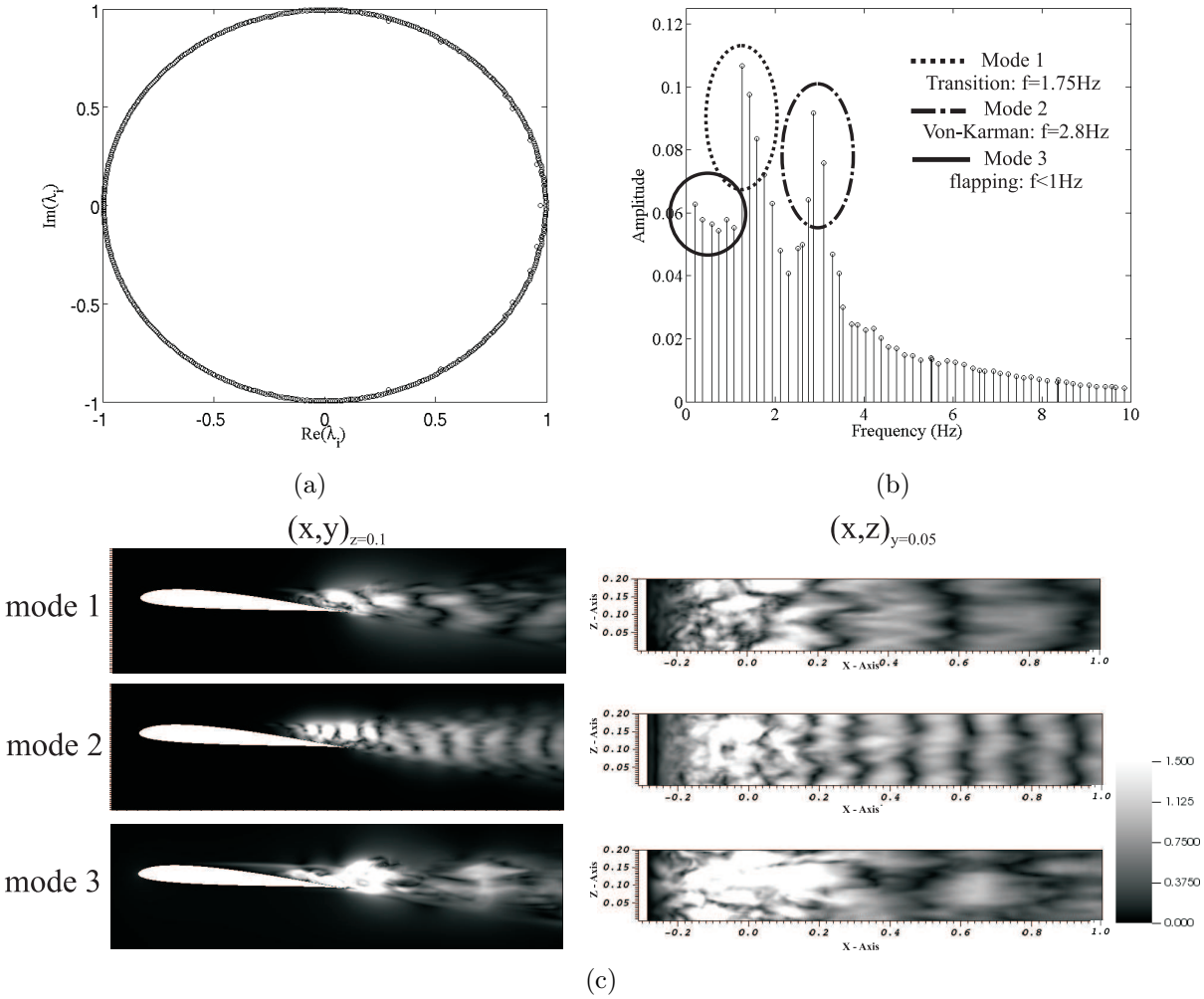

Figure II.12: (a) and (b) Eigenvalues of the Koopman operator. (c) Velocity field for the first three modes. (X, Y) plane are taken at mid span. (X, Z) planes are taken at LSB level. Figure from [56]

optimal energy amplification, also known as the *optimal gain*, is given by:

$$G(t) = \max_{\mathbf{q}_0} \frac{E(\mathbf{q}(t))}{E(\mathbf{q}_0)} \tag{II.41}$$

where $\mathbf{q}_0$ is the initial perturbation, $\mathbf{q}(t)$ the response of the system at time t and E the energy-norm of the perturbations. Recollecting that the time-evolution of $\mathbf{q}(t)$ is governed by the linear dynamical system (II.28) and hence one has:

$$\mathbf{q}(t) = e^{\mathbf{A}t}\mathbf{q}_0$$

the expression of the optimal gain can be rewritten as:

$$G(t) = \max_{\mathbf{q}_0} \frac{\|\mathbf{q}(t)\|_E}{\|\mathbf{q}_0\|_E} = \max_{\mathbf{q}_0} \frac{\|e^{\mathbf{A}t}\mathbf{q}_0\|_E}{\|\mathbf{q}_0\|_E} = \|e^{\mathbf{A}t}\|_E \tag{II.42}$$

As a consequence, the initial condition $\mathbf{q}_0$ and the optimal perturbation at a given time t are linked as follows:

$$e^{\mathbf{A}t}\mathbf{q}_0 = \|e^{\mathbf{A}t}\|\mathbf{q} \tag{II.43}$$

with $\mathbf{q}_0$ and $\mathbf{q}$ being unit-norm vectors, and $\|e^{\mathbf{A}t}\|$ the optimal gain. Recalling that the dominant singular value σ_1 of a given matrix is equal to its L_2-norm, and re-introducing the exponential propagator $\mathbf{M}(t) = e^{\mathbf{A}t}$, one can recast the previous expression into a singular value problem:

$$\mathbf{M}\mathbf{v}_1 = \sigma_1\mathbf{u}_1 \tag{II.44}$$

with $\mathbf{v}_1$ being the initial condition yielding to the optimal energy amplification σ_1 at time t, and $\mathbf{u}_1$ the associated response ot the system. Introducing the operator $\mathbf{M}^*$, i.e. the Hermitian of $\mathbf{M}$, one can recast the singular value problem (II.44) into an eigenvalue problem:

$$\mathbf{M}^*\mathbf{M}\mathbf{v} = \sigma\mathbf{v} \tag{II.45}$$

where the singular value σ now plays the role of an eigenvalue and the singular vector $\mathbf{v}$ the role of an eigenvector. Unfortunately, as for global stability analysis, the matrices $\mathbf{M}$ and $\mathbf{M}^*$ are of too large dimension to be explicitly computed. Hence, in order to solve this eigenvalue problem one has to compel to time-stepper approach once again. However, one also require to introduce the linear adjoint state equations to approximate the action of $\mathbf{M}^*$ onto a given vector.

II.4.1 Adjoint linearised Navier-Stokes equations

Adjoint state is a concept originating from the optimisation theory. Over the past years, resulting adjoint-based methods have been used successfuly in flow control and stability analysis. In the hydrodynamic instability framework, such methods can be used to identify optimal perturbations, highlight the most receptive path to break down, select the most destabilising base flow defect in an otherwise stable configuration, and map the structural sensitivity of an oscillator. All of these uses have been recently reviewed by Luchini & Bottaro [108].

Let us consider the linear dynamical system (II.25) already introduced when investigating the eigenspectrum of the linearised Navier-Stokes operator:

$$\mathbf{B}\frac{\partial \mathbf{q}}{\partial t} = \mathbf{J}\mathbf{q}$$

The adjoint operator of $\mathbf{J}$ has the property that:

$$\langle \mathbf{y}, \mathbf{J}\mathbf{x} \rangle = \langle \mathbf{J}^*\mathbf{y}, \mathbf{x} \rangle \tag{II.46}$$

where $\langle \cdot, \cdot \rangle$ denotes the appropriate inner product for the flow domain. Provided one defines correctly its inner product, the adjoint linearised Navier-Stokes equations then read:

$$\begin{cases} \dot{\mathbf{u}}^\dagger + (\mathbf{U}_b \cdot \nabla)\mathbf{u}^\dagger - (\nabla \mathbf{U}_b)^T \mathbf{u}^\dagger = -\nabla p^\dagger + Re^{-1}\Delta \mathbf{u}^\dagger \\ \nabla \cdot \mathbf{u}^\dagger = 0 \end{cases} \tag{II.47}$$

For a complete derivation of the adjoint linearised Navier-Stokes equations as well as the consequences on the boundary conditions, the reader is referred to [25]. As for the linearised Navier-Stokes equations (II.24), this set of equations can be recast into a dynamical system form:

$$\mathbf{B}\frac{\partial \mathbf{q}^\dagger}{\partial t} = \mathbf{J}^*\mathbf{q}^\dagger \tag{II.48}$$

where $\mathbf{q}^\dagger = (\mathbf{u}^\dagger, p^\dagger)^T$ is the adjoint state vector and $\mathbf{J}^*$ the adjoint Jacobian matrix. Futhermore, projection onto a divergence-free vector yields to the following expression:

$$\frac{\partial \mathbf{u}^\dagger}{\partial t} = \mathbf{A}^*\mathbf{u}^\dagger \tag{II.49}$$

with $\mathcal{A}^*$ being the projected adjoint Jacobian matrix. From here on, one can introduce the adjoint exponential propagator defined as:

$$\mathbf{M}^*(t) = e^{\mathbf{A}^* t} \tag{II.50}$$

It is worthy to note that, as for its direct counterpart, because of the number of degrees of freedom involved and the challenging task an exponential matrix is, this operator cannot be explicitly computed. However, the action of this adjoint time propagator onto a given vector can be approximated by using an adjoint linearised Navier-Stokes solver.

II.4.2 Optimal perturbation and eigenvalue analysis of $\mathbf{M}^*\mathbf{M}$

It has been shown in a previous subsection that the singular value problem (II.44) could be reformulated into the eigenvalue problem (II.45) by introducing the adjoint state's exponential propagator $\mathbf{M}^*(t) = e^{\mathbf{A}^* t}$. Because the first singular triplet gives the worst case possible for transient energy amplification at a given time horizon of an otherwise infinitesimal perturbation, computing only this particular triplet is often sufficient to assess the short-time non-modal stability of the flow. As a consequence, the simplest eigenvalue algorithm, i.e. the power iteration method, can be used in order to compute this singular value and associated singular vectors. This simple algorithm consists in repeated applications of the operator $\mathbf{M}^*(t)\mathbf{M}(t)$ onto an initial unit-norm vector $\mathbf{u}_0$

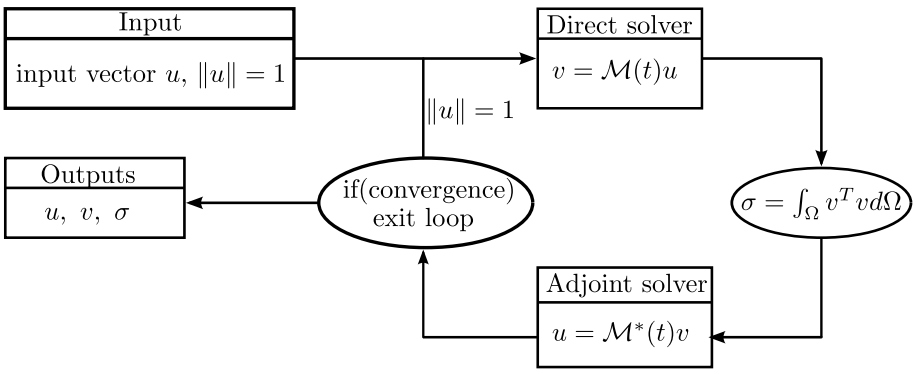

Figure II.13: Block diagram of direct-adjoint loop implemented in Nek5000 for the power-iteration method.

until convergence is achieved. Its associated block-diagram representation is depicted on figure II.13. Despite the significance of the first singular triplet in the transient dynamics of the flow, one might also be interested in the sub-optimal perturbations. Unfortunately, such sub-optimal perturbations cannot be computed using the simple power-iteration algorithm. Moreover, from a purely computational point of view, the power-iteration method is known to be slowly converging toward the leading singular triplet and can thus be relatively time-consuming. An alternative to overcome these two problems is to use a modified version of the Arnoldi algorithm presented previously. As one can see from the block-diagram depicted on figure II.14, this SVD-Arnoldi algorithm is very similar to the one presented earlier differing only by the fact that the input vector u_k is not only multiplied by the time propagator $\mathbf{M}(t)$ but also by its adjoint counterpart $\mathbf{M}^*(t)$. It is noteworthy that the version of the algorithm presented here only enables the computation of the right singular vectors, i.e. the optimal perturbations. A modified version where the operator $\mathbf{M}^*(t)\mathbf{M}(t)$ is replaced by $\mathbf{M}(t)\mathbf{M}^*(t)$ can be used in order to obtain the left singular vectors, i.e. the optimal responses. However, these responses can also be computed from a simple linearised DNS once the optimal perturbations obtained by the SVD-Arnoldi algorithm. Last but not least, both the Arnoldi and SVD-Arnoldi algorithms presented in this manuscript can be seen as simpler versions of the algorithm introduced by Barkley *et al.* [25].

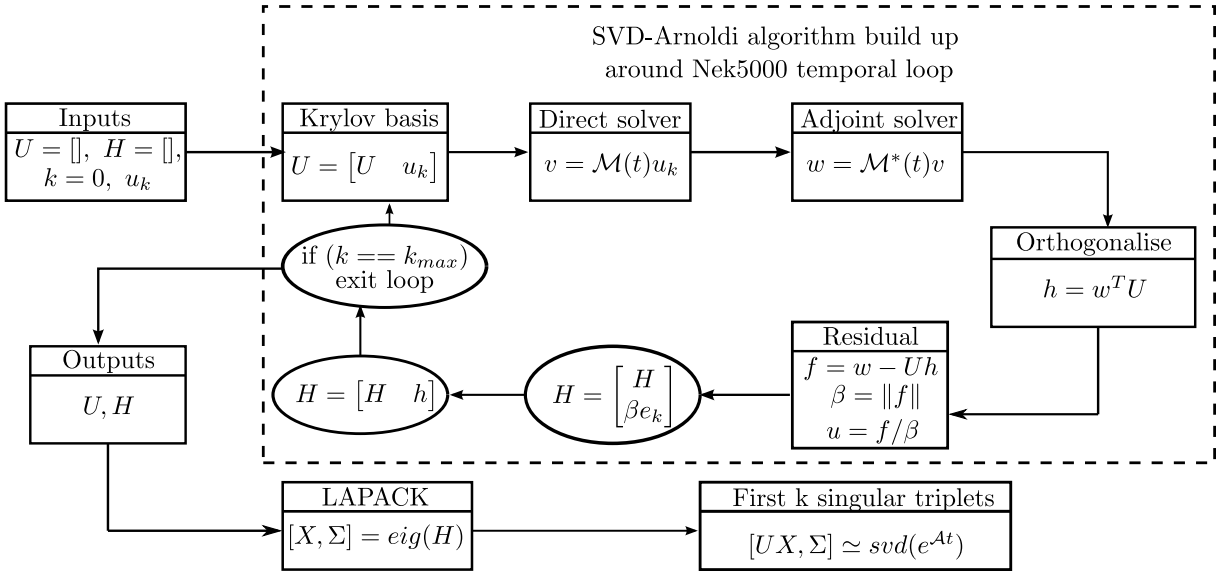

Figure II.14: Block diagram of the SVD-Arnoldi algorithm implemented in Nek5000.

Chapter III

Three-dimensional lid-driven cavity flow

Contents

III.1 Problem formulation **47**

III.2 State of the art **49**

III.3 Results **52**

III.3.1 Steady state solutions 52

III.3.2 Linear stability analysis 56

III.3.3 Non-linear evolution 66

III.4 Conclusion **77**

III.1 Problem formulation

The motion of the fluid contained within a three-dimensional enclosure of depth L, length L (square section), width ΛL and driven by a moving lid is considered. The flow, assumed to be incompressible and Newtonian, is governed by the three-dimensional Navier-Stokes equations:

$$\begin{cases} \dfrac{\partial \mathbf{U}}{\partial t} + (\mathbf{U} \cdot \nabla)\mathbf{U} = -\nabla P + \dfrac{1}{Re}\Delta \mathbf{U} \\ \nabla \cdot \mathbf{U} = 0 \end{cases} \tag{III.1}$$

The lid of the cavity moves with a constant velocity U in the x-direction. The Reynolds number is then defined as $Re = UL/\nu$, where ν is the kinematic viscosity. The origin of the axes system is assigned to be the geometrical center of the cavity such that the non-dimensional domain considered is: $\Omega = [-0.5, 0.5] \times [-0.5, 0.5] \times [-\Lambda/2, \Lambda/2]$. A sketch of the computational domain considered is depicted on figure III.1(a). For the sake of clarity, Λ will refer hereafter to the spanwise aspect ratio of the cavity under consideration. Apart from the lid, no-slip boundary conditions are applied on all the walls of the cavity. According to figure III.1(b), the two faces normal to the x-axis will be referred as the downstream and upstream walls, dependant on their position relatively to the motion of the lid, whereas the faces normal to the z-axis will be referred to side walls. The remaining face parallel to the moving lid will be called the bottom wall.

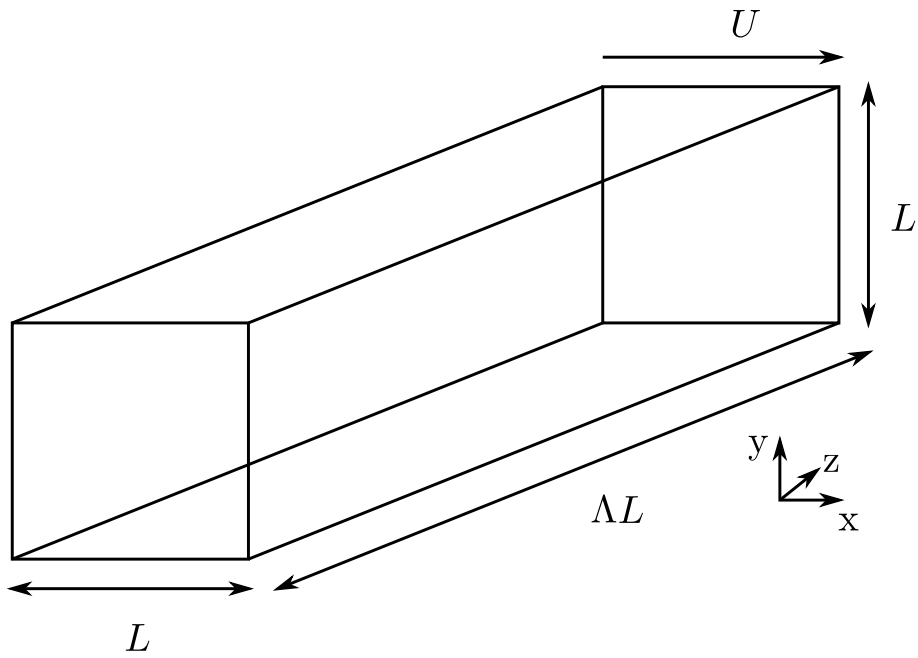

(a)

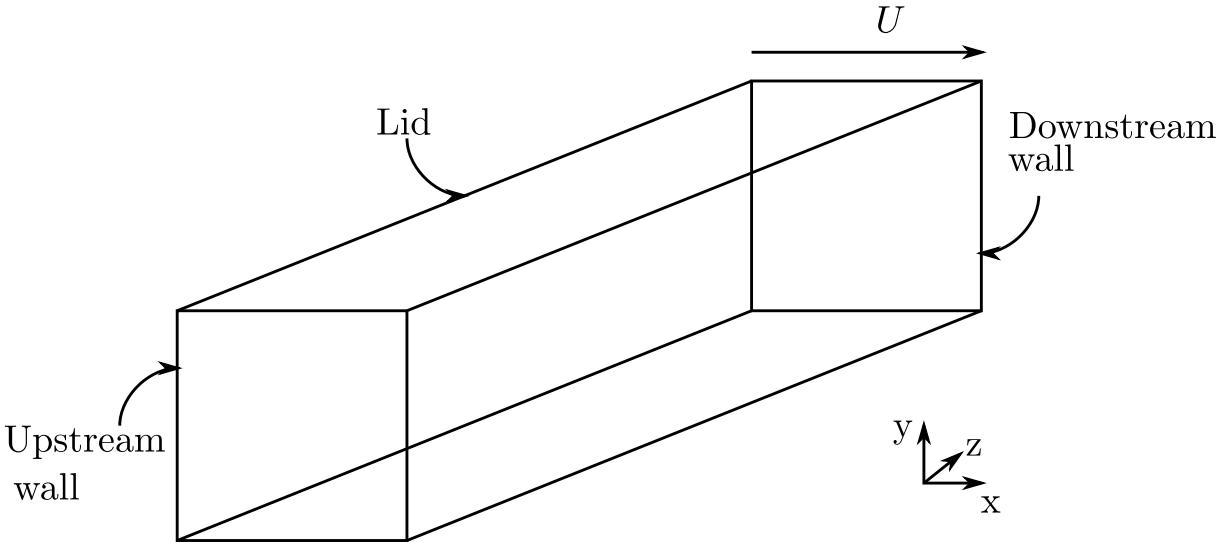

(b)

Figure III.1: (a) Sketch of the computational domain considered. (b) Nomenclature used to refer to the different walls of the cavity.

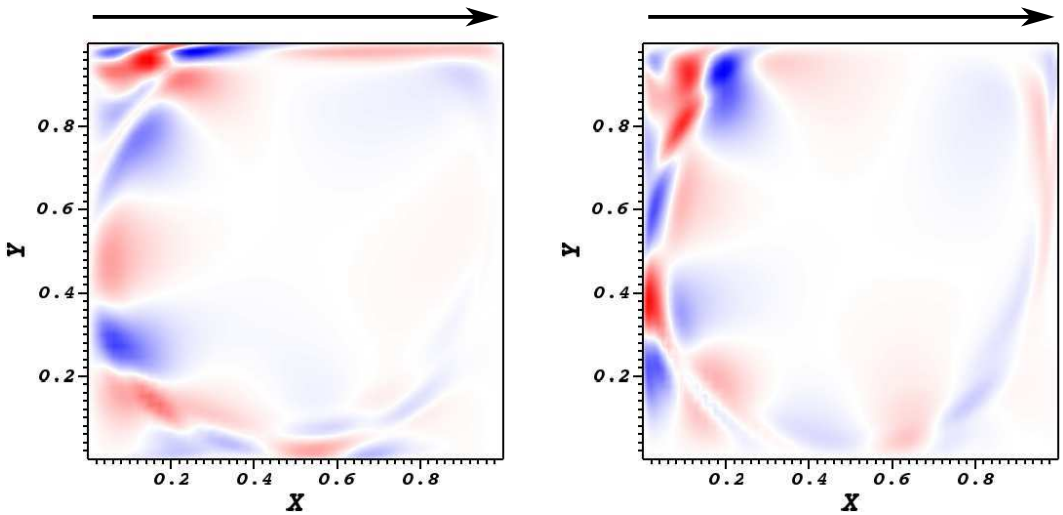

(a) (b)

Figure III.2: Real part of the (a) x-velocity and (b) y-velocity components of the most unstable global mode in the square lid-driven cavity problem at a Reynolds number $Re = 8500$. The arrow indicates the motion of the lid.

III.2 State of the art

The flow within a lid-driven cavity (LDC) is an idealisation of a number of fluid mechanics problems and qualitatively presents most of the important features responsible for transition in a wide variety of other flows (e.g. shear layers, counter-rotating pairs of vortices, high- and low-speed streaks, ...). From a practical point of view, the lid-driven cavity is a simplification of several engineering situations such as slots on the walls of heat exchangers or simplification of coating devices used in the paper industry for producing high grade paper and photographic film [5]. Spatial variations in coating thickness and in coat weight profiles were observed when increasing the machine speed and three-dimensional hydrodynamic instabilities are thought to be responsible for these variations [5]. The simplified lid-driven cavity problem may help the understanding of such flow phenomena. Due to this idealisation, lid-driven cavity flows have been the subject of numerous studies over the past decades but only very few references exist on experimental studies. Because of the extremely large body of literature existing on the subject, an exhaustive review would be quite impractical to perform and only the most important papers (from a stability analysis point of view) will be reported hereafter.

Two-dimensional LDC

Because of the extremely large body of literature, the two-dimensional lid-driven cavity flow has become a standard benchmark problem for testing the accuracy of new numerical methods and algorithms. Since the pioneering work of Burggraf [37] in the mid 1960's on the structure of steady separated flows, high quality data of the two-dimensional flow within a square lid-driven cavity have been produced by Botella & Peyret [33] using a Chebyshev collocation method at Reynolds number $Re = 1000$. Regarding the linear instability of such flow, the first relevant results on a square lid-driven cavity flow are

those obtained by Poliashenko *et al.* [124] in 1995, as well as those by Fortin *et al.* [64] and Gervais *et al.* [68] in 1997. All these studies have only assessed the stability of the two-dimensional LDC flow toward perturbations being two-dimensional as well. For the square lid-driven cavity under consideration, transition to unsteadiness has been reported to occur around a critical Reynolds number $Re_c \simeq 8000$ via a Hopf bifurcation. The leading two-dimensional unstable global mode, depicted on figure III.2, consists in vortices located along the streamline separating the central vortex core from the corner eddies. Despite the flow within such cavity being a standard benchmark, it is however worthy to note that the specific critical Reynolds number at which the Hopf bifurcation occurs seems to be relatively dependant on the discretisation technique used, on the fixed point computation method employed as well as on the treatment (or not) of the corner singularities existing at the intersections between the lid and the vertical walls (see [129] and references therein for a complete review).

Assessing the transition thresholds by investigating the stability of two-dimensional base flows toward perturbations being two-dimensional as well is unfortunately often an over idealisation for practical applications. As a consequence, numerous papers have been published since the early 2000's where the stability of the two-dimensional LDC flow toward perturbations exhibiting a given spanwise periodicity is now investigated. Hereafter, such stability analysis will be referred to 2.5D stability analysis. To our knowledge, the firsts to have investigated the LDC flow stability properties toward such perturbations are Ramanan & Homsy [126] as early as 1994. A few years later, Ding & Kawahara [53], Albensoeder *et al.* [9], Theofilis *et al.* [152] and Chicheportiche *et al.* [42] have performed similar investigations. In 2006, Non *et al.* [117] further refined the stability calculations performed in [9, 53, 152]. All of these authors have shown that, depending on the Reynolds number Re and the spanwise wavenumber β of the prescribed perturbation, the 2.5D lid-driven cavity flow is unstable toward four different families of modes. The neutral curves in the (Re, β)-plane of these branches are reproduced on figure III.3(a) adapted from [42]. All of these modes are related to a centrifugal instability of the base flow developing along the curved streamline separating the primary vortex from the downstream eddy. The first bifurcation occurs at a critical Reynolds number $Re_{S1} = 780$, i.e. a lot earlier than the two-dimensional instability, and for a spanwise wavenumber $\beta \simeq 15$. The associated branch is known as the $S1$ family of modes. It is a familly of non-oscillating Taylor-Görtler like vortices whose typical spatial structure is depicted on figure III.3(b). Further increasing the Reynolds number drives a larger range of wavenumbers to become unstable and the flow eventually experiences a Hopf bifurcation ($T1$ family) yielding transition to unsteadiness beyond a critical Reynolds number $Re_{T1} = 840$ for the same spanwise wavenumber, i.e. $\beta \simeq 15$. Comparison of these results with experimental data (where the cavity necessarily has side walls) turned out to be in not too bad agreements only when considering cavities with a relatively large spanwise extent. For smaller cavities, discrepancies might come from the fact that the flow in the symmetry plane cannot be approximated as being two-dimensional anymore, as well as due to the viscous damping induced by the experimental side walls inexistent in the numerically investigated base flows.

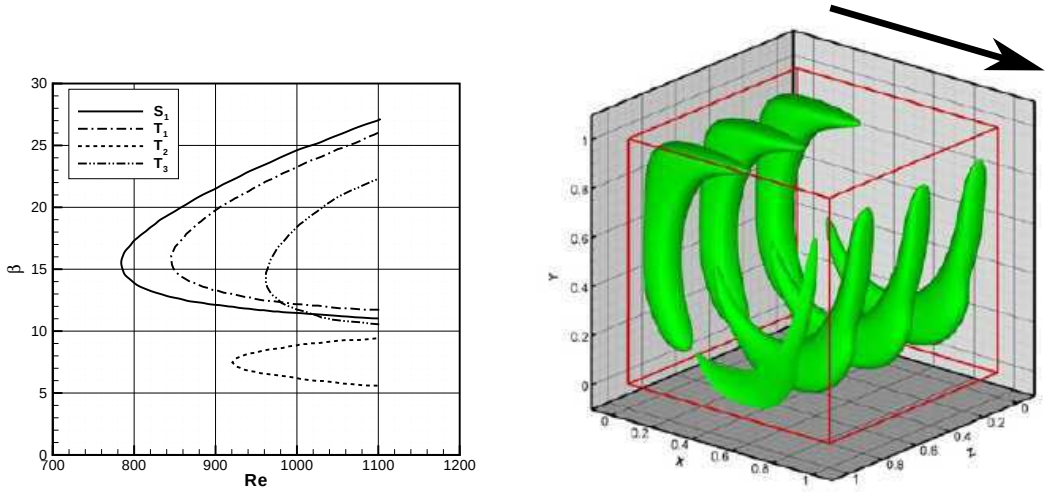

(a) (b)

Figure III.3: Global stability analysis of the 2D lid-driven cavity flow with respect to spanwise-periodic perturbations. (a) Neutral stability curve. (b) Leading unstable global mode. Figures reproduced from [42]. The arrow indicates the motion of the lid.

Three-dimensional LDC

The problem of the flow within a three-dimensional enclosure has received much less attention than its two-dimensional counterpart. In the mid 1970's, Davis & Mallinson [47] have been the first to investigate the fully three-dimensional lid-driven cavity flow. They have observed that the flow developing within such a three-dimensional setup qualitatively exhibits the same features as its two-dimensional counterpart: a central primary vortex flanked with corner eddies. For extensive details regarding the topology of three-dimensional LDC flows, the reader is referred to the exhaustive review by Shankar & Deshpande [141]. To our knowledge, only a few experimental data are available in the literature. Most of them have to be credited to Koseff *et al.* [91–93]. The former authors have presented qualitative and quantitative experimental observations of the flow developing within three-dimensional lid-driven cavities. In [93], they have particularly focused on the influence of the spanwise end walls on the flow. Their main conclusions are that reducing the spanwise extent of the cavity increases the viscous drag of the side walls. Consequently, the critical Reynolds number for transition to unsteadiness increases and as such it affects the intensity and the distribution of the Taylor-Görtler like vortices. From a numerical perspective, Albensoeder & Kuhlmann [7] have provided in 2005 accurate data of the steady flow within a cubical LDC at a Reynolds number $Re = 1000$ using a Chebyschev collocation method. However, because investigating the linear stability analysis of such fully three-dimensional flow still is quite computationally challenging, very few references can be found in the literature on the transition thresholds. To our knowledge, Feldman & Gelfgat [60] have only addressed the stability of the cubical lid-driven cavity by means of direct numerical simulations. They have found that the flow experiences a Hopf bifurcation at a critical Reynolds number $Re_c = 1914$. As for the 2.5D global stability analysis, the exponentially growing perturbation they have found in their DNS takes the form of Taylor-Görtler like vortices. Since a Hopf bifurcation has

been encountered, these are however oscillating at a circular frequency $\omega = 0.575$. Quite recently, Kuhlmann & Albensoeder [94] and Gómez *et al.* [71, 72] have also investigated this problem and found similar critical Reynolds numbers. In 2011, Liberzon *et al.* [105] have conducted experimental investigation on the same cubical setup. Beside a slight disagreement on the value of the critical Reynolds number above which unsteadiness sets in (though this might be explained by some imperfectness in the experimental setup or by genuine characteristics of the bifurcation such as sub-criticality), both the frequency and the rms fluctuations observed in the experiment are in qualitatively and quantitatively good agreements with the numerical predictions.

As part of this thesis, the work presented in this chapter aims at improving our understanding of instability and transition occuring in fully three-dimensional lid-driven cavity flows. More specifically, we will try to give answers to the following questions:

- What are the physical mechanisms underlying the instability of such three-dimensional flows? Do they differ from those found in the two-dimensional LDC flows?
- How does the spanwise aspect ratio of the LDC influence these instabilities?
- How does the prediction of the threshold of the first bifurcation occuring in these fully three-dimensional flows compare with those of the two-dimensional lid-driven cavity flow?

This chapter is organised as follows. First, the most important features of the steady equilibriums are presented along with a grid convergence analysis. Then, the stability of the flows towards infinitesimal perturbations is investigated by means of global stability analyses. Both the analysis of the underlying mechanism as well as the influence of the cavity's aspect ratio on the stability are part of this investigation. Finally, as shown very recently by Kulhmann & Albensoeder [94], beyond its critical Reynolds number, the flow within a cubical lid-driven cavity exhibits chaotic dynamics. These dynamics are thus studied and characterised using direct numerical simulations, Koopman mode decomposition and state-space representations.

III.3 Results

III.3.1 Steady state solutions

Computing steady equilibriums is a pre-requisite to any stability analysis. These peculiar solutions, also called base flows, have been computed for lid-driven cavities of constant square section and spanwise aspect ratios ranging from $\Lambda = 0.5$ up to $\Lambda = 3$. The selective frequency damping approach introduced in section II.2 has been used whenever these equilibriums turned out to be unstable and typical values of the χ and ω_c parameters are reported in table III.1. Figure III.4 depicts one of the streamlines of the steady flows obtained for (a) $(\Lambda, Re) = (0.5, 4250)$, (b) $(\Lambda, Re) = (1, 1950)$ and (c) $(\Lambda, Re) = (3, 1000)$, respectively. It can be seen from figure III.4 that, in all cases, the streamline remains enclosed within the left half of the cavity. Such behaviour of the streamlines indicates that all of these steady flows are symmetric with respect to the spanwise mid-plane of the

	$(\Lambda, Re) = (0.5, 4250)$	$(\Lambda, Re) = (1, 1950)$	$(\Lambda, Re) = (3, 1100)$
χ	0.01	0.01	0.01
ω_c	0.05	0.25	0.05

Table III.1: Typical values for the χ and ω_c parameters used in the selective frequency damping approach to compute the unstable steady states for various aspect ratio LDC.

cavities. Two major features of these flows can furthermore be observed in this symmetry plane: a central vortex surrounded by bottom corner eddies. According to the streamline's trajectory, the fluid is attracted by the central vortex from the spanwise end-walls toward the center of the cavity. This effect is known as the Eckman pumping. The fluid is then expelled within the central plane in a rotating motion due to the core vortex solid rotation before being captured by the bottom corner eddies. Finally, once captured by these secondary eddies, it is eventually expelled from the central plane toward the spanwise walls of the cavity. Because of these end-walls, the velocity has to drop to zero between the central plane and the walls. This drop creates a non-zero spanwise pressure gradient which eventually creates the spanwise motion of the fluid visualised by the streamlines in figure III.4. Though the vortical structures are qualitatively similar, the fluid's motion just described is the major difference between the two-dimensional and three-dimensional lid-driven cavity flows and might thus influence the stability of the flow.

Figure III.5 highlights the influence of the spanwise end-walls on the flow within the central mid-plane at a fixed Reynolds number $Re = 1000$ as compared to the strictly two-dimensional lid-driven cavity flow at the same Reynolds number. Figure III.5 depicts the x-velocity profile along the $y = 0$ line (blue) and the y-velocity profile along the $x = 0$ line (red) in the central plane for the different three-dimensional LDC (solid lines) and their two-dimensional counterpart (dashed line). It obviously appears from these plots that, though the overall features of the flows look similar, assuming the flow in the three-dimensional cavities to be essentially two-dimensional always yields to an over-prediction of the strength of the boundary layers developing along the downstream, bottom and upstream walls of the cavity. This can easily be explained when thinking in terms of energy. Indeed, whereas all of the energy input from the moving lid is only transfered to the x- and y-velocity components in the two-dimensional setup, part of this energy is transfered to the z-component of the velocity field as well within the three-dimensional cases. Moreover, whereas no spanwise end-walls are present within the two-dimensional flow, such walls are a genuine feature of the three-dimensional setup. Hence, the energy dissipated in their vicinity cannot be accounted for in the strictly two-dimensional assumption of the flow. Consequently, due to the redistribution of the input energy and the dissipation associated to the spanwise walls, the boundary layers in the three-dimensional flow cannot be as energetic as their two-dimensional counterparts. It is nonetheless apparent that, as the spanwise extent of the three-dimensional lid-driven cavity is increased, the discrepancies between the 3D and 2D flows seem to be reduced. This is further highlighted by table III.2 providing the relative contribution of each of the velocity components to the total kinetic energy of the base flows. The contribution of the spanwise velocity component is almost negligible in all cases. Moreover, increasing the spanwise aspect ratio of the cavity essentially redistribute the energy along the x- and y-velocity components

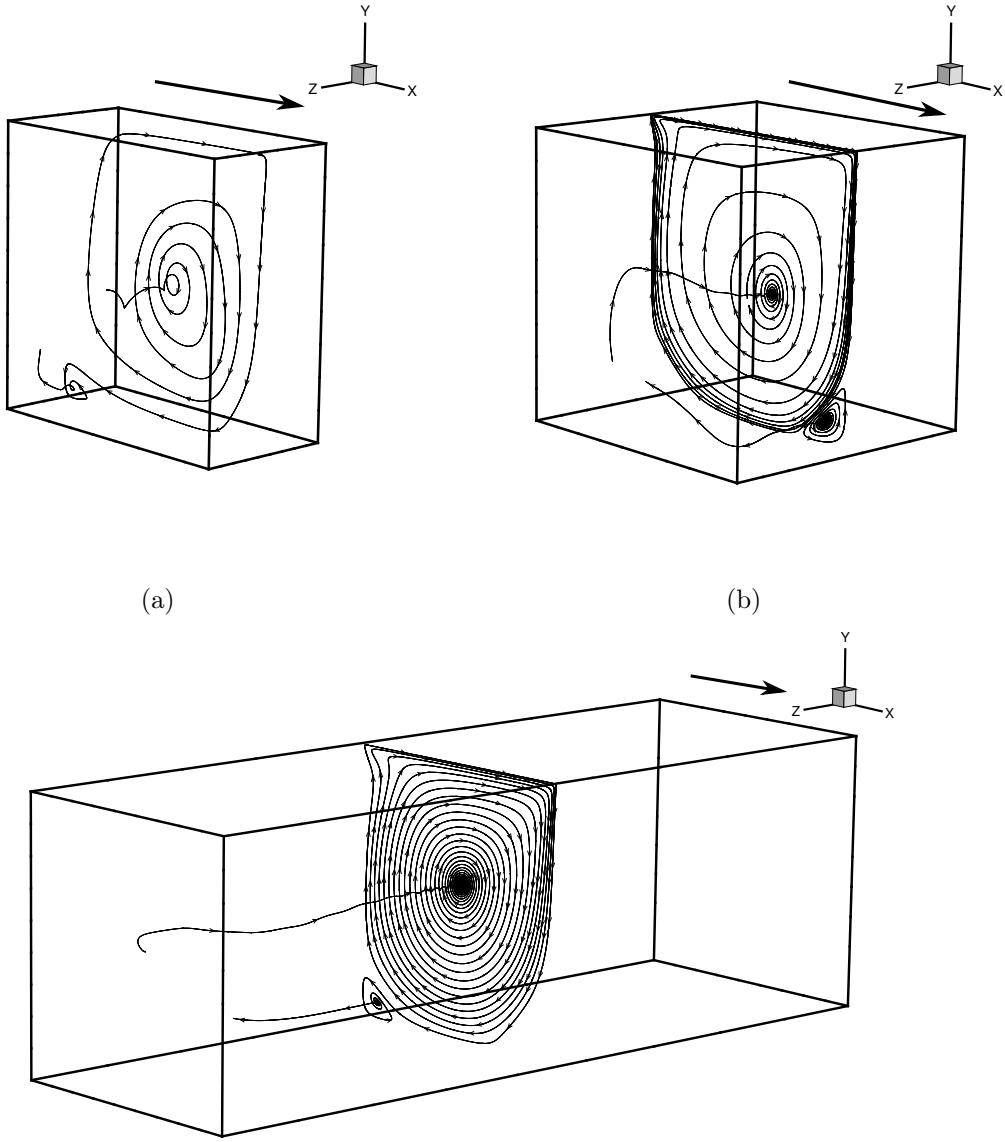

(a) (b)

(c)

Figure III.4: Visualisation of the base flow' structure using a streamline for (a) $(\Lambda, Re) = (0.5, 4250)$, (b) $(\Lambda, Re) = (1, 1950)$ and (c) $(\Lambda, Re) = (3, 1000)$. The arrows indicate the motion of the lid.

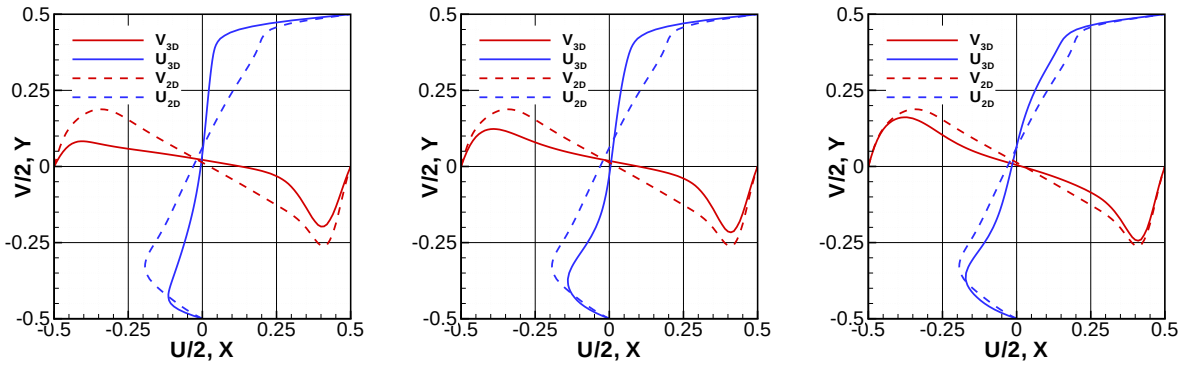

(a) $\Lambda = 0.5$ (b) $\Lambda = 1$ (c) $\Lambda = 3$

Figure III.5: Comparison of the flow in the spanwise mid-plane (solid lines) with the two-dimensional lid-driven cavity flow (dashed lines) both at $Re = 1000$. Blue solid and dashed lines display the evolution of the x-velocity along the $x = 0$ line, and red lines the evolution of the y-velocity along the $y = 0$ line.

	$\Lambda = 0.5$	$\Lambda = 1$	$\Lambda = 3$	2D
$\int_V U_b^2 \, \mathrm{d}V/E$	0.58577	0.55880	0.53738	0.52917
$\int_V V_b^2 \, \mathrm{d}V/E$	0.40842	0.43381	0.45730	0.47083
$\int_V W_b^2 \, \mathrm{d}V/E$	0.00581	0.00737	0.00531	0

Table III.2: Contribution of the various components of the velocity field to the total kinetic energy $E = \int_V (U_b^2 + V_b^2 + W_b^2)/2 \, \mathrm{d}V$ for LDC flows of various spanwise aspect ratios Λ at fixed Reynolds number $Re = 1000$.

accordingly to the two-dimensional reference. It is thus expected that considering an even larger lid-driven cavity (see appendix A for an example), the energy distribution among the velocity components would tends asymptotically toward the two-dimensional distribution.

Grid independence analysis

Figure III.6(a) shows the distribution of Legendre spectral elements used in a spanwise section for all of the cavities considered, whereas figure III.6(b) shows the grid resulting from the use of Legendre polynomials of order $N = 7$ within each spectral element. Both the x and y directions are discretised using ten spectral elements located according to a two-dimensional set of Gauss-Lobatto-Legendre quadrature points. Such partionning allows us to refine along the different walls of the cavities where the gradients of the velocity are the largest. In the spanwise direction, the number of spectral elements used to discretise the problem depends on the aspect ratio of the cavity considered. Five elements are used for $\Lambda = 0.5$, ten and thirty are used for $\Lambda = 1$ and $\Lambda = 3$, respectively. It is worthy to note that these elements are also located according to Gauss-Lobatto-Legendre quadrature points such that the problem is finely discretised in the vicinity of the spanwise end walls as well.

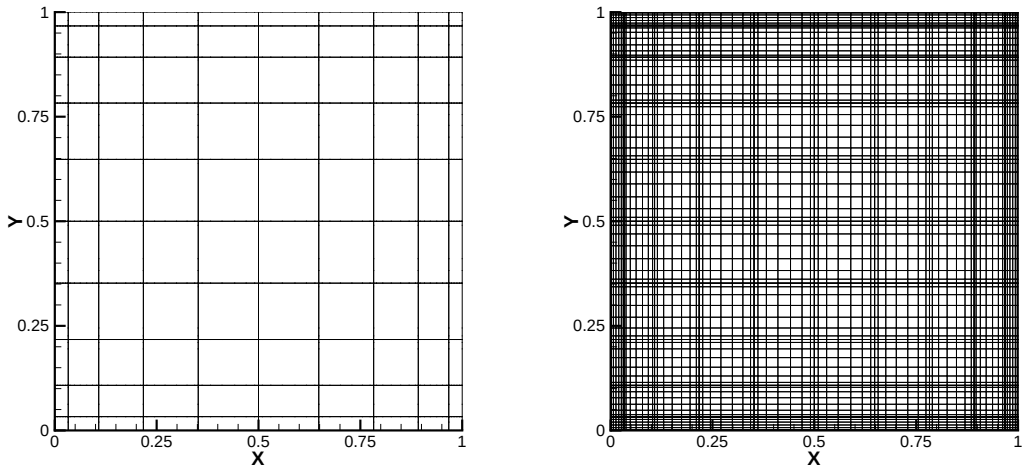

(a) (b)

Figure III.6: (a) Distribution of the Legendre spectral elements for the lid-driven cavity flow problem. Ten elements are used in each direction and located along a GLL grid. (b) Resulting mesh using an order 7 Legendre polynomial reconstruction within each element.

Independence of the computed solutions with respect to the grid resolution has been assessed by increasing the order of the polynomial order within each spectral elements from $N = 5$ up to $N = 11$. Tables III.3 and III.4 provide the reader with a comparison of the values of the x- and y-velocity components for $(\Lambda, Re) = (1, 1000)$ and different polynomial orders with those reported by Albensoeder & Kuhlmann [7] using a Chebyschev spectral collocation method on 96^3 mesh. Values of our present computations have been spectrally interpolated onto the points coordinates given in [7] to ease the comparison. Even for the coarser resolution, the values obtained with the present computation are in excellent agreements with those obtained by Albensoeder & Kuhlmann [7]. The mean relative errors for the x-component are $\epsilon = 0.03\%$ for $N = 5$, $\epsilon = 0.002\%$ for $N = 7$ and $\epsilon = 0.0004\%$ for $N = 11$, respectively. For the y-component, these errors are $\epsilon = 0.04\%$ for $N = 5$, $\epsilon = 0.0008\%$ for $N = 7$ and $\epsilon = 0.0002\%$ for $N = 11$, respectively. No clear difference can be observed between the three different resolutions. The intermediate grid $N = 7$ then presents a pretty good trade-off between accuracy and computational time for all the cases and will thus be used to pursue the investigations.

III.3.2 Linear stability analysis

As to understand how the steady solutions computed in the previous section lose their stability, the underlying physical mechanisms are investigated by mean of global stability analyses. Figure III.7 depicts the eigenspectrum of the linearised Navier-Stokes operator for (a) $(\Lambda, Re) = (0.5, 4000)$, (b) $(\Lambda, Re) = (1, 1950)$ and (c) $(\Lambda, Re) = (3, 1075)$, respectively. They have been computed using Krylov subspaces of dimension 250 and a sampling period $\Delta T = 1$ enabling good convergence of the eigenvalues up to $\omega = 1.6$ (with ω being the circular frequency). Since these eigenspectra are symmetric, only their right

y	$U_{Alb.}$	$U_{present}$		
		$N = 5$	$N = 7$	$N = 11$
0.5000	1.0000000	1.0000000	1.0000000	1.0000000
0.4766	0.5896414	0.5895510	0.5896338	0.5896418
0.4688	0.4844275	0.4843287	0.4844196	0.4844286
0.4609	0.3982086	0.3980585	0.3982002	0.3982090
0.4531	0.3317110	0.3316870	0.3317025	0.3317109
0.3516	0.1218293	0.1217866	0.1218260	0.1218286
0.2344	0.0733444	0.0733271	0.0733437	0.0733443
0.1172	0.0390483	0.0390543	0.0390491	0.0390486
0.0000	0.0080177	0.0080268	0.0080194	0.0080184
-0.0469	-0.0061192	-0.0061142	-0.0061172	-0.0061183
-0.2187	-0.1099894	-0.1100487	-0.1099850	-0.1099881
-0.3281	-0.2516006	-0.2515849	-0.2515946	-0.2515998
-0.3984	-0.2729293	-0.2726963	-0.2729276	-0.2729297
-0.4297	-0.2369550	-0.2367250	-0.2369556	-0.2369555
-0.4375	-0.2228255	-0.2225908	-0.2228259	-0.2228259
-0.4453	-0.2062332	-0.2059942	-0.2062333	-0.2062335
-0.5000	0.0000000	0.0000000	0.0000000	0.0000000

Table III.3: Comparison of the values of the x-velocity component along the $y = 0$ lines for different polynomial orders with those reported in [7] for $(\Lambda, Re) = (1, 1000)$.

x	$V_{Alb.}$	$V_{present}$		
		$N = 5$	$N = 7$	$N = 11$
0.5000	0.0000000	0.0000000	0.0000000	0.0000000
0.4688	-0.1886420	-0.1884574	-0.1886396	-0.1886391
0.4609	-0.2409470	-0.2406544	-0.2409442	-0.2409442
0.4531	-0.2903172	-0.2900838	-0.2903130	-0.2903146
0.4453	-0.3351117	-0.3348599	-0.3351107	-0.3351095
0.4063	-0.4342302	-0.4340571	-0.4342278	-0.4342311
0.3594	-0.3111715	-0.3111979	-0.3111748	-0.3111731
0.3047	-0.1522299	-0.1523298	-0.1522293	-0.1522300
0.0000	0.0367355	0.0367529	0.0367383	0.0367362
-0.2656	0.1698661	0.1698358	0.1698623	0.1698654
-0.2734	0.1758025	0.1757662	0.1757982	0.1758017
-0.3437	0.2292360	0.2291543	0.2292297	0.2292352
-0.4062	0.2440743	0.2439377	0.2440691	0.2440740
-0.4219	0.2350273	0.2349018	0.2350224	0.2350271
-0.4297	0.2274623	0.2273439	0.2274581	0.2274621
-0.4375	0.2173841	0.2172601	0.2173798	0.2173838
-0.5000	0.0000000	0.0000000	0.0000000	0.0000000

Table III.4: Comparison of the values of the y-velocity component along the $x = 0$ lines for different polynomial orders with those reported in [7] for $(\Lambda, Re) = (1, 1000)$.

half is depicted. As one can see, in all cases, complex conjugate pairs of eigenvalues lie in the vicinity of the upper-half complex plane. This indicates that the three base flows presented in the previous section are all equilibriums on the verge to or having already experienced a Hopf bifurcation. Table III.5 provides the critical Reynolds numbers Re_c^1 for the different cavities investigated. It appears from this table that, for the range of spanwise aspect ratios considered, the larger the spanwise extent of the cavity considered, the lower the value of the critical Reynolds number. The decrease of the critical Reynolds number with an increase of the spanwise extent of the cavity is related to the increased viscous damping induced by the spanwise end-walls and has already been foreseen experimentally by Koseff *et al.* [93]. It is moreover in good agreements with the observations made concerning the two-dimensionality of the flow in the spanwise mid-plane. Indeed, the closer the flow in the symmetry plane is to its two-dimensional counterpart, the lower the critical Reynolds number.

Depicted on figure III.8 are the vertical velocity components of the real part of the leading unstable mode for (a) $(\Lambda, Re) = (0.5, 4000)$, (b) $(\Lambda, Re) = (1, 1950)$ and (c) $(\Lambda, Re) = (3, 1075)$, respectively. As one can see, all these modes share at least one common feature: vertical low- and high-speed streaks on the downstream wall. It is moreover obvious that the mode for $(\Lambda, Re) = (1, 1950)$ and $(\Lambda, Re) = (3, 1075)$ share even closer connections: they display a banana-like structure remininscent of the modes found by Theofilis *et al.* [152] and Chicheportiche *et al.* [42] on a 2.5D lid-driven cavity flow and similar to what has been observed by Feldman & Gelfgat [60] and Goméz *et al.* [71] on similar three-dimensional setups. Moreover, they all exhibit a symmetry with respect to the spanwise mid-plane of the cavities. In the mean time, the x- and z-velocity components (not shown) display a symmetry and an anti-symmetry with respect to this mid-plane, respectively. To get a better understanding of the motion these unstable eigenmodes induce, table III.7 provides the contribution of the different components of the global mode to its kinetic energy. It can be seen that though fewer energy is along the z-component, the three velocity component are more or less of the same order of magnitude. Figure III.9 depicts the perturbation's velocity field in a y-cut plane whose location is dependent on the mode considered: vectors highlight the in-plane motion, whereas colored contours show the vertical motion (blue: negative, red: positive). All these mode share common features: they induce spanwise pairs of counter-rotating vortices located in the vicinity of the upstream wall and high- and low-speed streaks on the downstream wall. It is striking moreover that, apart from $\Lambda = 0.5$, such streaks are also to be found on the upstream wall. For $\Lambda = 1$ and $\Lambda = 3$, these vortices, known as Taylor-Görtler-like (TGL) vortices transfer vertical high-speed fluid from the inner part of the cavity toward the upstream wall, whereas low-speed fluid is transfered from the wall toward the inner part of the cavity. This transfer of momentum, known as the lift-up effect [97], causes the emergence of low- and high-speed vertical streaks identified by the colored contours. It is morover obvious from figure III.9 that the number of TGL vortices induced by the mode is dependent on the spanwise extent of the cavity. Indeed, apart from $\Lambda = 0.5$ where vortices are hardly visible, two pairs of TGL vortices can be seen in the $\Lambda = 1$ cavity, and six of them in the largest cavity considered herein. It appears finally from these slices as well that the diameter D of the TGL vortices seems almost constant, i.e. $D \simeq 0.2$, no matter the spanwise extent of the cavity considered (provided it is sufficiently large). Associated

	$\Lambda = 0.5$	$\Lambda = 1$	$\Lambda = 3$	$\Lambda = \infty$
Re_c^1	4000	1910	1070	780 (S1)
Re_c^2	4375	2000	1072	840 (T1)

Table III.5: Instability onsets predicted by linear stability theory for the symmetric (first row) and anti-symmetric (second row) instabilities.

	$\Lambda = 0.5$	$\Lambda = 1$	$\Lambda = 3$	$T1$ branch	Benson & Aidun
$\omega/2\pi$	0.023	0.09	0.119	0.1012	0.108

Table III.6: Comparison of the frequency predicted by fully three-dimensional global stability analysis with those predicted by 2.5D global stability [152] and experiments [28].

	$(\Lambda, Re) = (0.5, 4000)$	$(\Lambda, Re) = (1, 1950)$	$(\Lambda, Re) = (3, 1075)$
$\int_V u_r^2 + u_i^2 \, \mathrm{d}V$	0.334059	0.425757	0.394354
$\int_V v_r^2 + v_i^2 \, \mathrm{d}V$	0.533169	0.371588	0.388477
$\int_V w_r^2 + w_i^2 \, \mathrm{d}V$	0.132771	0.202654	0.217168

Table III.7: Relative contribution to the total kinetic energy of the various components of the symmetric global modes velocity field for LDC flows of various spanwise aspect ratios Λ. The norm $E = \int_V \mathbf{q}^* \cdot \mathbf{q} \, \mathrm{d}V$ is set to one, where * denotes the complex conjugate and $\cdot$ the scalar product, and $\cdot_r$ and $\cdot_i$ the real and imaginary parts, respectively

	$(\Lambda, Re) = (0.5, 4000)$	$(\Lambda, Re) = (1, 1950)$	$(\Lambda, Re) = (3, 1075)$
$\int_V u_r^2 + u_i^2 \, \mathrm{d}V$	0.326470	0.422994	0.394237
$\int_V v_r^2 + v_i^2 \, \mathrm{d}V$	0.492067	0.362398	0.388622
$\int_V w_r^2 + w_i^2 \, \mathrm{d}V$	0.181461	0.214607	0.217139

Table III.8: Relative contribution to the total kinetic energy of the various components of the anti-symmetric global modes' velocity field for LDC flows of various spanwise aspect ratios Λ.

to this diameter D, one can then determine that the dominant spanwise number of the perturbation is $\beta_{3D} = 15.07$, i.e. extremely close to the most unstable wavenumber in the two-dimensional LDC flow subject to spanwise-periodic perturbations (see [42, 152]). Because of this close resemblance with the two-dimensional case, table III.6 provides a comparison of the frequency of the fully three-dimensional leading global modes found in the present investigation with the closest spanwise-periodic global mode from Theofilis *et al.* [152] and experimental data from Benson & Aidun [28]. First of all, one must remember that as the spanwise extent of the lid-driven cavity is increased, the critical value of the Reynolds number predicted by fully three-dimensional global stability analyses decreases. The leading unstable global modes seem to be related to the $T1$ family of modes as highlighted by the data from table III.6: the frequency at which the leading globally unstable mode oscillates for $\Lambda = 1$ and $\Lambda = 3$ is very close to the one observed in the experiment by Benson & Aidun [28] as well as to the frequency of the leading $T1$ mode found by Theofilis *et al.* [152]. One might wonder however if the fully three-dimensional instability could tend toward the $S1$-branch when considering very large spanwise LDC. This question is partially addressed in appendix A.

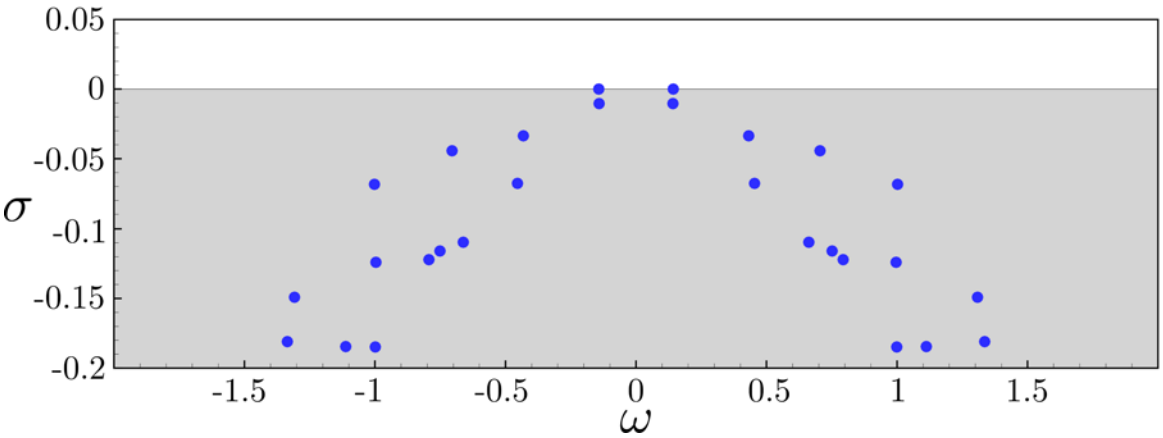

(a) $(\Lambda, Re) = (0.5, 4000)$

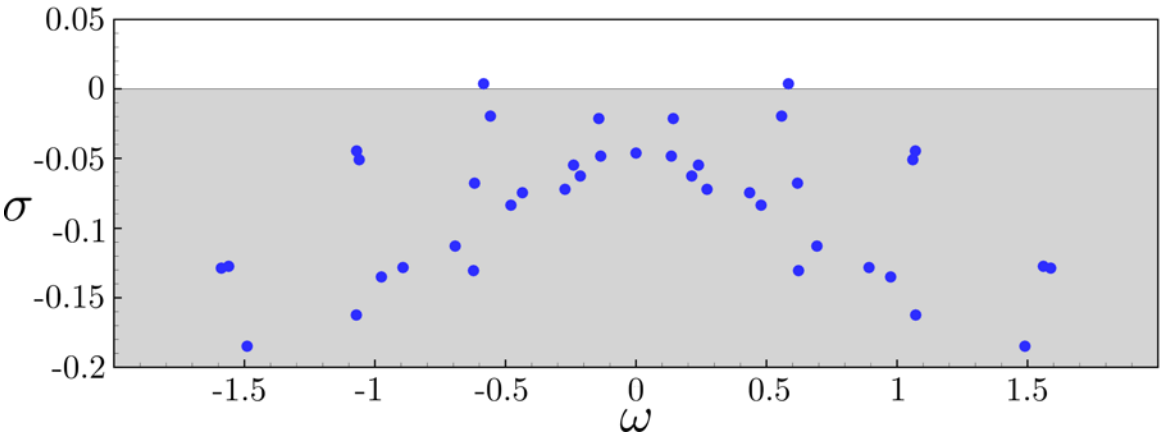

(b) $(\Lambda, Re) = (1, 1950)$

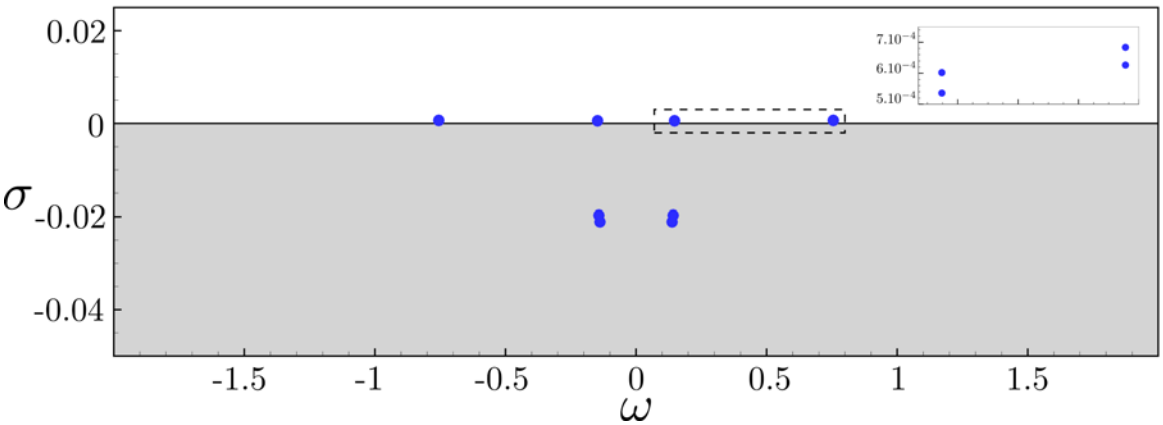

(c) $(\Lambda, Re) = (3, 1075)$

Figure III.7: Eigenspectra of the linearised Navier-Stokes operator. On figure (c), the subset shows a close-up view on the four leading eigenvalues contained within the dashed rectangle.

Despite transition to unsteadiness being always triggered by a symmetric instability, one might also be interested in the nature of the second leading pair of complex conjugate eigenvalues. The critical Reynolds numbers Re_c^2 associated to these instabilities are provided by table III.5 as well, whereas the spatial distribution of their real part's y-velocity component are depicted on figure III.10. The first striking piece of information from these figures is the symmetry of these modes: whereas the leading modes are always displaying a symmetry with respect to the spanwise mid-plane of the cavities, these now display an anti-symmetry. Beside this difference in the symmetry, they exhibit the same features as their symmetric counterparts letting us infer they might as well be related to the same underlying instability mechanisms. This is further confirmed by taking a look at the y-plane cuts depicted on figure III.11. Indeed, as one can see, vortices are clearly visible in the vector plots. Moreover, as previously, these vortices induce vertical low- and high-speed streaks due to the lift-up effect [97]. It is however striking that, whereas the symmetric modes always exhibit an even number of TGL vortices, these antisymmetric modes only display an odd number of such vortices. It can finally be noted that, as the spanwise aspect ratio Λ of the cavity is increased, the difference between Re_c^1 and Re_c^2 decreases down to a point where the symmetric and anti-symmetric global modes become unstable almost at the exact same critical threshold. Despite these differences in symmetry which are genuine to fully three-dimensional setups, as their symmetric counterparts, these modes are thus very likely to be related to the $T1$ family of modes observed by Theofilis *et. al* [152] in 2.5D lid-driven cavities.

Perturbation's kinetic energy transfer analysis

In order to ascertain that the underlying mechanism is the same as in 2D-periodic stability analyses[9, 42, 152] and to understand how the spanwise extent of the LDC influences this instability mechanism, the kinetic energy transfers between the base flow and the perturbations are investigated. The time-evolution of the kinetic energy E of the perturbation $\mathbf{u}$ is governed by the Reynolds-Orr equation:

$$\frac{\partial E}{\partial t} = \int_\Omega -\mathbf{u}\cdot(\mathbf{u}\cdot\nabla)\mathbf{U}_b \,\mathrm{d}\Omega - \frac{1}{Re}\int_\Omega \nabla\mathbf{u} : \nabla\mathbf{u} \,\mathrm{d}\Omega \tag{III.2}$$

where the first term on the right-hand side of equation (III.2) is the total production term, and the second one is the total dissipation in the computational volume $\int_\Omega D \,\mathrm{d}\Omega$. As proposed in [9], the perturbation velocity vector can decomposed into $\mathbf{u} = \mathbf{u}_\perp + \mathbf{u}_\parallel$, i.e. components perpendicular and parallel to the direction of the base flow $\mathbf{U}_b$. These two components are given by:

$$\begin{aligned} \mathbf{u}_\parallel &= \frac{(\mathbf{u}\cdot\mathbf{U}_b)}{\|\mathbf{U}_b\|^2}\mathbf{U}_b \\ \mathbf{u}_\perp &= \mathbf{u} - \mathbf{u}_\parallel \end{aligned} \tag{III.3}$$

Such decomposition highlights that, while the counter-rotating vortices are associated to a motion perpendicular to the base flow's direction, the high- and low-speed streaks are parallel to the flow. Using such decomposition, the production term $-\mathbf{u}\cdot(\mathbf{u}\cdot\nabla)\mathbf{U}_b$ can

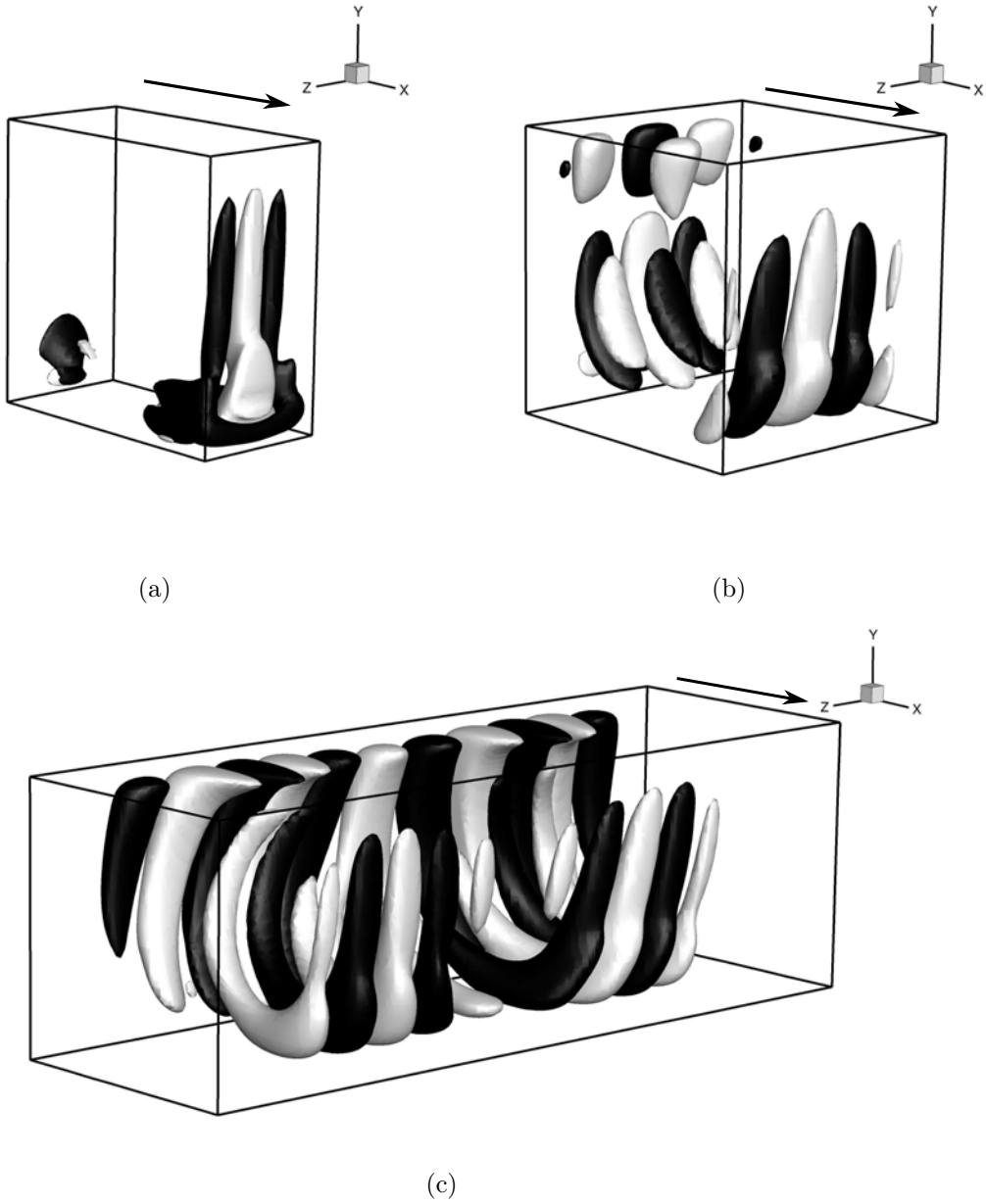

Figure III.8: Vertical velocity component of the leading symmetric global mode's real part for (a) $(\Lambda, Re) = (0.5, 4000)$, (b) $(\Lambda, Re) = (1, 1950)$ and (c) $(\Lambda, Re) = (3, 1075)$. Isosurfaces depict in all cases $\pm 10\%$ of the vertical velocity's maximum.

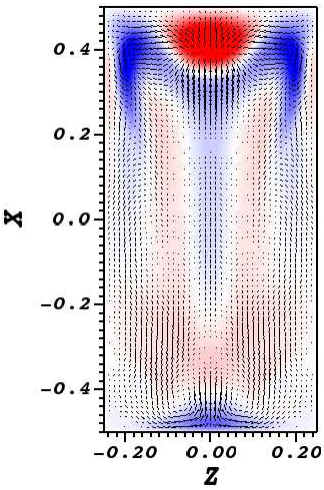

(a) $(\Lambda, Re) = (0.5, 4250)$

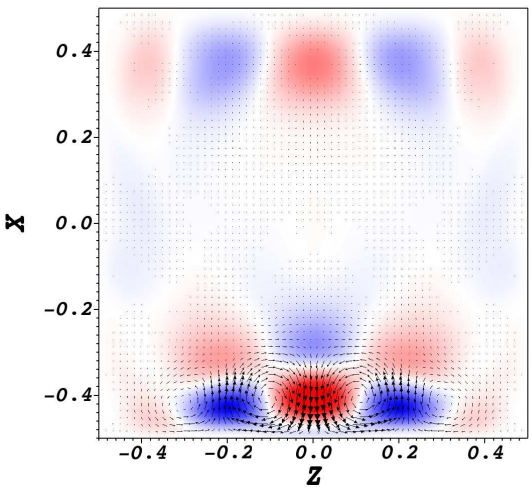

(b) $(\Lambda, Re) = (1, 1950)$

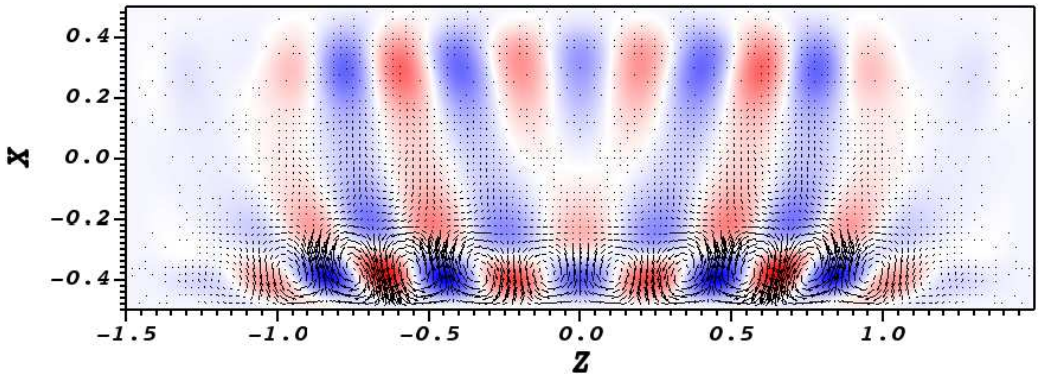

(c) $(\Lambda, Re) = (3, 1075)$

Figure III.9: Vector fields depict the horizontal in-plane motion induced by the symmetric modes, whereas coloured contours show the vertical motion. (a) $y = -0.45$ and $(\Lambda, Re) = (0.5, 4000)$,(a) $y = -0.25$ and $(\Lambda, Re) = (1, 1950)$ and (c) $y = -0.25$ and $(\Lambda, Re) = (3, 1075)$

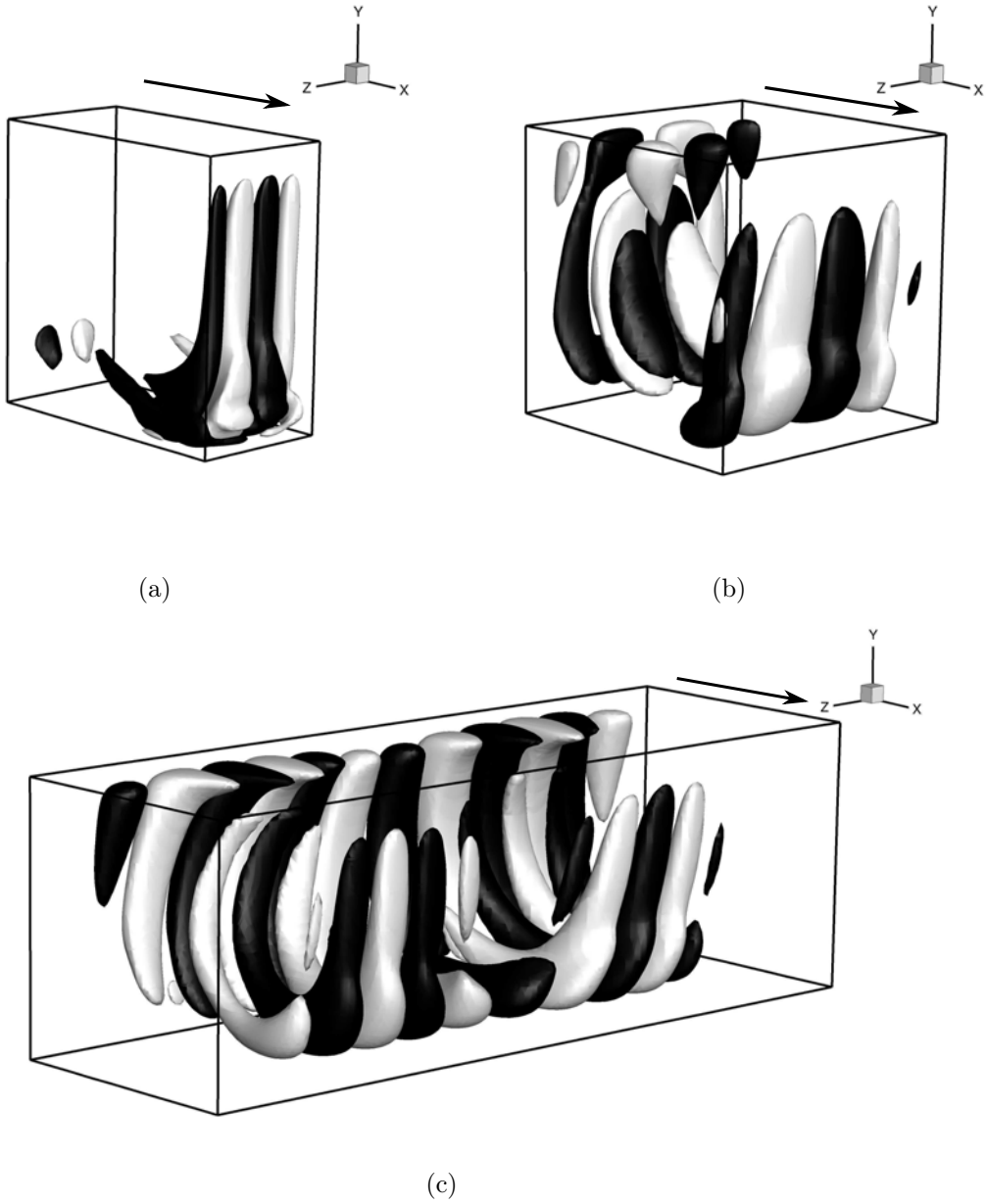

Figure III.10: Vertical velocity component of the leading antisymmetric global mode's real part for (a) $(\Lambda, Re) = (0.5, 4000)$, (b) $(\Lambda, Re) = (1, 1950)$ and (c) $(\Lambda, Re) = (3, 1075)$. Isosurfaces depict in all cases $\pm 10\%$ of the vertical velocity's maximum.

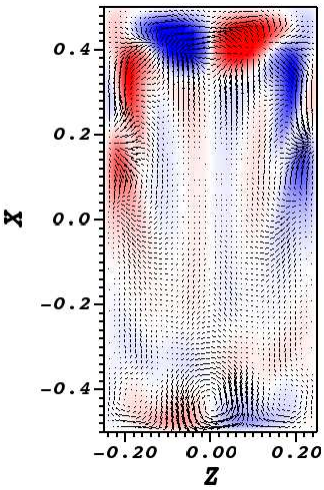

(a) $(\Lambda, Re) = (0.5, 4250)$

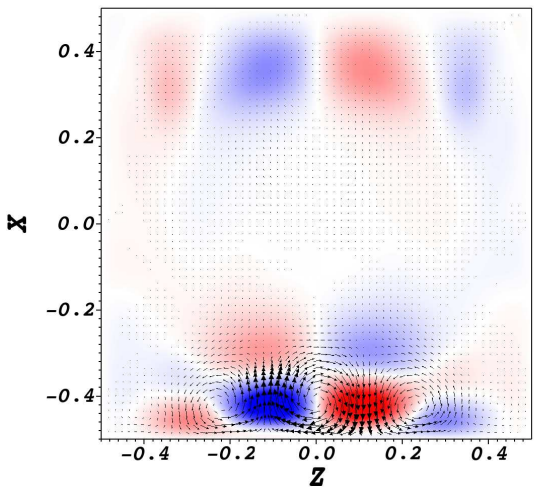

(b) $(\Lambda, Re) = (1, 1950)$

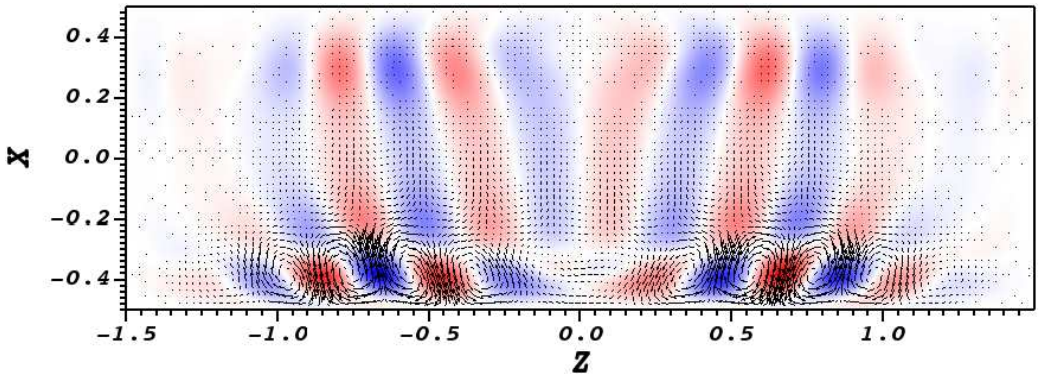

(c) $(\Lambda, Re) = (3, 1075)$

Figure III.11: Vector fields depict the horizontal in-plane motion induced by the anti-symmetric modes, whereas coloured contours show the vertical motion. (a) $y = -0.45$ and $(\Lambda, Re) = (0.5, 4000)$,(a) $y = -0.25$ and $(\Lambda, Re) = (1, 1950)$ and (c) $y = -0.25$ and $(\Lambda, Re) = (3, 1075)$

then be decomposed into four different contributions, namely:

$$\begin{aligned} I_1 &= -\mathbf{u}_\perp \cdot (\mathbf{u}_\perp \cdot \nabla)\mathbf{U}_b \\ I_2 &= -\mathbf{u}_\parallel \cdot (\mathbf{u}_\perp \cdot \nabla)\mathbf{U}_b \\ I_3 &= -\mathbf{u}_\perp \cdot (\mathbf{u}_\parallel \cdot \nabla)\mathbf{U}_b \\ I_4 &= -\mathbf{u}_\parallel \cdot (\mathbf{u}_\parallel \cdot \nabla)\mathbf{U}_b \end{aligned} \tag{III.4}$$

Each of these contributions to the total production term can be associated to a different physical mechanism. The sign of the different integrals $\int_\Omega I_i \, \mathrm{d}\Omega$ then informs whether the physical mechanism associated to them acts as promoting (positive) or quenching (negative) the global instability under consideration.

The symmetric instability of the flow is the first one encountered in all the cases investigated. Figure III.12 provides the total kinetic energy transfers for lid-driven cavities of various spanwise extents Λ. As for the 2D-periodic lid-driven cavity flow [9], the I_2 production term dominates these energy budgets for all of the spanwise extents considered. Figure III.13 depicts the spatial distribution of this I_2 production term averaged in the z-direction for lid-driven cavities of different spanwise aspect ratio Λ. As can be assessed from these figures, the global modes essentially extract their kinetic energy from the left side of the cavities, along the shear layer delimiting the primary vortex from the corner eddy. Comparing these kinetic energy budget and the spatial distribution of the dominant production term with the work of Albensoeder & Kuhlmann [9], it appears obvious that the fully three-dimensional instability mechanism at play here is similar to that of the 2D-periodic lid-driven cavity flow. It has been argued by the latter authors [9] that this particular I_2 production term should be the dominating one in the case of a centrifugal instability of the flow. Though we agree with their explanations, another physical interpretation can nonetheless be given to this production term. Indeed, the I_2 term characterises the transfer of kinetic energy from the vortical structure $\mathbf{u}_\perp$ to the streaky one $\mathbf{u}_\parallel$. As a consequence, it shares close connections with the lift-up effect [96] in boundary layer flows wherein streamwise velocity streaks (i.e. $\mathbf{u}_\parallel$) are promoted by streamwise-oriented counter-rotating vortices (i.e. $\mathbf{u}_\perp$). As a consequence in a control perspective, one might need to act only on the vortical stucture $\mathbf{u}_\perp$ to modify the whole kinetic energy transfer from the base flow to the perturbation. Finally, it is worthy to note that similar results hold for the anti-symmetric instability (not shown here).

III.3.3 Non-linear evolution

Among the large body of literature on the lid-driven cavity flow, few references can be found regarding the unsteady non-linear flow developing within a cubical LDC. Unfortunately, as in Leriche [102], Leriche & Gavrilakis [104], most of these numerical studies have considered relatively high Reynolds number flows making their insights inconclusive regarding the dynamics of the flow close to the critical Reynolds number. After having investigated the linear stability of the flow in the cubical lid-driven cavity, Feldman & Gelfgat [60] have also rapidly looked at its non-linear evolution close to the critical Reynolds number $Re_c = 1914$. They have shown that, once linearly unstable, the flow was driven from the steady equilibrium to a periodic limit cycle. Unfortunately, as shown

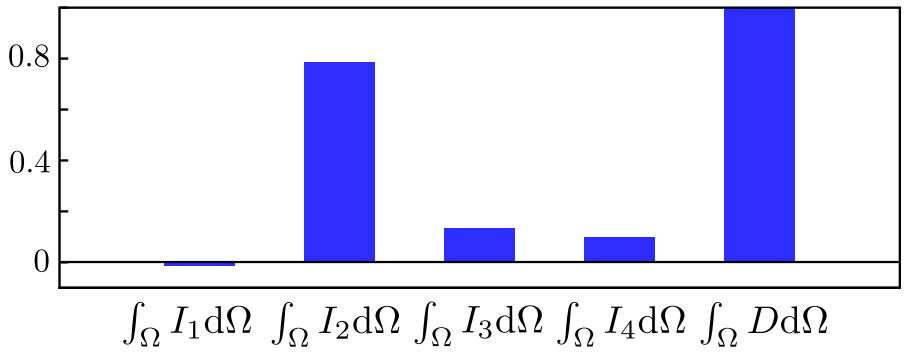

(a) $(\Lambda, Re) = (1, 1950)$

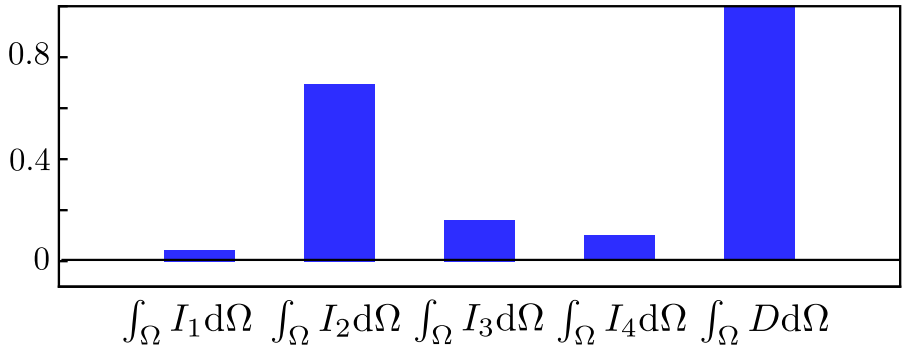

(b) $(\Lambda, Re) = (3, 1075)$

Figure III.12: Total kinetic energy budget of the leading unstable global mode for cavities of various spanwise extents Λ. All of the production terms $\int_\Omega I_i \, \mathrm{d}\Omega$ have been normalised by the total dissipation $\int_\Omega D \, \mathrm{d}\Omega$ for the sake of comparison.

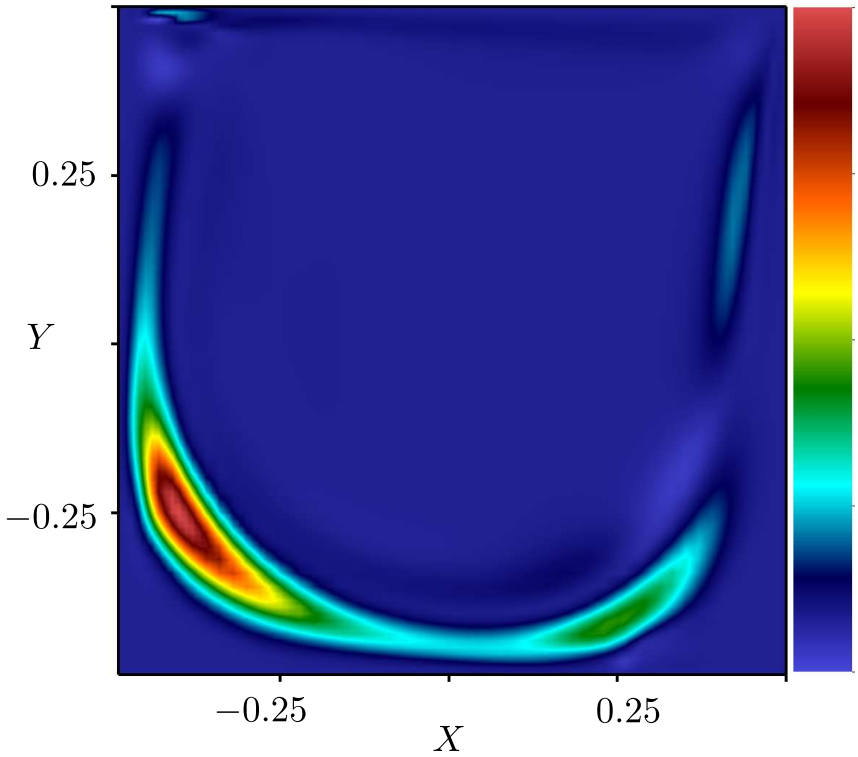

(a) $(\Lambda, Re) = (1, 1950)$

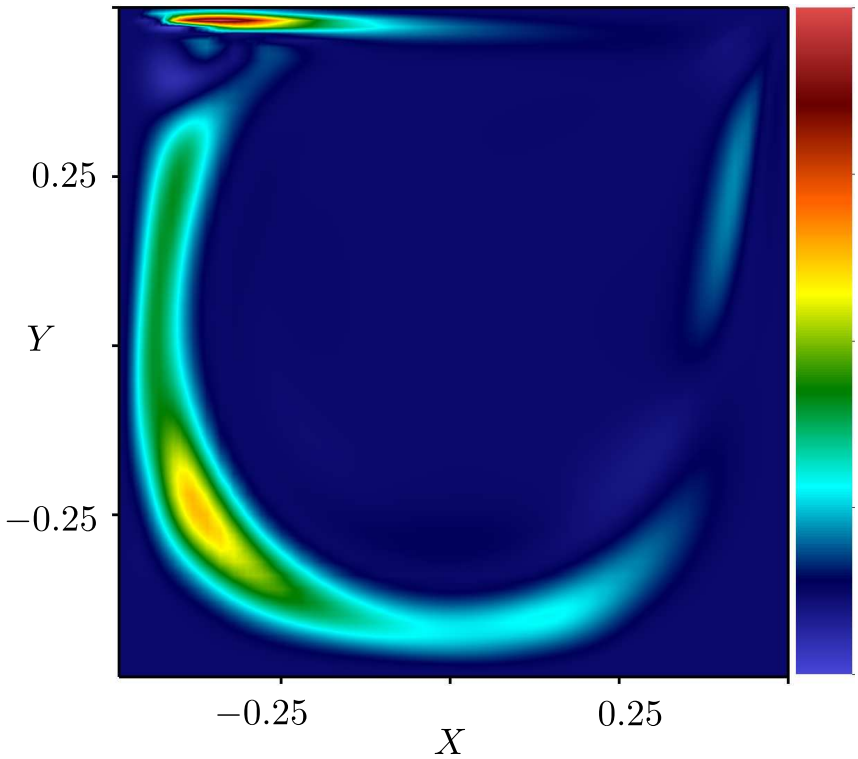

(b) $(\Lambda, Re) = (3, 1075)$

Figure III.13: Spatial distribution of the I_2 production term averaged in the z-direction for lid-driven cavities of various spanwise aspect ratio Λ.

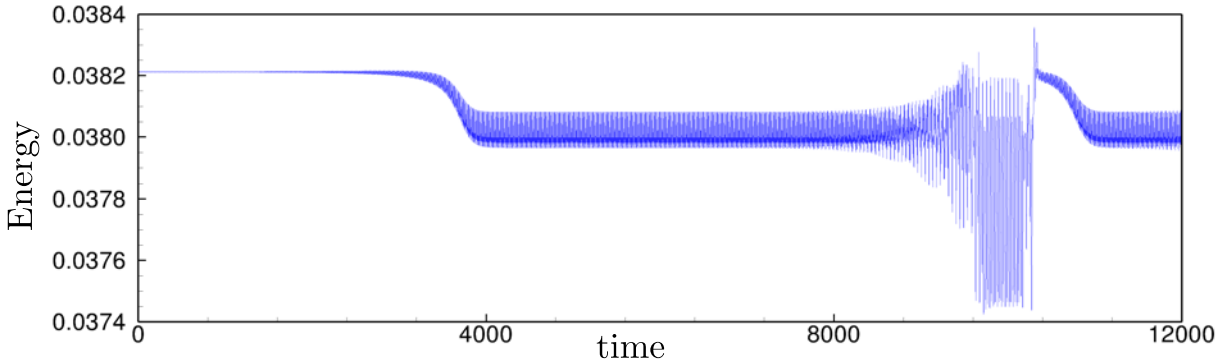

Figure III.14: Long time evolution of the flow's kinetic energy in an aspect ratio $\Lambda = 1$ lid-driven cavity at $Re = 1930$

very recently by Kuhlmann & Albensoeder [94], the total time integration of the Navier-Stokes equations performed in [60] was not sufficiently long to unravel the most interesting feature of the resulting non-linear flow: its intermittent chaotic nature.

Figure III.14 shows the long time evolution of the kinetic energy of the flow in the cubical lid-driven cavity ($\Lambda = 1$) at a slightly supercritical Reynolds number $Re = 1930$. The direct numerical simulation has been initialised with the appropriate unstable base flow as the initial condition. This base flow being linearly unstable, the flow slowly deviates from its initial state. The speed at which it deviates is however obviously Reynolds number-dependent: the higher the Reynolds number, the larger the growth rate of the most unstable global mode and the quicker does the flow depart from its equilibrium state. Once deviation is large enough, non-linearities kick in and the flow settles on what would appear to be a periodic limit cycle. Unfortunately, as shown by the long time integration of the equations, this limit cycle is unstable and the flow eventually experiences a burst of the kinetic energy. The flow then comes back in the vicinity of the unstable steady state before slowly deviating from it and settles on the unstable limit cycle once again. After a slightly smaller period of time, a new burst occurs and the scenario just described repeats itself over and again. According to Pomeau & Manneville [125], such transition scenario is characteristic of intermittent chaos. Except the recent work by Kuhlmann & Albensoeder [94], such intermittent chaotic dynamics have never been mentionned in the literature before for the lid-driven cavity flow at the onset of transition. In the following subsections, some insights about the dynamics during the unstable limit cycle and the burst will be given essentially for $Re = 1930$.

III.3.3.1 Unstable limit cycle at Re=1930

Figure III.15(a) depicts a subset of the time evolution of the kinetic energy along the unstable limit cycle at $Re = 1930$ whereas figure III.15(b) depicts the associated Fourier spectrum and figure III.15(c) a phase space representation of the flow dynamics during this period of time. It is clear from these figures that, during the period of time considered on figure III.15(a), the dynamics exhibited by the flow are indeed those of an established limit cycle. The time evolution of the flow only involves the fundamental circular frequency

$\omega_E = 0.5848$ as well as it sub-harmonics due to the non-linearities. The frequency at which the non-linear flow oscillates is moreover in good agreements with the predictions obtained from linear global stability analyses ($\omega = 0.584$). Based on the kinetic energy of the flow and its time derivative, one can reconstruct the phase plot depicted on figure III.15(c). Using such a representation, it is clear that the trajectory of the flow in the phase space for the time window considered is a closed orbit characteristic of limit cycles.

To further characterise these dynamics and more specifically the spatial distribution of the associated perturbations, a Koopman modes decomposition [131] of a sequence of snapshots obtained during this limit cycle is performed. The Krylov subspace is a sequence of 300 snapshots having a sampling period $\Delta T = 0.5$. Each period is thus sampled by almost 20 snapshots. According to the Nyquist criterion, such sampling period enables us to capture the high frequencies up to $\omega = \pi$, that is well beyond the dominant circular frequency of the flow. Figure III.16(a) shows the computed spectrum of Ritz eigenvalues whereas figure III.16(b) shows a classification of the relative importance of the modes in the sequence showing their amplitude versus their circular frequency. Apart from the zero frequency peak associated to the mean flow, two dominant peaks can be found at circular frequencies identical to that identified by the Fourier analysis of the kinetic energy[1]. Figure III.16(c) depicts isosurfaces of the real part's vertical velocity of the leading Koopman mode, whereas figure III.16(d) depicts the motion in the $y = -0.25$ horizontal plane. As for the leading unstable global mode identified from global stability analyses, it consists in oscillating symmetric Taylor-Görtler like vortices inducing vertical low- and high-speed streaks on the upstream and downstream walls of the cavity. Moreover, comparing figure III.16(c) and figure III.8(b), it is clear that the leading Koopman mode found by the present analysis and the most unstable global mode share a striking resemblance. It can thus be interpreted as the non-linear evolution of the unstable global mode. From the frequencies involved in the dynamics and the shape of the dominant Koopman mode, it would thus appear that this limit cycle is solely induced by the linear instability identified in section III.3.2 and its non-linear interactions.

Figure III.17(a) depicts the logarithmic transformation of the Ritz eigenvalues corresponding to the first twenty dominant Koopman modes. Such representation allows one to determine whether each of these Koopman modes has a growing or decaying relative importance in the sequence of snapshots analysed. It can be seen that most of the modes have a zero growth rate, typical of Koopman mode decomposition of limit cycles. Moreover, the neutral modes are all harmonic of the same fundamental frequency. Yet, it is striking that a complex conjugate pair lies in the upper half complex plane. Though the amplitude of the associated Koopman mode is extremely small ($A \simeq 6.10^{-9}$), such complex conjugate pair indicates that the relative importance of these modes in the sequence of snapshots is slowly growing in time. More importantly, the circular frequency associated to these eigenvalues is not a subharmonic of the fundamental frequency. Indeed, one has $\omega_0 = 0.5848$ for the fundamental frequency, whereas the frequency of these modes is $\omega = 0.1432$ ($\omega_0/\omega = 4.1$). Such low frequency is in good agreement with the one found

[1]It has been shown by Chen *et al.* [40] that, when considering a strictly periodic signal, the Koopman mode decomposition and the Fourier analysis are equivalent. Hence, retrieving the peaks observed in the Fourier spectrum when using the Koopman mode decomposition is a somewhat expected result.

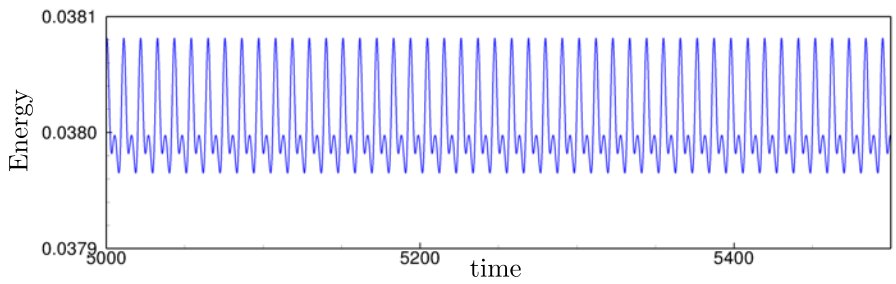

(a)

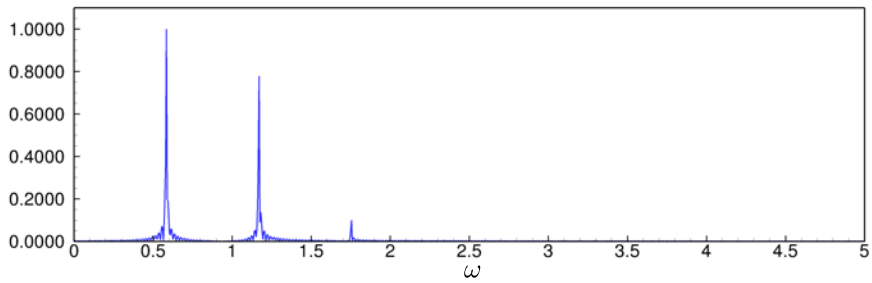

(b)

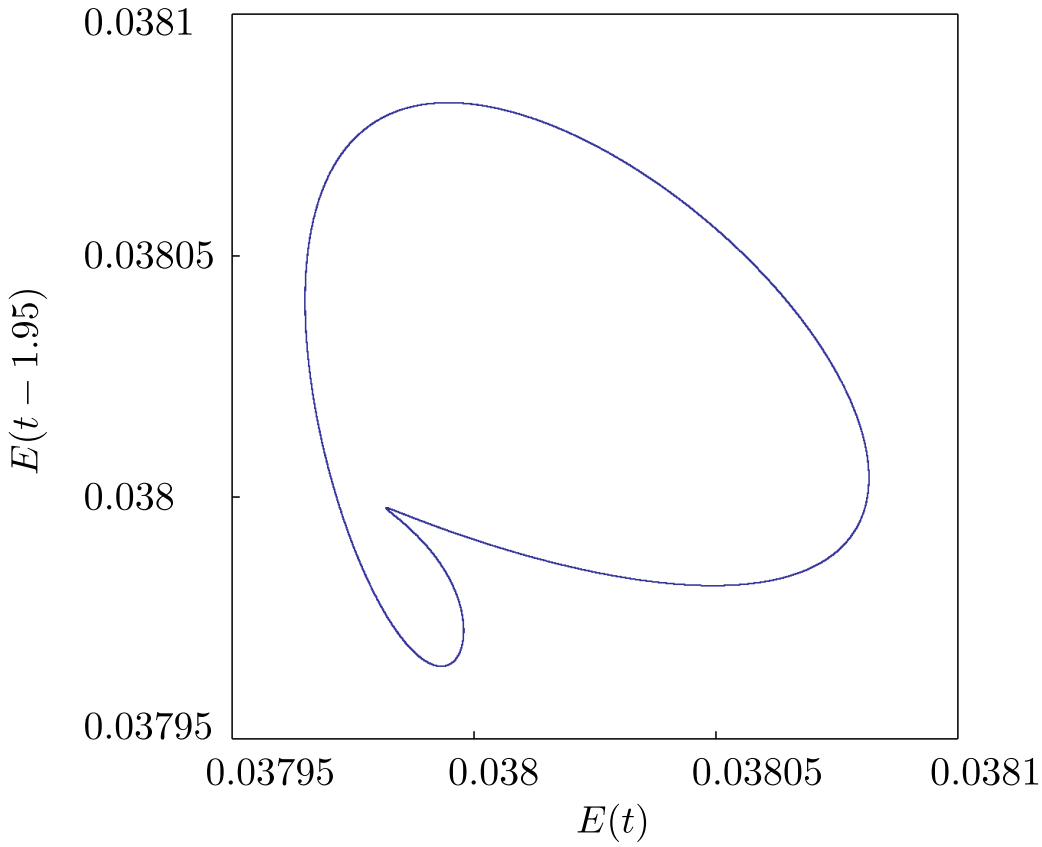

(c)

Figure III.15: (a) Subset of the kinetic energy's evolution when the flow at $Re = 1930$ is in the vicinity of the limit cycle. (b) Associated Fourier spectrum. (c) Corresponding phase plot.

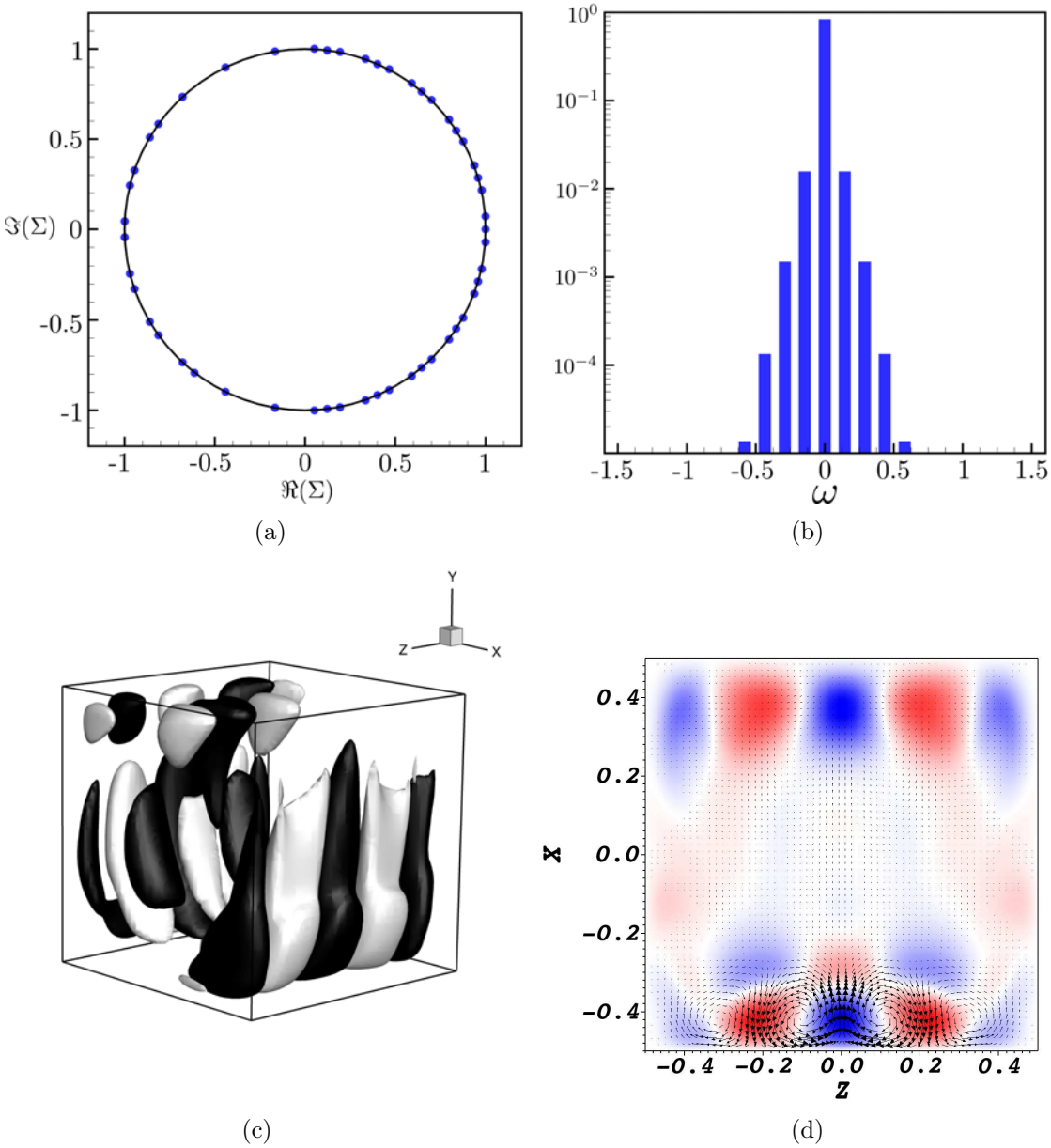

Figure III.16: Koopman analysis of the limit cycle dynamics. (a) Ritz eigenspectrum. Only the leading 50 modes are depicted (b) Amplitude vs circular frequency classification of the mode. (c) Vertical velocity component of the leading Koopman mode's real part. Isosurfaces depict $\pm 10\%$ of the maximum y-velocity. (d) Vector field depicts the horizontal in-plane motion induced by the Koopman mode, whereas coloured contours show the vertical velocity component in the $y = -0.25$ horizontal plane.

by Kuhlmann & Albensoeder [94] when investigating the dynamics of the bursts. Preliminary Floquet stability calculations have moreover revealed that this complex conjugate pair of Ritz eigenvalues indeed corresponds to unstable modes of the periodic limit cycle investigated. According to the classification by Pomeau & Manneville [125], the intermittent chaotic dynamics observed in the time evolution of the flow's kinetic energy depicted on figure III.14(a) would thus be a type-2 intermittency.

Figures III.17(b) and (c) depict the spatial distribution of the Koopman mode's vertical velocity associated to $\omega = 0.1432$ and the motion it induces in the $y = -0.25$ plane, respectively. As for the leading Koopman mode depicted on figure III.16(b) and the leading unstable global mode depicted on figure III.8(b), this mode exhibits a symmetry with respect to the spanwise mid-plane of the cavity for its x- (not shown) and y-velocity components, and an antisymmetry for its z-velocity component (not shown). Similarly to the other modes identified, it consists in Taylor-Görtler like vortices inducing low- and high-speed streaks along the walls of the cavity. It is thought by the author that, once it has grown sufficiently large, the non-linear interactions between this unstable mode and the periodic limit cycle identified previously are responsible for what would appear to be a secondary periodic cycle that can be observed during the burst (see figure III.18, $9750 \leq t \leq 10250$). Further in-depth analyses are however required to fully characterise the dynamics during such burst and to assess the validity of this working hypothesis.

III.3.3.2 Fully chaotic dynamics at Re=2000

Figure III.19 shows the long time evolution of the kinetic energy of the flow in the cubical lid-driven cavity ($\Lambda = 1$) at a supercritical Reynolds number $Re = 2000$. Whereas the intial dynamics are similar to what has been observed for the $Re = 1930$ case, it is clear that they greatly differ after the burst has occured. Indeed, whereas for $Re = 1930$ the flow was then relaxing toward the unstable steady state followed by the unstable limit cycle before eventually experiencing a new burst, in the present case the dynamics become fully chaotic right after the burst took place. Figures III.20(a), (c) and (e) show the evolution of the x-, y- and z-velocity recorder by a probe located in $(x, y, z) = (-0.45, -0.25, 0)$. It is clear from figure III.20(e) that the transition to chaos is followed by a breaking of the flow symmetry. The Fourier spectra depicted on figures III.20(b), (d) and (f) highlight the frequencies involved only in the post-burst dynamics for each velocity component. As one can see, the frequential signature of the unstable limit cycle is clearly visible on the Fourier spectra of the x- and y-velocity components. On the other hand, the Fourier spectrum of the spanwise velocity appears to be largely dominated by a low-frequency unsteadiness. It is not clear yet if this low frequency unsteadiness is related to the unstable Floquet mode identified by the Koopman analysis.

Figure III.21 depicts the *rms* fluctuations of the three velocity components in the $z = 0$ plane (left) and $y = -0.25$ plane (right), respectively. It appears from these figures that the *u-rms* and *w-rms* fluctuations have their maxima in the vicinity of the upstream wall of the cavity, while the *v-rms* has its maximum in the vicinity of the downstream corner eddy. The location of the *v-rms* maxima is in agreement with what has been observed at higher Reynolds number by Leriche [103]. On the other hand, the location of the *u-rms* and *w-rms* maxima on the streaks located along the upstream wall appear to be essentially

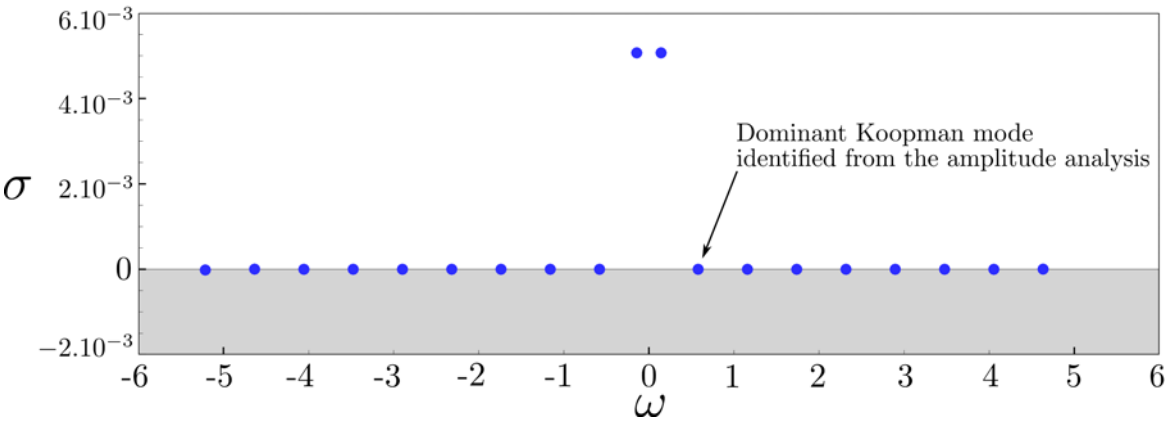

(a)

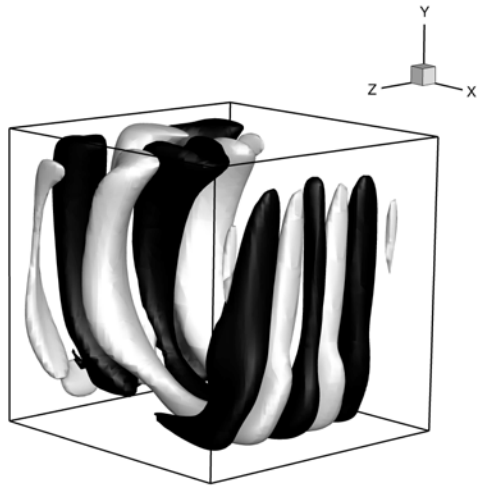

(b)

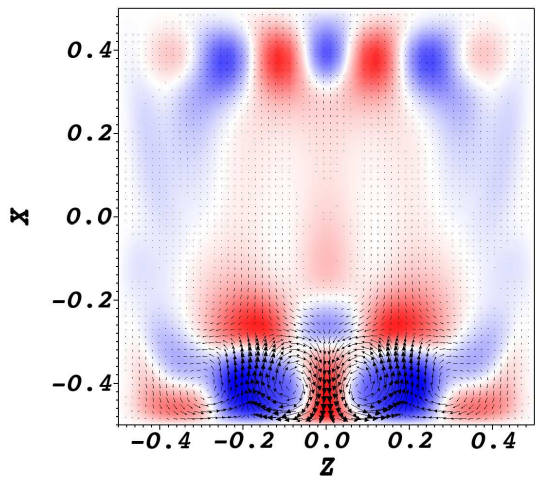

(c)

Figure III.17: (a) Logarithmic transformation of the Ritz eigenvalues corresponding to the first 20 leading Koopman modes. (b) Vertical velocity component of the unstable Koopman mode's real part identified from this spectrum. Isosurfaces depict $\pm 10\%$ of the maximum y-velocity. (d) Vector field depicts the horizontal in-plane motion induced by the Koopman mode, whereas coloured contours show the vertical velocity component in the $y = -0.25$ horizontal plane.

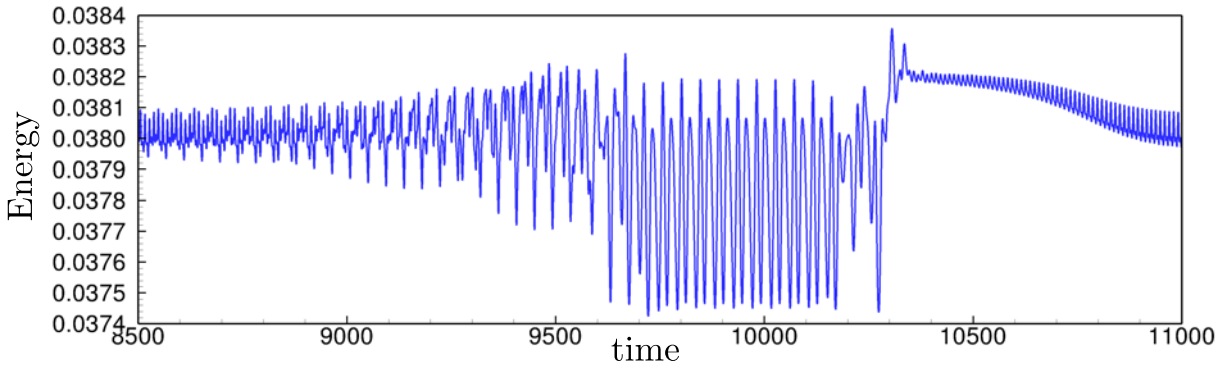

Figure III.18: Subset of the kinetic energy's time evolution during the burst at $Re = 1930$.

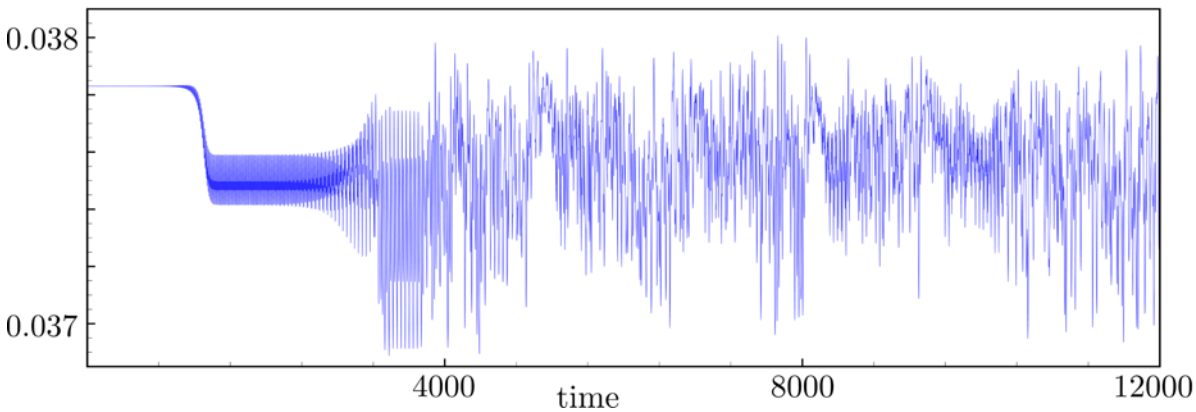

Figure III.19: Long time evolution of the flow's kinetic energy in an aspect ratio $\Lambda = 1$ lid-driven cavity at $Re = 2000$

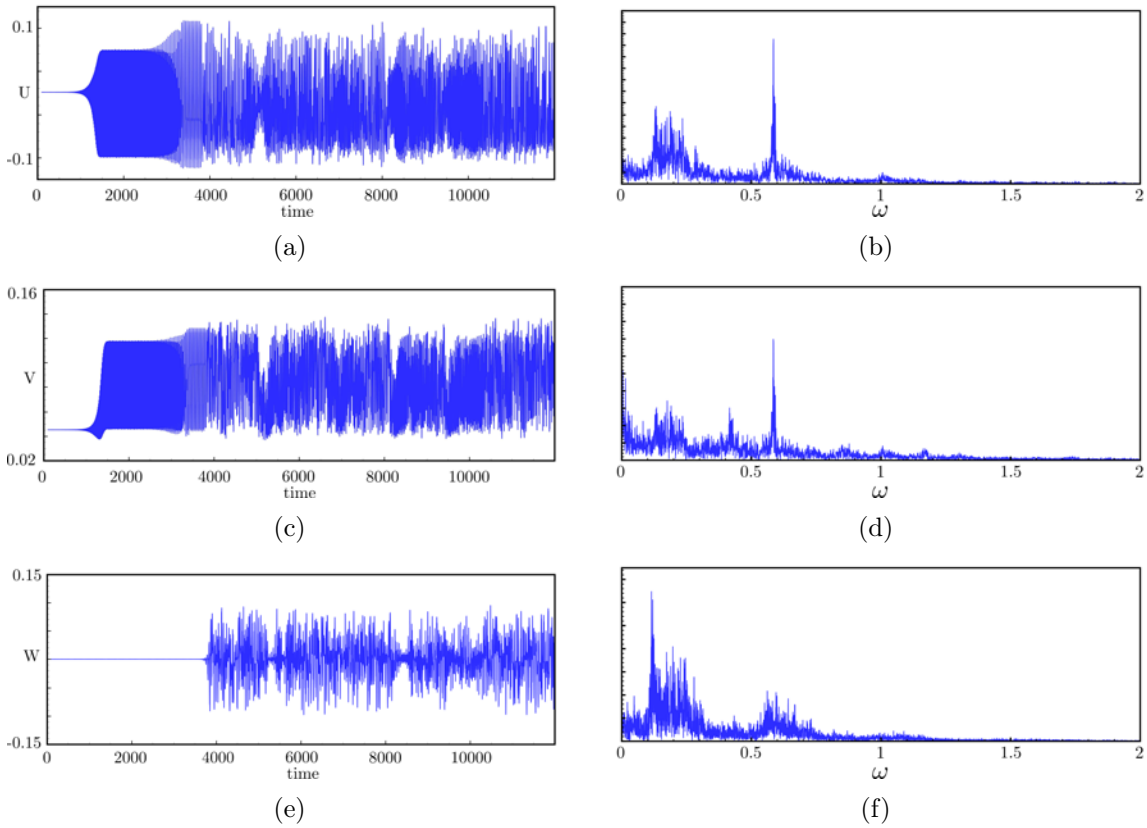

Figure III.20: Fourier spectra of the velocity measurements recorded by probe located at $(x, y, z) = (-0.45, -0.25, 0)$. (a) x-velocity, (b) y-velocity and (c) z-velocity.

a feature of the low Reynolds number considered. Indeed, in [103], the maxima of *u-rms* and *w-rms* is located in the vicinity of the downstream corner eddy as well.

III.4 Conclusion

The transition from steady to unsteady flow in fully three-dimensional lid-driven cavities with spanwise end-walls has been investigated using the joint application of unstable steady states computations, fully three-dimensional global stability analyses and direct numerical simulations. A focus on the influence of the spanwise extent of the cavity on the stability of the resulting flow has also been given.

The various base flow computations have shown that the most important spatial structures to be found in such fully three-dimensional lid-driven cavity flows are quite similar to their two-dimensional counterparts. Indeed, as for the 2D LDC, the 3D LDC exhibits a central vortex core as well as corner vortices. Moreover, the flow in the spanwise $z = 0$ symmetry plane also closely resembles the two-dimensional one. However, because of the fundamental three-dimensionality of the flow field in the present case, some differences are still obviously observed. Indeed, due to the existence of the spanwise end-walls, a non-zero spanwise pressure gradient exists in the cavity triggering a spanwise motion of the fluid particles as well. Because of this spanwise motion, though they closely resemble one another, the flow in the spanwise symmetry plane and its two-dimensional counterpart are fundamentally different. Indeed, whereas in the 2D lid-driven cavity flow, fluid particles have closed trajectories, the ones in the three-dimensional cavity flow have much more complex three-dimensional trajectories. Three spatial locations however appear to be of crucial importance in their motion, the cores of the primary vortex and of the corner eddies. Indeed, on the one hand, the core of the central vortex appears to be a saddle attracting fluid from the spanwise walls toward the center of the cavity and expelling it from the center of the cavity toward the upper and bottom walls in a spiralling motion. The attraction of the fluid particles just described and clearly visible on figure III.4 is known as the Eckman pumping. However, on the other hand, the cores of the secondary eddies, though they act as saddles as well, are attracting the fluid particles already lying within the spanwise symmetry plane before expelling these towards the spanwise end-walls, thus enabling the flow to remain divergence-free. Though the spanwise extent of the cavity clearly has an impact on the flow, the motion just described has been observed for all cavities investigated in the present study.

The transition to unsteadiness of these flows has been investigated by means of global linear stability analyses. It has appeared in all cases that the flow was undergoing a Hopf bifurcation induced by a globally unstable mode exhibiting a symmetry with respect to the spanwise mid-plane for all of the various cavities considered. It is however worthy to note that shortly after the flow has experienced this first Hopf bifurcation, it experiences a second one induced this time by an anti-symmetric global mode. No matter their symmetry, all these modes induce vertical low- and high-speed streaks along the upstream and downstream walls as well as Taylör-Gortler-like vortices. Though the number of TGL vortices induced by the modes is found to be dependent on both the symmetry of the mode and the spanwise aspect ratio of the cavity considered, they are associated

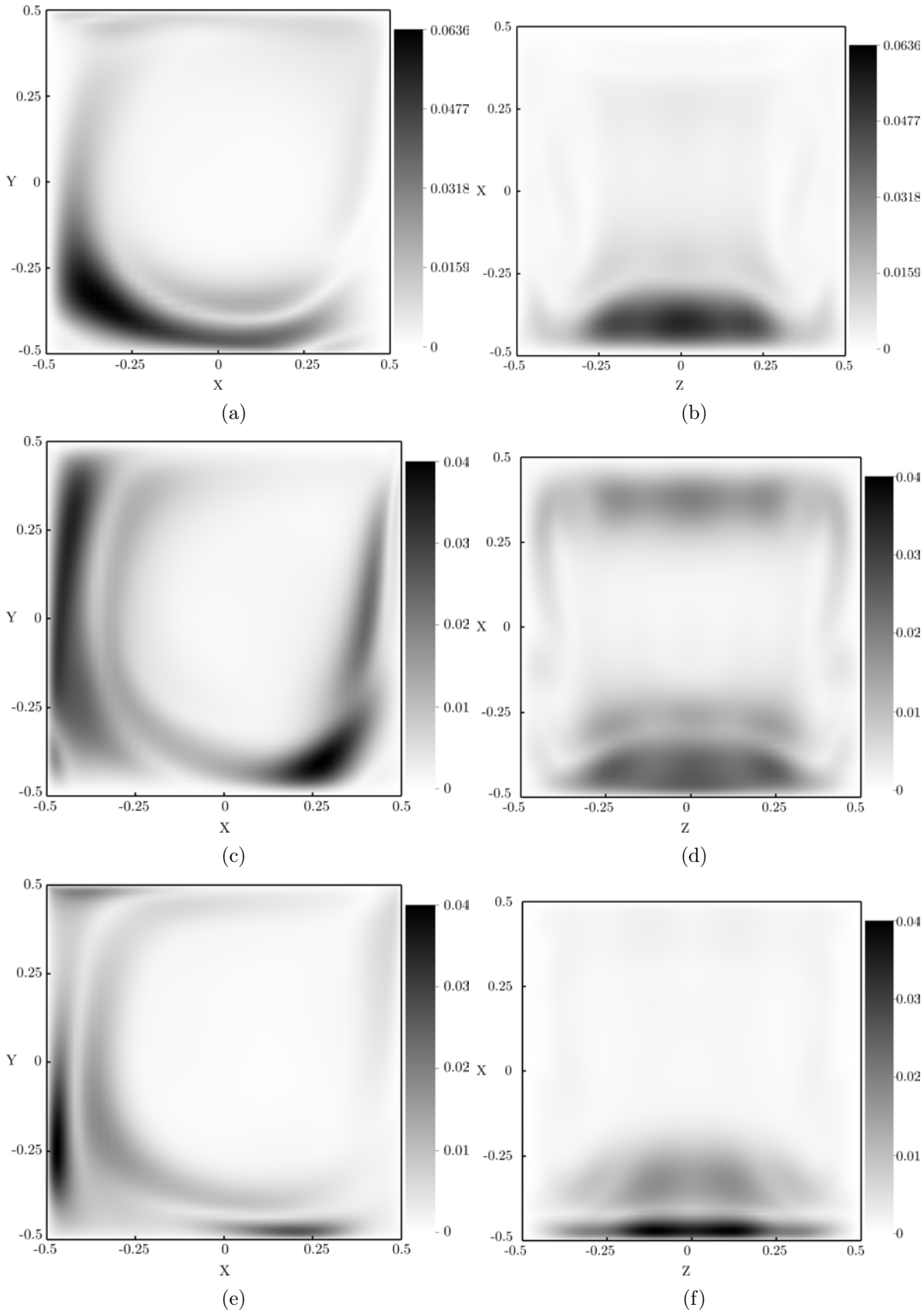

Figure III.21: Left: *rms*-fluctuations in the $z = 0$ plane. (a) x-velocity, (c) y-velocity, (e) z-velocity. Right: *rms*-fluctuations in the $y = -0.25$ plane. (b) x-velocity, (d) y-velocity, (f) z-velocity.

in all cases to a dominant spanwise wavenumber $\beta_{3D} \simeq 15$ extremely close to what has been found by Theofilis *et al.* [152] and Chicheportiche *et al.* [42] regarding the three-dimensional instability of an otherwise two-dimensional lid-driven cavity flow. Despite the transition scenario appearing to be identical no matter the spanwise aspect ratio of the cavity considered, close investigations of the shape of the globally unstable modes and of the regions of the base flows providing them with energy have suggested that two slightly different instability mechanisms may actually be at play. Indeed, for the smaller cavity considered (i.e. $\Lambda = 0.5$), though they induce hardly visible Taylor-Görtler-like vortices along the upstream wall of the cavity, the globally unstable modes are located mainly along the downstream wall and are oscillating are a relatively low frequency. Moreover, investigation of the associated kinetic energy transfer has put in the limelight that, in this case, the symmetric and anti-symmetric global modes essentially extract their energy from the region separating the central vortex core from the downstream corner eddy. On the other hand, for the larger cavities considered (i.e. $\Lambda = 1$ and $\Lambda = 3$), the globally unstable modes have similar amplitudes in the vicinity of the upstream and downstream walls. The motion they induced is however quite different from $\Lambda = 0.5$. Whereas only vertical low- and high-speed streaks can be observed on the downstream wall, pairs of counter-rotating TGL vortices are clearly visible in the vicinity of the upstream wall. Due to the lift-up effet [97], these TGL vortices further amplify the velocity streaks. Investigation of the kinetic energy transfers have shown that these global modes were now mostly extracting their energy from the region separating the central vortex core from the upstream eddy and along the upstream wall. Close resemblance of these modes and of the spatial distribution of their production term with what has been found by Albensoeder *et al.* [9] strongly suggests that the underlying instability mechanism is a centrifugal instability of the central vortex core as in the two-dimensional lid-driven cavity flow. Finally, the values critical Reynolds numbers beyond which the Hopf bifurcations are taking place are dependent on the spanwise aspect ratio Λ of the cavity: the larger the spanwise aspect ratio, the smaller the threshold to unsteadiness. It is interesting to observe however that results obtained on the larger cavity considered herein (i.e. $\Lambda = 3$) might suggest that, as the spanwise aspect ratio is further increased, the value critical Reynolds number might asymptotically tends toward the value $Re_{T1} = 840$, i.e. the critical threshold found by Theofilis *et al.* [152] for spanwise periodic oscillatory instability in a two-dimensional lid-driven cavity flow.

Direct numerical simulations have put in the limelight, at least for the cubical lid-driven cavity ($\Lambda = 1$), that once linearly unstable, the flow was bifurcating toward a periodic limit cycle. Long time integration has however shown that this limit cycle is itself unstable and the flow eventually experiences bursts that are the signature of intermittent chaos. Koopman modes analysis of the data highlights that the dynamics of the flow while on the periodic limit cycle are essentially correctly predicted by global stability analysis. Indeed, both the dominant frequency and the shape of the associated Koopman mode share striking resemblance with the globally unstable mode and the associated circular frequency. Nonetheless, the Koopman mode analysis has also put in the limelight that an unstable mode was slowly evolving onto this limit cycle. The frequency at which this unstable Koopman mode oscillates is in good agreement with the low frequency observed by Kuhlmann & Albensoeder [94] as well as with preliminary results from Floquet anal-

ysis of the limit cycle' stability. Accordingly to the classification proposed by Pomeau & Manneville [125], these dynamics would then be classified as type-2 chaotic intermittency. The direct numerical simulations have moreover revealed that, whereas for relatively low supercritical Reynolds numbers ($Re = 1930$) the flow eventually relaxes toward the unstable limit cycle before eventually experiencing a new burst, for higher Reynolds numbers ($Re = 2000$) the flow becomes fully chaotic right after the first burst has occured. Further in-depth quantification of the chaotic dynamics are however necessary.

Perspectives

The present study has given us the opportunity to peak a glance at the new investigation capabilities offered by fully three-dimensional global stability analysis. Moreover, results obtained in the present study open the way for numerous other researches on the transition in cavity flows. From the author's point of view, three of these possible offsprings are of major interest:

- Extension to very large aspect ratio LDC: The present investigation has essentially been focused on the transition in low to moderate aspect ratio three-dimensional lid-driven cavity flow. One might thus wonder how do these apply to very large aspect ratio LDC. Indeed, as the aspect ratio is increased, the flow within the mid-plane of the cavity resembles more and more to its two-dimensional counterpart. It thus seems reasonnable to assume that, beyond a critical aspect ratio, results from three-dimensional global stability analyses might asymptotically tend toward those obtained regarding the stability of a two-dimensional LDC with respect to spanwise periodic perturbations as in [42, 152]. Preliminary results obtained on an aspect ratio $\Lambda = 6$ LDC (see Appendix A) seem to confirm this hypothesis.

- Extension to shear-driven cavity flows: Shear-driven cavity flows, also known as open cavity flows, are encountered in numerous industrial applications such as slots on the walls of heat exchangers or on airplane's wings. As for the two-dimensional lid-driven cavity, a relatively large body of literature exist on the two-dimensional shear-driven cavity flow. As shown by Brès & Colonius [36] on compressible shear-driven cavities, the dynamics of the flow can be divided into two-parts: intra-cavity dynamics and shear layer dynamics. Though they are coupled, the intra-cavity dynamics closely resembles the ones observed in lid-driven cavity flows. Extension to three-dimensional shear-driven cavity flows of the analyses presented herein thus seems quite natural and might help to obtain better predictions of the transition thresholds once again.

- In-depth investigation of the chaotic dynamics: As shown in section III.3.3, the flow in a cubical lid-driven cavity can exhibit chaotic dynamics. Because of time limitations, only rough analyses of these dynamics have been made possible so far. Further quantitative analyses might thus be necessary in order to provide a better understanding of the laminar-turbulent transition taking place in such flows. Moreover, since LDC flows exhibit features that can be found in numerous other flows, having a better understanding of its underlying transition mechanisms might as well

help the understanding of a large variety of other flows (shear-driven cavity flows and boundary layer flows along concave walls for instance).

Chapter IV

Stenotic pipe flow

Contents

IV.1 Introduction **83**
IV.1.1 Axisymmetric stenotic pipe flows 84
IV.1.2 Asymmetric stenotic pipe flows 86
IV.2 Problem formulation **87**
IV.3 Reference case: the axisymmetric stenotic pipe flow **88**
IV.3.1 Steady state solutions 88
IV.3.2 Linear stability analysis 89
IV.3.3 Non-linear saturation and transition to turbulence 93
IV.4 Asymmetric stenotic pipe flows **94**
IV.4.1 Influence of the eccentricity at fixed Reynolds number 94
IV.4.2 Influence of the Reynolds number at fixed eccentricity 100
IV.5 Discussion **108**
IV.6 Conclusion **111**

IV.1 Introduction

The association of arterial diseases with flow-related mechanisms has motivated the study of the flow within a model geometry of arterial stenosis. Atherosclerosis is a widely spread cardio-vascular disease predominant in most industrialised countries. It is a condition in which an artery wall thickens as a result of the accumulation of fatty material, such as cholesterol, that might eventually lead to serious health conditions as dangerous as a break-up of the plaque of atherosclerosis. Figure IV.1 depicts the modification of the geometry of the artery due to the accumulation of fatty materials resulting in the formation of a plaque of atherosclerosis. The genesis of this plaque is closely related to wall shear stress in the arterial flow. It involves an accumulation of cholestorol on the walls of large arteries, typically where the local wall shear stress is low and periodic. The process can be considered as a long time non-linear instability of the geometry of the arterial wall, wherein

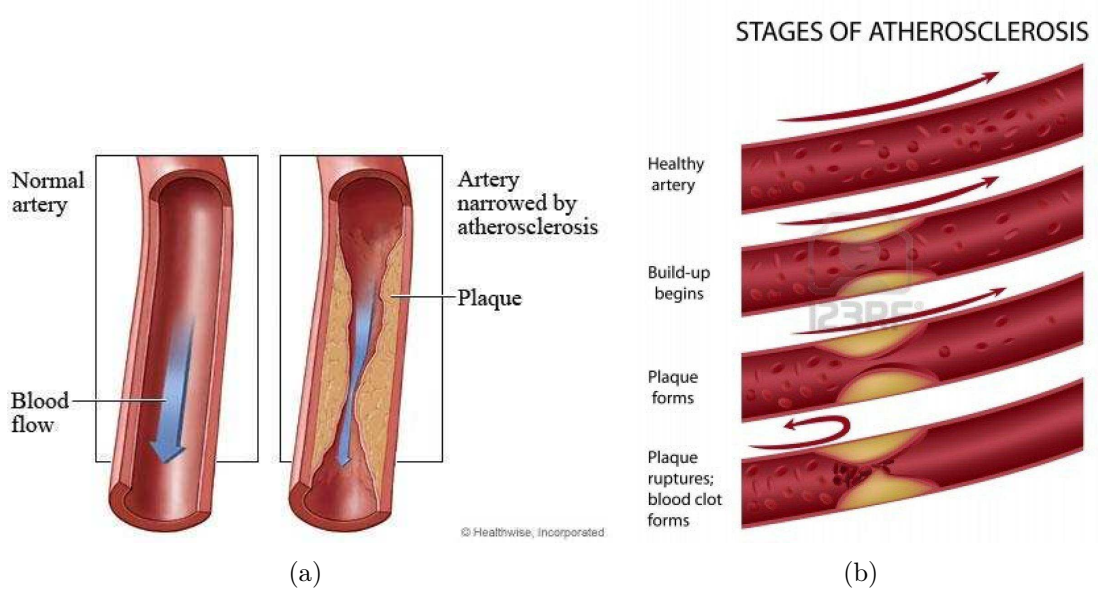

(a) (b)

Figure IV.1: (a) Modification of the artery's geometry. (b) Growth of the stenosis in the artery. Image courtesy: [1, 2]

a local constriction can grow through the promotion of flow separation. The increased pressure losses associated with flow separation can reduce the flow rate causing problems related to oxygen level in the blood. Over the past decades, due to the crucial impact of this disease on human health, numerous investigations of the flow's dynamics within simplified versions of stenotic geometries have been conducted. Quite often, for the sake of simplicity, two dimensional or axisymmetric partially blocked channels and pipe with non-elastic walls and steady or pulsatile inflows have been assumed to be proxies good enough to unravel the basic physical mechanisms underlying the transition to turbulence.

IV.1.1 Axisymmetric stenotic pipe flows

Assuming a strictly two-dimensional geometry being a model good enough to unravel the underlying transition mechanisms of the flow within arteries has proven to be partially wrong. Indeed, the transition threshold predicted by global stability of such two-dimensional flows turn out to be almost an order of magnitude lower than the ones typically observed in experimental investigation of the stenotic artery flow. Over the past decade, researchers have tended to favor an axisymmetry assumption of the geomtry as a first approximation when dealing with such blood-flow related problems. Among the large body of literature existing on stenotic artery flows, only a few references must retain our attention as being extremely relevant to the problem of global instability and transition of the flow considered in the present PhD thesis.

The flow developing within axisymmetric stenotic pipes with steady inlets have been investigated experimentally since the late 1970's by Cassanova & Giddens [38], Khalifa & Giddens [88] as well as Ahmed & Giddens [4]. In these pioneering works, transition was observed to take place for Reynolds numbers in-between 500 and 1000, based on the pipe's diameter and the mean inflow velocity. More recently, Long *et al.* [107] and Mallinger &

Drikakis [109] have used computational fluid dynamics and direct numerical simulations to investigate the properties of such idealised flows. Under standard physiological conditions, the blood flow within arteries is considered to be laminar. Unfortunately, the growth of atherosclerosis plaque induces an inflection point in the velocity profile that can yield the flow to transition. To our knowledge, the first global stability analysis ever done on an axisymmetric stenotic pipe flow with steady and pulsatile inlets has to be credited to Sherwin & Blackburn [142]. Using the pipe's diameter D as length scale, the mean value $\bar{U}$ of the inlet Hagen-Poiseuille velocity profile as velocity scale and the kinematic viscosity ν to define the Reynolds number Re, the axisymmetric base flow velocity field they had obtained for a stenotic constriction given by a sine function displays two major features similar to what has been observed in similar two-dimensional cases, i.e. a confined axisymmetric jet stemming from the stenotic constriction and a toric reversed flow region surrounding the jet and quite elongated in the streamwise direction. It is moreover noticeable that after reattachment, the flow very slowly relaxes back toward the Hagen-Poiseuille velocity profile. For the geometry under consideration, the authors have shown that the flow becomes unstable for $Re > 722$ due to a pitchfork bifurcation. The associated unstable global mode has an azimuthal wavenumber $m = \pm 1$. It consists in a positive and a negative streamwise velocity tube. This unstable mode triggers a small deflection of the stenotic jet from the pipe's centerline eventually yielding a weak Coanda-like wall reattachment of the jet as explained in [142]. It is worthy to note however that, after having conducted a direct numerical simulation, the authors have presented some evidences for the pitchfork bifurcation to be subcritical. Griffith *et al.* [75] have investigated a similar problem where the stenotic constriction is now given by a hemisphere. Whereas the blockage induced by the stenotic constriction in [142] was kept constant, the major contribution of [75] is the investigation of the influence of this parameter on the stability of the flow. For a similar flow configuration (75% blockage of the pipe cross-sectional area), the first mode to become unstable and the associated critical threshold are in qualitatively good agreements with [142]. However, when the blockage induced by the stenotic constriction is reduced, though the bifurcation taking place remains a pitchfork bifurcation, the azimuthal symmetry of the first global mode to become unstable changes from $m = \pm 1$ to $m = \pm 2$.

More recently, Sanmiguel-Rojas & Mullin [133] have studied the influence of defect of the inlet Hagen-Poiseuille velocity profile in an otherwise axisymmetric sudden-expansion pipe. Though the geometry is different, the dynamics observed in this flow configuration share close connections with those observed in the stenotic pipe. It is thus believed that it is worthwhile to introduce the reader to the results presented in this paper. They have observed that introducing a small asymmetric finite-amplitude disturbance to the inlet Hagen-Poiseuille velocity profile eventually yields the flow to transition at a Reynolds number lower than the critical threshold predicted by global linear stability analyses of the axisymmetric base flow. The threshold beyond which the very slightly asymmetric flow transition is however dependant on the amplitude of the inlet disturbance. Moreover, they have also shown that once unsteadiness is observed, it self-sustains eventhough axisymmetry is restored in the inlet velocity profile. Moreover, incrementally decreasing the Reynolds number has helped unravelling the existence of an hysteresis cycle associated to a subcritical bifurcation. It is remarkable that the lower bound of this hysteresis cycle

is in good agreement with the critical Reynolds number beyond which unsteadiness is observed experimentally. It is not yet clear though if the instability mechanisms yielding the axisymmetric and slightly asymmetric flow to transition to unsteadiness are the same or not. These results however suggest that, since even small imperfectness are part of any experimental work, observing the axisymmetric solutions up to the critical Reynolds number for linear instability would be a formidable experimental task likely to be never achieved and highlight the importance to investigate the properties of flow fields even in very slighlty asymmetric geometries.

IV.1.2 Asymmetric stenotic pipe flows

Whereas the body of literature on the axisymmetric stenotic pipe flow is quite large, the one on the asymmetric stenotic pipe flow is much more sparse. One of the first computational studies to investigate the transition to unsteadiness and turbulence in asymmetric stenotic pipe flow with a steady inlet is the one by Varghese *et al.* [156]. The geometry of the stenotic constriction they have considered is the same as in [142], i.e. a stenosis given by a sine function. Two cases have been considered: an axisymmetric stenotic constriction for the sake of reference and validation, and one that has been offset from the pipe's centerline by 5% of the pipe's diameter. Though the overall features of the steady axisymmetric solutions are similar to the ones obtained in [142], the flow remains stationnary and axisymmetric for Reynolds numbers as high as 1000. Unfortunately, no clear explanation is given as to why the axisymmetric flow computed in [156] is much more stable than the ones in [142] and [75]. With the recent knowledge acquired on the influence of the streamwise extent of the computational on the global stability of the flow, one might however wonder if the computational domain considered in [156] (i.e. $-2 \leq z \leq 24$ as compared to $-5 \leq z \leq 40$ in [142]) is not too short to appropriately capture the steady instability. It is however believed that the general conclusions drawn in [156] still hold. For the 5% eccentricity, it has been observed that the confined stenotic jet experiences a weak Coanda-like wall reattachment for a Reynolds number as low as 500 with the resulting velocity field remaining however stationnary. Transition to turbulence for eccentric stenotic pipe flow then takes place in-between $Re = 500$ and 1000. At $Re = 1000$, the mean flow field essentially looks like its $Re = 500$ counterpart in the near-stenosis region, i.e. an early wall-reattached stenotic jet surrounded by an asymmetric toric reversed flow region. A turbulent breakdown of the stenotic jet is however occuring in the vicinity of $z \simeq 10$ thus yielding the mean reversed flow region to be almost 50% smaller than its axisymmetric laminar counterpart. From the various flow visualisations they had performed, it is believed by the authors that the turbulent structure resulting from the breakdown of the stenotic jet might share some connections with the turbulent puffs observed in the subcritical transition to turbulence in the pipe flow [19] and slowly diverging pipe flow [120].

IV.2 Problem formulation

The dynamics of a three-dimensional incompressible Newtonian flow is described by the incompressible Navier-Stokes equations:

$$\begin{cases} \dot{\mathbf{U}} = -(\mathbf{U}\cdot\nabla)\mathbf{U} - \nabla P + \dfrac{1}{Re}\Delta\mathbf{U} \\ \nabla\cdot\mathbf{U} = 0 \end{cases} \tag{IV.1}$$

where $\mathbf{U} = (U, V, W)^T$ is the velocity vector and P the pressure term. Variables are made non-dimensional with respect to the pipe's diameter D and the mean inlet Hagen-Poiseuille velocity $\bar{U}$. Therefore, the Reynolds number is defined as $Re = \bar{U}D/\nu$, with ν being the kinematic viscosity. Figure IV.2 depicts a sketch of the geometry considered. The stenosis is centered on $x = 0$. Its height varies with the streamwise distance as:

$$H(x) = 0.5D(1 - 0.25(1 + \cos(2\pi x/L))) \tag{IV.2}$$

where L is the stenosis length. Throughout the present study, this length is fixed to $L = 2D$. Such definition of the stenosis constriction yields to a 75% reduction of the cross-sectional area of the pipe at the stenosis throat. Such reduction of the cross-sectional area of the pipe will be kept constant throughout this study. The cross-stream coordinates of the stenosis are then given by:

$$\begin{cases} y = H(x)\cos(\theta) \\ z = H(x)\sin(\theta) \end{cases} \tag{IV.3}$$

The eccentricity of the stenosis throat is defined as:

$$E(x) = 0.5ED(1 + \cos(2\pi x/L)) \tag{IV.4}$$

with E being the eccentricity parameter. The offset is in the z direction such that one actually has $z = E(x) + H(x)\sin(\theta)$. The eccentricity parameter E is varied from $E = 0\%$ (axisymmetric case) up to $E = 10\%$.

The computational domain considered extends from $x_{in} = -15$ up to $x_{out} = 40$ in the streamwise direction. The following boundary conditions are applied:

- at the inlet ($x_{in} = -15$), a Dirichlet boundary condition is imposed on the velocity (parabolic Hagen-Poiseuille velocity profile for DNS and steady state computations, zero velocity boundary condition for linear stability analyses),
- at the outlet ($x_{out} = 40$), a Neumann boundary condition is imposed on the velocity $\nabla\mathbf{U}\cdot\mathbf{x} = 0$;
- finally, a no-slip boundary condition is imposed on the pipe's walls.

Calculations have been performed using the code Nek5000 developed at Argonne National Laboratory by Fischer *et al.* [62]. Spatial discretisation is done by a Legendre spectral elements method with polynomials of order $N = 8$ to 12. The number of spectral elements is set to 2500, resulting in computational problems having between 1.3 and 4.3 millions grid points. The convective terms are advanced in time using an extrapolation of order 3, whereas the viscous terms use a backward differentiation of order 3 as well, resulting in the time-advancement scheme labelled BDF3/EXT3.

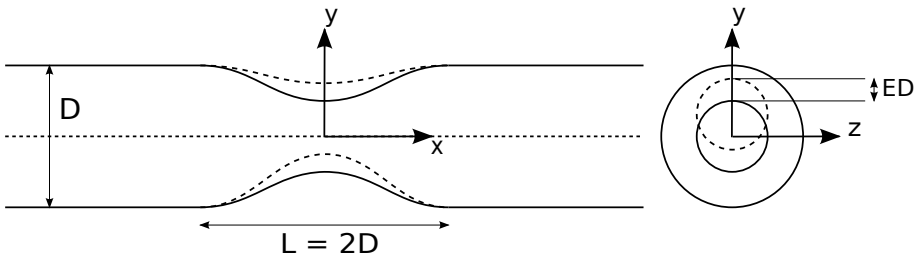

Figure IV.2: Sketch of the geometry of the stenotic pipe considered.

IV.3 Reference case: the axisymmetric stenotic pipe flow

In order to provide the reader with a complete and up-to-date picture of stenotic pipe flow transition, the case of an axisymmetric stenotic constriction will first be considered. Such geometry has already been studied using a similar approach by Sherwin & Blackburn [31, 32, 142] and Griffith *et al.* [75, 76].

IV.3.1 Steady state solutions

Steady state solutions in an axisymmetric stenotic pipe with a 75% reduction of the area at the stenosis throat have been computed for Reynolds numbers ranging from $Re = 300$ up to $Re = 750$. Their main features are presented on figure IV.3.1. As one can see, the flow essentially consists in a jet emerging from the stenotic constriction. As explained by Sherwin & Blackburn [142], since an incompressible flow is considered, due to mass conservation, the sectionally averaged velocity at the throat of the stenosis is four times larger than the inlet mean velocity $\bar{U}$. During the stenosis expansion ($0 \leq x \leq 1$), the flow is then unable to remain attached and the laminar axisymmetric jet is formed in the centre of the pipe. As shown on figure IV.3.1, it is surrounded by an elongated reversed flow region. Once it has reattached, the flow then slowly relaxes toward the Hagen-Poiseuille flow. Nonetheless, it is worthy to note that for the computational domain considered, even at $x = 39$, it still is not yet fully restablished. Indeed, even this close from the outlet of the computational domain, at $Re = 700$, the centerline velocity still is almost 20% higher than the Hagen-Poiseuille centerline velocity $2\bar{U}$.

Several different quantities can be used to monitor the evolution of the base flow. In separated flows, the maximum length of the reversed flow region is often a good candidate. Though it works perfectly fine for two-dimensional flows, such criterion might hide part of the evolution of the base flow when a fully three-dimensional recirculation bubble is considered. In the present work, it has thus been decided to use the volume of the reversed flow region instead. Let us consider a Heaviside function $H(x, y, z)$ such that:

$$H(x, y, z) = \begin{cases} 0 \text{ if } U_b(x, y, z) > 0 \\ 1 \text{ if } U_b(x, y, z) < 0 \end{cases}$$

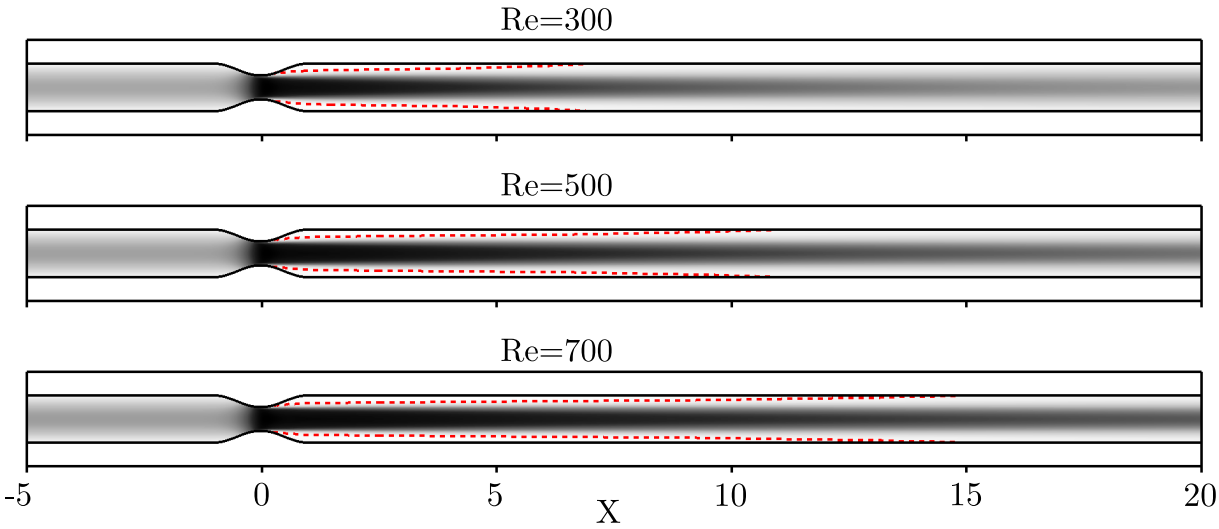

Figure IV.3: Evolution of the axisymmetric base flow when increasing the Reynolds number. Dashed red lines depict the streamwise extent of the reversed flow region.

the volume V^- of the reversed flow region is then given by:

$$V^- = \int_V H(x, y, z) \, \mathrm{d}V$$

with V the total volume of the computational domain considered. Figure IV.4 depicts the evolution of this quantity V^- with an increase of the Reynolds number for the axisymmetric stenotic pipe flow. As for the recirculation length, it can be seen that the volume V^- of the base flow's reversed flow region increases linearly with the Reynolds number. When investigating the influence of the eccentricity of the stenosis throat on the flow, this linear scaling of the volume V^- of the reversed flow region in the axisymmetric case will be used as a baseline for the sake of comparison.

IV.3.2 Linear stability analysis

The linear stability of the axisymmetric stenotic pipe flow is investigated by mean of linear global stability analysis. The Krylov subspace used to compute the leading eigenvalues of the linearised Navier-Stokes has dimension $k = 250$ and a sampling period $\Delta T = 1$. The flow is found to be unstable beyond a critical Reynolds number $Re_c = 721$, i.e. in extremely good agreement with the critical Reynolds number found by Sherwin & Blackburn [142] ($Re_c = 722$). Figure IV.5 depicts the subset of computed eigenvalues at the critical Reynolds number $Re_c = 721$. As one can see, it is dominated by a real eigenvalue indicating the flow experiences a pitchfork bifurcation. Such bifurcation are usually related to a symmetry breaking instability. Figure IV.6 depicts the spatial distribution of the leading global mode in (a) the $x = 5$ plane and (b) a three-dimensional visualisation of its streamwise component. Due to the real eigenvalue it is attached to, this mode is a non-oscillating one. It is clear from these two figures that the leading global mode is symmetric with respect to the $y = 0$ plane while being anti-symmetric with respect to the

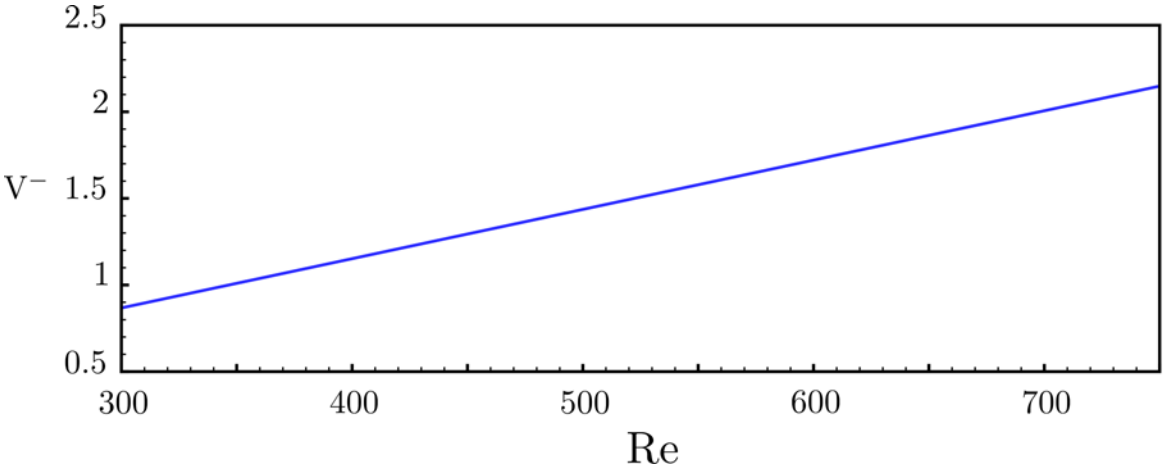

Figure IV.4: Evolution of the volume V^- of the reversed flow region with an increase of the Reynolds number Re for the axisymmetric stenotic pipe base flows. The reduction of the cross-sectional area at the stenosis throat in 75%.

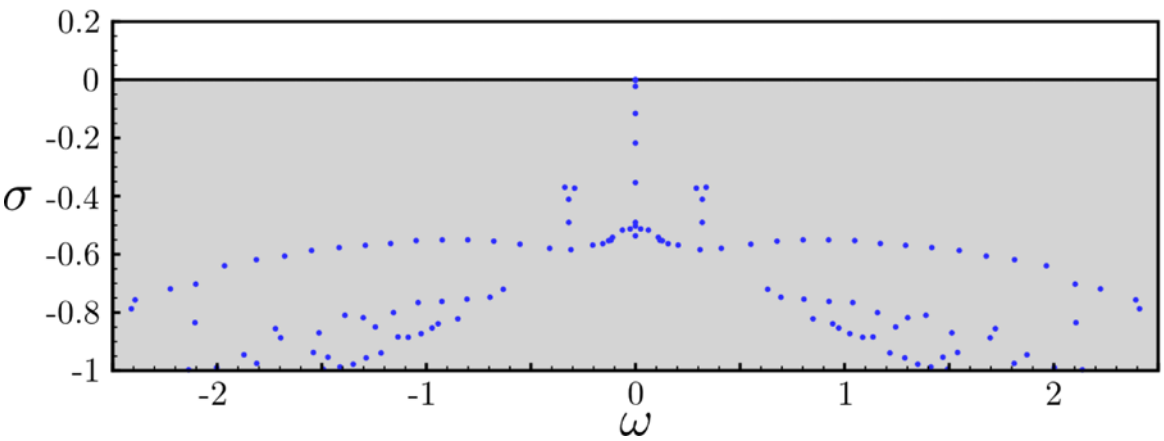

Figure IV.5: Eigenspectrum of the linearised Navier-Stokes operator for an axisymmetric stenotic pipe flow at $Re = 721$.

$z = 0$ plane. Moreover, a Fourier decomposition in the azimuthal direction shows that it is associated to a $m = \pm 1$ azimuthal wavenumber as in [142]: the mode exhibits positive streamwise velocity on the upper side of the pipe and negative velocity on the lower side. Moreover, it arises right downstream the stenosis throat and is quite elongated in the streamwise direction. Figure IV.6(a) depicts the motion it induces in the $x = 5$ plane. It is clear from the vector plot that the instability mode tends to promote a deflection of the stenotic jet from the pipe's centerline eventually yielding to a mild Coanda-type wall reattachment. Such symmetry-breaking Coanda-type instabilities have been reported for a wide variety of two-dimensional confined jet flows. However, for strictly two-dimensional flows, it usually arises at substantially lower critical Reynolds numbers ($O(10)$) and the resulting deflection is far stronger (see [11, 99, 123, 144] for examples).

Kinetic energy budget analysis

In order to get a better understanding of the instability mechanism, the kinetic energy transfer between the base flow and this mode is investigated. The kinetic energy transfer is governed by the Reynolds-Orr equation already introduced in chapter III and recalled here for the sake of clarity:

$$\frac{\partial E}{\partial t} = -D + \sum_{i=1}^{9} \int_V I_i \, \mathrm{d}V$$

where the kinetic energy and the total dissipation of the perturbation in the computational domain's volume V are given by:

$$E = \frac{1}{2} \int_V (u^2 + v^2 + w^2) \, \mathrm{d}V,$$
$$D = \frac{1}{Re} \int_V \nabla \mathbf{u} : \nabla \mathbf{u} \, \mathrm{d}V$$

and where the integrands I_i which represent the production terms are:

$$I_1 = -u^2 \frac{\partial U_b}{\partial x}, \; I_2 = -uv \frac{\partial U_b}{\partial y}, \; I_3 = -uw \frac{\partial U_b}{\partial z}$$
$$I_4 = -uv \frac{\partial V_b}{\partial x}, \; I_5 = -v^2 \frac{\partial V_b}{\partial y}, \; I_6 = -vw \frac{\partial V_b}{\partial z}$$
$$I_7 = -wu \frac{\partial W_b}{\partial x}, \; I_8 = -wv \frac{\partial W_b}{\partial y}, \; I_9 = -w^2 \frac{\partial W_b}{\partial z}$$

with $(u, v, w)^T$ being the perturbation and $(U_b, V_b, W_b)^T$ the base flow under consideration. The sign of the different integrands indicates whether the local transfer of kinetic energy associated to them acts as stabilising (negative) or destabilising (positive). It is worthy to note that, since an axisymmetric base flow is considered, reformulating the kinetic energy budget in terms of wall-normal and azimuthal derivatives of the base flow would make more sense. However, for sake of comparison with the asymmetric stenotic pipe flow, it has been decided to stick to a cartesian formulation of the Reynolds-Orr equation.

Figure IV.7 depicts the kinetic energy transfer rates integrated over the whole volume normalised by the dissipation for the axisymmetric stenotic pipe flow at the critical

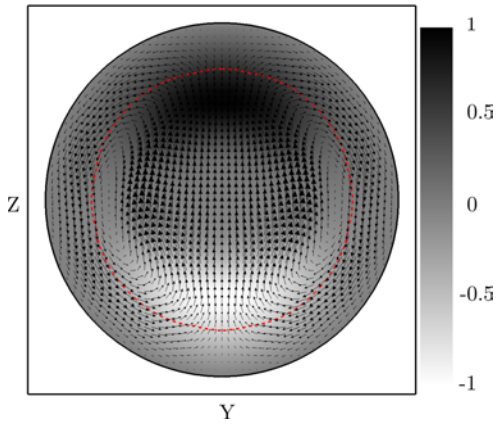

(a)

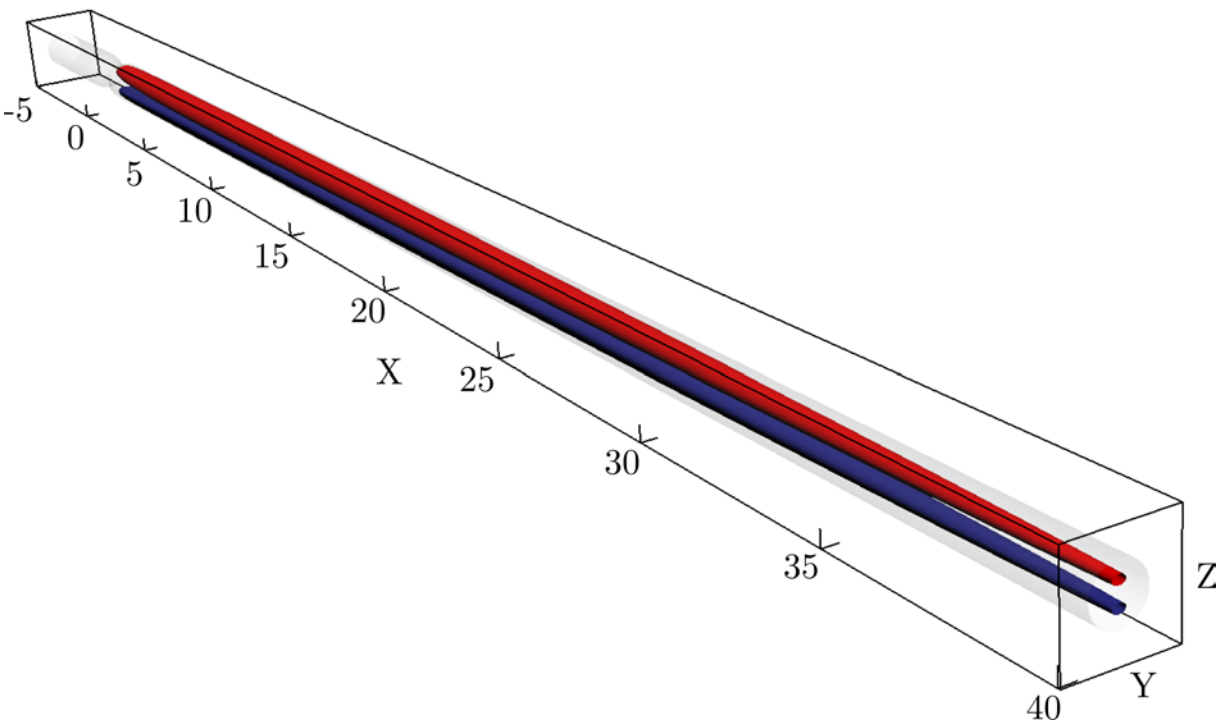

(b)

Figure IV.6: Streamwise velocity component of the leading global mode for the axisymmetric stenotic pipe at the critical Reynolds number $Re_c = 721$. (a) Motion induced in the $x = 5$ plane. (b) Isosurfaces depicting $\pm 10\%$ of the maximum streamwise velocity of the mode (red: negative, blue: positive).

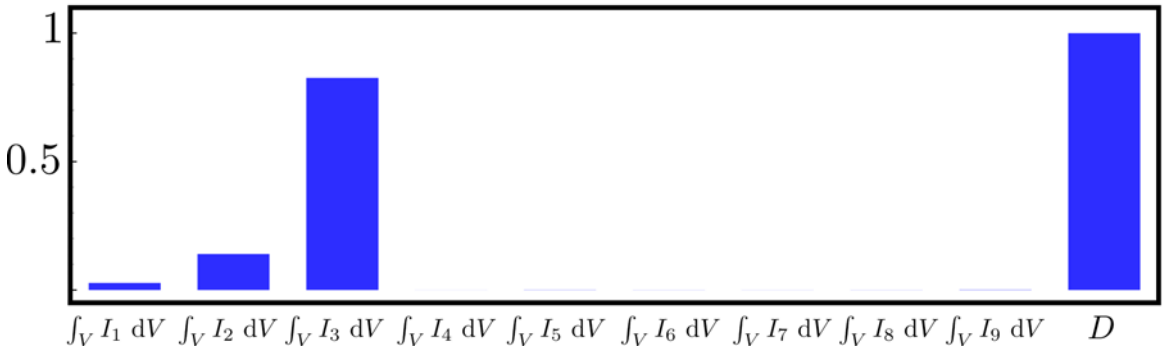

(a)

Figure IV.7: Kinetic energy budget of the leading global mode integrated over the whole volume of the axisymmetric stenotic pipe at $Re_c = 721$.

Reynolds number $Re_c = 721$. It is clear that the unstable global mode essentially extracts its energy from the wall normal gradient of the streamwise velocity component of the base flow. Moreover, this kinetic energy budget is largely dominated by the $\int_V I_3 \, \mathrm{d}V$ term. The instability thus mostly extracts its energy from the work of the uw Reynolds stress against the z-derivative of the base flow streamwise velocity component U_b. Figure IV.8 depicts the spatial distribution of this production term in (a) the $x = 5$ plane and (b) the $y = 0$ plane, respectively. It is clear from this figure that the instability essentially extracts its kinetic from the confined stenotic jet. This instability thus seems to be an instability of the confined jet rather than one of the reversed flow region itself further confirming the Coanda-like instability.

IV.3.3 Non-linear saturation and transition to turbulence

The non-linear evolution of this particular instability mode has not been investigated in the present work. The following explanatory section thus essentially relies on the work by Sherwin & Blackburn [142][1] to provide the reader with some insights about the non-linear evolution of the mode and the subsequent transition to turbulence.

The DNS code used in [142] employs a Fourier decomposition of the Navier-Stokes equations in the azimuthal direction. Consequently, the authors have been able to easily monitor the energy along the $m = \pm 1$ Fourier mode. Assuming one has $\Psi \propto E_1^{1/2}$, where Ψ stands for the mode's amplitude and $E_1^{1/2}$ is the square-root of the kinetic energy along the $m = \pm 1$ Fourier mode, the authors produced some evidences for the bifurcation occuring at $Re = 721$ to be a subcritical pitchfork bifurcation. Sherwin & Blackburn [142] mimicked the time-evolution of Ψ using the three-terms model:

$$\frac{\partial \Psi}{\partial t} = \gamma \Psi + \beta_1 \Psi^3 - \beta_2 \Psi^5 \tag{IV.5}$$

where β_1 and β_2 are postive numbers. Figure IV.9 depicts the time evolution of $E_1^{1/2}$ (solid line), the predicted evolution of Ψ (dashed line) and a comparison with the purely

[1]The author is very grateful to Spencer Sherwin and Hugh Blackburn for having kindly allowed the reproduction of the figures presented in this section. They have been taken from their paper [142].

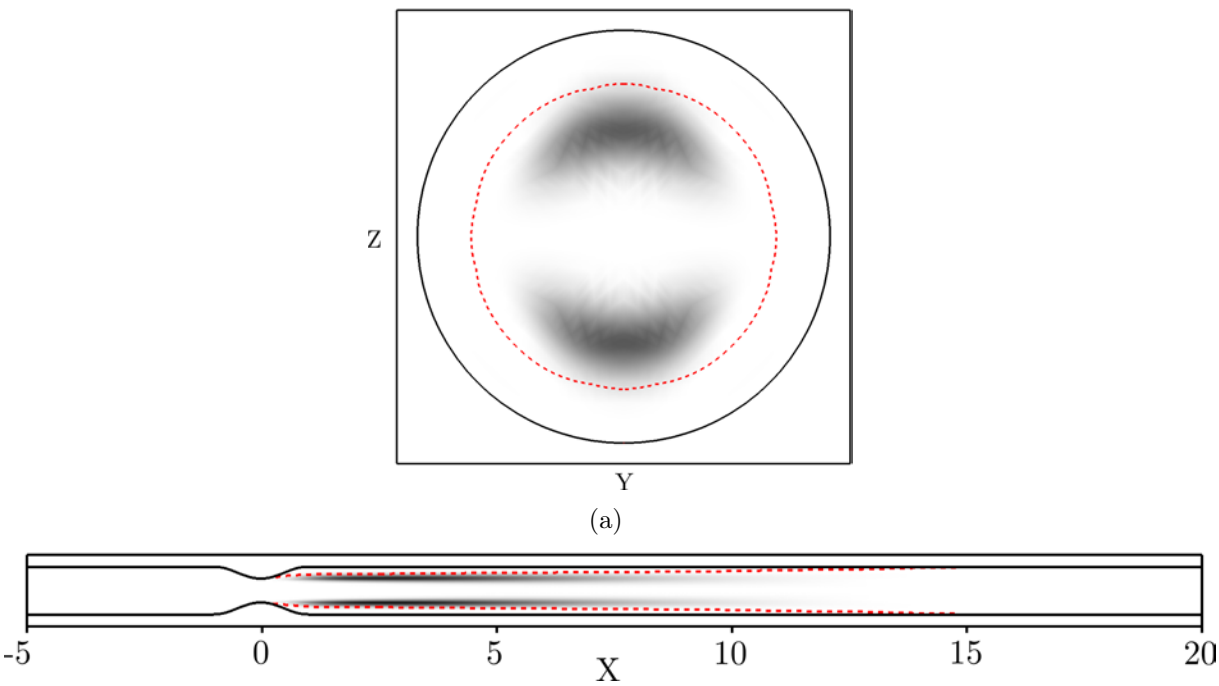

Figure IV.8: Spatial distribution of the $\int_V I_3 \, \mathrm{d}V = \int_V -uw\frac{\partial U_b}{\partial z} \, \mathrm{d}V$ production term in (a) the $x = 5$ plane and (b) the $y = 0$ plane. The dashed red line depicts the extent of the reversed flow region.

exponential growth (dotted line). As one can see, though both the growth of $E_1^{1/2}$ and Ψ initially follow closely the purely exponential growth, past $t \simeq 400$ they start to quickly depart from it before eventually saturating non-linearly. Such over-exponential growth right before non-linear saturation is the clear signature of subcriticality. In the non-linearly saturated regime, some low-frequency oscillations of the stenotic jet are observed. As explained by the authors, this low-frequency unsteadiness observed within the flow corresponds to a periodic rotation of the stenotic jet. Moreover, as highlighted by the instantaneous isosurfaces of streamwise and azimuthal vorticity depicted on figure IV.10 at various instants of the low-frequency cycle, this periodic rotation of the jet is accompanied by the shedding, roughly four diameters downstream the stenosis throat, of a structure similar to that of the turbulent puffs observed in subcritical pipe flow transition. For further visualisation of this turbulent-like puff, the reader is refered to Varghese *et al.* [156] where λ_2 visualisations are presented.

IV.4 Asymmetric stenotic pipe flows

IV.4.1 Influence of the eccentricity at fixed Reynolds number

As a first step toward comprehension of the influence of asymmetry defects on the properties of the steady inlet stenotic pipe flow, the Reynolds number is kept constant, $Re = 350$, and the eccentricity of the stenosis throat ranges from $E = 0\%$ (axisymmetric case) up to

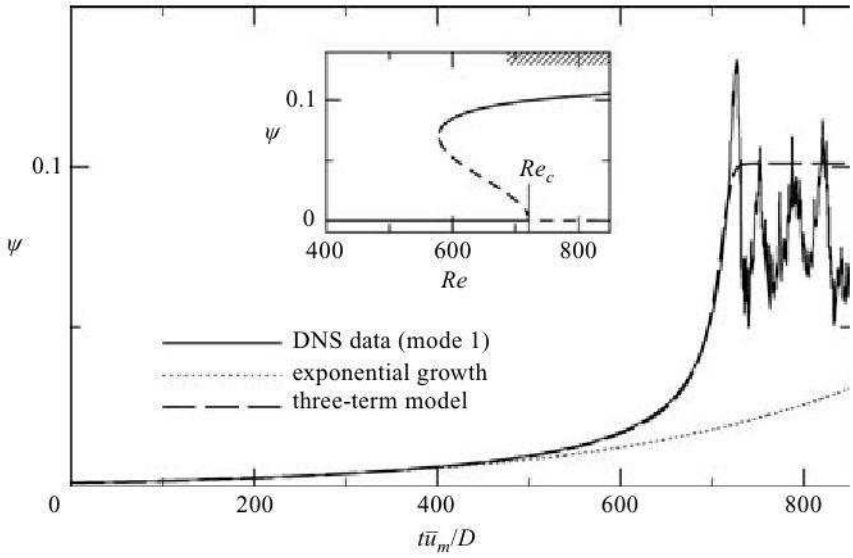

Figure IV.9: Growth to saturation and transition to turbulence of the steady inlet flow solution at $Re = 750$, where $E^{1/2}$ is used as a measure of perturbation amplitude Ψ. The three-term model fit is for (5,2). Inset: approximate bifurcation diagram, with observed Re-range of turbulent solutions indicated by hatching.

$E = 10\%$. Figure IV.11 shows the evolution of the volume V^- of the reversed flow region with an increase of the eccentricity of the stenosis throat. Three different stages can be observed in this diagram:

- From $E = 0\%$ to $E \simeq 0.25\%$: the volume of the reversed flow region remains almost constant. It can thus be infered that the base flow velocity field is almost axisymmetric.
- From $E \simeq 0.25\%$ to $E \simeq 1\%$: the volume of the reversed flow region is drastically reduced.
- From $E \simeq 1\%$ up to $E = 10\%$: the volume of the reversed flow region increases and eventually becomes more important than that of the axisymmetric reference solution.

Figures IV.12 and IV.13 depict streamwise velocity contours of the flow for eccentricities within each of the stages just described in the $x = 5$ and $y = 0$ planes, respectively. These figures make it obvious that, for $E \leq 0.25\%$, the flow only slightly deviates from the axisymmetric reference solution. On the other hand, for $E \geq 0.25\%$, great differences are observed. First, it is clear from figure IV.12 that the jet has been deflected toward the upper side of the pipe. Moreover, this deflection and early wall reattachment of the jet yield the upper part of the reversed flow region to shrink, thus explaining the drop in the volume V^- of the recirculation bubble. Finally, as the eccentricity E exceeds 1% of the pipe's diameter, the upper part of the reversed flow region has totally disappeared. Similar evolution has been observed by Griffith *et al.* [74] when investigating the same setup. For the Reynolds number under consideration herein, these authors have found

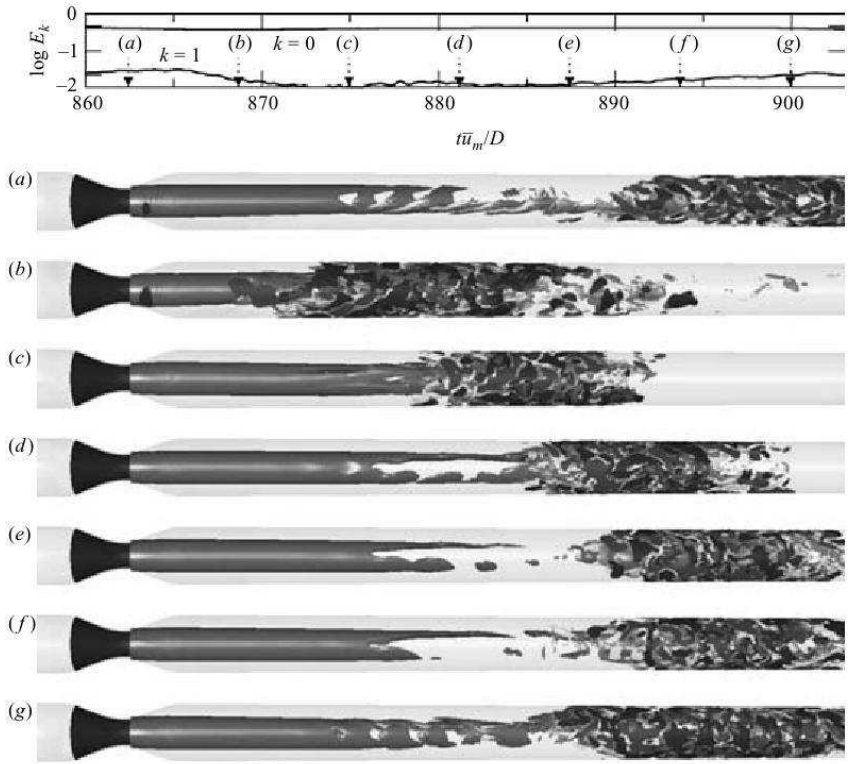

Figure IV.10: Time series of the energy in the first two azimuthal Fourier modes for steady inlet at $Re = 750$ during a long-period oscillation, and instantaneous isosurfaces of azimuthal and streamwise vorticity at seven points in the cycle. At the start of the cycle, the orientation of the jet is towards the top of the tube; at the end, it is towards the bottom.

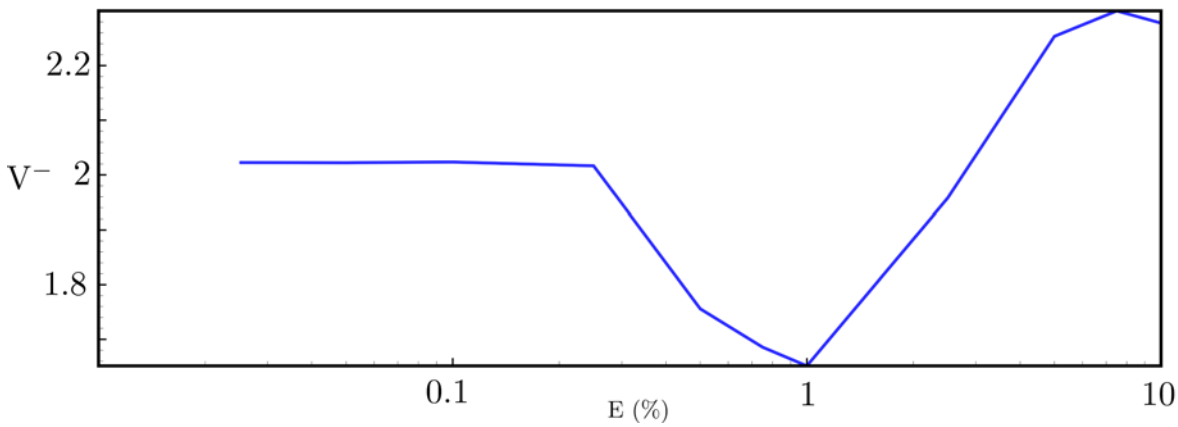

Figure IV.11: Evolution of the volume of the reversed flow region with an increase of the stenotis throat's eccentricity at $Re = 350$.

that the critical value for the stenosis offset is $E_c = 0.2525\%$, a critical value in good agreement with the present estimate.

IV.4.1.1 Linear stability analysis

In order to understand what is the physical mechanism responsible for this early wall reattachment of the jet and whether or not it is related to the pitchfork bifurcation taking place in the axisymmetric stenotic pipe flow at $Re = 722$, a global stability analysis of the 0.25% eccentric stenotic pipe flow at $Re = 350$ is performed. Figure IV.15 depicts the spectrum of the associated linearised Navier-Stokes operator. It has been computed using a Krylov subspace of dimension $k = 250$ and a sampling period $\Delta T = 1$. As one can see, two real eigenvalues lie very close to the upper half complex plane indicating the flow is about to experience two successive pitchfork bifurcations. Figure IV.15 shows (a) the motion induced by the leading global mode in the $x = 5$ plane and (b) a three-dimensional view of its streamwise velocity component, respectively. It is clear from these two figures that this mode shares striking resemblance with the leading global mode found in the axisymmetric reference case depicted on figure IV.6. It arises at the throat of the stenosis and induces a reduction of the velocity of the flow on the lower side of the pipe, whereas it slightly increases the velocity on the upper side. It can as well be deduced from the in-plane motion depicted on figure IV.15(a) that this mode essentially transfers the velocity from the upper side of the reversed flow region towards its lower side. It moreover triggers an upward deflection (in the direction of the stenosis offset) of the reversed flow region and of the jet from the pipe's centerline. As its axisymmetric counterpart, this global mode thus enhances the up-and-down symmetry breaking and can be related to a Coanda-like instability of the confined jet.

Figure IV.16 shows the spatial distribution of the second leading global mode. Once again, the mode arises right downstream the stenosis throat. However, the motion it induces is quite different from the motion induced by the leading global mode. First of all, whereas only two vortices can be observed in the motion induced by the leading global mode depicted on figure IV.16(a), three of these vortices are visible on figure IV.16(a).

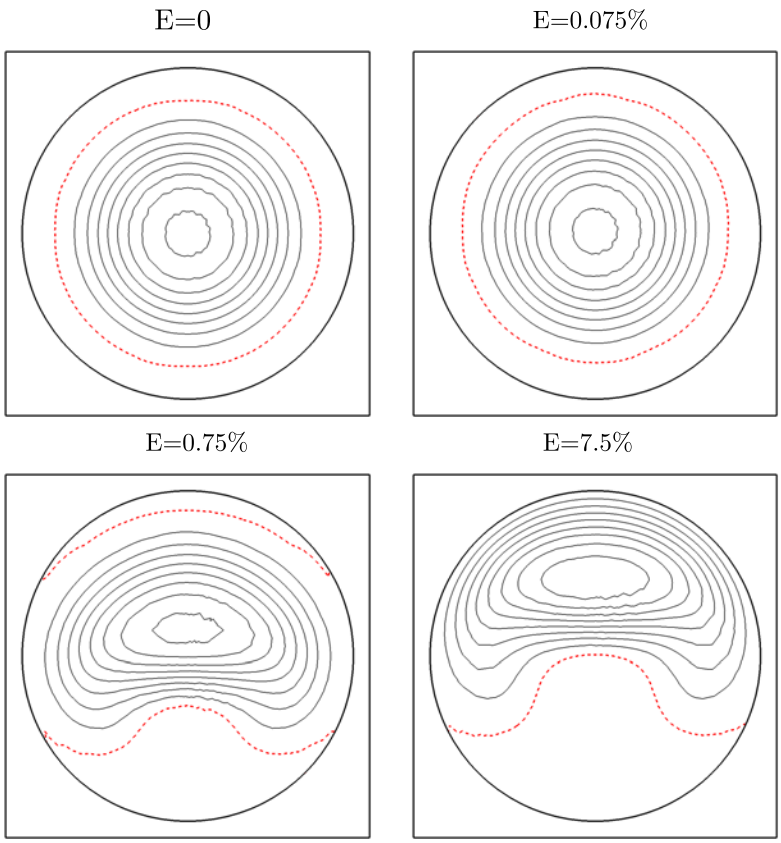

Figure IV.12: Streamwise velocity contours in the $x = 5$ plane. Thin solid lines depicts streamwise velocity contours from $U_b = 0.5$ up to $U_b = 4$. Red dashed line highlights the extent of the reversed flow region within this plane. The Reynolds number is set to $Re = 350$.

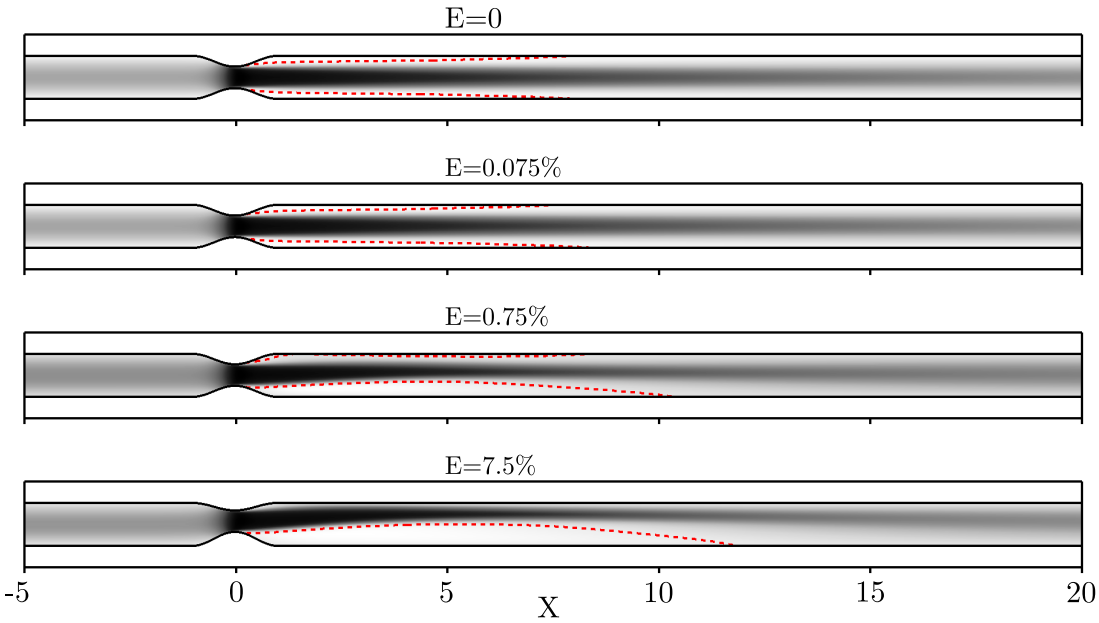

Figure IV.13: Streamwise velocity contours in the $y = 0$ plane. Red dashed line highlights the extent of the reversed flow region within this plane. The Reynolds number is set to $Re = 350$.

More importantly, though the leading global mode enhances the up-and-down symmetry breaking, it still remains symmetric with respect to the $y = 0$ plane. On the other hand, it is clear from figures IV.16(a) and (b) that this sub-dominant global mode increases the velocity of the flow on the left side of the pipe while reducing it on the right side, thus breaking the remaining left-rigth symmetry of the flow. Despite these differences, this sub-dominant global mode appears to be essentially deflecting the stenotic jet toward the left side of the pipe. It might thus be related to a secondary Coanda-like instability of the confined jet.

IV.4.1.2 Kinetic energy budget analysis

To get a better understanding of the instability mechanism at play for each of the two global modes identified, the kinetic energy transfer rates between the base flow and these two modes are investigated. Figure IV.17 depicts the kinetic energy transfer rates integrated over the whole volume of the stenotic pipe for (a) the leading symmetric global mode and (b) the sub-leading antisymmetric global mode. These rates have been normalised by the dissipation in both cases for the sake of comparison. It is obvious from these two figures that both instabilities essentially extract their energy from the work of the Reynolds stresses against the gradients of the streamwise velocity component U_b of the base flow. Yet, depending on the mode considered, the major contribution does not stem from the same component of the gradient. Indeed, as can be seen on figure IV.17(a), the kinetic energy transfer rates of the leading global mode are mostly dominated by the $\int_V I_3 \, \mathrm{d}V$ production term. This mode thus extracts most of its kinetic energy from the work of the uw Reynolds stress against the z gradient of the streamwise velocity component of the base flow, that is in the direction of the stenosis offset. Moreover, com-

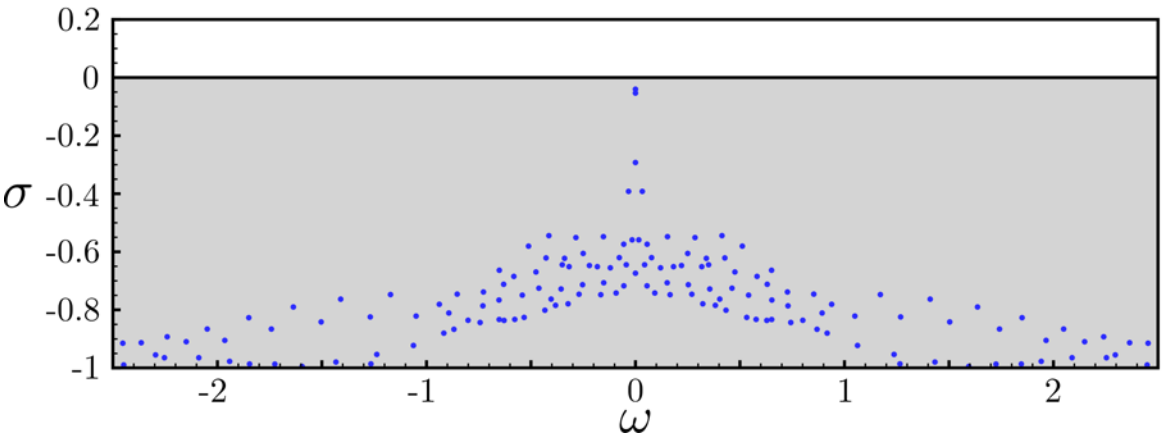

Figure IV.14: Eigenspectrum of the linearised Navier-Stokes operator for a $E = 0.25\%$ eccentric stenotic pipe flow at $Re = 350$.

parison with the kinetic energy budget of the axisymmetric mode depicted on figure IV.7 suggests that the underlying instability mechanism is similar. On the other hand, the sub-dominant antisymmetric global mode mostly extracts its kinetic energy from the work of the uv Reynolds stress against the y gradient of the streamwise velocity component of the base flow, i.e. in the direction perpendicular to the stenosis offset. Figure IV.18 depicts the spatial distribution of the kinetic energy production term in the $x = 5$ plane for (a) the leading symmetric mode and (b) the sub-dominant antisymmetric mode, respectively. Despite the genuine difference in their symmetry, it is clear from these figures that both modes essentially extract their kinetic energy from the confined stenotic jet similarly to what has been observed for the axisymmetric unstable global mode for which the spatial distribution of its leading production term is depicted on figure IV.8. It thus seems reasonnable to assume that these two modes, despite their different symmetry, are both related to Coanda-like instability of the jet stemming from the stenotic constriction as well.

IV.4.2 Influence of the Reynolds number at fixed eccentricity

Now that a survey of the stenosis eccentricy's influence on the flow at fixed Reynolds number has been given, one might wonder what is the influence of the Reynolds number at fixed eccentricity. To do so, the eccentricity of the stenosis is set to $E = 0.1\%$ while the Reynolds number is varied from $Re = 300$ up to $Re = 500$. Figure IV.19 depicts the evolution of the volume V^- of the reversed flow region with an increase of the Reynolds number. This bifurcation diagram clearly highlights the existence of a hysteresis cycle. Such hysteresis cycle is a genuine feature of subcritical pitchfork bifurcations. Subcriticality of the bifurcation has already been foreseen by Sherwin & Blackburn [142] and has been observed by Griffith *et al.* [74] as well. Figures IV.20 and figures IV.21 depict the features of the upper and lower branch solutions at $Re = 400$ in the $x = 5$ plane and $y = 0$ plane, respectively. As previously, one of the two solutions is a slightly asymmetric solution while the other one has experienced an early wall-reattachment of the confined stenotic jet. On figure IV.19, the blue line thus shows the evolution of the slightly asym-

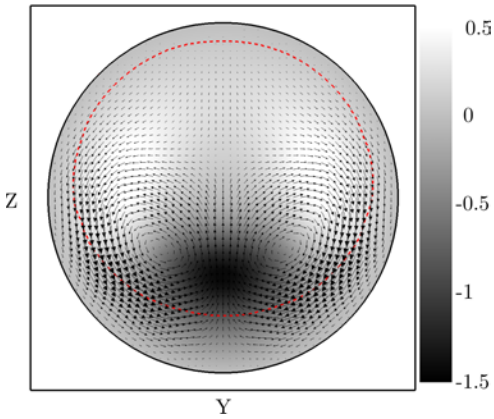

(a)

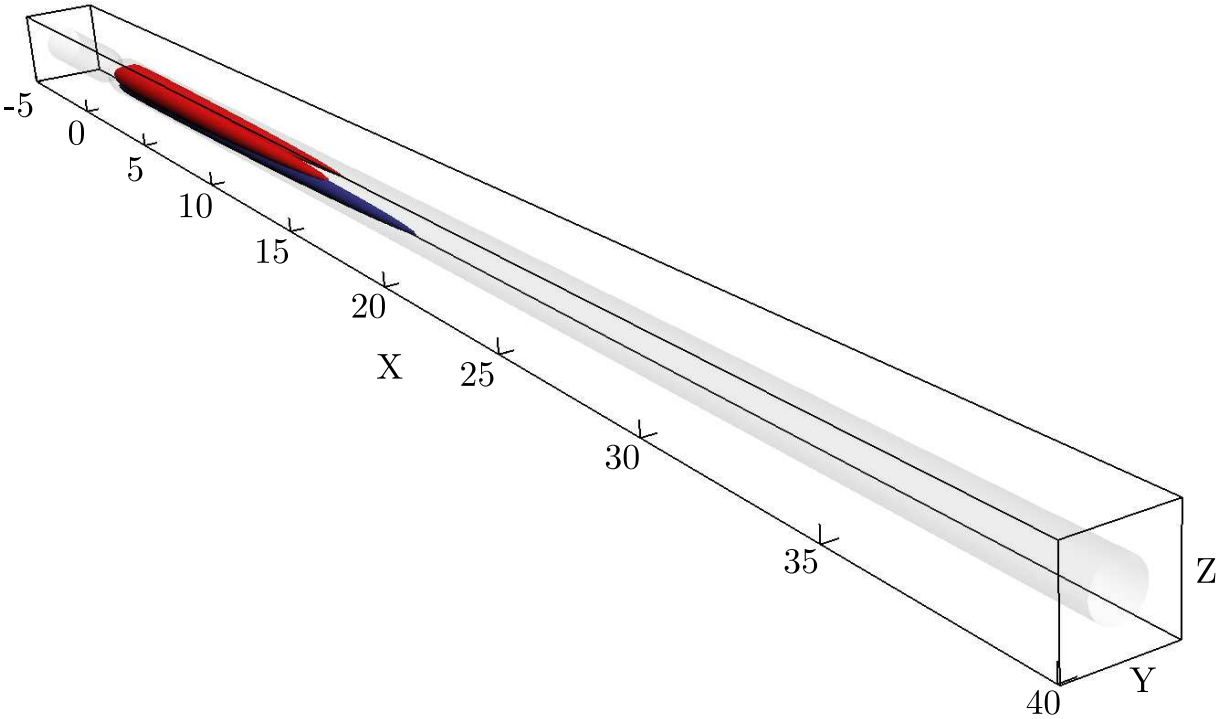

(b)

Figure IV.15: Streamwise velocity component of the leading global mode. (a) Motion induced in the $x = 5$ plane. (b) Isosurfaces depicting $\pm 10\%$ of the maximum streamwise velocity of the mode (red: negative, blue: positive).

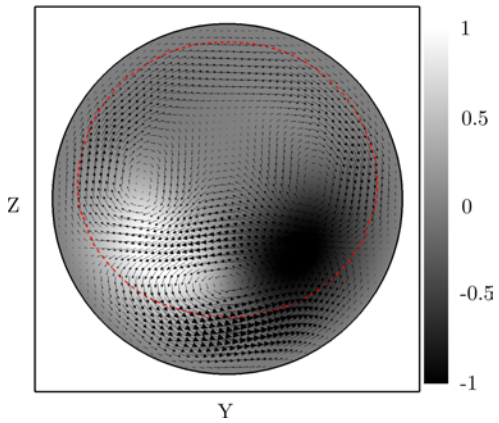

(a)

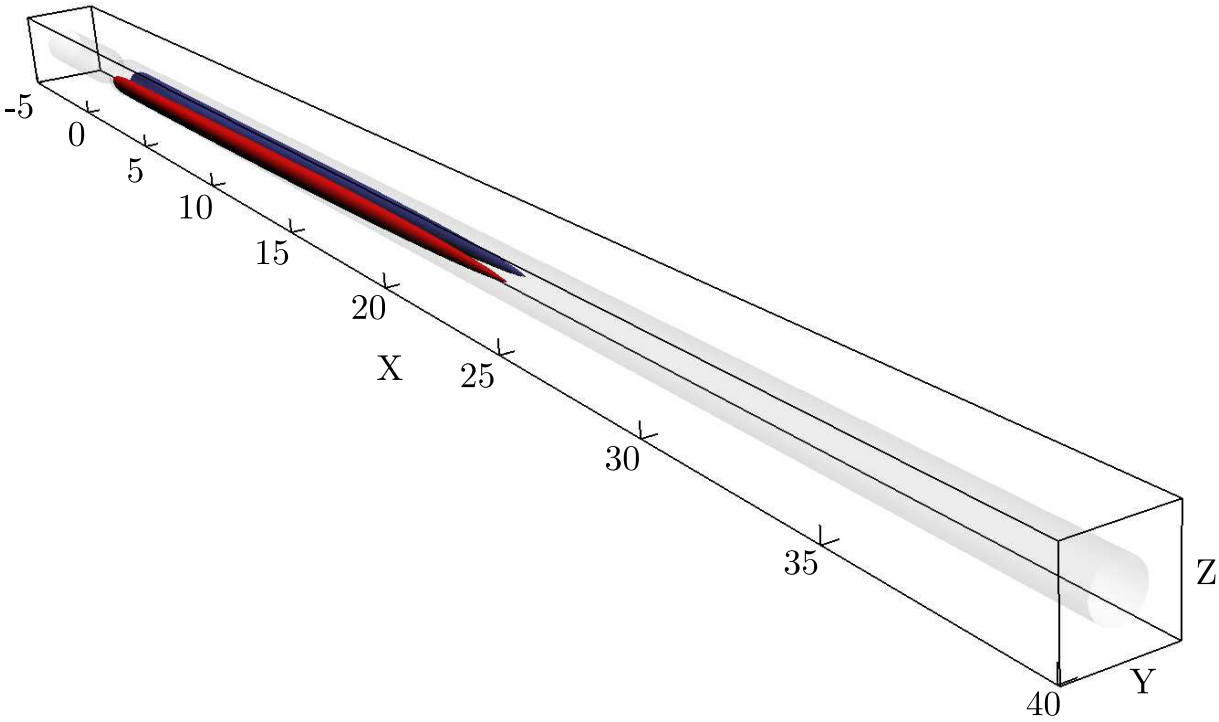

(b)

Figure IV.16: Streamwise velocity component of the second leading global mode. (a) Motion induced in the $x = 5$ plane. (b) Isosurfaces depicting $\pm 10\%$ of the maximum streamwise velocity of the mode (red: negative, blue: positive).

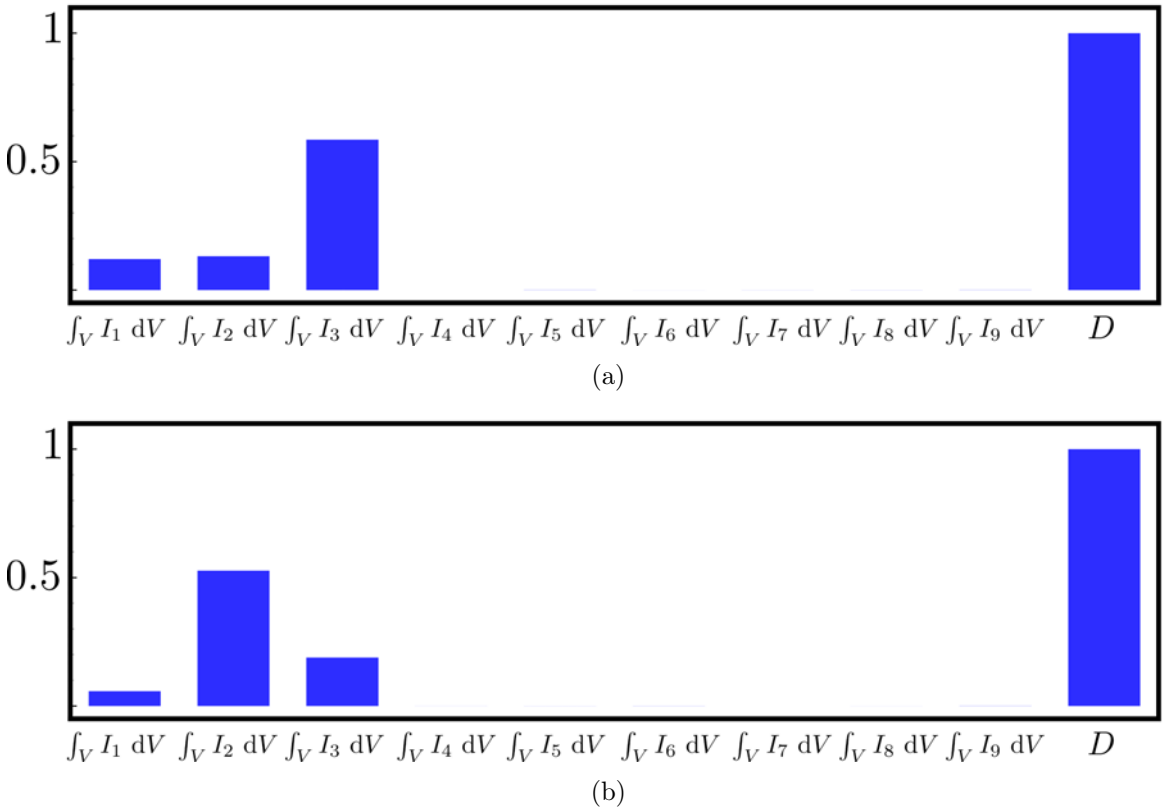

Figure IV.17: Kinetic energy budget integrated over the whole volume of the stenotic pipe. (a) Leading symmetric global mode. (b) Sub-dominant antisymmetric global mode.

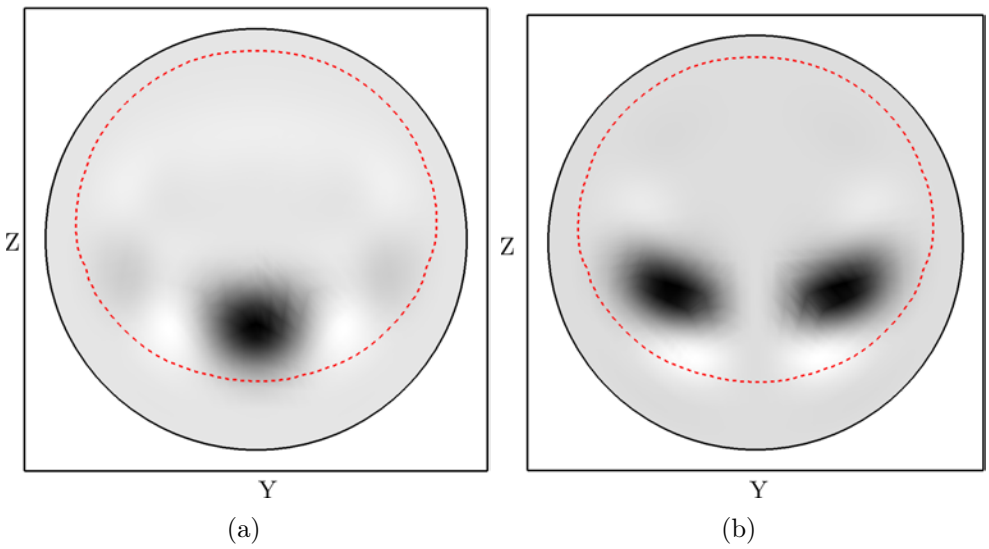

Figure IV.18: Spatial distribution in the $x = 5$ plane of the leading production term for (a) the leading unstable mode ($\int_V I_3$ dV) and (b) the sub-dominant one ($\int_V I_2$ dV). Regions coloured in black are regions where kinetic energy is produced, whereas regions in white are regions where it is dissipated.

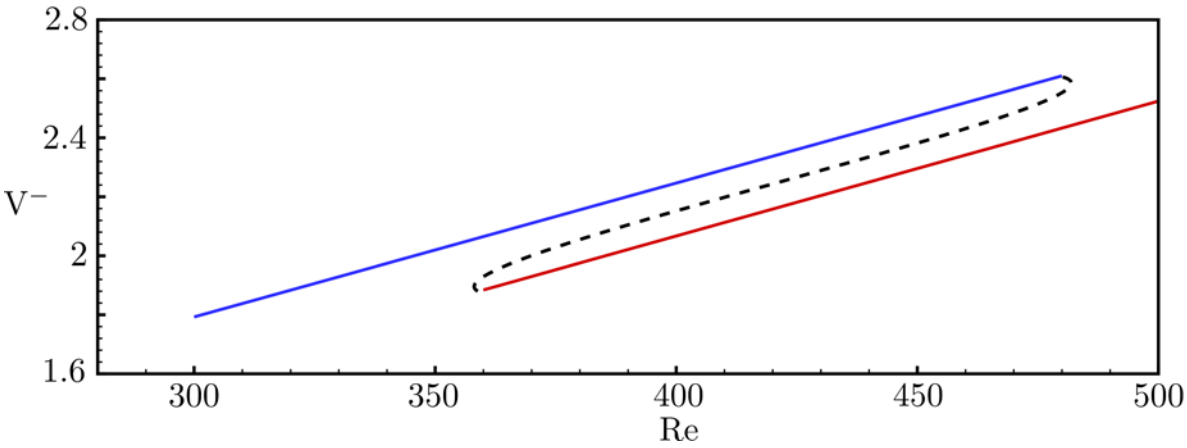

Figure IV.19: Evolution of the volume of the reversed flow region with an increase of the Reynolds number for a fixed eccentricity $E = 0.1\%$. Blue line depicts the evolution of the slightly asymmetric solution whereas red line shows the evolution of the wall-reattached solution. The dashed line is the suspected form of the unstable branch of solutions.

metric solution's reversed flow volume while the red line shows the evolution of the wall reattached solution.

Linear stability analysis

Figure IV.22 depicts the spectrum of the linearised Navier-Stokes operator of the slightly asymmetric stenotic pipe flow where the stenosis throat has been offset by $E = 0.1\%$ of the pipe's diameter and at a Reynolds number $Re = 450$. It has been computed using a Krylov subspace of dimension 250 and a sampling period $\Delta T = 1$. Though the stenosis throat's eccentricity and the Reynolds number considered are different than those considered in section IV.4.1.1, it is clear that the spectrum depicted here shares close connections with the one depicted on figure IV.14. It is dominated by two real eigenvalues lying very close to the upper-half complex plane thus indicating the flow is about to experience two successive pitchfork bifurcations once again. Figures IV.23 and IV.24 depict the spatial distribution of the streamwise component of these two modes. As previously, the leading global mode, depicted on figure IV.23, displays a symmetry with respect to the $y = 0$ plane while the sub-dominant mode, depicted on figure IV.24, displays an anti-symmetry with respect to this same plane. It is also clear from these figures that these two modes closely resemble the two leading modes identified in section IV.4.1.1. Whereas the leading symmetric mode enhances the up-and-down symmetry breaking, the sub-dominant anti-symmetric mode breaks the remaining left-right symmetry of the flow. An analysis of the kinetic energy transfer between the base flow and these modes (not shown here for the sake of conciseness) let us draw the same conclusions as previously: these modes are related to a Coanda-like instability of the jet stemming from the stenotic constriction rather than an instability of the reversed flow region itself. It would thus appear that, starting from the axisymmetric steady state at low Reynolds number, the first two bifurcations to be encountered are symmetry-breaking pitchfork bifurcations no matter the trajectory taken in the parameter space (E, Re)

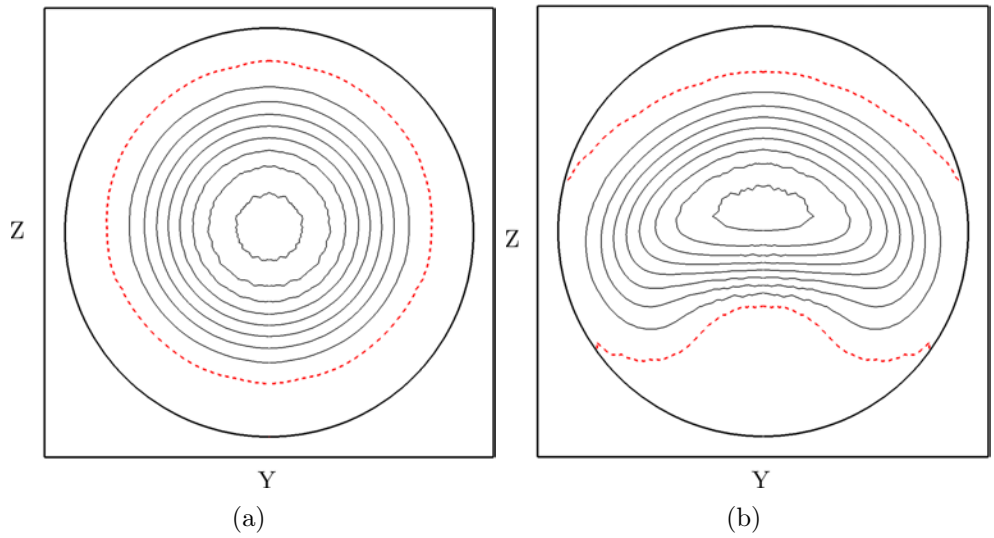

Figure IV.20: Streamwise velocity component of (a) the slightly asymmetric base flow and (b) the wall-reattached solution in the $x = 5$ plane. Red dashed line depicts the spatial extent of the reversed flow region. Thin solid lines depicts streamwise velocity contours from $U_b = 0.5$ up to $U_b = 4$.

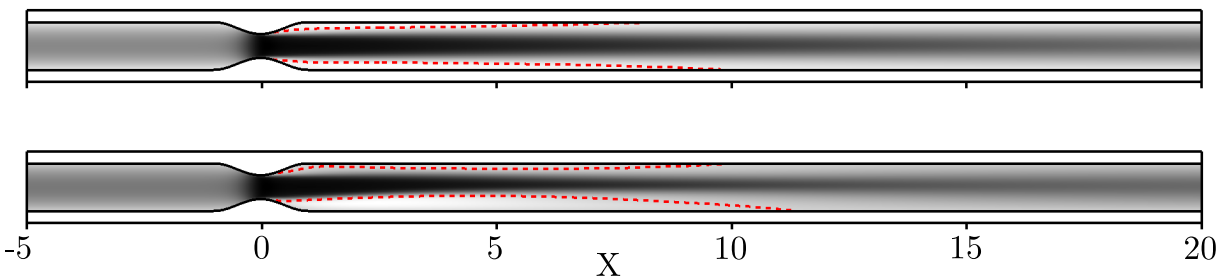

Figure IV.21: Streamwise velocity component of the slightly asymmetric base flow (top) and the wall-reattached solution (bottom) in the $y = 0$ plane. Red dashed line depicts the spatial extent of the reversed flow region.

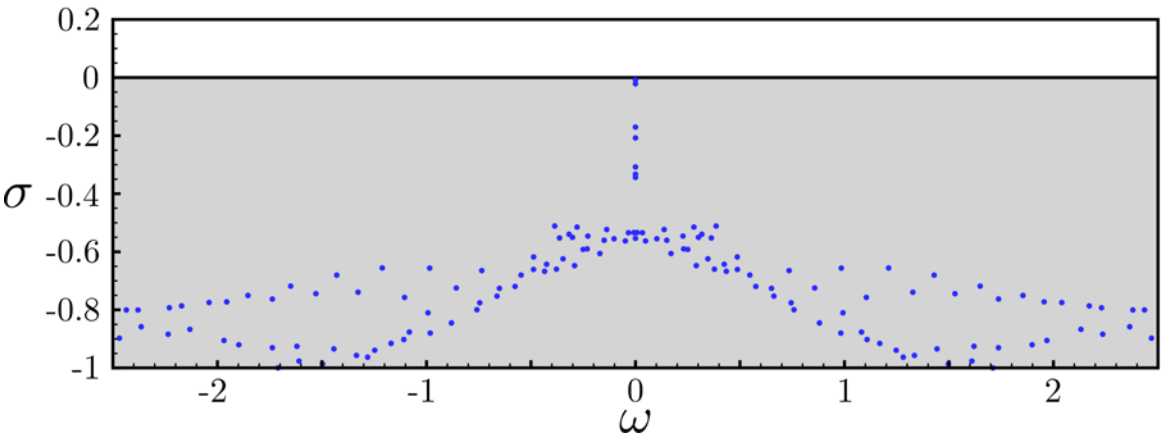

Figure IV.22: Eigenspectrum of the linearised Navier-Stokes operator for a $E = 0.1\%$ eccentric stenotic pipe flow at $Re = 450$.

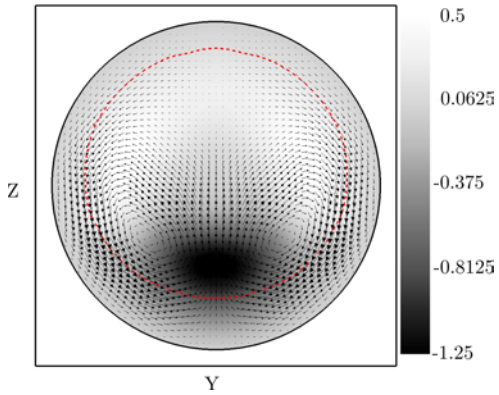

(a)

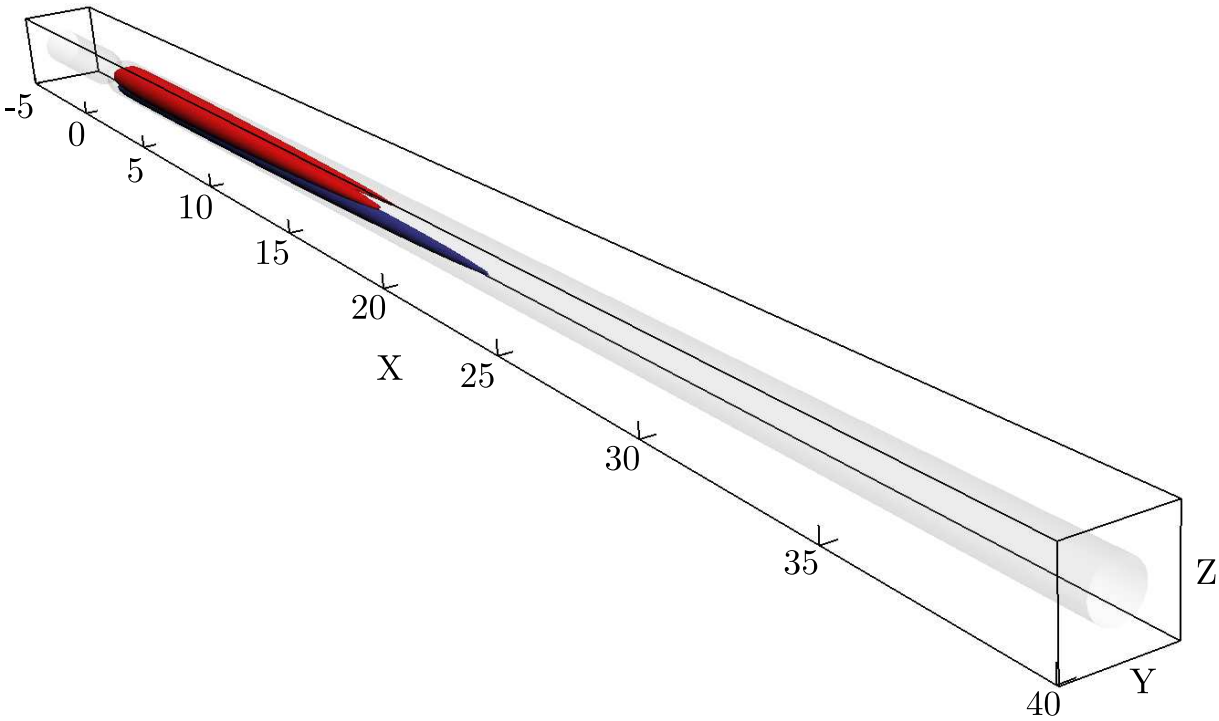

(b)

Figure IV.23: Streamwise velocity component of the leading global mode for $(E, Re) = (0.1\%, 450)$. (a) Motion induced in the $x = 5$ plane. (b) Isosurfaces depicting $\pm 10\%$ of the maximum streamwise velocity of the mode (red: negative, blue: positive).

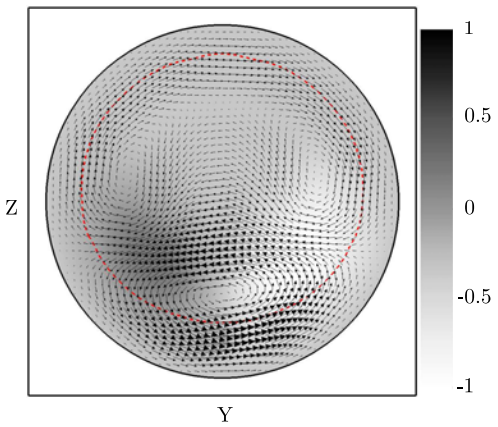

(a)

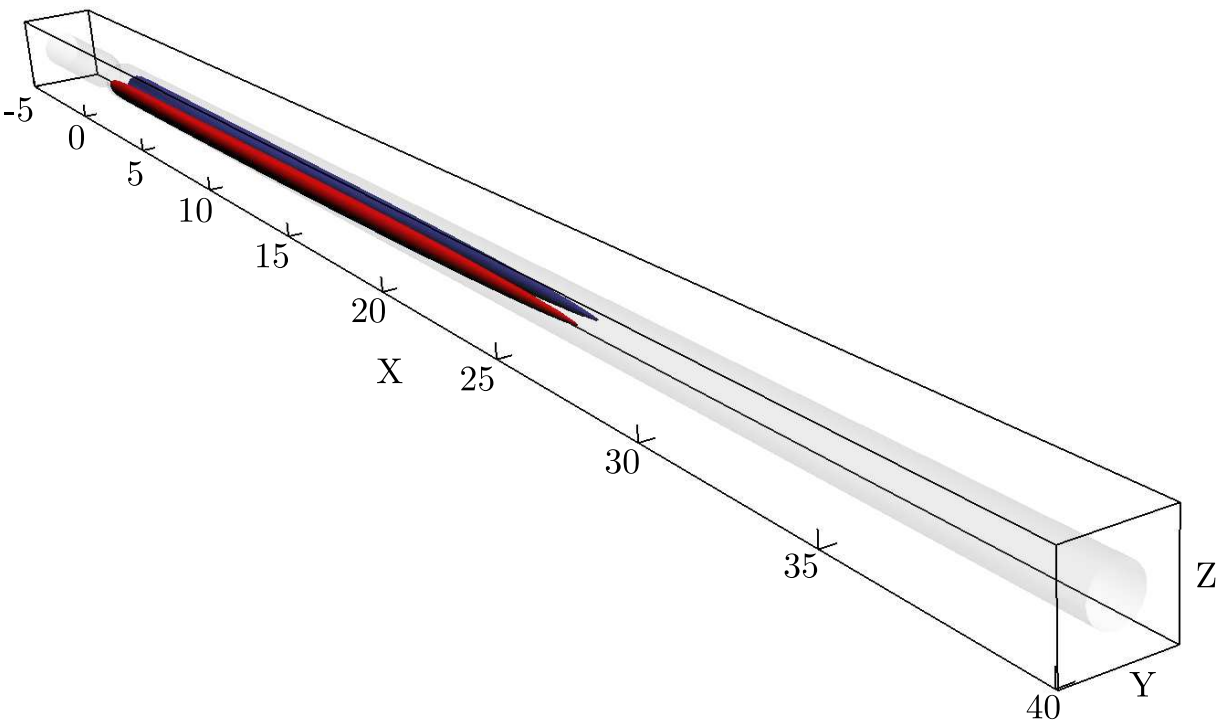

(b)

Figure IV.24: Streamwise velocity component of the second leading global mode for $(E, Re) = (0.1\%, 450)$. (a) Motion induced in the $x = 5$ plane. (b) Isosurfaces depicting $\pm 10\%$ of the maximum streamwise velocity of the mode (red: negative, blue: positive).

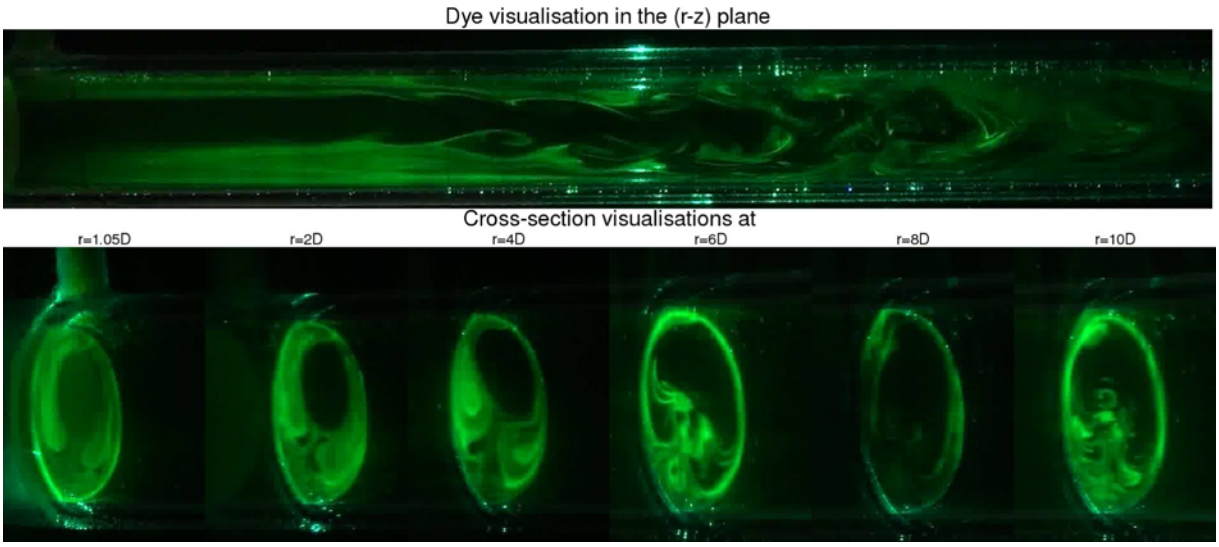

Figure IV.25: Dye visualisation of the unsteady structures in the $E = 5\%$ asymmetric stenotic pipe flow at $Re = 330$.

IV.5 Discussion

Comparison with the experimental work of Griffith & Passaggia

As part of the project SICOGIF, Martin D. Griffith and Pierre-Yves Passaggia have investigated the dynamics of the asymmetric stenotic pipe flow from an experimental perspective. Depending on the ecentricity of the stenosis, almost axisymmetric flows and wall-reattached ones have both been observed. However, their experimental work has also underlined a crucial feature not observed in the present numerical investigation: transition to unsteadiness. Figure IV.26 depicts the evolution of the critical Reynolds number beyond which unsteadiness is observed in the experiment with respect to the eccentricity of the stenosis throat. As one can see, as the eccentricity of the stenosis throat increases, the critical Reynolds number for unsteadiness decreases. The unsteadiness typically consists in oscillations of the shear layers of the reversed flow region as depicted on figure IV.25. The dye visualisations clearly highlight that these oscillations are closely related to a Kelvin-Helmholtz instability of the shear layers. The frequency at which these shear layers oscillate however appear to be dependent on both the eccentricity of the stenosis throat and the Reynolds number of the flow. Nonetheless, these experimental observations strongly question the validity of the numerical approach used in the present investigation. Figure IV.26 summarises the distribution in the (E, Re) parameter space of all the slightly asymmetric and wall-reattached solutions computed during the present thesis. Black dots enclose a region of the parameter space still under current investigation. It is worthy to note however that both the green and red dots only stand for stationnary solutions and that no unsteady flow has been numerically observed so far. This fact suggests great discrepancies between the experimental observations and the numerical predictions. The source of these discrepancies is still unknown at the present time. However, based on the form of the experimentally observed perturbations, a reasonnable assumption would be a subcritical transition to unsteadiness induced by transiently growing linear and non-

linear perturbations. Following the work of Blackburn *et al.* [32], preliminary optimal perturbation analysis of the flow in the $E = 0.1\%$ eccentric stenotic pipe at a Reynolds number $Re = 400$ has been performed. Figure IV.27(a) depicts the streamwise velocity component of the optimal perturbation. It is located in the vicinity of the separation point and is divergent to the right. On the other hand, the optimal response of the flow at the optimal time $\tau = 4.5$ is depicted on figure IV.27(b). As one can see, the optimal response takes the form of a wavepacket travelling along the shear layers of the reversed flow region as the experimentally observed perturbation. It is moreover apparent that the perturbation has been reoriented by the shear of the base flow, a linear mechanism known as the Orr mechanism on which transient growth is based. Due to this reorientation of the perturbation by the Orr mechanism, its energy has been multiplied by $G_{\max}(\tau) = 1.06\times10^6$ over a period of time $\tau = 4.5$ time units. These preliminary results thus suggest that, even in a well controlled experiment, the energy of small uncontrolled disturbances inherent to any experimental setup can grow up to one million times its initial level over a relatively short period of time. Such transient growth of small perturbation is thus very likely to trigger non-linear effects neglected in the present linear optimal perturbation analysis, hence potentially causing the flow to transition to unsteadiness as in the experiment.

The subcritical pitchfork bifurcation and the concept of base flow

In the introduction, the concept of base flow has been defined as follows:

> **Base flow:** A base flow is a peculiar solution of the Navier-Stokes equations. In the context of linear stability theory, this solution has to be stationnary or periodic in time.

For the range of eccentricities investigated herein, such peculiar solution is unique as long as the Reynolds number is below a given critical value ($Re \simeq 350$). However, the subcritical pitchfork bifurcation and the associated simultaneous existence of the slightly asymmetric stenotic flow and the wall-reattached one over a given range of Reynolds numbers challenges this definition. Indeed, both flows are stationnary solutions of the Navier-Stokes equations. Moreover, as explained previously, both solutions are symmetric with respect to the $y = 0$ plane, i.e. the only symmetry plane of the geometry, and thus both maximise the possible symmetries of the problem. As a consequence, for Reynolds numbers larger than 350, it is not clear which of these two solutions should be considered as the base flow. In order to solve this problem, another definition of the concept of base flow could be proposed. However, from the author's point of view, this problem is an ill-posed one and the answer should be based on physical considerations. For the 0.1% asymmetric stenotic pipe flow investigated in section IV.4.2, one should instead have the following reasonning:

- For $Re < 350$: only the slightly asymmetric solution exists. As a consequence, this solution is the only possible candidate for the base flow.
- For $350 < Re < 450$: both the slightly asymmetric and wall-reattached solution are permissible base flows. The linear stability of both solutions should thus be investigated as well as the transient growth of infinitesimal perturbations evolving

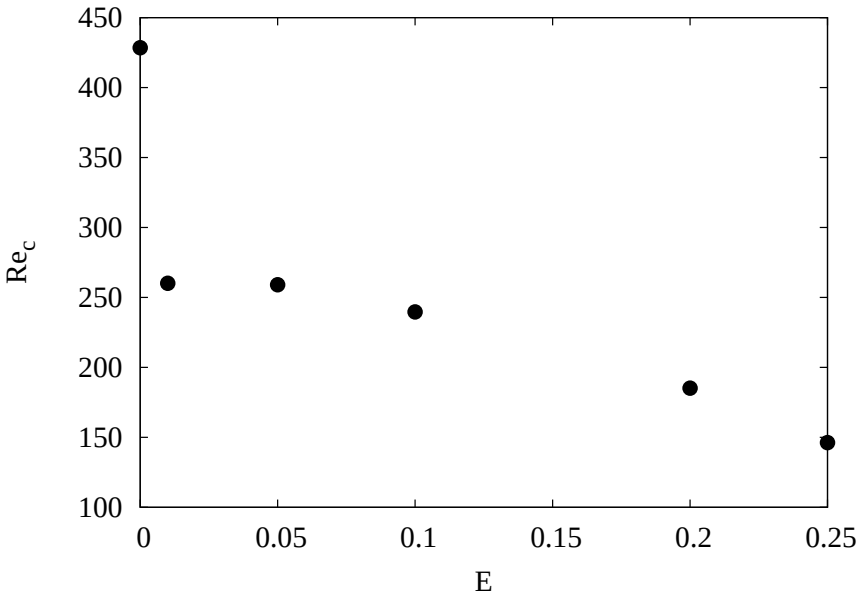

(a)

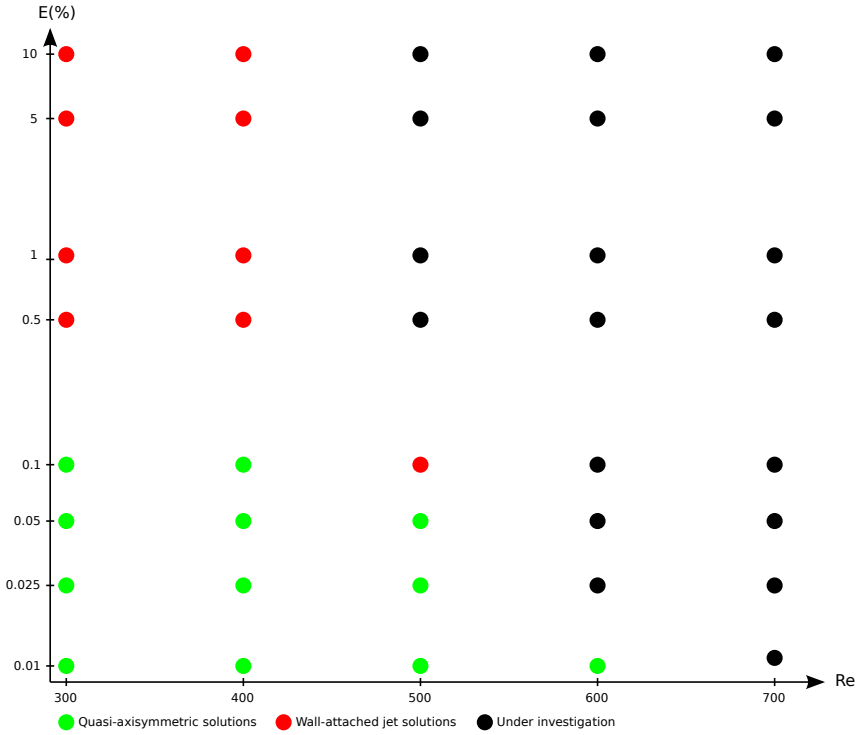

(b)

Figure IV.26: (a) Steady-unsteady transition observed in the asymmetric stenotic pipe flow experiment by Griffith & Passaggia. (b) Families of asymmetric stenotic pipe flows in the (E, Re) parameter space.

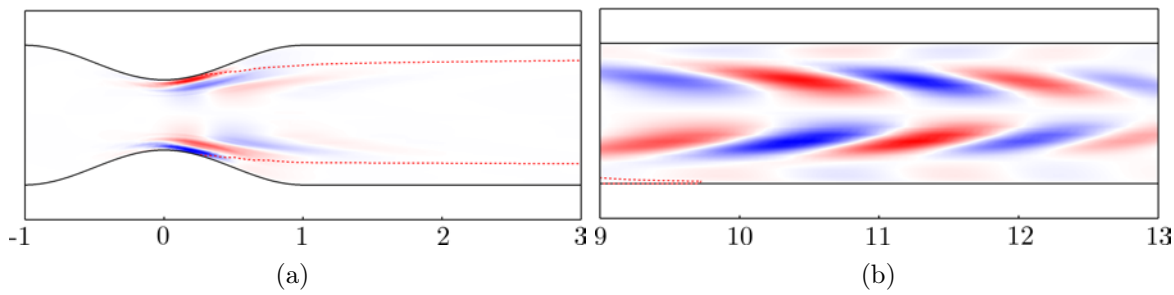

Figure IV.27: (a) Streamwise velocity component of the optimal perturbation for a $E = 0.1\%$ stenotic pipe flow at Reynolds $Re = 400$ in the $y = 0$ plane. (b) Optimal response of the flow.

onto both solutions. Conclusions should then be drawn accordingly to experimental observations if possible.

- For $Re > 450$: the slightly asymmetric solution is linearly unstable and thus cannot be observed anymore (nor numerically or experimentally) without a stabilising procedure. Past this point, only the stability of the wall-reattached solution should thus be investigated in order to appropriately investigate the secondary bifurcation eventually encountered by the flow.

Such physical considerations could also be applied to the case where the flow ecounters a Hopf bifurcation. Indeed, once the base flow has encountered a Hopf bifurcation, it is linearly unstable and thus cannot be physically observed anymore. Consequently, investigating the secondary instability of the stationnary base flow would make very little sense from the author's perspective and one should instead focus on the Floquet stability of the periodic solution to be physically accurate.

IV.6 Conclusion

The instabilities experienced by stenotic pipe flows have been investigated by mean of base flow computations and global stability analyses. A thorough illustration of the axisymmetric stenotic pipe flow has first been considered in order to provide the reader with a complete overview of the up-to-date picture about this peculiar flow's transition. The flow developing in such geometries consists in a confined jet stemming from the stenotic constriction and surrounded by an annulus reversed flow region. As for most separated flows, the characteristics of this reversed flow region evolve linearly with the Reynolds number. Nonetheless, beyond a critical Reynolds number $Re = 721$, the flow experiences a pitchfork bifurcation. The associated global mode triggers an upward deflection of the stenotic jet from the pipe's centerline while transferring the fluid from the upper part of the reversed flow region toward its lower part. As a consequence, the lower part of the recirculation bubble extends further downstream while the upper part starts to shrink. In the mean time, the upward deflection of the jet from the pipe's centerline eventually triggers a mild Coanda-type wall reattachment of the flow. Sherwin & Blackburn [142] have investigated the non-linear evolution of this instability. In their direct numerical simulation, they have observed that, once unstable, the jet starts to be deflected from the

pipe's axis as predicted by linear stability theory. Nonetheless, beyond a given deflection, the jet experiences a breakdown and the flow eventually displays localised transition to turbulence. The associated structures were found to share some connections with the turbulent puffs observed in subcritical pipe flow transition [19]. Moreover, some evidence suggests that this pitchfork bifurcation is subcritical.

Unfortunately, experimental results about the dynamics axisymmetric stenotic pipe flows put in the limelight that the flow might transition as early as $Re = 425$. Based on the assumption that these discrepencies might originate from very small asymmetry defects, the throat of the stenosis has been slightly offset from the pipe's centerline and the stability properties of the resulting flows have been investigated. Though for small eccentricities the flows appear to be quite similar to their axisymmetric counterpart, they experience global instability at substantially lower Reynolds numbers. Indeed, even for an eccentricity of the stenosis throat as small as 0.1% of the pipe's diameter, it has been shown that the flow becomes linearly unstable for $Re_c \simeq 450$. Nonetheless, for the range of eccentricities considered, the first bifurcation to occur always is a pitchfork bifurcation. Despite the different critical thresholds, the leading unstable mode in the asymmetric stenotic pipe flow is seen to be closely related to its axisymmetric counterpart. Indeed, as for the axisymmetric reference case, it triggers an upward deflection of the stenotic jet and transfers fluid from the upper side of the reversed flow region toward its lower side. As a consequence, the jet experiences a Coanda type wall reattachment once again hence promoting flow separation on the lower side of the pipe. It is noteworthy that this leading global mode only enhances the up-and-down symmetry breaking induced by the stenosis offset but still is symmetric with respect to the $y = 0$ plane. It must be highlighted however that once unstable, the sub-dominant global mode eventually breaks the remaining left-right symmetry of the flow. Unfortunately, due to time limitation, their non-linear evolutions have not been investigated yet. It is thought by the author that, once this sub-dominant global mode is unstable, since the resulting flow field has no symmetry left, it might eventually transition to unsteadiness. This still is however an open question and requires further analyses.

Finally, comparison with the experimental work of Martin D. Griffith and Pierre-Yves Passaggia has however revealed that great discrepancies exist between the experimental observations and the predictions obtained by global stability analyses. Indeed, for the range of eccentricties and Reynolds numbers considered herein, no unsteady flow has been observed. Unfortunately, experimental observations put in the limelight that the flow transitions to unsteadiness for Reynolds numbers as low as $Re \simeq 250$ for a 1% eccentric stenotic pipe. These discrepancies strongly suggest that global stability analysis might not be the most suited tool to investigate the transition of such flow. On the other hand, preliminary optimal perturbation analysis appears to give results in better agreements with the experimental observations. These preliminary results suggest that the unsteadiness observed in the experiment might be the consequence of a by-pass transition. This hypothesis however requires further investigations to be confirmed.

Perspectives

The present study has shown that the stability properties of the axisymmetric stenotic pipe flow and those of the asymmetric one were quantitatively very different even when a very small asymmetry of the geometry has been considered. From the author's point of view, several different leads can be explored to continue this work:

- It has been shown that the global stability properties of slightly asymmetric stenotic pipe flows significantly differ from those of the axisymmetric reference case. In-depth mathematical investigations of the properties of the axisymmetric linearised Navier-Stokes operator and of the slighly asymmetric one might help us to understand why is that so and get a better idea of the range of validity of the axisymmetric flow assumption when investigating such geometries.

- During their post-doctoral stays at IRPHE, Martin D. Griffith and Pierre-Yves Passaggia have conducted a series of experiments on the asymmetric stenotic pipe flow. As already explained, the transition to unsteadiness was observed to occur at substantially lower Reynolds numbers than those predicted by global stability theory. Preliminary results however suggest that optimal perturabtion theory might be a more suitable tool to investigate what would appear to be a by-pass transition to unsteadiness.

- Though the geometry considered here is a model of the geometry of stenotic arteries, assuming the inlet velocity profile to be steady is too much of an idealisation for practical biomedical applications. This problem has already been partially addressed by Sherwin & Blackburn [142] as well as Varghese *et al.* [155]. In the future, extending the present analysis to time-dependant base flows is seriously considered. Such extension would allow one to go one step further in the comprehension of the transition to turbulence taking place in stenotic arteries and might eventually provide valuable insights to bio-mechanical engineers working on this crucial health problem.

Chapter V

Roughness-induced transition

Contents

V.1 Introduction **115**
V.2 Problem formulation **119**
V.3 The Fransson experiment **122**
V.3.1 Base flow 122
V.3.2 Global stability 124
V.4 Parametric investigation **126**
V.4.1 Base flow 127
V.4.2 Global stability 129
V.4.3 Perturbation kinetic energy budget 136
V.4.4 Wavemaker 139
V.5 Non-linear evolution **142**
V.5.1 Varicose global instability 142
V.5.2 Sinuous global instability 144
V.5.3 Comparison with von Doenhoff-Braslow transition diagram 149
V.6 Summary and conclusions **149**

V.1 Introduction

Understanding, predicting and eventually delaying the laminar-turbulent transition in boundary layer flows still is a long time challenge for researchers ever since the pioneering work by Ludwig Prandtl and his two students, Walter Tollmien and Hermann Schlichting. For small amplitude disturbances and supercritical Reynolds numbers, the linear stability theory predicts the slow transition process due to the generation, amplification and secondary instability of Tollmien-Schlichting (TS) waves. It has however been known for quite a long time that this transition process can be greatly modified by environmental noise or by the presence of localised or distributed surface roughness. Depending on the

flow's characteristics and the nature of the surface roughness, the transition process can either be promoted or delayed.

On the one hand, in their experimental work, Klebanoff & Tidstrom [89] have shown that this *natural* transition could be promoted using spanwise invariant roughness elements. This earlier transition is related to the modified stability properties of the boundary layer flow developing downstream the roughness element. More precisely, this transition process is explained by the enhancement of the unstable TS waves due to modifications of the flow's properties in the downstream reversed flow and recovery regions. More recently, Perraud *et al.* [121] have shown that the higher the two-dimensional roughness element, the closer to it does transition to turbulence take place. On the other hand, the influence of fully three-dimensional roughness elements on the transition to turbulence is very different. Indeed, whereas fully three-dimensional roughness elements hardly promote flow separation, they induce streamwise velocity streaks. It has been shown by Cossu & Brandt [46] that these streaks act as stabilising the TS waves and thus delay the natural transition process. This delay of the transition to turbulence by fully three-dimensional roughness elements has been further confirmed experimentally by Fransson *et al.* [65–67], using an array of cylindrical roughness elements. Though promising, this delay technique needs a careful choice of the main parameters of the set up, namely the Reynolds numbers, the shape and spacing of the roughness elements, as well as their height with respect to the thickness of the boundary layer. In fact, the previously mentioned authors have observed that, beyond a given threshold, the velocity streaks induced by the three-dimensional roughness elements can become themselves unstable yielding the flow to transition to turbulence right downstream the roughness elements.

It is known that in the presence of moderate to high environmental noise, free-stream disturbances can penetrate into the boundary layer and trigger by-pass transition. The developing perturbations no longer take the form of TS waves but of velocity streaks which are quasi-optimal disturbances (i.e. with the optimal perturbation being the one inducing the largest transient energy growth in the considered base flow). Because three-dimensional roughness elements also induce velocity streaks in the boundary layer, it is believed that such by-pass transition and fully three-dimensional roughness-induced transition share close connections. The formation process of these high- and low-speed streaks has been explained by Landahl [98] and relies on the lift-up effect. The free-stream disturbances entering the boundary layer give birth to streamwise aligned counter-rotating vortices. Such vortices then transfer high-speed fluid from the outer part of the boundary layer toward the wall and low-speed fluid from the wall toward the outer region of the boundary layer. Due to this transfer of momentum, the resulting perturbation takes the form of high- and low-speed streaks. The dynamics of optimal streaks has been investigated by Andersson *et al.* [13]. These can potentially undergo secondary instability taking the form of a sinuous modulation of the streaks when their amplitude exceeds approximately 26% of the free-stream velocity. Instability with respect to varicose perturbations has also been reported for optimal streaks having an amplitude larger than roughly 37% of the free-stream velocity. However, more recently, Konishi & Asai [90] have shown experimentally that the stability properties of isolated streaks, as the ones induced by a three-dimensional roughness element, are different from the ones of spanwise-periodic, optimal streaks as those considered by Andersson *et al.* [13]. In fact, even if one

can carefully chose the shape and aspect ratio of an isolated roughness element trying to reproduce the wavelength of spanwise-periodic streaks (see Ergin & White [59]), the shape of the induced streaks will be rather different, especially concerning the lateral ones, which would easily fade away in the absence of side vortices able to sustain them.

Concerning the flow past three-dimensional roughness elements and its transition to turbulence, Sedney [140] has reviewed most of the literature available until the early 1970's. The flow pattern induced by an isolated three-dimensional roughness element has been known for almost 60 years (see Gregory & Walker [73]). When impinging the three-dimensional roughness element, the spanwise vorticity of the incoming boundary layer wraps around it thus creating horseshoe vortices. One of the most thorough investigations of the structure of such vortical structures has been carried out by Baker [22], for an isolated cylindrical roughness mounted on a flat plat. As shown by Baker [22], the number of horseshoe vortices wrapped around the roughness element, as well as their main features, are essentially dependent on the aspect ratio of the roughness element considered. However, in all of these cases, such horseshoe vortices give birth further downstream to quasi-aligned streamwise vortices. As already explained, due to the lift-up effect [98], these streamwise aligned vortices can trigger strong transient growth of the boundary layer streaks [85], strong enough to yield their breakdown and subsequent transition to turbulence.

The receptivity of the boundary layer flow to an array of three-dimensional cylindrical roughness elements and the associated transient growth of the velocity streaks have been thoroughly investigated by various authors as Fischer & Choudhari [61], Ergin & White [59], Fransson *et al.* [65, 66], as well as Denissen & White [49, 50]. Their major finding is that the streamwise transient growth of the induced streaks roughly scales with the square of the roughness Reynolds number, $Re_h = U_{Bl}(x_k, h)h/\nu$ (U_{Bl} being the value of the Blasius velocity profile evaluated at the roughness element's position x_k and height h). The crucial importance of the roughness Reynolds number in the roughness-induced transition to turbulence had already been outlined many years earlier. Indeed, as soon as the early 1960's, Tani *et al.* [149] had already observed experimentally that the transition to turbulence in the wake of an aspect ratio $\eta = 1$ cylindrical roughness element is occurring in the vicinity of $Re_h = 600$ almost independently of the other parameters characterising the flow (provided the roughness element is totally immersed within the boundary layer). Almost at the same time, von Doenhoff & Braslow [158] have reviewed most of the experimental results available back then, obtained for roughness elements of different shape, height and spanwise spacings, and compiled them into a transition diagram correlating the roughness element's aspect ratio to the roughness Reynolds number beyond which the induced flow would transition to turbulence. The von Doenhoff & Braslow's diagram [158] shows clearly that the fundamental parameters for predicting transition to turbulence past a roughness element are its aspect ratio and its height with respect to the Blasius boundary layer profile. In particular, the height of the roughness element appears to be fundamental for the development of streamwise streaks of finite amplitude and length. The crucial role of streaks in the onset of transition has been highlighted by Vermeersch [157] and Arnal *et al.* [15], who have developed a model grounded on optimal perturbation theory for determining transition to turbulence past roughness elements of any shape. In particular, they have conjectured that transition occurs when the ratio of

the shear stress generated by optimal streaks, with respect to the viscous stress, reaches a given critical value. Though promising, their approach relies on the strong assumption of quasi-parallelism of the flow induced by the three-dimensional roughness element, regardless of the separation zones which can be induced in the near-wake for large/high enough roughness elements. The same authors have also shown that arrays of smooth roughness elements share similar features with sharp-edged ones, both concerning stabilization of TS waves and transition to turbulence.

The receptivity of a boundary-layer flow to an array of bumps has been investigated by Tumin & Reshotko [154]. Similarly to what observed for cylindrical roughness elements, they found that behind each bump a pair of counterrotating vortices is generated, creating relatively high- and low-speed streaks in the wake downstream from the bump. An investigation of the local stability of streamwise streaks developing past a smooth, large, isolated roughness element has been carried out by Piot *et al.* [122]. Assuming that the flow past the smooth roughness element evolves slowly in the streamwise direction, they have studied its local stability at each streamwise location just behind the roughness element, assessing the stabilizing effect of such a *pre-streaky* flow on the growth of TS waves. The same configuration has been studied very recently by Cherubini *et al.* [41] from a global point of view. To investigate bypass transition in the presence of a large isolated bump, these authors have searched the optimal perturbation inducing the largest growth of disturbances over the fully three-dimensional flow field surrounding this smooth roughness element. In this three-dimensional framework, the optimal perturbation takes the form of a wavepacket-like structure initially localised in the vicinity of the separation line on the top of the roughness element and will eventually travel along the central low-speed streak induced by the roughness element. Interestingly enough, at small target times, this optimal perturbation exhibits a varicose symmetry, whereas at larger target times it exhibits a sinuous structure. It is worthy to note that for the geometry they have investigated, the varicose optimal perturbation is the most efficient to trigger localised transition and induces hairpin vortices once non-linearities are taken into account. However, due to the linearly stable nature of the flow considered, the unsteadiness observed is not self-sustaining once these linear transients have been washed out from the computational domain. In the mean time, de Tullio *et al.* [48] have investigated the roughness-induced transition in the case of a compressible boundary layer flow using the joint application of local stability analysis, parabolised stability equations and direct numerical simulations. These authors have shown that the flows they have investigated are much more convectively unstable, be it to varicose or sinuous perturbations, than the classic boundary layer flow. Moreover, for the sharp-edged rectangular roughness element they considered, the varicose perturbations exhibit larger temporal and spatial growth rates than their sinuous counterparts.

Though they provide valuable insights into the linear dynamics of the flow, stability analyses as performed by Piot *et al.* [122] (for bumps), de Tullio *et al.* [48] (for rectangular roughness elements), and Denissen & White [51] (for cylinders), rely on the strong assumption of a nearly parallel flow. However, the flow past three-dimensional roughness elements exhibits some reversed flow regions where such parallel assumption can not hold. As a consequence, for such class of flows, stability analyses relying on a parallel flow hypothesis totally discard the influence of the region in the vicinity of the roughness element

on the stability properties of the overall flow field which, as seen by Fransson *et al.* [66], appears to be the region triggering the unsteadiness. To circumvent this major drawback and to fully capture the instability mechanisms, one then has to turn to a fully three-dimensional global stability framework for which no such parallel assumption is required. Since the number of degrees of freedom involved in such formulation of the stability problem is extremely large, fully three-dimensional global stability analysis still is nowadays a heavy computational task. Hopefully, with the increase of computational ressources over the past decade and the recent popularisation of new eigenvalues algorithms [20, 57], investigation of the linear stability of flows with three inhomogeneous directions has become feasible. Recently, on the case of a jet in cross flow, Bagheri *et al.* [21] and Ilak *et al.* [82] have shown that fully three-dimensional global stability analysis is able to provide a better understanding of the underlying instability mechanisms. To our knowledge, no such global stability analysis has ever been attempted on the flow past a three-dimensional roughness element. The aim of the present work is to provide new insights on the roughness-induced transition using these new developments in the global stability theory. Indeed, it is believed that fully three-dimensional global stability analysis can help us addressing several questions among which:

(*i*) Can the varicose and sinous instability mechanisms found by local stability analyses, as well as the critical Reynolds number measured in experiments and numerical simulations, be accurately recovered using a fully three-dimensional global approach?

(*ii*) Can one link the roughness-induced transition to a global instability of the flow and not only to transient growth and associated convectively unstable perturbations as widely accepted until now?

(*iii*) Is it possible to predict the flow's non-linear patterns and dynamics using pieces of information stemming from linear analyses only?

The case of a cylindrical roughness element immersed within a laminar boundary layer flow developing along a flat plate is investigated. The present paper is structured as follows: first, in section V.2 the problem under consideration and the numerical methods used are presented. In section V.3, the experimental case investigated by Fransson *et al.* [66] is numerically reproduced and its global instability is investigated. In section V.4, a parametric investigation is carried out, highlighting two instability mechanisms, a sinuous and a varicose one, arising for roughness elements of different aspect ratio. Finally, in section V.5, direct numerical simulations revealing the non-linear evolution of these instabilities as well as the criticality of the bifurcation associated with the sinuous one are presented. Finally, in section V.6 concluding remarks are provided.

V.2 Problem formulation

The dynamics of a three-dimensional incompressible flow is described by the incompressible Navier-Stokes equations:

$$\begin{cases} \dfrac{\partial \mathbf{U}}{\partial t} + (\mathbf{U}\cdot\nabla)\mathbf{U} = -\nabla P + \dfrac{1}{Re}\Delta\mathbf{U} \\ \nabla\cdot\mathbf{U} = 0 \end{cases} \tag{V.1}$$

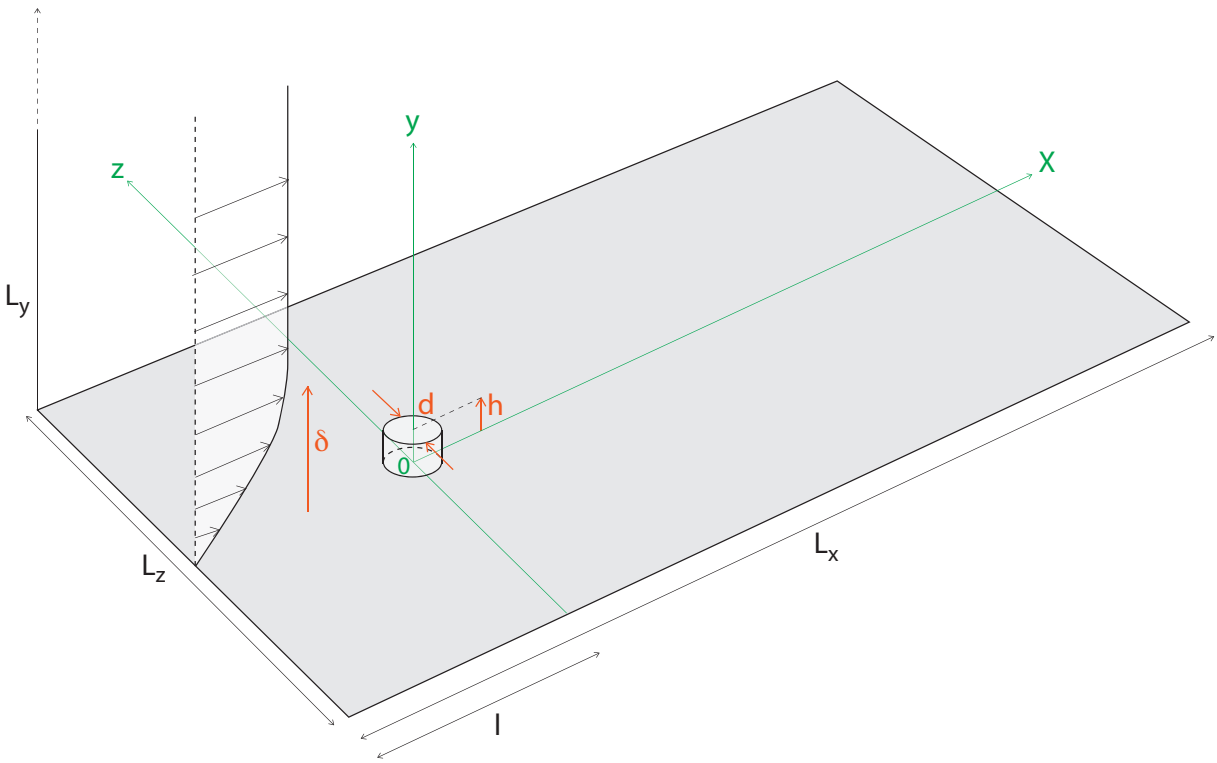

Figure V.1: Sketch of the computational domain under consideration. The parameters defining the geometry take the following values: $h = 1$, $l = 15$ and $(L_x, L_y) = (105, 50)$. Only the roughness element's diameter d will be varied and the spanwise dimension of the domain L_z.

where $\mathbf{U} = (U, V, W)^T$ is the velocity vector and P the pressure term. Dimensionless variables are defined with respect to the height h of the cylindrical roughness element and the free-stream velocity U_∞. Therefore, the Reynolds number is defined as $Re = U_\infty h/\nu$, with ν being the kinematic viscosity. Concerning the coordinate system, x, y and z are defined as the streamwise, wall-normal and spanwise directions, respectively, with x having its origin at the leading edge of the flat plate. However, since the domains used in this work do not include the leading edge of the flat plate, it is convenient to define a shifted streamwise axis $X = x - x_k$, having its origin in the location x_k of the roughness element along the flat plate. A sketch of the computational domain considered is depicted on figure V.1, along with this roughness-centered coordinate system. The cylindrical roughness element, having diameter d and height h, is thus centred in $(X, z) = (0, 0)$. The computational box has a streamwise extent $L_X = 105$ $(-15 \leq X \leq 90)$, a wall-normal extension of $L_y = 50$, whereas the spanwise extent L_z will be varied in the different computations as specified in the next sections. In particular, in most of the computations, the spanwise domain length is chosen in order to make sure the roughness element behaves as being isolated [158], by scaling it with respect to the aspect ratio of the roughness element, $\eta = d/h$.

The following boundary conditions have been applied:

- at the inlet ($X_{in} = -15$), a Dirichlet boundary condition is imposed on the velocity.
- at the outlet ($X_{out} = 90$), a Neumann boundary condition is imposed on the velocity $\nabla \mathbf{U} \cdot \mathbf{x} = 0$;
- on the spanwise end planes ($z_{side} = \pm L_z/2$), periodic boundary conditions are imposed for the three components of the velocity vector;
- at the upper boundary ($y_{top} = 50$), the following conditions are applied: $U = 1$ and $\partial V/\partial y = \partial W/\partial y = 0$;
- finally, a no-slip boundary condition is imposed on the flat plate and the walls of the roughness element.

Regarding the inflow boundary condition for the base flows, since the computational domain does not include the leading edge of the flat plate, a Blasius velocity profile is imposed at inlet points. The imposed profile is chosen by requiring that the theoretical Blasius boundary layer displacement thickness, δ^*, that the flow would have at $(X, z) = (0, 0)$ in the absence of the roughness element, has a prescribed value with respect to the roughness height. The prescribed values of δ^*, as well as the associated values of the displacement thickness Reynolds number, $Re_{\delta^*} = U_\infty \delta^*/\nu$, will be given in the next sections, allowing a comparison with the configurations used in previous studies. Note that two other domains extending down to $X_{out} = 30$ and $X_{out} = 60$ in the streamwise direction have been considered, whereas the inlet of the domain has been kept at a streamwise distance $l = 15$ upstream the center of the roughness element (see figure V.1). However, in order to present results independent of the domain size, only the longest domain (i.e. $X_{out} = 90$) will be considered in the present work, as discussed in detail in Appendix B providing a numerical convergence analysis.

	Case 1	Case 2	Case 3	Case 4
$\delta^*(x_k)$	0.6026	0.5547	0.5425	0.5310
Re_{δ^*}	281	305	312	319
Re	466	550	575	600
Stability	Stable	Stable	Unstable	Unstable

Table V.1: Summary of the different cases considered in Section V.3. For all of them, the roughness elements are located at a distance $x_k = 57.14$ from the leading edge, separated by $L_z = 10$ and have an aspect ratio $\eta = 3$.

Calculations have been performed using the code Nek5000 developed at Argonne National Laboratory by Fischer *et al.* [63]. Spatial discretisation is done by a Legendre spectral elements method with polynomials of order 12. Depending on the aspect ratio considered, the number of spectral elements in the mesh ranges from 10 000 for $\eta = 1$ up to 18 800 for $\eta = 3$. The convective terms are advanced in time using an extrapolation of order 3, whereas for viscous terms a backward differentiation of order 3 is used, resulting in the time-advancement scheme labelled BDF3/EXT3.

V.3 The Fransson experiment

Following the theoretical work by Cossu & Brandt [46], Fransson *et al.* [65–67] have conducted a series of experiments demonstrating the ability for finite amplitude streaks to stabilise the Tollmien-Schlichting waves and thus delay the natural transition of the boundary layer flow. With this aim, they have placed an array of roughness elements, having an aspect ratio $\eta = 3$, located at $x_k = 57.14$ from the leading edge of a flat plate and separated one from another by a spanwise distance $L_z = 10$ [66]. Despite the stabilising effect of the streaks on the TS waves, transition was however observed to take place right downstream the roughness elements beyond a critical Reynolds number. In this section, the case described by Fransson *et al.* [66] is reproduced numerically, in order to ascertain that fully three-dimensional global instability analysis is able to predict with reasonable accuracy the critical Reynolds number experimentally obtained by the previously mentioned authors. The prescribed Reynolds numbers as well as the displacement thickness $\delta^*(x_k)$ are given in table V.1.

V.3.1 Base flow

Figure V.2 depicts the base flow obtained for $(Re, Re_{\delta_*}, \eta) = (466, 281, 3)$, i.e. the same setup as the reference one in [66]. It exhibits the two major features of all the steady solutions that have been investigated within the present work: an upstream and a downstream reversed flow region (visualised by the $U_b = 0$ isosurface in the top frame), as well as a system of multiple vortices stemming from the upstream recirculation zone, wrapping around the roughness element and eventually getting almost aligned with the streamwise direction of the flow as shown by the streamlines. The topology of this upstream vortical system has been investigated experimentally by Baker [22] and exhibits between one and three counter-rotating vortex pairs. According to Baker [22], the particular vortical

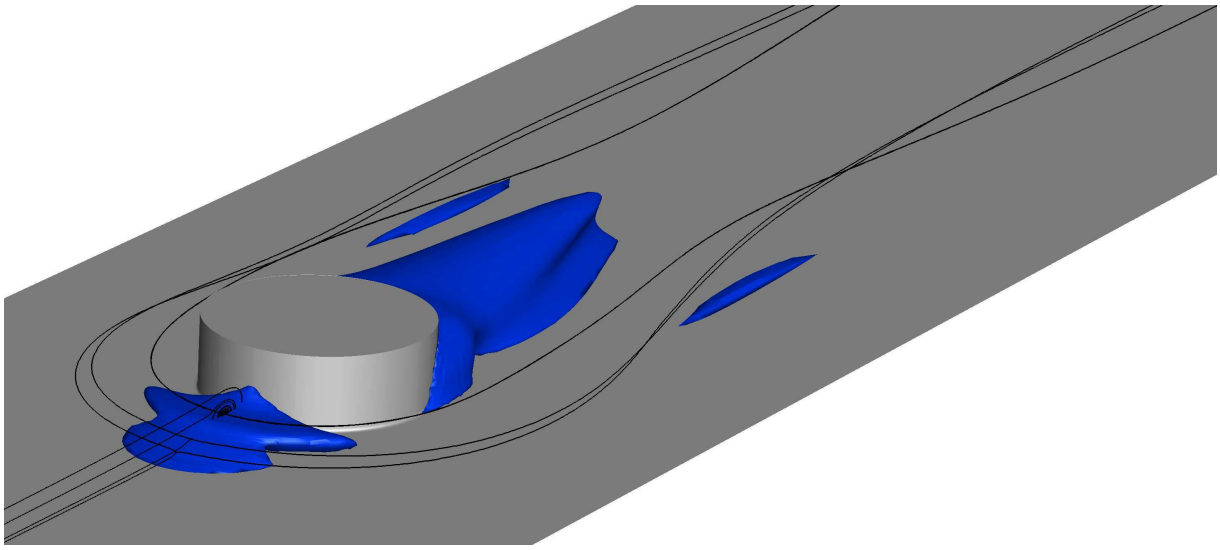

(a)

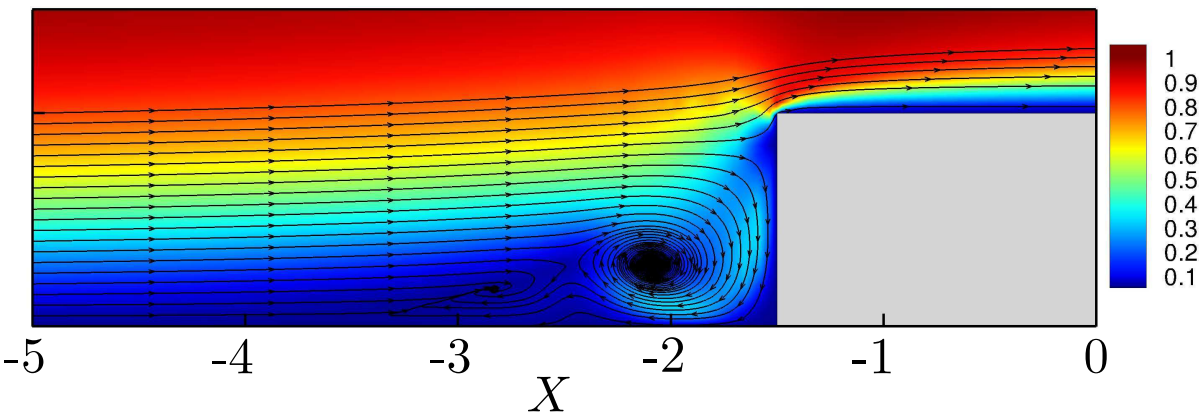

(b)

Figure V.2: Computed base flow for $(Re, Re_{\delta_*}, \eta) = (466, 281, 3)$. (a) Visualisation of the vortical system using streamlines and isosurfaces of the upstream and downstream reversed flow regions (visualised by the $U_b = 0$ isosurface). (b) Close-up of the upstream vortical system highlighted by streamlines in the symmetry plane coloured with the velocity magnitude.

topology chosen by the flow essentially depends on the Reynolds number and on the ratio of the roughness element's diameter d over the boundary layer displacement thickness δ^*. This vortical system can be seen on figure V.2(b) depicting streamlines in the symmetry plane. The impact of this vortical system on the boundary layer flow is as follows:

(i) Upstream the roughness element, all of the vorticity is in the spanwise direction.

(ii) When the flow encounters the roughness element, the upstream spanwise vorticity rolls up, forming the vortical system observed in figure V.2(b).

(iii) It then wraps around the roughness element and is transferred into streamwise vorticity further downstream thus creating the legs of the horseshoe vortices.

The legs of these horseshoe vortices being streamwise-aligned vortices, high speed fluid is transported from the outer region of the boundary layer toward the wall, whereas low speed fluid is transported away from the wall toward the outer region of the boundary layer. This transport of momentum, known as the lift-up effect, thus gives birth to streamwise streaks [98].

Figure V.3 depicts the spatial distribution of the central low-speed region and outer streaks induced by the array of roughness elements at various streamwise stations. These streaks have been identified using the deviation of the base flow streamwise component from the corresponding Blasius boundary layer flow (U_{Bl}), as used by Fischer & Choudhari [61], i.e. $\bar{u} = U_b - U_{Bl}$. As depicted on figure V.3(a), the roughness element generates: a central low-speed region created by the streamwise velocity deficit induced by the roughness element and a pair of high- and low-speed streaks on each side induced by the legs of the primary horseshoe vortex. On the one hand, the central low-speed region appears to fade away relatively rapidely in the streamwise direction, while on the other hand the outer pairs of streaks appear to sustain over quite a long distance. This can be better visualised on figures V.3(b) to (e) depicting contours of the streamwise velocity deviation in various $X = constant$ planes. It indeed appears clearly from these figures that, while the central low-speed region has almost disappeared as soon as $X = 60$, the amplitude of the outer low- and high-speed streaks varies very little. Such behavior has already been observed experimentally by Fransson *et al.* [65] (see figure 2 of the cited paper).

V.3.2 Global stability

In order to investigate the early transition observed in the experiment [66], global stability analyses of various base flows are conducted. All of the cases considered are reported in table V.1. Figure V.4 depicts the spectra of eigenvalues for $Re = 550$ ($Re_{\delta^*} = 305$) and $Re = 575$ ($Re_{\delta^*} = 319$). It is clear from these eigenspectra that the flow experiences a Hopf bifurcation for $550 < Re_c < 575$ due to an isolated pair of complex conjugate eigenvalues of the linearised Navier-Stokes operator moving into the upper-half complex plane. A linear interpolation provides a critical Reynolds number $Re_c = 564$ ($(Re_{\delta^*})_c = 309$) only 6% larger than the critical Reynolds number experimentally obtained by Fransson *et al.* [66]. This good agreement for the value of the critical Reynolds number strongly suggests that the transition observed in the experiment might be the consequence of a three-dimensional

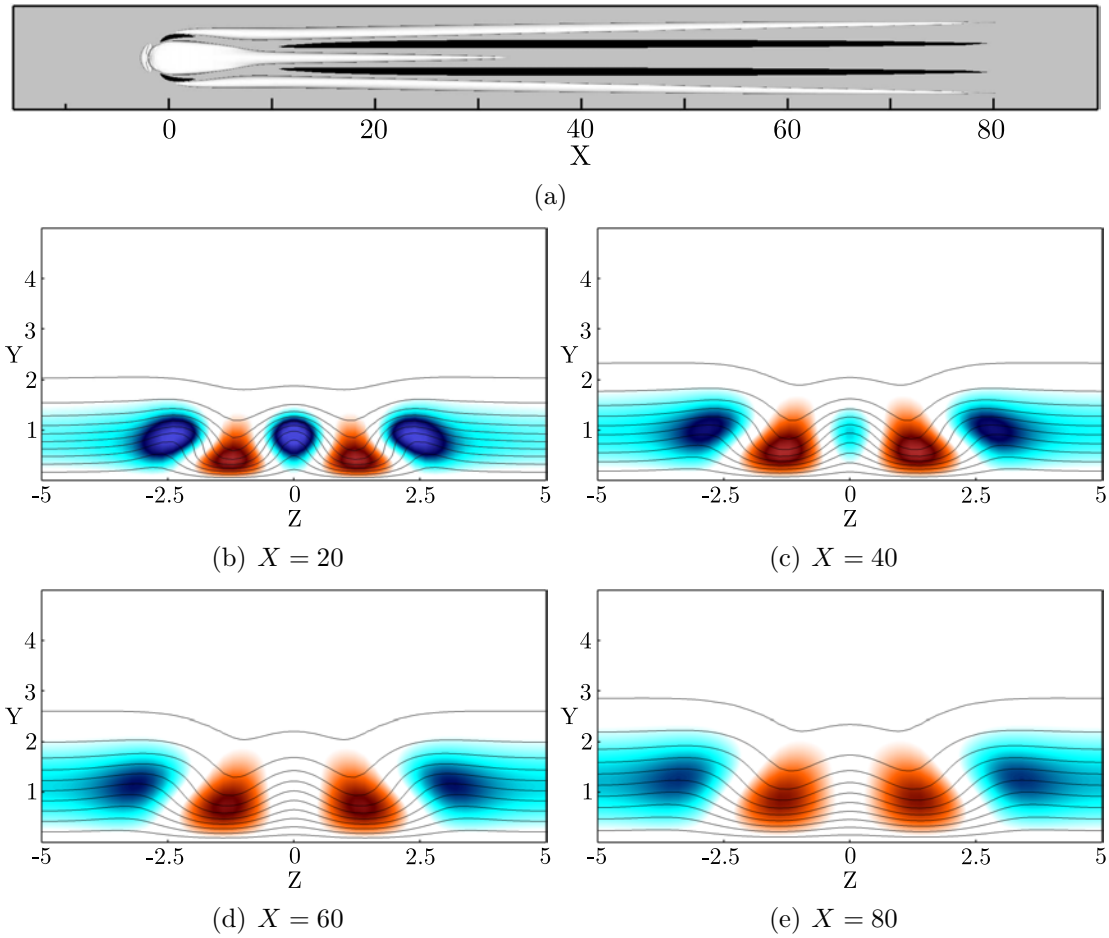

Figure V.3: Streamwise evolution of the streaks induced by the array of roughness elements for $(Re, Re_{\delta^*}) = (466, 281)$: top view of the $\bar{u} = \pm 0.3$ surfaces (black and white), with $\bar{u} = U_b - U_{Bl}$ being the deviation of the base flow from the Blasius boundary layer flow (a); slices extracted at $X = 20$ (b), $X = 40$ (c), $X = 60$ (d), and $X = 80$ (e). The shaded contours range from $\bar{u} = 0.3$ (red) to $\bar{u} = -0.3$ (blue), whereas the solid lines depict the base flows streamwise velocity isocontours from $U_b = 0.1$ to 0.99.

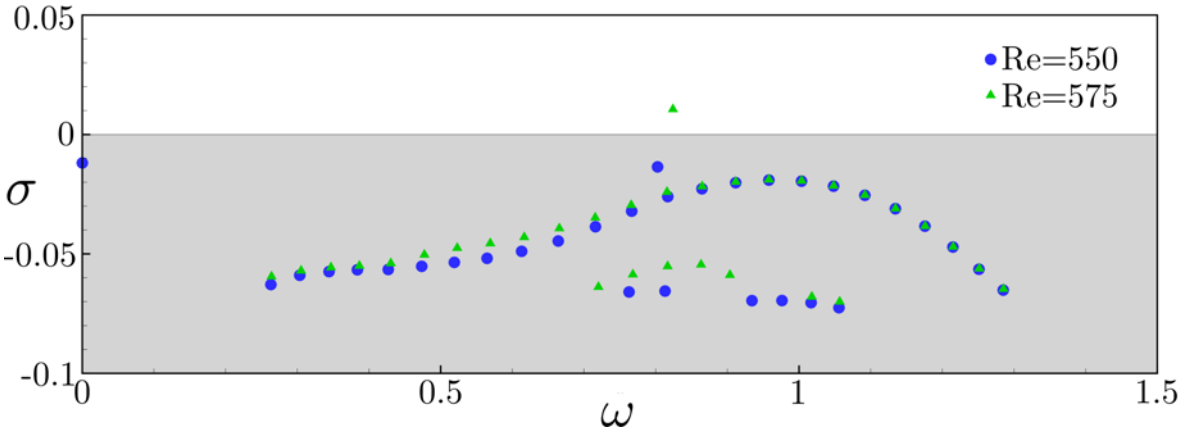

Figure V.4: Eigenspectra of the linearised Navier-Stokes operator. Blue dots show the eigenvalues for $(Re, Re_{\delta^*}) = (550, 305)$, whereas green triangles show the ones for $(Re, Re_{\delta^*}) = (575, 312)$.

global instability of the flow. Comparison of the dominant frequency in the flow dynamics however turned out to be unconclusive essentially because the frequency reported by Fransson *et al.* [66] has been measured far beyond the end of the computational domain considered herein ($X \simeq 175$ compared to $X_{out} = 90$).

The shape of the associated unstable global mode is depicted on figure V.5. As one can see on figure V.5(a), this mode takes the form of streamwise alternated patches of positive and negative velocity exhibiting a varicose symmetry with respect to the spanwise mid-plane. To get a better insight of the structure of the mode and of its location with respect to the base flow's features, figure V.5 provides slices of its spatial support in the $X = 23$ (b) and the $X = 40$ (c) plane. The mode is identified using its streamwise velocity contours (shaded) whereas the solid black lines depict the baseflow U_b isocontours. These figures make it clear that, though the mode is initially located along the central low-speed region, it then contaminates almost the whole spanwise extent of the domain before fading away for $X > 60$. Moreover, for all of the streamwise planes considered, the maximum of the mode is located along the shear layers delimiting the central low-speed region and the streaks.

V.4 Parametric investigation

In order to get a better understanding of the physical mechanisms underlying the roughness-induced transition, a parametric investigation is conducted. As to avoid the potential interaction between roughness elements, the spanwise extent of the computational domain has been changed from $L_z = 10$ to $L_z = 8\eta$ (with η being the aspect ratio of the roughness element considered) such that they behave as being isolated no matter the aspect ratio considered. Moreover, for the sake of clarity, the theoretical displacement thickness of the incoming Blasius boundary layer at the position of the roughness element is kept equal to $\delta^*(x_k) = 0.6883$ (the boundary layer thickness being fixed at $\delta_{99}(x_k) = 2$) throughout this investigation. This allows to isolate the influence of changes in the Reynolds number

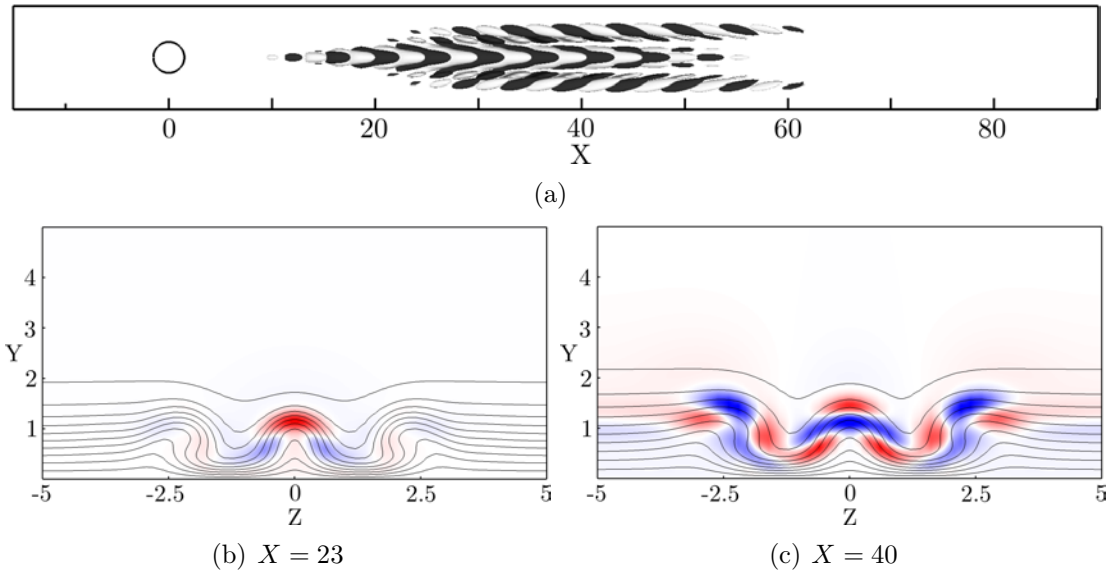

Figure V.5: Visualisation of the streamwise velocity component of the leading unstable global mode at $(Re, Re_{\delta^*}) = (575, 312)$. (a) Top view of isosurfaces depicting $\pm 10\%$ of the mode's maximum streamwise velocity. Slices in the (b) $X = 23$ plane (i.e., where the mode achieve its maximum amplitude) and in the (c) $X = 40$ plane. Both figures (b) and (c) have been normalised by the local maximum velocity. The solid lines depict the base flows streamwise velocity isocontours from $U_b = 0.1$ to 0.99.

η	1-3	1-3	1-3	1-2	1-2	1	1
Re	600	700	800	900	1000	1100	1250
x_k	96	112	128	144	160	176	200
Re_{δ^*}	413	482	551	620	688	757	860

Table V.2: Location x_k of the roughness element along the flat plate such that $\delta^*(x_k) = 0.6883$ and the associated Reynolds numbers Re, Re_{δ^*} for most of the different cases considered in Section V.4's parametric investigation.

only and not a mixed combination of changes in the Reynolds number and displacement thickness at the same time. Finally, the aspect ratio η of the roughness elements considered will be varied from $\eta = 0.85$ up to $\eta = 3$, while the Reynolds number ranges from $Re = 600$ up to $Re = 1250$. Table V.2 summarises most of the different cases treated during this parametric investigation.

V.4.1 Base flow

V.4.1.1 Influence of the Reynolds number

The influence of the Reynolds number Re on the base flow can be assessed from figures V.6 and V.7. Figures V.6 (a) and (b) provide slices of the streamwise velocity component of the base flow in the symmetry plane for $(Re, \eta) = (600, 1)$ and $(Re, \eta) = (1250, 1)$, respectively. It can be seen that when increasing the Reynolds number, the shape of the reversed flow regions remains almost unchanged. The main impact on the flow of an

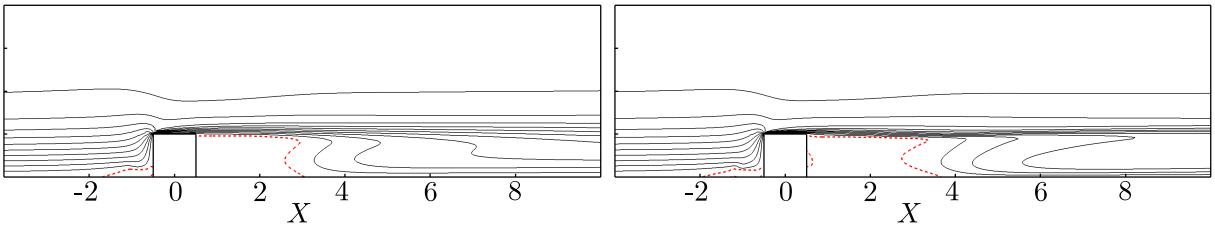

(a) $(Re, \eta) = (600, 1)$ (b) $(Re, \eta) = (1250, 1)$

Figure V.6: Slices in the symmetry plane of different base flows. The dashed red line depicts the spatial extent of the reversed flow regions, whereas the thin solid black lines are the streamwise velocity contours ranging from 0.1 up to 0.99.

increase of the Reynolds number, and hence a decrease of the effect of viscosity, is however to strengthen the gradients as can be assessed from the stronger deformation of the iso-contours in figure V.6(b). Increasing the Reynolds number has also an effect on the streaks induced by the vortical system identified previously. As can be seen on figure V.7(a) in the lower Reynolds number case, the central low-speed streak induced by the roughness element's blockage is fading away quite rapidly in the streamwise direction and one can even observe a merging of the two outer high-speed streaks resulting in only three streaks near the outflow: a central high-speed streak flanked with two low-speed ones. The merging of the high-speed streaks and the resulting pattern near the outflow can be better observed by visualizing the streamwise velocity contours on different $X = constant$ planes, as provided in figure V.8 (a). A very similar behaviour has already been observed experimentally by Fransson *et al.* [65] in a highly subcritical configuration. On the other hand, in the higher Reynolds number case shown in figures V.7(b) and V.8(b), the decrease of the viscosity's effect allows the central low-speed region to sustain over a much longer streamwise extent and prevents, at least in the computational domain considered, the merging of the two high-speed streaks.

In both cases, the amplitude of the different streaks has been measured from $X = 10$, i.e. sufficiently far from the roughness element such that the strongly non-parallel effects induced by the reversed flow region can be discarded. Though the amplitude of the central low-speed region decays monotically in the streamwise direction for both cases, the initial amplitudes are quite different: $\min_{y,z}(\bar{u}) = -0.21$ for $Re = 600$ and $\min_{y,z}(\bar{u}) = -0.47$ for $Re = 1250$ at the streamwise position $X = 10$. On the other hand, the amplitude of the outer streaks varies between ± 0.14 for $Re = 600$ and roughly ± 0.3 for $Re = 1250$. From the work of Andersson *et al.* [13], it would thus appear that the $Re = 600$ case is stable while the $Re = 1250$ case might be prone to streaks instability.

V.4.1.2 Influence of the aspect ratio

Figures V.9 (a) and (b) provide slices of the steady solutions streamwise component in the spanwise mid-plane obtained for the same Reynolds number and two different aspect ratios, namely $(Re, \eta) = (600, 2)$ and $(Re, \eta) = (600, 3)$, respectively. As one could have expected, due to the larger blockage induced by the roughness element, the reversed flow regions (depicted by the dashed red line) in the case of the $\eta = 3$ roughness element have

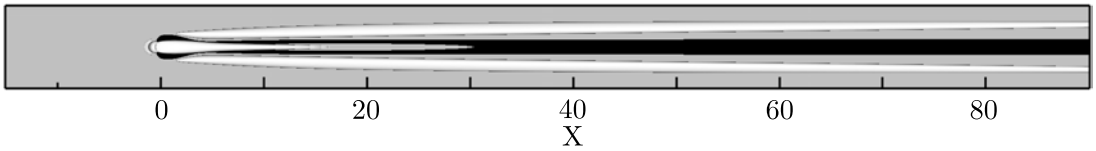

(a) $(Re, \eta) = (600, 1)$, $\bar{u} = \pm 0.075$

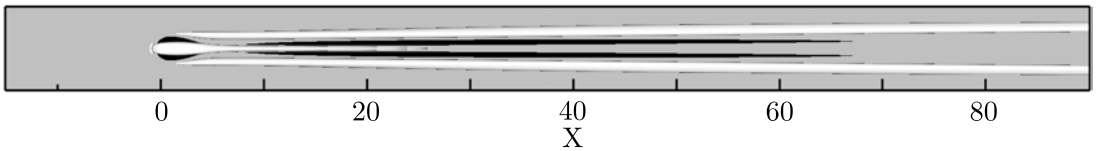

(b) $(Re, \eta) = (1250, 1)$, $\bar{u} = \pm 0.2$

Figure V.7: Top view of the streaks induced by the roughness elements. Low-speed (white) and high-speed streaks (black) are depicted using isosurfaces of the streamwise velocity deviation of the baseflows from the theoretical Blasius boundary layer flow, $\bar{u} = U_b - U_{Bl}$.

a longer upstream and downstream extent than for the roughness elements of aspect ratio $\eta = 1$ and 2 (compare with figure V.6(a) as well). Moreover, increasing the roughness element's aspect ratio also slightly strengthens the gradients of the base flows. It is as well worth noting that increasing the spanwise blockage given by the cylinder, more and more upstream spanwise vorticity has to wrap around the roughness element, influencing the strength of the vortical system identified previously and, hence, the amplitude of the induced low- and high-speed streaks further downstream. These can be visualised on figure V.10 where the deviation from the theoretical Blasius boundary layer of the steady equilibrium solutions for $(Re, \eta) = (600, 2)$ and $(Re, \eta) = (600, 3)$ are shown. Though for the present flows no merging of the high-speed streaks is observed, increasing the aspect ratio of the roughness element allows once again the central low-speed region to sustain on a longer streamwise extent indicating that the amplitude of the streaks is stronger.

As previously, the amplitude of the different streaks have been measured from $X = 10$ such that one can almost neglect the strongly non-parallel influence of the roughness element. While the central low-speed region has an amplitude of -0.4 at $X = 10$ for the $\eta = 2$ roughness element, its amplitude is -0.54 for the $\eta = 3$ case. However, the amplitude of the outer streaks roughly varies between $\bar{u} = \pm 0.27$, for $\eta = 2$, and $\bar{u} = \pm 0.4$, for $\eta = 3$. Once again, from the work of Andersson *et al.* [13], it would thus appear that both cases might be prone to streaks local instabilities.

V.4.2 Global stability

Figure V.12 depicts the eigenspectra obtained for three of the cases considered here. For all of them, the flow experiences a Hopf bifurcation due to an isolated complex conjugate pair of eigenvalues moving toward the upper-half complex plane. These isolated modes show a different type of structure depending on the aspect ratio considered. In particular, a sinuous global mode is observed for $\eta = 0.85$ and $\eta = 1$ (see the green dot in figure V.12 (a)), whereas a varicose mode is obtained for $\eta = 2$ and $\eta = 3$ (see figures V.12 (b-c)).

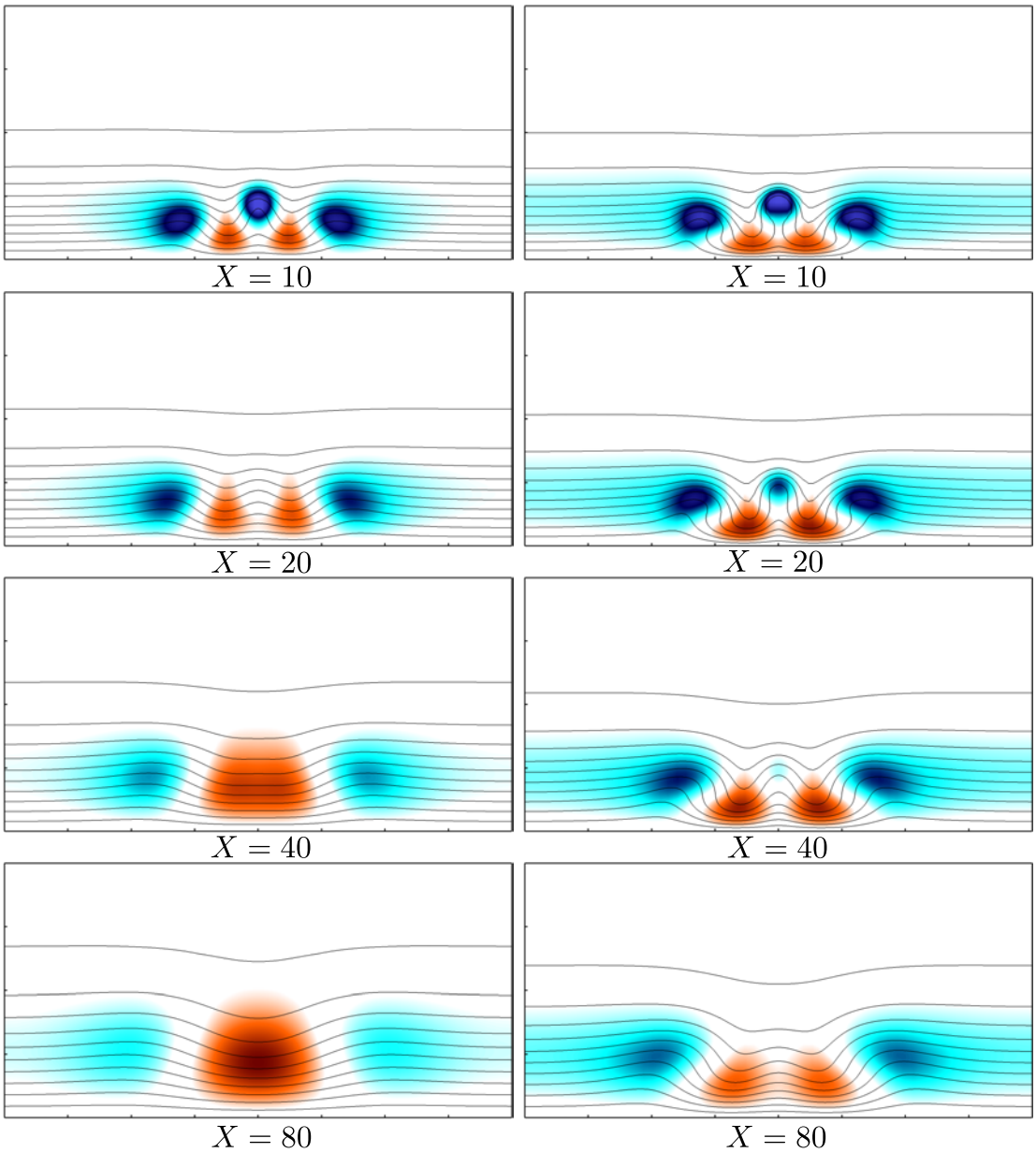

(a) $(Re, \eta) = (600, 1)$ (b) $(Re, \eta) = (1250, 1)$

Figure V.8: Visualisation of the streaks pattern in several different streamwise planes. On figure (a), the color table ranges from $\bar{u} = -0.2$ (blue) to $\bar{u} = 0.2$ (red), while it ranges from $\bar{u} = -0.4$ (blue) to $\bar{u} = 0.4$ in figure (b). The solid lines depict the base flows streamwise velocity isocontours from $U_b = 0.1$ to 0.99.

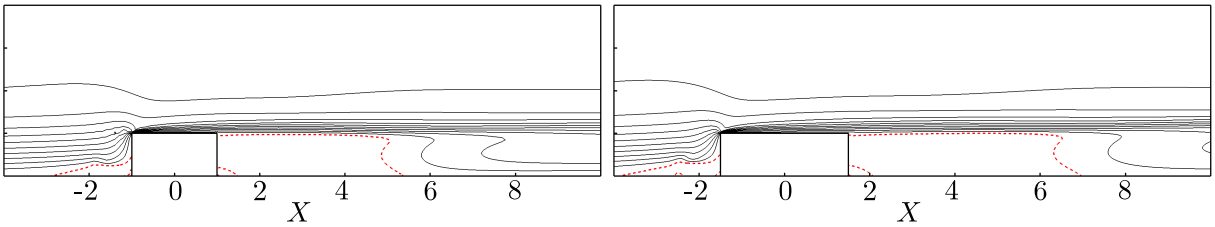

(a) $(Re, \eta) = (600, 2)$ (b) $(Re, \eta) = (600, 3)$

Figure V.9: Slices in the symmetry plane of different base flows. The dashed red line depicts the spatial extent of the reversed flow regions, whereas the thin solid black lines are the streamwise velocity contours ranging from 0.1 up to 0.99.

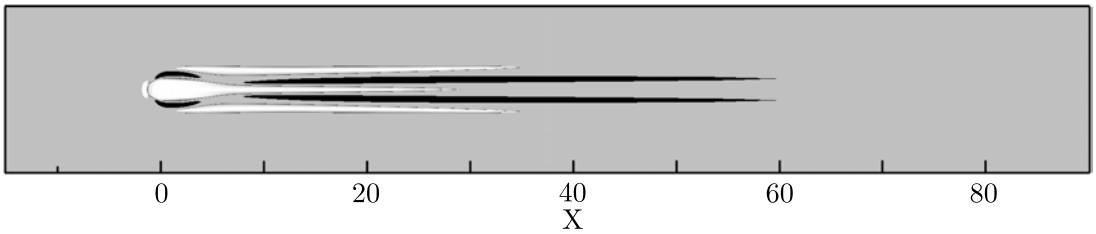

(a) $(Re, \eta) = (600, 2)$, $\bar{u} = \pm 0.2$

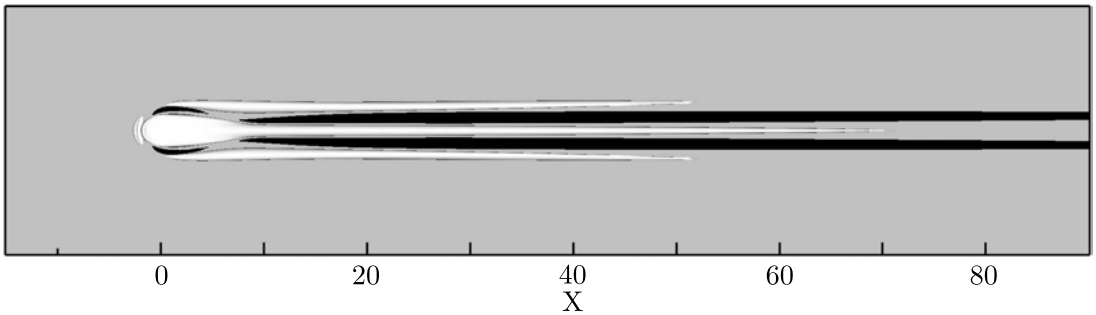

(b) $(Re, \eta) = (600, 3)$, $\bar{u} = \pm 0.2$

Figure V.10: Top view of the streaks induced by the roughness elements. Low-speed (white) and high-speed streaks (black) are depicted using isosurfaces of the streamwise velocity deviation of the baseflows from the theoretical Blasius boundary layer flow, $\bar{u} = U_b - U_{Bl}$.

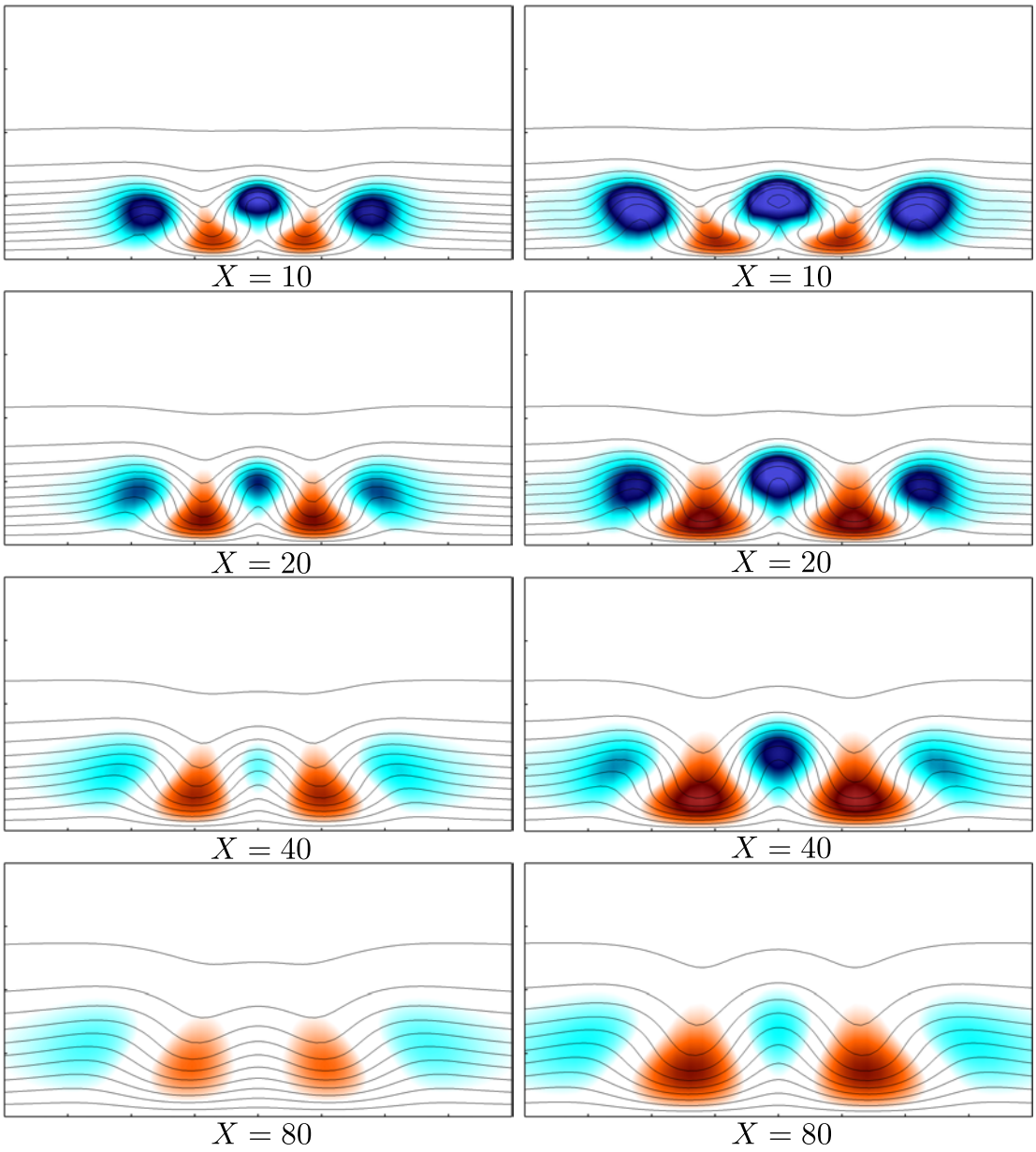

(a) $(Re, \eta) = (600, 2)$ (b) $(Re, \eta) = (600, 3)$

Figure V.11: Visualisation of the streaks pattern in several different streamwise planes. For both columns, the color table ranges from $\bar{u} = -0.4$ (blue) to $\bar{u} = 0.4$ (red). Solid lines depict the base flows streamwise velocity isocontours from $U_b = 0.1$ to 0.99.

Shortly below, all these isolated eigenvalues are followed by a branch of modes exhibiting exclusively a varicose symmetry. For $\eta = 3$ this branch is closer to the isolated mode, so that a second unstable mode can be observed already at $Re = 700$. However, since the frequency and the structure of these two unstable modes are very similar, this does not result in strong changes on the related route to transition. It is worthy to notice that, whereas the isolated eigenvalues do not seem to be to very sensitive to the streamwise extent of the computational domain (provided $X_{out} \geq 60$), the branches of eigenvalues on the other hand appear to be extremely sensitive and tend to move toward the upper-half complex plane as the streamwise length of the domain is reduced. For the longest domain considered (i.e. $X_{out} = 90$), table V.3 provides the critical Reynolds numbers and the symmetry of the associated leading global mode for roughness elements of various aspect ratio η. Figure V.13 depicts the leading unstable mode for each of the aspect ratios considered here, at different Reynolds numbers. Since for all of these modes the streamwise component is at least almost 4 times larger than the other components, only the real part of this component is depicted. As can be seen, all the modes are mostly localised along the central low-speed region, differently from the case of non-isolated cylinder analysed in the previous section for which a large part of the mode migrates on the outer streaks downstream of the roughness element. The crucial importance of such low-speed streaks in the roughness-induced transition process to turbulence has already been underlined by previous studies such as the experimental work by Asai *et al.* [17, 18], or the numerical investigation by Brandt [34] and Denissen & White [51]. More recently, several different authors have observed a similar behaviour in the case of roughness-induced compressible boundary layer flows [23, 29, 48, 83, 148].

It is obvious from table V.3 and figure V.13 that an exchange of symmetry of the leading unstable global mode occurs as the aspect ratio of the roughness element is increased. Indeed, whereas sinuous modes are found to be the dominant instability for thin cylindrical roughness elements ($\eta \leq 1$), the varicose global instability turns out to be the dominant one when roughness elements of larger aspect ratio ($\eta \geq 2$) are considered. This exchange of symmetry of the leading unstable mode beyond a given threshold of the roughness element's aspect ratio had already been underlined experimentally by Sakamoto & Arie [132] and Beaudoin [27]. The former authors have investigated the nature of the vortices shed periodically from prismatic and cylindrical roughness elements immersed within a turbulent boundary layer. For thin roughness elements, they have reported a shedding of von Kármán (sinuous) vortices, whereas they have labelled vortices shed from larger roughness elements as being arch-type vortices exhibiting a varicose symmetry. Though the present setup is different, due to the laminar nature of the incoming boundary layer flow, results from global stability analyses regarding the spatial structure of the dominant eigenmode are in qualitatively good agreement with their experimental observations, as it will shown in more detail in Section V.5 by direct numerical simulations.

V.4.2.1 Analysis of the modes

We will first focus our attention on the sinuous global mode. The spatial structure of this mode has already been shown in figure V.13(a) and (b). As one can see, it consists

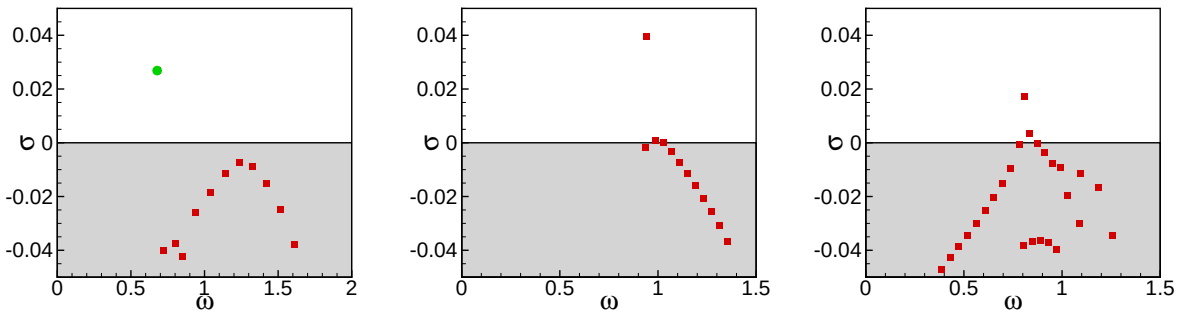

(a) $(Re, \eta) = (1200, 1)$ (b) $(Re, \eta) = (900, 2)$ (c) $(Re, \eta) = (700, 3)$

Figure V.12: Spectrum of eigenvalues for different cases considered in the present work. Red squares denote varicose modes whereas the green dot stands for a sinuous one.

η	0.85	1	2	3	Fransson *et al.* [66]
Re_c	910	1040	805	656	564
Re_h^c	712	813	630	513	519
Symmetry	S	S	V	V	V

Table V.3: Critical Reynolds number Re_c and symmetry of the associated leading unstable global mode for various aspect ratio η. S stands for a sinuous global mode, and V for a varicose one.

in positive and negative patches of velocity mostly localised along the central low-speed region. Its streamwise and wall-normal components are exhibiting a sinuous symmetry with respect to the spanwise mid-plane, whereas its spanwise component exhibits a varicose symmetry with respect to the same plane (not shown). To get a better insight of the structure of the mode and of its location with respect to the base flow's features, figure V.14(a) provides a slice of it in the $X = 25$ plane for $(Re, \eta) = (1125, 1)$. The mode is identified using its streamwise velocity contours (shaded) whereas the solid black lines depict the baseflow U_b isocontours. The fully three-dimensional shear layer developing around the velocity streaks, here depicted by the red dashed line, is identified using the points of null curvature in the U_b distribution, i.e. $\partial^2 U_b/\partial y^2 + \partial^2 U_b/\partial z^2 = 0$. It can be seen that the regions of maximum amplitude of the mode are located on the flanks of the central low-speed region along its shear layer. Such particular location, where the wall-normal and spanwise gradients of the base flow are relatively strong, let us think that this sinuous global instability is likely to extract the energy for its growth from the transport of these two shears along the central low-speed region, as it will be shown in detail in subsection V.4.3.

The second type of global instability identified from figures V.13 (c), (d) is a varicose global instability. As for its sinuous counterpart, this second family of unstable modes is essentially localised along the central low-speed region and consists in streamwise alternated patches of positive and negative velocity. The major difference is however the symmetry of the mode: its streamwise and wall-normal components now exhibit a varicose symmetry with respect to the spanwise mid-plane, whereas its spanwise component

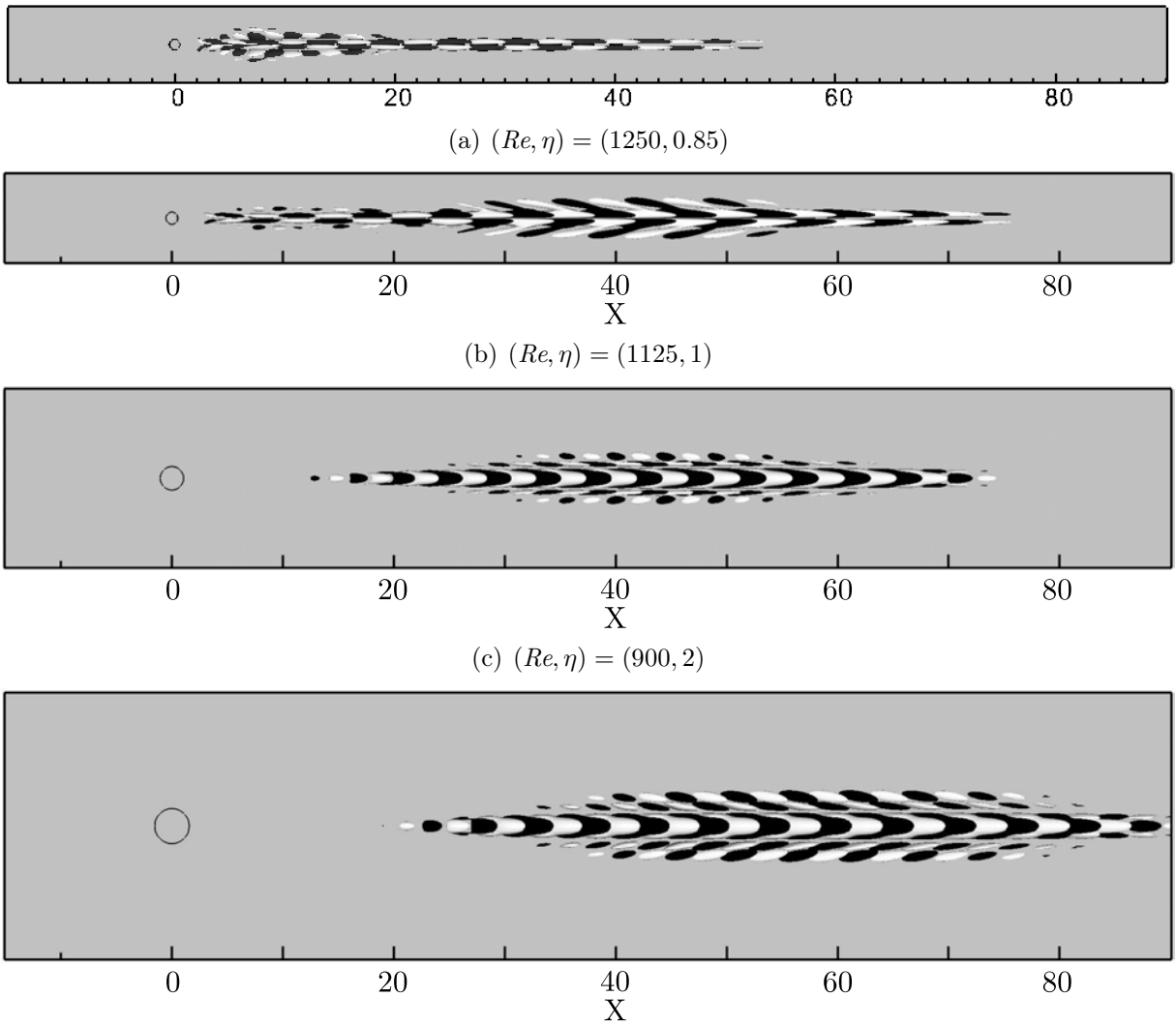

(a) $(Re, \eta) = (1250, 0.85)$

(b) $(Re, \eta) = (1125, 1)$

(c) $(Re, \eta) = (900, 2)$

(d) $(Re, \eta) = (700, 3)$

Figure V.13: Real part of the leading unstable mode streamwise component with increasing roughness element's aspect ratio η from top to bottom, and different Reynolds numbers indicated within the figure. The isosurfaces depict $u = \pm 10\%$ of the maximum amplitude of the modes, whereas open black circles denote the location of the roughness elements.

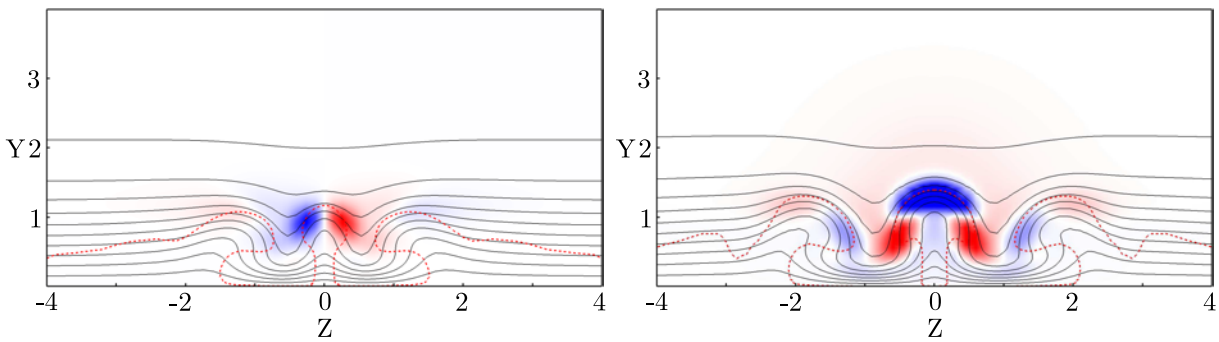

(a) $(Re, \eta) = (1125, 1)$ (b) $(Re, \eta) = (850, 2)$

Figure V.14: Slice of the streamwise component of the sinuous unstable global mode (a) and varicose global mode (b) in the $X = 25$ plane identified by the shaded red and blue contours. Solid lines depict the base flows streamwise velocity isocontours from $U_b = 0.1$ to 0.99, whereas the red dashed line stands for the location of the shear layer identified by the points of null curvature (i.e. $\partial^2 U_b/\partial y^2 + \partial^2 U_b/\partial z^2 = 0$).

exhibits a sinuous symmetry (not shown). As previously, in order to gain a better understanding of the mode structure, a slice of it in the streamwise $X = 25$ plane is depicted on figure V.14(b) for $(Re, \eta) = (850, 2)$. As for its sinuous counterpart, the varicose mode is essentially located along the shear layer delimiting the central low-speed region. It is worthy to note however that, for the set of parameters considered here, small non-zero patches of velocity are visible on the shear layers of the lateral low-speed streaks as well. Once again, such location of the mode let us conjecture that it essentially extracts the energy necessary for its growth from the transport of the base flow streamwise component shears along the whole shear layer. One must also be aware that all of the modes belonging to the branches of eigenvalues observed in the spectra depicted on figure V.12 share common features with this particular varicose mode.

It is worthy to note finally that, relatively far from the roughness element, the shapes of these global modes visualized in different $X = constant$ planes are very similar to that found by Brandt [34] and more recently by de Tullio *et al.* [48] and Denissen & White [51] using a local stability approach. Indeed, due the strong predominance of the base flow streamwise component and its nearly parallel nature far from the roughness element, it is expected that the two approaches, global and local, give similar results regarding the shape of the modes in the almost parallel parts of the flow. However, the critical Reynolds numbers can be greatly over- or under-predicted when the non-parallel flow regions in the vicinity of the roughness element are not taken into account, as it will be discussed in subsection V.4.4.

V.4.3 Perturbation kinetic energy budget

Aiming to get a better understanding of the mechanisms yielding the flow to become unstable and to understand how and where the sinuous and varicose unstable global modes do extract their energy, the kinetic energy transfer between the base flow and the global modes is investigated. Similar analysis has already been conducted in a local

framework by Brandt [34]. Calculating this kinetic energy transfer has proven to be very helpful in order to get a better insight of the instability mechanisms. The kinetic energy rate of change is given by the Reynolds-Orr equation:

$$\frac{\partial E}{\partial t} = -D + \sum_{i=1}^{9} \int_V I_i \mathrm{d}V \tag{V.2}$$

where the total kinetic energy and the total dissipation in the computational domain's volume V are given by:

$$E = \frac{1}{2} \int_V \mathbf{u} \cdot \mathbf{u} \, \mathrm{d}V, \; D = \frac{1}{Re} \int_V \nabla \mathbf{u} : \nabla \mathbf{u} \, \mathrm{d}V \tag{V.3}$$

and where the integrands I_i which represent the production terms are:

$$\begin{aligned} I_1 &= -u^2 \frac{\partial U_b}{\partial x}, \; I_2 = -uv \frac{\partial U_b}{\partial y}, \; I_3 = -uw \frac{\partial U_b}{\partial z} \\ I_4 &= -uv \frac{\partial V_b}{\partial x}, \; I_5 = -v^2 \frac{\partial V_b}{\partial y}, \; I_6 = -vw \frac{\partial V_b}{\partial z} \\ I_7 &= -wu \frac{\partial W_b}{\partial x}, \; I_8 = -wv \frac{\partial W_b}{\partial y}, \; I_9 = -w^2 \frac{\partial W_b}{\partial z} \end{aligned} \tag{V.4}$$

The sign of the different integrands I_i indicates whether the local transfer of kinetic energy associated to them acts as stabilising (negative) or destabilising (positive). For the sake of comparison, all the kinetic energy budgets presented in this section have been normalised by the dissipation D.

V.4.3.1 Sinuous instability

Figures V.15(a) and (b) provide the integral over the whole computational domain of the production terms I_1 to I_9 along with the diffusion term D for $(Re, \eta) = (1125, 1)$ and $(Re, \eta) = (1250, 1)$, respectively. As one can see, only the base flow streamwise component related shears ($\int_V I_1 \, \mathrm{d}V$, $\int_V I_2 \, \mathrm{d}V$ and $\int_V I_3 \, \mathrm{d}V$) provide a significant contribution to the energy transfer. More particularly, as expected from the analysis of the shape of the mode in the $X = 25$ plane shown in figure V.14(a), this sinuous instability essentially extracts its energy from the work of the Reynolds stresses uv against the wall-normal gradient of the base flow streamwise component $\partial U_b / \partial y$ (I_2), as well as from the work of uw against the spanwise gradient $\partial U_b / \partial z$ (I_3) no matter the Reynolds number considered. Figures V.15(c) and (d) provide the streamwise evolution of $\int_{y,z} I_2 \, \mathrm{d}y\mathrm{d}z$ (red dashed line) and $\int_{y,z} I_3 \, \mathrm{d}y\mathrm{d}z$ (blue solid line) for the two Reynolds numbers considered. As one can see, in both cases, a large peak in the streamwise evolution of the spanwise production term occurs in the vicinity of the downstream reversed flow region. The major impact of an increase of the Reynolds number beyond its critical value is to greatly amplify the amount of energy extracted from this near-wake region, whereas the energy extraction process further downstream seems to be only slightly influenced. This might indicate that the instability mechanism linked to the sinuous mode finds its origin mostly in the near wake region, as will be further discussed in subsection V.4.4. The spatial distribution of

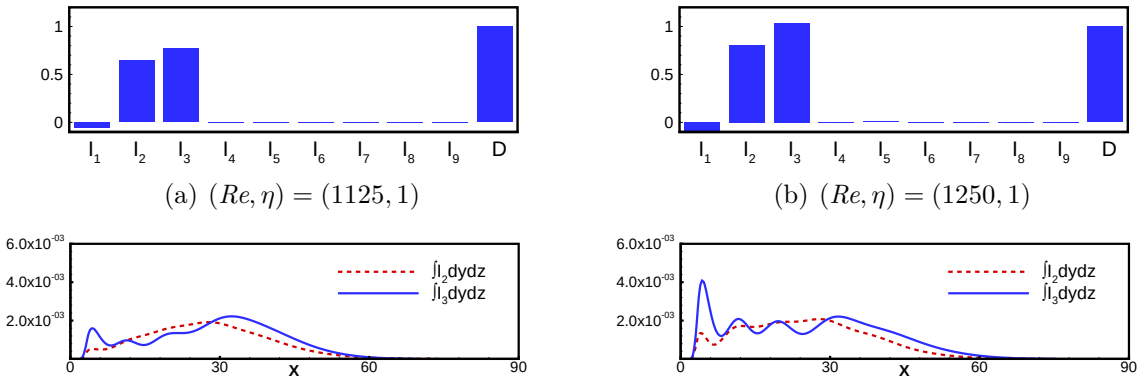

(a) $(Re, \eta) = (1125, 1)$ (b) $(Re, \eta) = (1250, 1)$

(c) $(Re, \eta) = (1125, 1)$ (d) $(Re, \eta) = (1250, 1)$

Figure V.15: Top: Sinuous unstable mode's kinetic energy budget integrated over the whole domain. Bottom: Streamwise evolution of the production terms $\int_{y,z} I_2 \, \mathrm{d}y\mathrm{d}z$ (red dashed line) and $\int_{y,z} I_3 \, \mathrm{d}y\mathrm{d}z$ (blue solid line).

the I_2 and I_3 production terms in the $X = 25$ plane for $(Re, \eta) = (1125, 1)$ are depicted on figures V.16(a) and (b), respectively. As one can see, the sinuous global mode mostly extracts its energy spatially from the lateral parts of the central low-speed region's delimiting shear layer. Moreover, the spatial distribution in the $y = 0.75$ horizontal plane of I_3 is depicted on figures V.16(c). As highlighted by the kinetic energy budget, this production term appears to be very active right downstream the roughness element as well as further downstream along the sides of the central low-speed region.

V.4.3.2 Varicose instability

Results for the varicose instability are summarised in figures V.17(a) and (c) for $(Re, \eta) = (850, 2)$ and figures V.17(b) and (d) for $(Re, \eta) = (1000, 2)$. At $Re = 850$, slightly above the critical Reynolds number, one can see on figure V.17(a) that, though $\int_V I_2 \, \mathrm{d}V$ gives a small non-zero contribution to the energy extraction process, the mode surprisingly extracts most of its energy from the work of uw against the spanwise gradient of the base flow streamwise component $\partial U_b/\partial z$, whereas in a local framework, varicose modes are mostly linked to the transport of the wall-normal gradient. Looking at the streamwise evolution of these two terms depicted on figure V.17(c) helps us to understand this surprising dominance of $\int_V I_3 \, \mathrm{d}V$. Indeed, whereas $\int_{y,z} I_3 \, \mathrm{d}y\mathrm{d}z$ is positive throughout the whole streamwise extent of the domain, one can see that $\int_{y,z} I_2 \, \mathrm{d}y\mathrm{d}z$ actually acts as slightly stabilising in a large portion of the computational domain (from $x \simeq 40$ up to $x \simeq 70$). This can be explained by the features of the associated base flow: while the spanwise gradient remains more or less constant throughout the computational domain, the destabilising effect of the wall-normal gradient induced by the central low-speed region quickly drops as the central low-speed region starts to fade away beyond $X \simeq 40$. Figures V.17(b) and (d) provide the same analysis for $(Re, \eta) = (1000, 2)$. It is clear from the global kinetic energy budget depicted on figure V.17(b) that, whereas the contribution of $\int_V I_3 \, \mathrm{d}V$ does not change much, the contribution of $\int_V I_2 \, \mathrm{d}V$ significantly increases. This is also clearly visible on figure V.17(d) where the region within which the wall-normal shear was acting

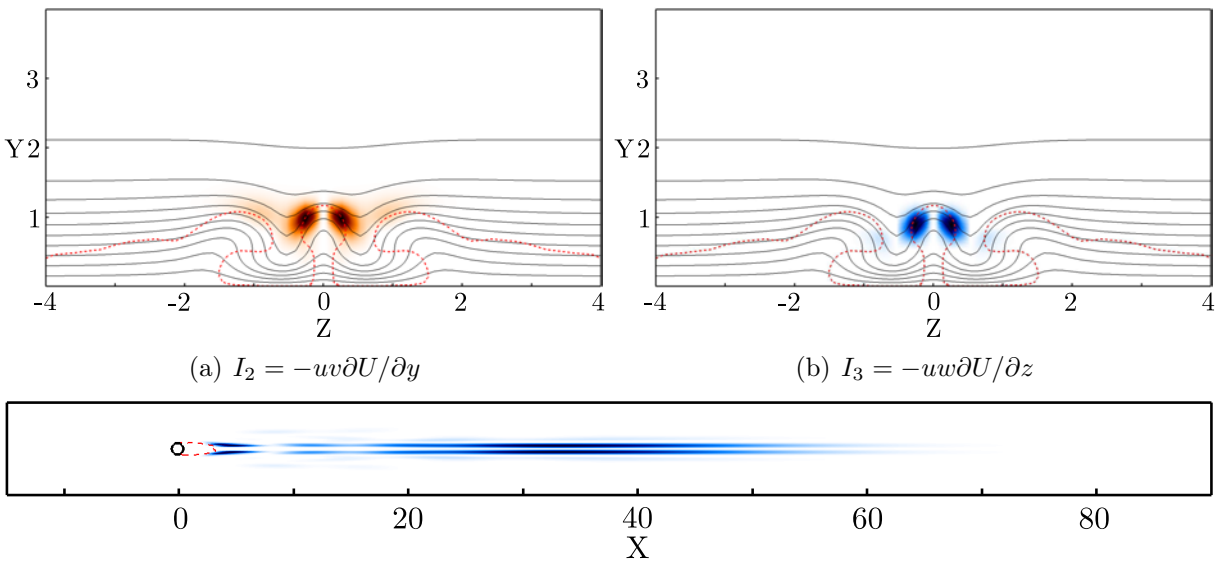

(a) $I_2 = -uv\partial U/\partial y$

(b) $I_3 = -uw\partial U/\partial z$

(c) $I_3 = -uw\partial U/\partial z$

Figure V.16: Top: Spatial distribution of the $I_2 = -uv\partial U_b/\partial y$ (a) and $I_3 = -uw\partial U_b/\partial z$ (b) production terms in the plane $X = 25$ for $(Re, \eta) = (1125, 1)$. Solid lines depict the base flows streamwise velocity isocontours from $U_b = 0.1$ to 0.99, whereas the red dashed lines stand for the location of the shear layer. (c) Spatial distribution of I_3 in the $y = 0.75$ horizontal plane.

as stabilising at lower Reynolds numbers has now disappeared. This behaviour can once again be explained by the features of the associated base flow. Indeed, as shown in section 3.1.1, increasing the Reynolds number yields a strengthening of the wall-normal gradients and causes the central low-speed region to sustain on a much longer streamwise extent. As a consequence, the varicose perturbation can then take advantage of this to extract more energy from the wall-normal gradient of U_b over a longer streamwise distance. Two other major differences with respect to the sinuous instability can also be recovered from these kinetic energy transfer analyses. First of all, figures V.18(a) and (b) provide the spatial distribution of the I_2 and I_3 integrands in the streamwise $X = 25$ plane. Whereas the sinuous instability is essentially extracting its energy from the lateral parts of the low speed region's shear layer, one can see in the present case that the varicose mode seems to be an instability of the fully three-dimensional shear layer as a whole. More importantly, no peak of energy extraction can be found in the near wake region for the varicose instability as highlighted by the curves on figures V.17(c) and (d) as well as on the spatial distribution of the I_3 term in an horizontal plane as shown on figure V.18 (c).

V.4.4 Wavemaker

Investigating the perturbation kinetic energy budget has proven helpful to get a better understanding of the instability mechanisms. Yet, such analysis provides only limited information about the core region of the instability, i.e. the region known as the wavemaker. The concept of wavemaker has been introduced by Giannetti & Luchini [69] and Marquet *et al.* [112] where it has been illustrated on the global instability of the two-dimensional

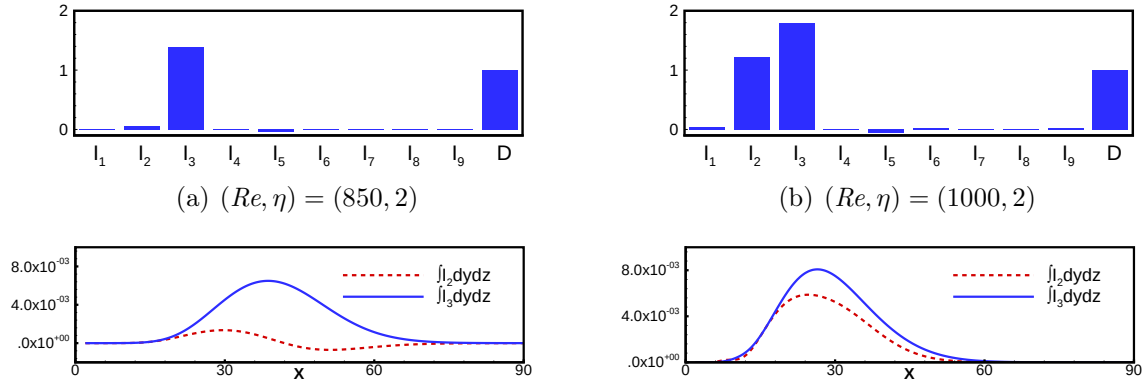

(a) $(Re, \eta) = (850, 2)$ (b) $(Re, \eta) = (1000, 2)$

(c) $(Re, \eta) = (850, 2)$ (d) $(Re, \eta) = (1000, 2)$

Figure V.17: Top: Varicose unstable mode's kinetic energy budget integrated over the whole domain. Bottom: Streamwise evolution of the production terms $\int_{y,z} I_2 \, dydz$ (red dashed line) and $\int_{y,z} I_3 \, dydz$ (blue solid line).

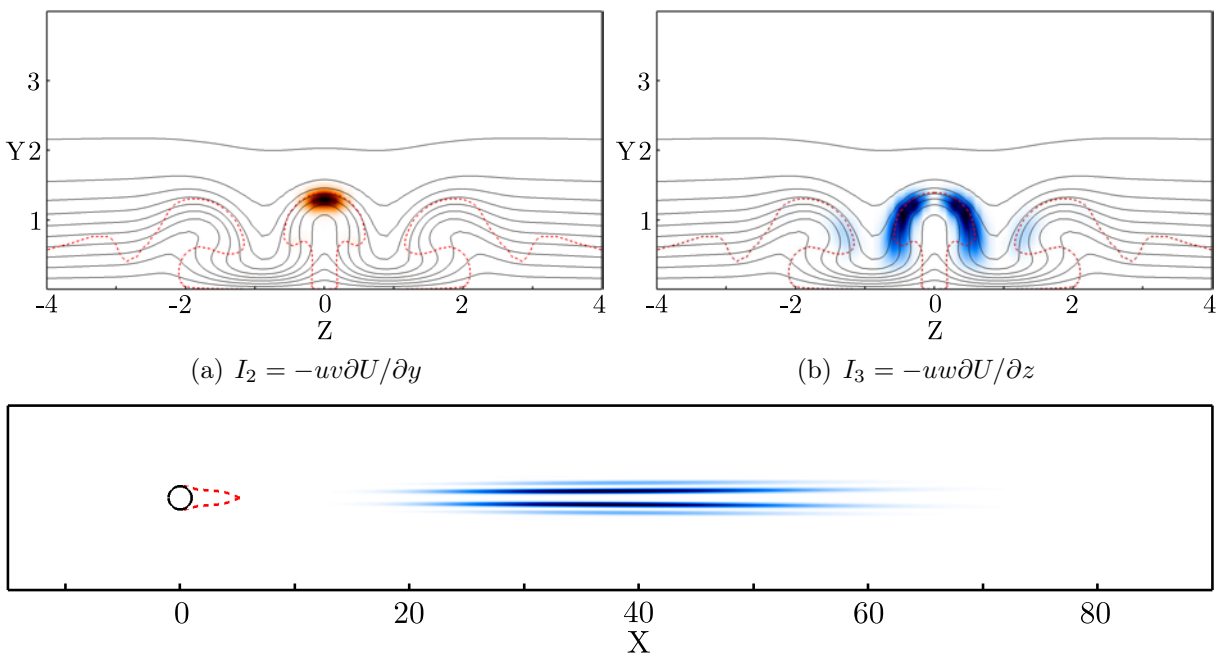

(a) $I_2 = -uv\partial U/\partial y$ (b) $I_3 = -uw\partial U/\partial z$

(c) $I_3 = -uw\partial U/\partial z$

Figure V.18: Spatial distribution of the $I_2 = -uv\partial U_b/\partial y$ (a) and $I_3 = -uw\partial U_b/\partial z$ (b) production terms in the plane $X = 25$ for $(Re, \eta) = (850, 2)$. Solid lines depict the base flows streamwise velocity isocontours from $U_b = 0.1$ to 0.99, whereas the red dashed lines stand for the location of the shear layer. (c) Spatial distribution of I_3 in the $y = 0.75$ horizontal plane.

cylinder flow. It enables one to identify the most likely region for the inception of the global instability under consideration. Following the definition given in [69], the wavemaker is given as the overlap of the direct and adjoint modes:

$$\zeta(x,y,z) = \frac{\|\mathbf{u}(x,y,z)\|\|\mathbf{u}^{\dagger}(x,y,z)\|}{\langle \mathbf{u}^{\dagger}, \mathbf{u}\rangle} \tag{V.5}$$

where $\mathbf{u}^{\dagger}$ is the adjoint of the global mode considered. For the set of adjoint equations and visualisations of the adjoint sinuous and varicose modes, the reader is refered to appendix A. Figures V.19 depict the wavemaker region for (a) the sinuous instability and (b) the varicose one, respectively. It is clear from these figures that the sinuous and varicose instabilities have very different sensitivity regions.

***Sinuous instability*:** As shown on figure V.19(a), the sinuous global mode's wavemaker is exclusively localised within the downstream reversed flow region, having its maximum values along the flanks of the recirculation bubble, very similarly to what is found for a two-dimensional cylinder flow (compare with figure 17 in [69]). Once combined with the knowledge acquired from the kinetic energy analysis, it thus appears that the sinuous global mode extracts its energy from two different underlying instability mechanisms:

(*i*) First, a global instability of the downstream reversed flow region takes place. According to the nature of the mode and the location of its wavemaker, the sinuous global mode seems to be related to the von Kármán global instability encountered in a supercritical two-dimensional cylinder flow [69, 112]

(*ii*) Then, due to the spatially convective nature of the central low-speed region, the sinuous mode experiences weak spatial convective growth before eventually fading away.

It thus appears from these results that the sinuous global instability observed in the present investigation is very different from the sinuous instability of optimal streaks underlined by Andersson *et al.* [13].

***Varicose instability*:** It is clear from figure V.19(b) that the core region of the varicose instability is quite different from that of the sinuous one. Indeed, its wavemaker is not only localised within the downstream reversed flow region but also extends along the top of the central low-speed region. This spatial extent further highlights the key role of the central low-speed region and outer streaks on this global instability. However, despite its elongated nature, it is worthy to note that the amplitude of the varicose wavemaker within the downstream reversed flow region still is almost ten to fifteen times larger than that within the wake of the roughness element. From these elements, it thus appears that:

(*i*) The varicose mode finds its roots in a global instability of the downstream reversed flow region. However, based on the kinetic energy budget, this particular region appears to behave essentially as a wave generator and plays very little role in the energy extraction process of the varicose instability.

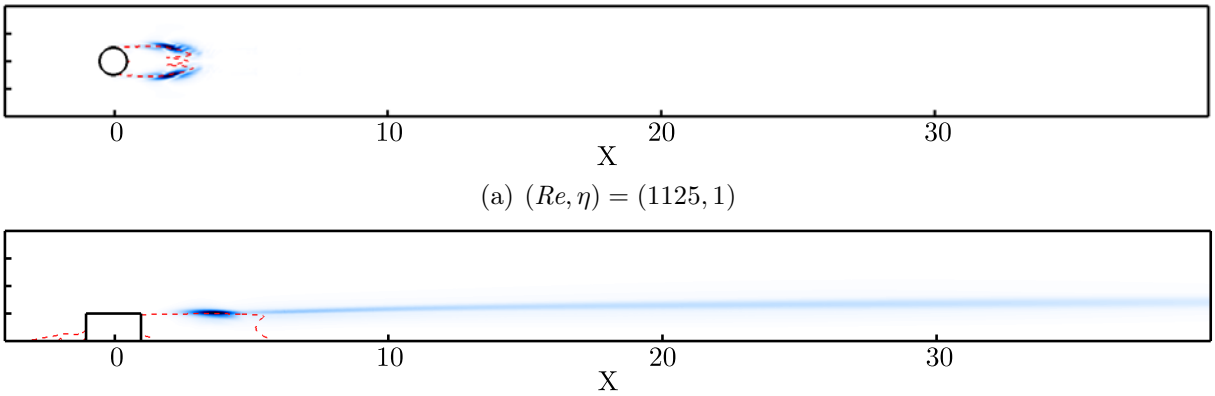

(a) $(Re, \eta) = (1125, 1)$

(b) $(Re, \eta) = (900, 2)$

Figure V.19: Visualisation of the wavemaker region of the leading mode for (a) the sinuous instability in the $y = 0.5$ plane and (b) the varicose instability in the $z = 0$ plane, respectively. The red dashed lines depict the spatial extent of the reversed flow region.

(*ii*) Once generated from the wavemaker, the varicose global mode then experiences large spatial transient growth along the central low-speed region induced by the roughness element that dominates the whole energy budget.

As will be shown in section 5.1, such varicose global instability non-linearly seems to give rise to hairpin vortices shed directly from the roughness element. It thus appears that the linear mechanism identified from the perturbation kinetic energy and wavemaker analyses of this varicose global instability is similar to the one proposed by Acarlar & Smith [3] for the creation of hairpin vortices right downstream a hemispheric protuberance, i.e. a small roll-up of the downstream shear layer that is then convected by the flow and greatly amplified along the central-low speed region, eventually giving birth to a hairpin vortex by non-linear effects.

V.5 Non-linear evolution

V.5.1 Varicose global instability

In order to have a glimpse of the non-linear evolution of the varicose global instability identified previously, a direct numerical simulation (DNS) of the Fransson's setup already introduced in section V.3 is conducted for $Re = 575$, for which the global stability analysis of the base flow predicts that only a single varicose global mode is unstable. The non-linear Navier-Stokes equations have been initialised using the base flow solution and are marched in time until a statistically steady state has been reached. Figure V.20(a) shows the streamwise velocity signal recorded by a probe located at $(X, y, z) = (10, 0.5, 0)$, while figure V.20(b) presents the associated Fourier spectrum. It is clear from figure V.20(a) that the dynamics of the flow exhibits well established periodic oscillations. As shown in figure V.20 (b), these oscillations of the flow have a circular frequency $\omega_{DNS} = 0.832$, very close to that of the unstable varicose global mode identified in section 3.2 (i.e. $\omega = 0.824$). Figure V.21 provides the instantaneous streamwise velocity distribution of the

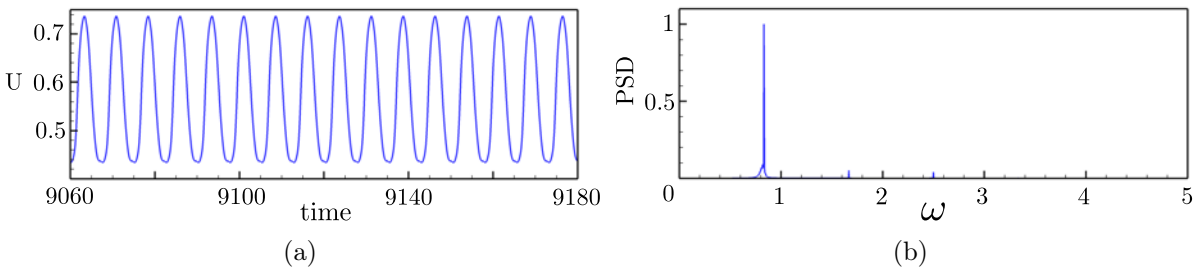

Figure V.20: Probe measurements and normalised Fourier spectrum of the spanwise velocity in the near wake region at $(X, y, z) = (10, 0.5, 0)$ for the Fransson's set up.

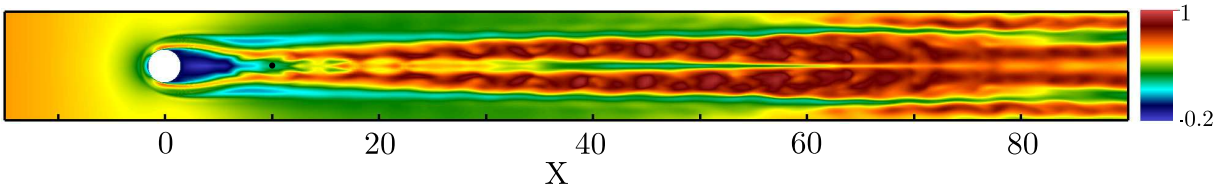

Figure V.21: Visualisation of the streamwise velocity distribution in the horizontal $y = 0.5$ plane for the Fransson's set up at $Re = 575$. The black dot depicts the position of the probe recording data shown in figure V.20.

non-linearly saturated flow within the $y = 0.5$ plane. It appears that the self-sustaining oscillations of the flow recorded by the probe consist in a varicose time-periodic modulation of the central low-speed region and surrounding velocity streaks. Figure V.22 depicts instantaneous vortical structures present within the flow that have been identified using the λ_2 criterion [84]. It seems obvious from this figure that these vortical structures are hairpin vortices shed directly downstream the roughness element. Moreover, it can be assessed from the large population of hairpin vortices that transition is triggered very close to the roughness element, coherent with the numerous experimental observations reviewed by von Doenhoff & Braslow [158]. Based on these observations and on results from global stability analyses, one can conclude that the unstable varicose global mode contributes to the birth of the set of hairpin vortices non-linearly generated and might thus explain the early transition observed in the experimental work by Fransson *et al.* [66] for supercritical Reynolds numbers.

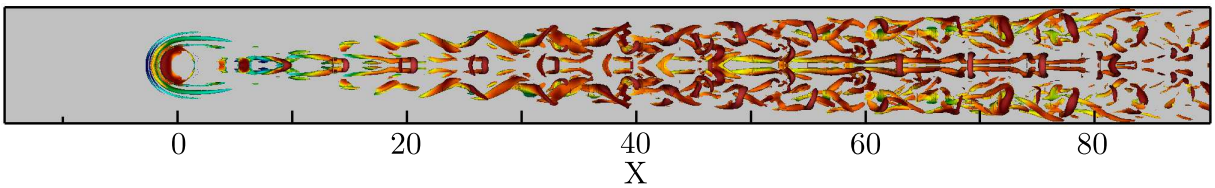

Figure V.22: Top view of the hairpin vortices visualised by the isosurfaces of the $\lambda_2 = -0.025$ criterion coloured with the local kinetic energy of the flow.

V.5.2 Sinuous global instability

Most studies on roughness-induced transition have focused on relatively large aspect ratio roughness elements ($\eta \geq 2$) and, as a matter of fact, on the unsteadiness related to the varicose instability mechanism only [3, 48, 147, 153, 160], whereas very little can be found in the literature regarding the non-linearly saturated sinuous instability [27, 132]. Thus, in the following we focus our attention more closely on the non-linear evolution of the sinuous global mode using direct numerical simulations of the non-linear Navier-Stokes equations. More specifically, the nature of the bifurcation will be determined as well as the flow pattern and dynamics resulting from the non-linear saturation of the sinuous unstable global mode. The direct numerical simulations to be described have been performed for an aspect ratio $\eta = 1$ roughness element and Reynolds numbers ranging from 1030 up to 1125. The velocity field used for initializing the DNS consists in the unstable equilibrium state onto which a small disturbance made of the sinuous global mode is superimposed. The initial energy of the perturbation field is chosen to be 10^8 times smaller than the energy of the base flow to ensure that no by-pass transition could be triggered due to the initial amplitude of the perturbation. The resulting flow field is then marched in time until non-linear saturation is reached and a statistically steady state is obtained.

V.5.2.1 Criticality of the bifurcation

Before investigating the non-linear dynamics, the super- or subcritical nature of the sinuous Hopf bifurcation is characterised. To do so, the Reynolds number of the non-linearly saturated flow is incrementally decreased from $Re = 1125$ until a steady flow is reached. Provided a steady solution is recovered for $Re = Re_c$, the bifurcation is then determined as being supercritical. Otherwise, the bifurcation is labelled as being subcritical. Since the base flow is symmetric with respect to the $z = 0$ plane, the spanwise velocity recorded by a probe located at $(X, y, z) = (10, 0.5, 0)$ is standing for a clear signature of the sinuous unstable mode's evolution. As a consequence, such measurement appears to be a good indicator to monitor how far the non-linearly saturated flow has departed from the base flow solution. The evolution of the maximum amplitude of this variable with respect to changes in the Reynolds number is depicted on figure V.23. As the Reynolds number is decreased from $Re = 1125$ to 1030, the maximum amplitude of the spanwise velocity recorded by the probe is also decreasing. Moreover, below the critical Reynolds number $Re_c = 1040$, no more self-sustained oscillations of the flow are observed. Similar observations have been made from the signals recorded by other probes placed within the flow. This particular behaviour, i.e. no oscillation below the critical Reynolds number predicted by linear stability analysis, provides striking evidence for the sinuous Hopf bifurcation to be supercritical. This is further confirmed by how the maximum amplitude of the perturbation depends on the off-criticality parameter $\epsilon = Re - Re_c$. The solid line in figure V.23 depicts the least-square best fit obtained using $\sqrt{Re - Re_c}$ as the fitting function. It is clear that the maximum amplitude evolves as the square-root of the off-criticality parameter, another clear signature of the supercritical nature of this bifurcation. Consequently, the unsteadiness observed in the near-wake region in the direct numerical simulation can be traced back to the sinuous unstable global mode and not to any kind of by-pass transition.

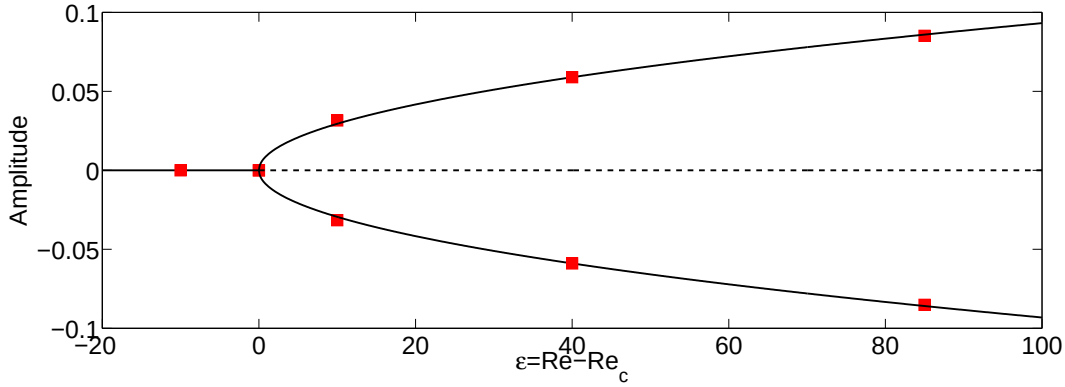

Figure V.23: Bifurcation diagram of the sinuous instability for $\eta = 1$. Red squares depict the perturbation spanwise amplitude at $(X, y, z) = (10, 0.5, 0)$ whereas the black solid line stands for the least-square best fit. The dashed line at $Amplitude = 0$ indicates the branch of equilibrium solutions which becomes unstable for $Re \geq Re_c$.

V.5.2.2 Mean flow characteristics

Figure V.24 depicts lines of constant streamwise velocity within the spanwise mid-plane both for the base flow (top) and the mean flow (bottom) at $(Re, \eta) = (1125, 1)$. While the reversed flow region appears to be quite similar in both cases (see the left frames of figure V.24), the shear layers developing further downstream are quite different (right frames). Whereas the shear layer in the base flow is relatively thin, the one developing in the mean flow is a lot thicker. Despite the thickening of the shear layer, the boundary layer's thickness of the two flows are almost the same in the near wake region as can be assessed from the location of the $U = 0.99$ line in the left parts of figure V.24. In the far wake region however, the boundary layer thickness of the two flows greatly differs. Indeed, only a relatively small increase of δ_{99} can be observed in the case of the base flow (right part of figure V.24(a)), while it has thicken by almost 50% in the mean flow. Such large thickening of the mean flow's boundary layer underlines the transitioning nature of the far wake region.

The overlap between the mean flow shear layer with the location of the rms-fluctuations can be seen on figure V.25. Depending on the streamwise station considered, two different behaviours can be observed. While in the near-wake region the rms-fluctuations are essentially localised along the central low-speed region (see figure V.25(a)), they then start to transfer along the outer low-speed streaks (see figure V.25(b)) before eventually invading the whole spanwise extent of the boundary layer (figures V.25(c) and (d)). Extremely far from the roughness element one might even expect to recover fully turbulent boundary layer's characteristics. In the present study however, the Reynolds number is too low and the computational domain not long enough to achieve such state. Hence, near the outflow, though the flow field observed has already departed quite far from laminarity, it can not yet be considered as being fully turbulent.

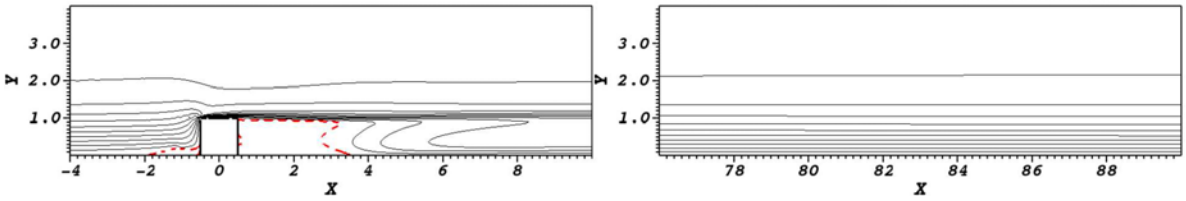

(a) Base flow

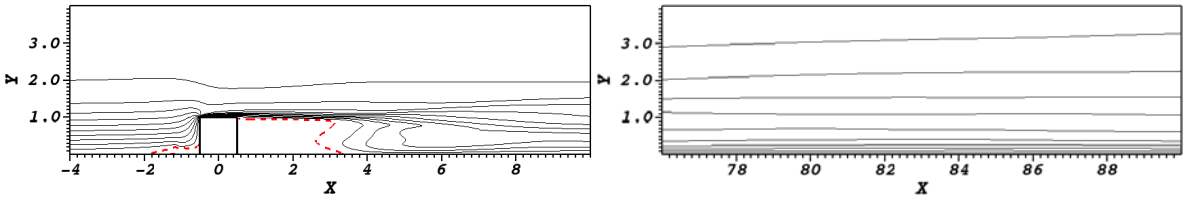

(b) Mean flow

Figure V.24: Streamwise velocity contours in the spanwise mid-plane for $(Re, \eta) = (1125, 1)$. Isolines range from 0 (dashed red) up to 0.99. Left frames show the flow in the vicinity of the roughness element, whereas right frames show the flow in the far wake region close to the ouflow of the computational domain.

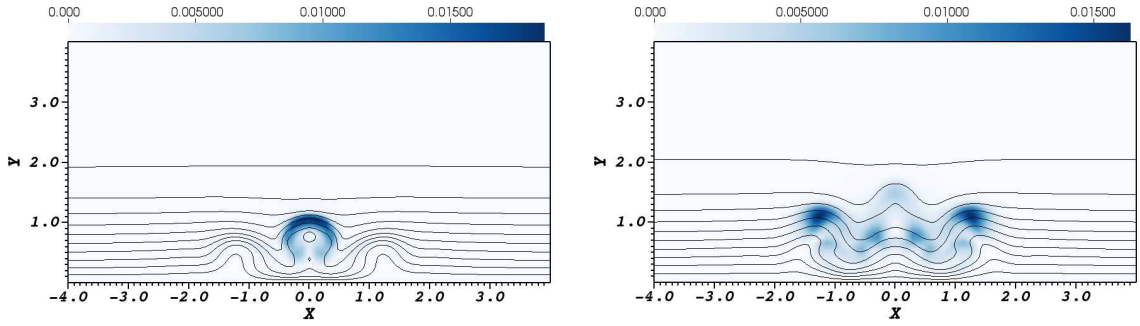

(a) $X = 5$

(b) $X = 17.5$

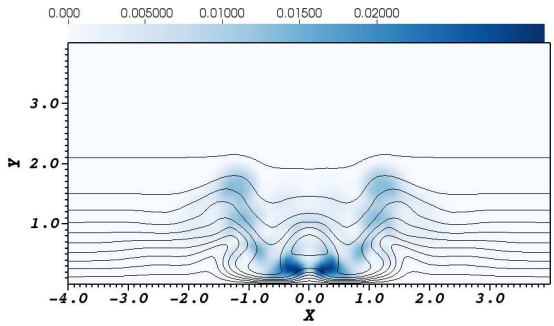

(c) $X = 30$

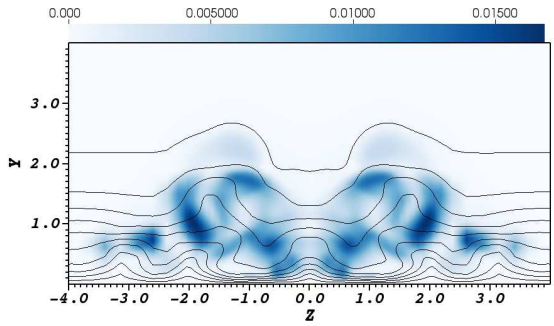

(d) $X = 45$

Figure V.25: *rms*-fluctuations of the streamwise velocity (shaded contours) in various $X-$planes. Solid lines depict contours of the streamwise velocity ranging from 0.1 up to 0.99.

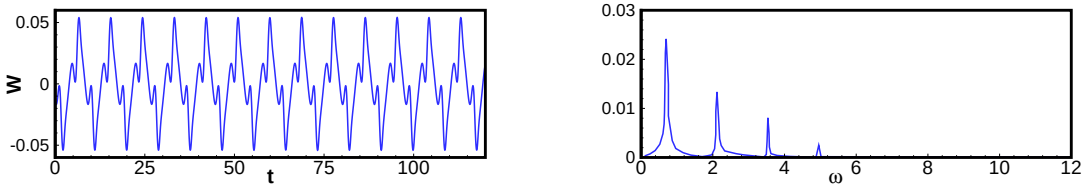

(a) (b)

Figure V.26: Probe measurements and Fourier spectrum of the spanwise velocity in the near wake region at $(X, y, z) = (10, 0.5, 0)$

V.5.2.3 Dynamics

Self-sustained oscillations are defined as persistent oscillations of the system arising in the absence of any forcing or regardless of the nature of the small-amplitude forcing eventually due to experimental or environmental noise. Such oscillations can be observed in the near-wake region as highlighted by the spanwise velocity measurement recorded from the probe located at $(X, y, z) = (10, 0.5, 0)$ and the associated Fourier spectrum (see figure V.26(a) and (b), respectively). It is clear that saturated periodic dynamics are well established in the near-wake laminar region with a dominant circular frequency $\omega_{DNS} = 0.687$ close to that predicted by global stability analysis (i.e. $\omega = 0.672$). Figure V.27 depicts the instantaneous streamwise velocity distribution in the $y = 0.5$ plane. It appears obvious from this figure that the self-sustained oscillations recorded by the probe are related to a sinuous wiggling of the central low-speed region induced by the sinuous global instability of the flow identified previously. The main wavelength of this wiggling has been extracted by taking the Fourier transform in the X direction of the saturated flow signal extracted at $(y, z) = (0.5, 0)$. A dominant streamwise wavelength of about 6.1 has been found, which matches well with the one characterising the sinuous eigenmode, 6.9, extracted by Fourier transform of the eigenmode in x. However, despite the sinuous wiggling of the central low-speed region, λ_2 visualisations [84] of the instantaneous vortical structures depicted on figures V.28 and V.29 show the existence of hairpin vortices shed directly from the roughness element. Such shedding of hairpin vortices behind roughness elements has already been investigated by Acarlar & Smith [3], Tufo *et al.* [153] and Zhou *et al.* [160] on hemispherical elements, and more recently by Stephani & Goldstein [147] on a cylindrical one. One major difference with these works and the results presented in section 5.1 however is the nature of the shedding. Indeed, in cited works, hairpin vortices are exhibiting a varicose symmetry with respect to the spanwise mid-plane. In the present case on the other hand, figure V.29 clearly highlight that the hairpin vortices shed from the roughness element considered herein are initally modulated by the sinuous wiggling of the central low-speed region before eventually yielding the flow to transition to turbulence further downstream as illustrated on figure V.28. It is not clear at the present time however whether the mechanism responsible for the creation of these hairpin vortices is the same as the one described by Acarlar & Smith [3] for hemispherical roughness elements or if they result from more complicated interactions between the mean flow and the non-linearly saturated sinuous global instability.

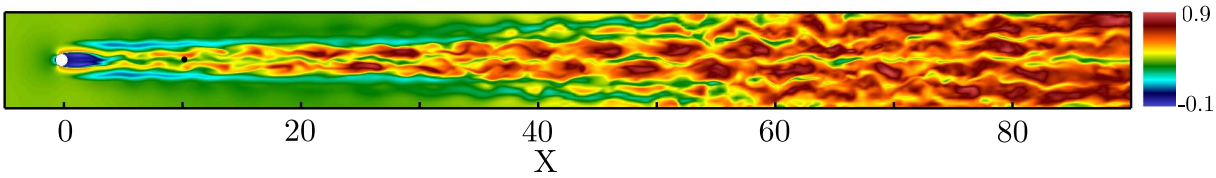

Figure V.27: Visualisation of the streamwise velocity distribution in the horizontal $y = 0.5$ plane. The black dot depicts the position of the probe recording data shown in figure V.26.

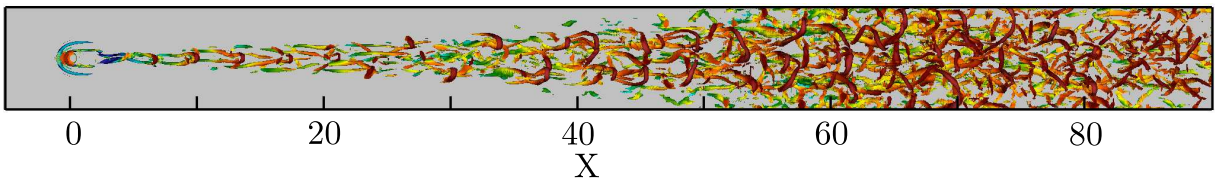

Figure V.28: Hairpin vortices visualised by the isosurfaces of the $\lambda_2 = -0.06$ criterion coloured with the local kinetic energy. Only one single roughness element has been simulated.

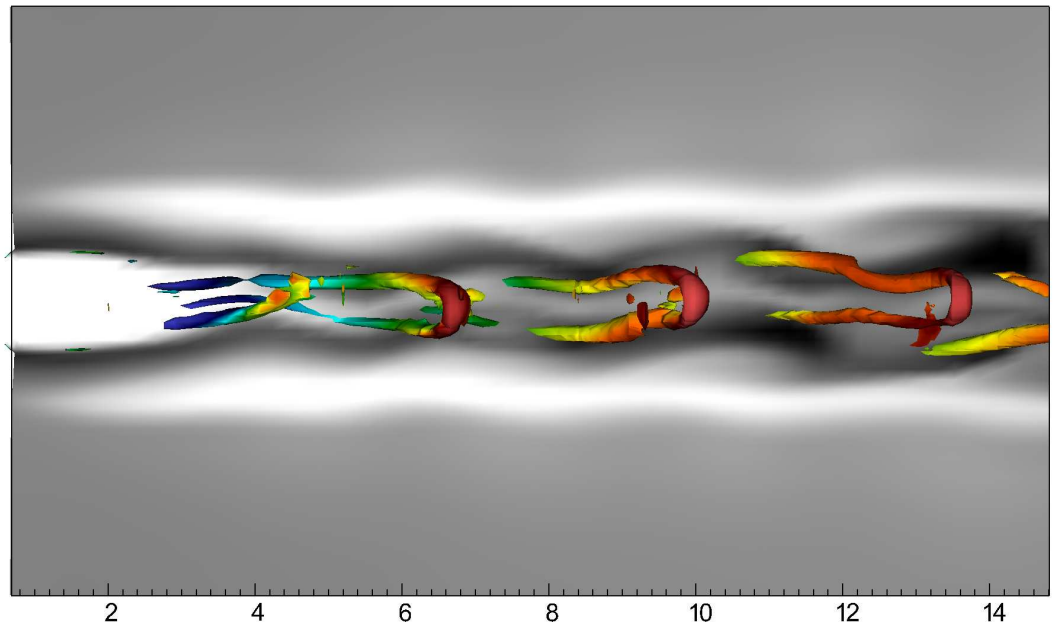

Figure V.29: Close-up of the hairpin vortices (visualised by the coloured isosurface of $\Lambda_2 = -0.06$) shed in the near-wake region. Shaded grey contours depict the streamwise velocity in the $y = 0.5$ horizontal plane. A clear sinuous wiggling of the streaks can be observed.

V.5.3 Comparison with von Doenhoff-Braslow transition diagram

Roughness-induced transition has been extensively investigated since the early 1950's. The large body of literature existing on the subject has been well summarized by von Doenhoff & Braslow [158] on a transition diagram, reproduced on figure V.30. Based on the roughness Reynolds number $Re_h = U_{Bl}(x_k, h)h/\nu$ (where $U_{Bl}(x_k, h)$ is the value of the Blasius velocity profile evaluated at the roughness element's position x_k and height h) and the aspect ratio of the roughness elements considered, this diagram allows one to predict the outcome of his experiment:

(i) If the parameters characterising the flow setup lie below the grey zone of this diagram, it is then expected that the flow observed downstream the roughness element is laminar and steady.

(ii) If these parameters lie above the grey zone, it is expected that transition has already occured right downstream the roughness elements considered.

(iii) Finally, within the grey zone, the flow may undergo transition to turbulence or experience unsteadiness, depending on the other configuration parameters (shape, spanwise spacing, etc..).

It is noteworthy that the results summarized in the von Doenhoff & Braslow's diagram [158] stem from various experimental investigations of transition induced by isolated and/or periodic arrays of roughness elements of different shapes (cylindrical, hemispheric, prismatic, ...) and wind tunnels of variable quality, thus explaining the large spread of the transition region (grey shaded area in figure V.30). Nonetheless, this transition diagram allows qualitative comparison of the theoretical predictions with experimental results and still is widely used nowadays in industries.

The various critical thresholds predicted by the global stability analyses performed here have been rescaled to their roughness Reynolds number counterparts and reported on this transition diagram. Red dots stand for the critical Reynolds numbers for varicose global instability, whereas the green squares stand for the critical Reynolds numbers for sinuous global instability. All of these critical Reynolds numbers lie within the transition band of the diagram. Such positions suggest that a fully three-dimensional global instability of the reversed flow region might be one of the possible explanations of the roughness-induced transition. The authors are nonetheless aware that mechanisms based on the local stability properties of the flow, such as local transient growth [15], also provide satisfactory explanations thus leaving this question still open at the present time.

V.6 Summary and conclusions

The properties of the incompressible flow induced by three-dimensional cylindrical roughness elements of various aspect ratios have been investigated by the joint application of fully three-dimensional global stability analyses and direct numerical simulations. In all cases considered, horseshoe vortices are created around the roughness element, whose legs create two pairs of high- and low-speed streamwise streaks due to the lift-up effect. Furthermore, a central low-speed region, whose crucial importance in the transition process has been indicated by several authors, as well as in the present work, is created due

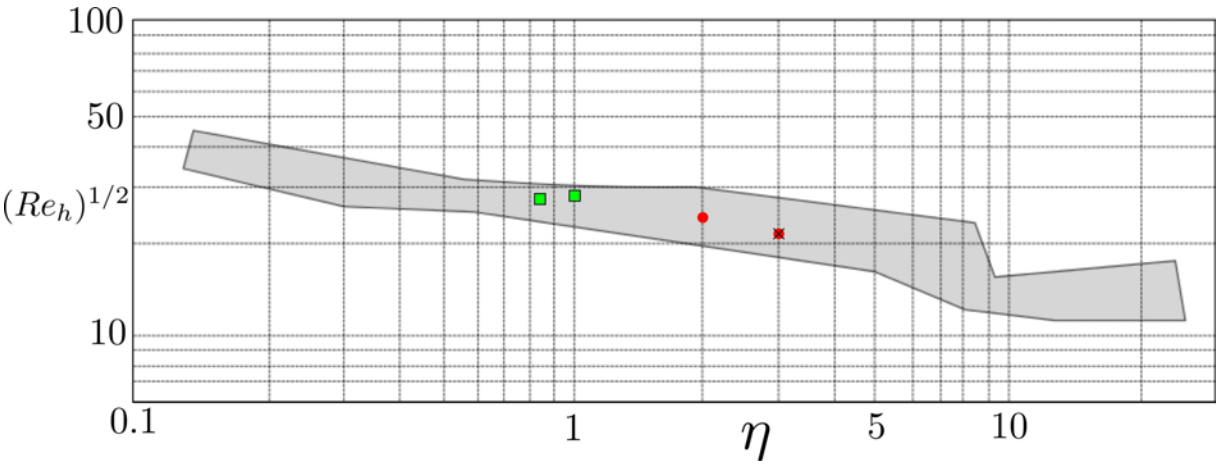

Figure V.30: Reproduction of the transition diagram by von Doenhoff & Braslow [158]. Green squares stand for the critical value of the sinuous instability, whereas red dots denote the critical value for varicose instability and the black cross the critical threshold in the experiment by Fransson *et al.* [66].

to the streamwise velocity blockage induced by the presence of the roughness element. The strength of this central low-speed region, and whether or not it sustains over a long streamwise distance, is closely linked both to the roughness element's aspect ratio and to the Reynolds number.

Regarding the stability of such flows, two different types of global instabilities have been identified. The symmetry of the dominant unstable mode depends on the aspect ratio of the roughness element considered. For thin cylindrical roughness elements, the first bifurcation encountered is related to a sinuous global instability of the lateral parts of the shear layers developing in the downstream flow, whereas for larger roughness elements it is related to a varicose instability of the three-dimensional shear layer as a whole. The underlying physical mechanisms are investigated by means of a kinetic energy transfer analysis between the base flow and the perturbations as well as by the computation of the wavemaker of the two global instabilities identified. Though both instabilities are essentially fed by the work of the Reynolds stresses against the wall-normal and spanwise gradients of the base flow streamwise component, some major differences are observed that allow us to clearly differentiate between the underlying mechanisms. On the one hand, the sinuous instability is related to a global instability of the near-wake region and of the associated reversed flow region similar to what occurs in a supercritical two-dimensional cylinder flow. On the other hand, the varicose mode appears to be related to a global instability of the whole three-dimensional shear layer surrounding the central low-speed streak. In particular, a weak pocket of instability is originated in the near wake, which is strongly amplified further downstream due to the highly convective nature of the downstream flow similarly to the explanation proposed by Acarlar & Smith [3] regarding the creation of hairpin vortices right downstream hemispheric roughness elements.

The non-linear evolutions of both instabilities have been investigated using direct numerical simulations. For roughness elements having a relatively large aspect ratio, it has

been shown that the varicose global instability of the flow gives rise to a shedding of hairpin vortices right downstream the roughness elements. These hairpin vortices trigger a very rapid transition of the flow right after the roughness elements. Despite the transitional dynamics, Fourier analysis has shown that the dominant frequency involved in the dynamics are in good agreement with the predictions made by global stability analysis. The non-linear evolution of the sinuous global instability has been investigated more deeply. Varying the Reynolds number of the simulation has revealed that the amplitude of the sinuous perturbation, measured by a probe in the spanwise mid-plane, evolves as the square root of the off-criticality parameter (i.e. $\epsilon = Re - Re_c$). Such evolution is typical of supercritical bifurcations. Analyses of the dynamics show that the sinuous global mode induces a wiggling of the central low-speed region. Once again, the dominant frequency involved in these dynamics is well predicted by global stability analyses. Nonetheless, identification of the vortical structures present within the flow also revealed the existence of hairpin vortices shed right downstream the roughness element. These hairpin vortices slightly oscillate showing a sinuous wiggling, and are then convected by the flow eventually triggering transition to turbulence further downstream. It is not clear at the present time if these hairpin vortices are created by a mechanism similar to that described by Acarlar & Smith [3] or if they result from complicated non-linear interactions between the mean flow and the non-linearly saturated sinuous instability.

Finally, the different transition thresholds computed by the fully three-dimensional global stability analyses have been reported onto the transition diagram by von Doenhoff & Braslow [158]. Qualitatively good agreement is found between the predictions obtained from linear global stability analyses and those of the transition diagram. Moreover, the experimental configuration used by Fransson *et al.* [66] has been numerically reproduced; the predictions of the global instability analysis in this configuration show a very good agreement with the critical Reynolds number measured by the previously mentioned authors. These elements allows us to conjecture that a global instabilities of the reversed flow region developing right downstream the roughness element may be a possible explanation of the roughness-induced transition, at least in the configurations considered herein.

Concluding remarks

The present work has provided some answers on the global origin of two different instabilities arising past a cylindrical roughness element, on their onset depending on the aspect ratio of the cylinder, and on the vortical structures and frequencies observed in the route to turbulence for both transition scenarios. However, several questions still remain however unanswered and require further qualitative and quantitative investigations, namely:

(*i*) What is the mechanism responsible for the creation of hairpin vortices in the case of a sinuous global instability of the flow?

(*ii*) What is the role of fully three-dimensional linearly and non-linearly transiently growing perturbations in the transition process? Under which conditions, if any, such optimal perturbations can trigger transition to turbulence and, as such, bypass all of the linear instability scenario?

(*iii*) How does the shape of the three-dimensional roughness element influence the transition process?

Concerning transiently growing perturbations, previous works have provided some elements indicating that they also might have a role in the transition process. In the case of the streaky flow induced by a rectangular panel, Asai *et al.* [17, 18] and Brandt [34] have shown that the flow can exhibit local convective instability. As shown by Chomaz [43], such convective instability is closely related to transient growth. Very recently, Cherubini *et al.* [41] have moreover demonstrated that three-dimensional linear optimal perturbations can trigger localised transition of the flow induced by a smooth roughness element. For the range of subcritical roughness Reynolds numbers investigated, the unsteadiness was however observed not to be self-sustaining and was eventually washed out from the computational domain, the flow slowly recovering toward its initial state. Under which conditions these optimal perturbations may lead to a self-sustaining instability, and whether including the effects of non-linearity in the computation of this perturbations may lead to an early transition are points that still remain to be unraveled.

Finally, concerning the influence of the shape of the roughness element on the stability of the flow, the present authors [106] have already presented preliminary results indicating that, for a fixed aspect ratio, the smoother the roughness element the higher the critical Reynolds number beyond which linearly global instability of the flow can set in. Future work will aim at clarifying these aspects.

Acknowledgements

This work has received the financial support of the French National Agency for Research (ANR) through the grant ANR-09-SYSCOMM-011-SICOGIF. Moreover, most of the computations have been performed on the IBM x3750 (Ada) at IDRIS, Orsay, France. Finally, the authors would like to thank Grégory Dergham for the preliminary stability calculations he had run when this investigation has been started.

Appendix A: Adjoint equations and adjoint modes

Adjoint state is a concept originating from the optimisation theory. Over the past years, adjoint-based methods have been used successfully in flow control and stability analysis. In the hydrodynamic instability framework, such methods have been used to identify optimal perturbations, highlight the most receptive path to break down, select the most destabilising base flow defect in an otherwise stable configuration, and map the structural sensitivity of a flow oscillator. All of these uses have been recently reviewed in [108]. The adjoint state equations read:

$$\begin{cases} \dfrac{\partial \mathbf{u}^\dagger}{\partial t} + (\mathbf{U}_b \cdot \nabla)\mathbf{u}^\dagger - (\nabla \mathbf{U}_b)^T \mathbf{u}^\dagger = -\nabla p^\dagger + \dfrac{1}{Re}\Delta \mathbf{u}^\dagger \\ \nabla \cdot \mathbf{u}^\dagger = 0 \end{cases} \tag{V.6}$$

For a complete derivation of the adjoint linearised Navier-Stokes equations as well as the consequences on the boundary conditions of the problem, the reader is referred to [26].

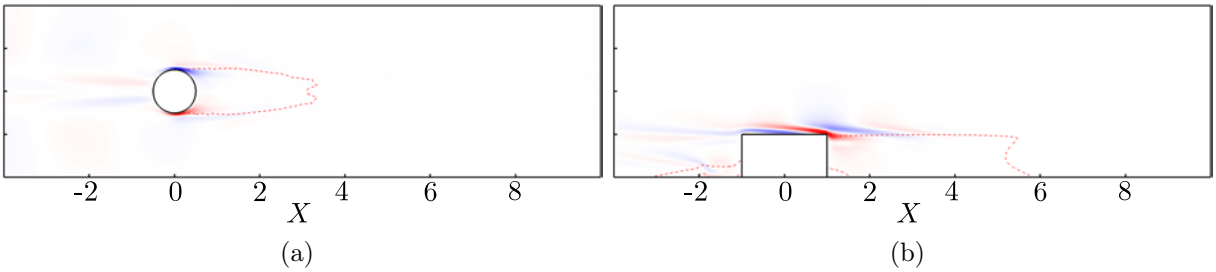

Figure V.31: Visualisation of the streamwise velocity component of the leading adjoint mode for (a) the sinuous instability in the $y = 0.75$ plane and (b) the varicose instability in the $z = 0$ plane, respectively. Red dashed line depicts the spatial extent of the reversed flow region.

η	1	2	Fransson *et al.* [66]
Re	1125	900	575
λ (Direct)	$0.0123 \pm i0.6718$	$0.0395 \pm i0.9395$	$0.0105 \pm i0.8240$
$\lambda^\dagger$ (Adjoint)	$0.0122 \pm i0.6717$	$0.0396 \pm i0.9394$	$0.0106 \pm i0.8240$

Table V.4: Comparison of the leading eigenvalue of the direct and adjoint linearised Navier-Stokes operators.

Nonetheless, as for the linearised Navier-Stokes equations, this set of equations can be recast into a linear dynamical system form:

$$\mathbf{B}\frac{\partial \mathbf{q}^\dagger}{\partial t} = \mathbf{J}^* \mathbf{q}^\dagger \tag{V.7}$$

where $\mathbf{q}^\dagger = (\mathbf{u}^\dagger, p^\dagger)^T$ is the adjoint state vector and $\mathbf{J}^*$ the adjoint Jacobian matrix. The eigenspectrum of this adjoint Jacobian matrix is then computed using the same algorithm as the one introduced in section 2.3.

Figure V.31 depicts the leading adjoint mode for (a) the sinuous instability with $(\eta, Re) = (1, 1125)$ and (b) the varicose instability with $(\eta, Re) = (2, 900)$, respectively. As for its direct counterpart, the streamwise and wall-normal components of the sinuous adjoint mode are antisymmetric with respect to the $z = 0$ plane while its spanwise velocity component is symmetric. Its maximum is located in the vicinity of the separation lines on the vertical walls of the cylindrical roughness element. On the other hand, the leading varicose adjoint mode has its maximum located within the symmetry plane of the problem, in the vicinity of the separation point right downstream the cylindrical roughness element. Its streamwise and wall-normal components are symmetric with respect to the $z = 0$ plane while its spanwise velocity component is antisymmetric. Table V.4 provides a comparison of the leading eigenvalue of the direct and adjoint linearised Navier-Stokes operator. It can be seen that, for all the different cases, they agree up to the fourth digit.

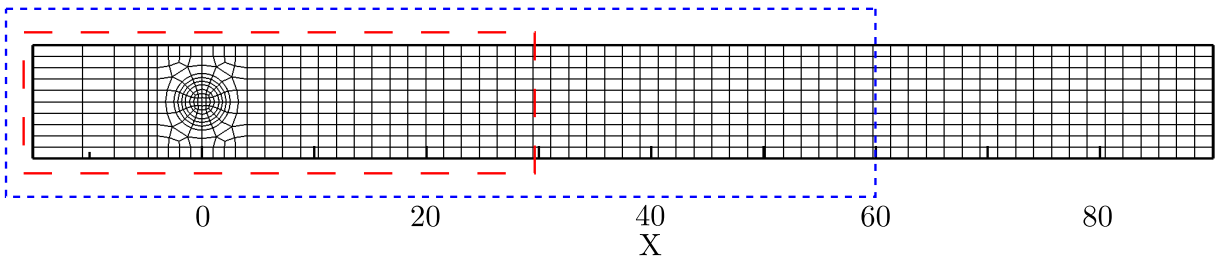

Figure V.32: Distribution of the spectral elements in an arbitrary horizontal plane. Red long-dashed box depicts the extent of the smallest computational domain considered ($X_{out} = 30$), while the blue dashed box depicts that of the intermediate one ($X_{out} = 60$).

Appendix B: Convergence of the eigenvalue computations

In this appendix, we highlight the influence of the domaine size and mesh refinement on the computation of the leading eigenvalues and eigenvectors of the linearised Navier-Stokes operator using the Fransson *et al.* [66] setup investigated in section 3. Figure V.32 depicts the distribution of spectral elements in an arbitrary horizontal plane. In all cases, the wall-normal and spanwise extents of the computational domain have been kept constant (i.e. $L_y = 50$ and $L_z = 10$), while the location of the outflow plane has been changed from $X_{out} = 30$ (red long-dashed box), to $X_{out} = 60$ (blue dashed box) and eventually to the longest domain considered herein $X_{out} = 90$. For all cases, the order of the Legendre polynomials has been kept equal to 8. Figure V.33 depicts the eigenspectrum of the linearised Navier-Stokes for each domain. On the one hand, the $X_{out} = 30$ spectrum appears to be made of a branch of eigenvalues only. On the other hand, the $X_{out} = 60$ and $X_{out} = 90$ exhibit an isolated eigenvalue lying in the upper-half complex plane. Figure V.34 depicts the streamwise velocity component of the leading eigenmode for each domain considered. It is obvious from these figures that a sufficiently long domain is required in order to capture appropriately the whole spatial extent of the mode and might explain the difference between the spectrum obtained for $X_{out} = 30$ with those for $X_{out} = 60$ and 90. Morover, considering a short streamwise extent of the computational domain yields to an under-prediction of the critical Reynolds number as shown in table V.5. Based on these conclusions, all the results presented in this paper have been obtained for $X_{out} = 90$.

Now that it has been shown that the domain needs to be long enough to capture appropriately the global instability under investigation, the influence of the mesh refinement on this instability is highlighted by table V.6. All the results within this table have been obtained on the longest domain considered (i.e. $X_{out} = 90$). The order of the Legendre polynomials is changed from $N = 6$ to $N = 12$, resulting in an increase of the gridpoints from 1.43 million up to almost 12 million. As one can see, provided $N \geq 8$, it is clear from table V.6 that the leading eigenvalue appears to be almost independant of the mesh refinement. All the results presented in this paper have been obtained using the finest grid ($N = 12$).

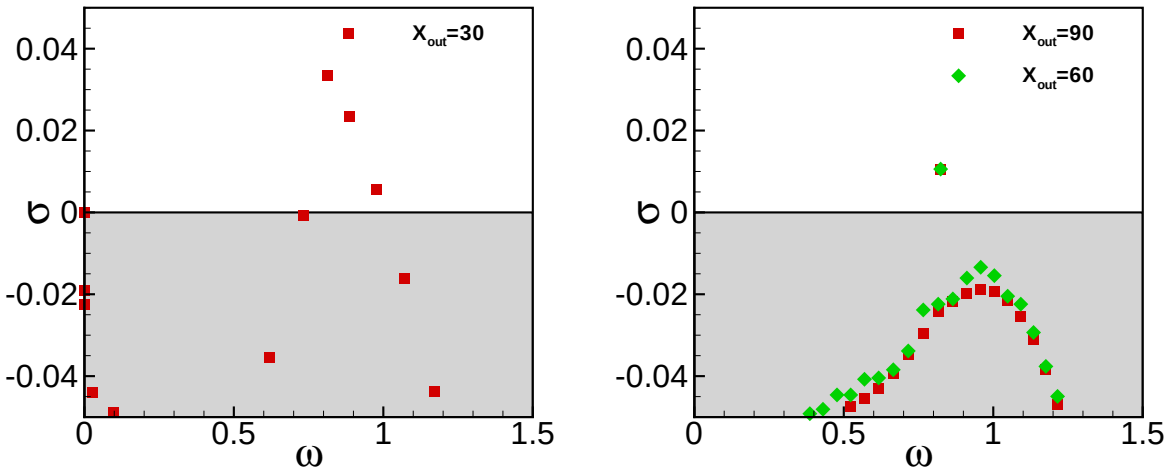

(a) (b)

Figure V.33: Comparison of the eigenspectrum for (a) $X_{out} = 30$ and (b) $X_{out} = 60$ and 90.

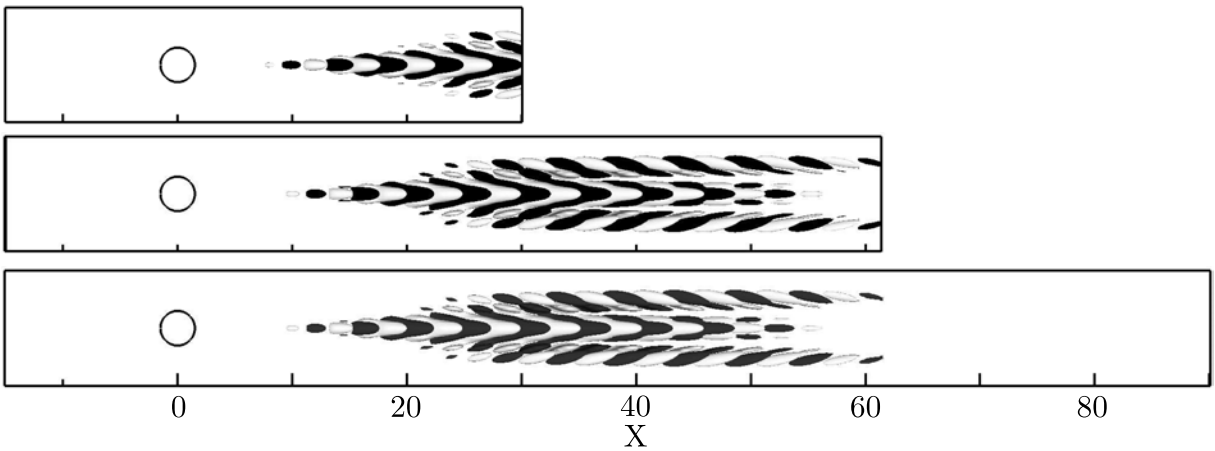

Figure V.34: Streamwise velocity component of the leading global mode of the [66] setup at $Re = 575$ for three different streamwise length of the computational domain. Top: $X_{out} = 30$, middle: $X_{out} = 60$, bottom: $X_{out} = 90$.

X_{out}	30	60	90
Re_c	520	560	564

Table V.5: Evolution of the critical Reynolds number with respect to changes in the location of the outflow plane.

N	6	8	12
Gridpoints	1.43 10^6	3.4 10^6	11.5 10^6
σ	0.0265	0.0105	0.0098
ω	± 0.7932	± 0.8240	± 0.8240

Table V.6: Evolution of the growth rate σ and circular frequency ω of the leading eigenvalue with an increase of the mesh refinement.

Chapter VI

Overall conclusion

This thesis is part of a larger project, the SICOGIF (SImulation and COntrol of Geometrically Induced Flows) project funded by the French National Agency for Research (ANR), involving several different parties. In order to improve their control, this project aims at a better comprehension of the instabilities and non-linear dynamics of flows displaying a geometrically induced separation. Within this framework, the aim of the present thesis has been to develop tools allowing the investigation of the global stability of fully three-dimensional flows. Among the tools that have been developed and implemented within the spectral element code Nek 5000 [62] are:

- the selective frequency damping approach,
- a time-stepper Arnoldi algorithm,
- the Koopman modes decomposition.

In order to illustrate the new capabilities offered by these tools, three flow configurations have been investigated:

- the lid-driven cavity flow,
- the asymmetric stenotic pipe flow,
- the boundary layer flow over a cylindrical roughness element mounted on a flat plate

These three flow configurations, having very different practical applications, have very different properties. The lid-driven cavity flow is essentially an academic problem intensively investigated over the past twenty years. The stenotic pipe flow serves as a first order model to investigate the genesis of atherosclerosis in arteries. Finally, the boundary layer flow over a cylindrical roughness element mounted on a flat plate is practical problem of transition to turbulence on the wings of an airplane.

The lid-driven cavity flow

The flow within a lid-driven cavity is an idealisation of a number of fluid mechanics problems and qualitatively presents most of the important features responsible for transition

in a wide variety of other flows (e.g. shear layers, counter-rotating pairs of vortices, high- and low-speed streaks, ...). From a practical point of view, the lid-driven cavity is a simplification of several engineering situations such as slots on the walls of heat exchangers or simplification of coating devices used in the paper industry for producing high grade paper and photographic film [5].

An extremely large body of literature exists on the instability and transition of strictly two-dimensional lid-driven cavities as well as about 2.5D lid-driven cavities. For 2.5D square lid-driven cavities, the flow is subject to a centrifugal instability of the primary vortex core beyond a critical Reynolds number $Re_c = 780$ [42, 53, 117, 152**?**]. The unstable global mode takes the form of Taylor-Görtler like vortices inducing low- and high-speed streaks on the vertical walls of the cavity. Unfortunately, the body of literature about the instability and transition of fully three-dimensional lid-driven cavities with spanwise end walls is much more sparse. It has been shown by Feldman & Gelfgat [60, 105] and the present work, that the three-dimensional LDC experiences a centrifugal instability of the primary vortex core as well. However, for low to moderate spanwise aspect ratio LDC, the first bifurcation encountered by the flow is no more a pitchfork bifurcation but a Hopf one. Moreover, due to the increased viscous damping induced by the spanwise end walls and the redistribution of the energy input on the three components of the velocity, the critical Reynolds number beyond which the flow transition is higher than that of 2.5 LDC flow. It is remarkable nonetheless that, for very large aspect ratio LDC, this critical Reynolds number tends toward the value predicted from 2.5D global stability analyses. Moreover, the frequency predicted by fully three-dimensional global stability turns out to be in good agreements with the exprimental observations made by Benson & Aidun [28].

Non-linear direct numerical simulations of the unstable flow in a cubical lid-driven cavity have revealed that, once linearly unstable, the flow exhibits intermittent chaotic dynamics. Except the very recent work by Kulhmann & Albensoeder [94], such chaotic dynamics have never been reported in the literature before. Long time integration of the Navier-Stokes equations at $Re = 1930$ (the critical Reynolds number being $Re_c = 1914$) have highlighted that flow remains for a long period of time on a period limit cycle whose properties are well predicted by global stability analysis. However, the flow eventually experiences a chaotic burst. A Koopman mode analysis has put in the limelight that this periodic limit actually is Floquet unstable. Even for a Reynolds number this close to the critical Reynolds number of the Hopf bifurcation, these results show that the Poincarré map associated to the limit cycle has already experienced a Neimarck-Sacker bifurcation. This particular route to chaos and the associated intermittent dynamics have been labelled by Pomeau & Manneville [125] as being intermittent chaos. Further in-depth analyses are currently conducted in order to fully characterise this transition.

The asymmetric stenotic pipe flow

The association of arterial diseases with flow-related mechanisms has motivated the study of the flow within a model geometry of arterial stenosis. Atherosclerosis is a widely spread cardio-vascular disease predominant in most industrialised countries. It is a condition in which an artery wall thickens as a result of the accumulation of fatty material, such as

cholesterol, that might eventually lead to serious health conditions as dangerous as a break-up of the blood vessel's walls.

Numerous experimental and numerical investigations have been conducted on the instability and transition of axisymmetric stenotic pipe flow with steady or periodic inlet velocity profiles [4, 38, 75, 88, 142]. For the particular stenotic geometry considered, the flow experiences a Coanda-like instability beyond a critical Reynolds number $Re_c = 721$. Due to the unstable global mode, the confined jet stemming from the stenotic constriction is deflected away from the pipe's centerline. This deflection eventually triggers a Coanda-type wall reattachment of the flow. These results, found in [142], have been reproduced with the tools developed during this thesis. Unfortunately, recent experimental works [] have revealed that the flow transition to unsteadiness at a substantially lower Reynolds number.

Based on the assumption that this early transition might be caused by small defects of axisymmetry of the geometry, the stenotic constriction has been slightly offset from the pipe's centerline. The stability properties of the resulting slightly asymmetric stenotic pipe flows have then been investigated by means of steady state computations and global stability analyses. For low to moderate Reynolds numbers and relatively small eccentricities of the stenosis, the flow is seen to closely resemble the axisymmetric solution. However, beyond a critical value, the eccentric triggers an early wall reattachement of the confined stenotic jet. Global stability analyses have revealed that the underlying instability mechanism is similar to that of the axisymmetric problem: a Coanda-like instability of the jet stemming from the stenotic constriction. Though the flow already is asymmetric, this global instability further enhances the up-and-down symmetry breaking of the flow. These analyses have moreover shown that, shortly after, the flow should encounter a secondary pitchfork bifurcation. The global mode associated to this secondary bifurcation differs from the leading one. Indeed, it now breaks the remaining left-right symmetry of the flow. Unfortunately, due to time limitations, its non-linear evolution have not been investigated. Yet, based on physical considerations, it is believed by the author that, once this mode is unstable as well, the flow is likely to transition to unsteadiness. Indeed, once this mode is unstable, the flow has no remaining symmetry and the reversed flow region surrounding the stenotic jet is very unlikely to self-sustain. Steady state computation have more revealed the existence of an hysteresis cycle. Such cycle is a genuine feature of subcritical bifurcations thus confirming the conjectures made by Sherwin & Blackburn [142]. Finally, comparison with experimental work of Martin D. Griffith and Pierre-Yves Passaggia has revealed great discrepancies between the experimental observations and the actual predictions obtained by global stability analysis. Preliminary optimal perturbation analysis however suggests that the unsteadiness observed in the experiment might be triggered by transient growth of small disturbances inherent to any experimental setup.

The roughness-induced boundary layer transition

Understanding, predicting and eventually delaying the laminar-turbulent transition in boundary layer flows is a long time challenge for researchers ever since the pioneering

work by Ludwig Prandtl and his two students, Walter Tollmien and Hermann Schlichting. For small amplitude disturbances and supercritical Reynolds numbers, the linear stability theory predicts the slow transition process due to the generation, amplification and secondary instability of Tollmien-Schlichting (TS) waves. It has however been known for quite a long time that this transition process can be greatly modified by environmental noise or by the presence of localised or distributed surface roughness. Depending on the flow's characteristics and the nature of the surface roughness, the transition process can either be promoted or delayed.

It is known since the mid 2000's that boundary layer streaks can delay the natural transition process by reducing the spatial growth rate of Tollmien-Schlichting waves [46**?**]. Following these works, the global stability of the fully three-dimensional boundary layer flow past a cylindrical roughness element mounted on a flat plate has been investigated in details. Two different types of global instability are observed. The symmetry of the first global instability to take place is highly dependent on the aspect ratio of the roughness element considered. For thin cylindrical roughness elements, the first bifurcation taking place is related to a sinuous global instability of the lateral parts of the shear layers developing in the downstream flow, whereas for larger roughness elements it is related to a varicose instability of the three-dimensional shear layer as a whole. The underlying global instability mechanisms are investigated by mean of a kinetic energy transfer analysis between the base flow and the perturbations. Though both instabilities are essentially fed by the work of the Reynolds stresses against the wall-normal and spanwise gradients of the base flow streamwise component, two major differences are still found that allow us to clearly differentiate between the underlying mechanisms. Indeed, on the one hand these investigations have put in the limelight that the sinuous instability is very likely to be related to a global instability of the near-wake region and of the associated reversed flow region similar to what occurs in the flow past a two-dimensional cylinder. On the other hand, the varicose mode is seen to be related to an instability of the downstream low-speed streaks exclusively. Finally, direct numerical simulations have revealed that the sinuous global instability of the wake is related a supercritical Hopf bifurcation of the flow.

Perspectives

The work described in this manuscript essentially deals with the global instability and transition of steady states from a purely numerical and theoretical point of view. From the author's perspective, the work done during this PhD thesis offers various ways to continue it. The short list that follows is not exhaustive and only reflects the current interests of the authors and his collaborators:

- The global instability encountered in the stenotic pipe flow is a non-oscillating one. Hence, the selective frequency damping cannot be used to compute the unstable steady states. In order to overcome this problem, the implementation of a Newton algorithm into the code Nek 5000 is seriously considered. However, since three-dimensional flows involve a relatively number of degrees of freedom, the approach

should be based on a Jacobian free Newton method. For the time being, preliminary work has been done using the Recursive Projection Method (RPM) [143]. This method assumes that the solution to the equations can be divided into two parts: a stable and an unstable part. The stable part of the solution is simply computed by time-marching the equations while the unstable part is computed using a Newton method restricted to the unstable subspace. This method requires very little intrusive modification of the DNS code and its memory footprint is not larger than a classical direct numerical simulation. Moreover, it can easily be coupled with an continuation technique thus allowing the computation of the whole bifurcation diagram of the problem under consideration.

- The whole study on the stenotic pipe flow has been based assuming the inlet velocity profile to be steady. However, in order to have a better understanding of the blood flow in such geometry, one should consider a periodic inflow as in Sherwin & Blackburn [142] and Varghese *et al.* [155]. Under this assumption of periodic flow, the stability analysis then falls in the framework of global Floquet stability theory. Provided an appropriate time sampling is used for the Krylov subspace, the time-stepper Arnoldi algorithm developed during this PhD is able to easily capture the leading Floquet multipliers of the monodromy matrix. Unfortunately, in order to do so, one must first be able to compute the unstable periodic solution. Once again, the selective frequency damping approach cannot be used to compute such solution. Fortunately, the Recursive Projection Method [143] can be reformulated in order to compute these peculiar solutions further underlining the endless possibilities offered by this method.

- The roughness-induced transition has been investigated only through the spectrum of its eigenvalues. Though eigenvalue analysis gives an upper bound for linear instability, it is now well known that non-normality of the linearised Navier-Stokes operator can induce large transient growth. If sufficiently large, this transient growth can eventually trigger the non-linearities and potentially self-sustain. Following the work of Cherubini *et al.* [41] where an optimal perturbation analysis has been perfomed in the fully three-dimensional framework, the author and his collaborators are seriously considering the extension of the tools developed during this thesis to linear and non-linear optimal perturbations. Indeed, as shown in [41], localised transition in linearly stable roughness-induced boundary layer flow can be triggered by optimal perturbations. It is moreover believed that the lower bound for transition observed in the von Doenhoff-Braslow diagram might be predicted by such optimal linear and/or non-linear perturbation analysis.

Depending on one's sensibility, numerous other perspectives could have been added to this non-exhaustive list. However, the present list clearly summarises the author's thoughts about the most challenging way to continue this work. Particularly, the optimal linear and non-linear perturbation analysis is currently investigated by Stefania Cherubini with the help of undergraduate students. Other perspectives can also be found at the end of each chapter. Finally, some aspects requiring further in-depth investigations and development are presented in the various appendices.

Scientific production

List of all the conferences attended during the PhD thesis as well as of all the papers submitted or currently in preparation. Most of these abstracts, conferences presentations and drafts of the paper can be found online on https://sites.google.com/site/loiseaujc.

National conferences

- J.-Ch. Loiseau, J.-Ch. Robinet and E. Leriche
  Stabilité globale 3D d'un écoulement sténosé
  20e Congrès Français de Mécanique, Besançon, France, August 29th-September 2nd, 2011

International conferences

- J.-Ch. Loiseau, S. Acharya Neelavara, J.-Ch. Robinet and E. Leriche
  Subcritical bifurcation in asymmetric stenotic pipe flow
  10th EUROMECH Fluid Mechanics Conference, Copenhagen, Denmark, September 14th-18th, 2014

- J.-Ch. Loiseau, S. Cherubini, J.-Ch. Robinet and E. Leriche
  Influence of the shape on the roughness-induced transition
  Instability and Control of Massively Separated Flows, Prato, Italy, September 4th-6th, 2013

- J.-Ch. Loiseau, J.-Ch. Robinet and E. Leriche
  Dynamics of a boundary layer flow over a cylindrical rugosity
  14th European Turbulence Conference, Lyon, France, September 1st-4th, 2013

- J.-Ch. Loiseau, J.-Ch. Robinet and E. Leriche
  Transition of the flow over a cylindrical rugosity mounted on a flat plate
  Trends in Open Shear Flow Instability, Euromech Colloquium 547, Palaiseau, France, July 1st-3rd, 2013

- J.-Ch. Loiseau, J.-Ch. Robinet and E. Leriche
  Cylindrical roughness-induced transition on a flat plate
  10th ERCOFTAC SIG 33 Workshop, Sandhamn, Sweden, May 29th-31st, 2013

- J.-Ch. Loiseau, J.-Ch. Robinet and E. Leriche
  Influence of the eccentricity on the global stability of stenotic pipe flows
  9th EUROMECH Fluid Mechanics Conference, Roma, Italy, September 9th-13th, 2012

- J.-Ch. Loiseau, J.-Ch. Robinet and E. Leriche
  Global stability of an isolated cylindrical rugosity
  XXIII ICTAM, Beijing, China, August 19th-24th, 2012

- F. Alizard, J.-Ch. Loiseau and J.-Ch. Robinet
  Bifurcations for an incompressible flow passing over an open-cavity
  XXIII ICTAM, Beijing, China, August 19th-24th, 2012

Papers

- J.-Ch. Loiseau, J.-Ch. Robinet, S. Cherubini and E. Leriche
  Investigation of the roughness-induced transition: global stability analyses and direct numerical simulations
  Submitted for publication in *Journal of Fluid Mechanics*.

- J.-Ch. Loiseau, S. Cherubini, J.-Ch. Robinet and E. Leriche
  Influence of the shape on the roughness-induced transition
  Fluid Mechanics and its applications series, Springer, **accepted**.

- A. Ducoin, J.-Ch. Robinet and J.-Ch. Loiseau
  The scenario of laminar to turbulent transition on a wing section - A numerical study
  To be submitted in *Journal of Fluid Mechanics*.

- J.-Ch. Loiseau, J.-Ch. Robinet and E. Leriche
  Influence of the spanwise aspect ratio on the stability of three-dimensional lid-driven cavities
  Under preparation.

- J.-Ch. Loiseau, J.-Ch. Robinet and E. Leriche
  Transition to chaos in the cubical lid-driven cavity flow
  Under preparation.

Appendices

Appendix A

Very large aspect ratio lid-driven cavity flow

Contents

A.1 Primary base flow **167**

A.2 Non-linear evolution **168**

A.3 Conclusion **168**

The linear instability and transition scenario of the flow developping within lid-driven cavities having small ($\Lambda = 0.5$) to moderate ($\Lambda = 3$) aspect ratios have been investigated in chapter III. It was shown that, for such cases, the first bifurcation to take place is a Hopf bifurcation resulting from an oscillatory centrifugal instability of the primary vortex core. The associated globally unstable mode was seen to be closely related to the $T1$-branch of modes found by Theofilis *et al.* [152] when investigating the stability of two-dimensional lid-driven cavities with respect to spanwise-periodic perturbations. Unfortunately, the conclusions drawn from these three-dimensional moderate aspect ratio cavities do not seem to hold for very large aspect ratio 3D ones. Indeed, steady Taylor-Görtler vortices have been observed experimentally by Albensoeder & Kuhlmann [8**?**] in an aspect ratio $\Lambda = 6.55$ LDC before any unsteadiness could be seen, thus relating the emergence of these steady TGL vortices to the $S1$-branch of stationnary modes instead. As to provide the reader with a few insights about the transition scenario of very large three-dimensional LDC, preliminary results obtained about the primary instability of an aspect ratio $\Lambda = 6$ lid-driven cavity are presented in this appendix.

A.1 Primary base flow

Figure A.1(a) depicts one of the streamlines for the flow in the lid-driven cavity having an aspect ratio $\Lambda = 6$ at a Reynolds number $Re = 900$. As one can see, as for the low to moderate aspect ratio LDC presented in chapter III, the streamline remains enclosed within the left part of the cavity indicating the flow is symmetric with respect to the spanwise mid-plane of the cavity. On figure A.1(b) is depicted the comparison of the flow along the $x = 0$ and $y = 0$ lines with its two-dimensional counterpart. It is obvious from

the latter figure that, contrary to the low to moderate aspect ratio LDC, assuming the flow within this plane to be essentially two-dimensional hardly yields to an over-prediction of the strength of the vertical upward and downward boundary layers developing along the upstream and downstream walls, respectively and is hence a relatively good proxy.

A global stability analysis of this three-dimensional base flow has been performed. The Krylov subspace used has dimension 250, whereas the sampling period is set to 1.5 enabling good convergence of the eigenvalues up to $\omega = 1$. Figure A.2 depicts the computed eigenspectrum. Whereas the eigenspectra for low to moderate spanwise aspect ratio cavities presented in section III.3.2 are dominated by complex conjugate pairs of eigenvalues, the one for large aspect ratio LDC seems to be dominated by a real eigenvalue. It is worthy to note however that two eigenvalues are actually overlapping on this spectrum ($\sigma_1 = -4.91611\ 10^{-3}$ and $\sigma_2 = -4.91636\ 10^{-3}$). It thus appears that one has either two really close eigenvalues or a single one with multiplicity 2. As previously however, these two eigenvalues are related to two modes having opposite symmetries. Anyhow, the first bifurcation the flow might encounter at a very slightly larger Reynolds number ($900 \leq Re_c \leq 925$) is no more a Hopf bifurcation but now appears to be either a transcritical or a pitchfork one.

Figure A.3(a) depicts the vertical velocity component of the symmetric mode, wheres figure A.3(b) highlights the motion it induces in the $y = -0.25$ plane. Once again, this mode takes the form of Taylor-Görtler like vortices and induces vertical low- and high-speed streaks in the vicinity of the upstream and downstream walls of the lid-driven cavity. However, since it is related to a real valued eigenvalue, the induced TGL vortices are now non-oscillating and, hence, related to the $S1$-branch observed in the 2.5D lid-driven cavity flow rather than to the $T1$-branch as previously.

A.2 Non-linear evolution

As shown by the global stability analysis, the steady equilibrium compted for $Re = 900$ is on the verge to become unstable. Increasing very slighlty the Reynolds number up to $Re = 925$ is enough to cause a change in the nature of this stable equilibrium. Surprisingly, though linear stability predicts the onset of a non-oscillating mode, unsteadiness is clearly present in the evolution of the kinetic energy depicted on figure A.4. These oscillations are related to spanwise travelling Taylor-Görtler vortices. Since these are preliminary calculations, no clear conclusion can be given. Nonetheless, it is clear that the onset of unsteadiness greatly differs between low to moderate LDC considered in chapter III and the present very large aspect ratio one.

A.3 Conclusion

Present results highlight the fact that for very large aspect ratio lid-driven cavity flows the transition scenario might be slightly different from the one presented in chapter III. Indeed, though the base flow in a $\Lambda = 6$ aspect ratio lid-driven cavity qualitatively presents the same essential features as its low to moderate spanwise aspect ratios counterparts, it

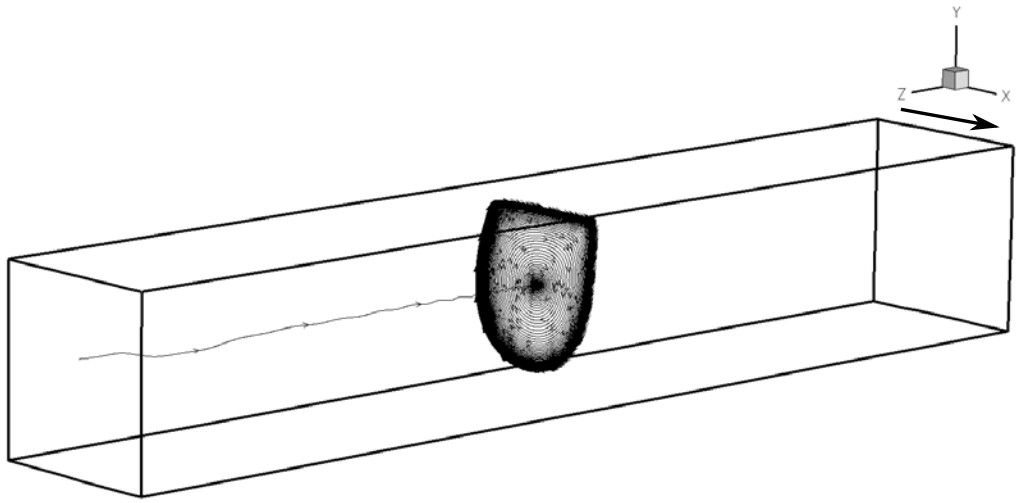

(a)

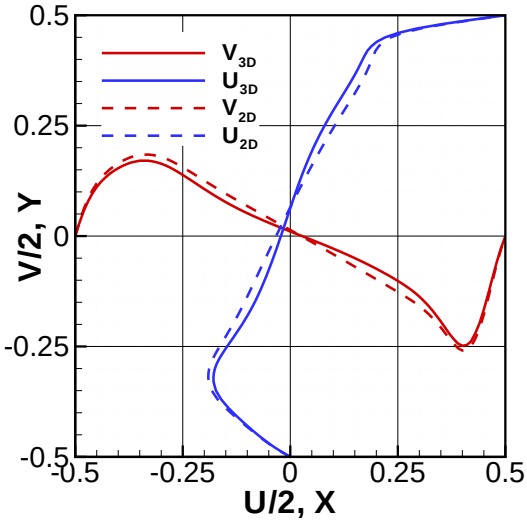

(b)

Figure A.1: Visualisation of the steady state solution for $(\Lambda, Re) = (6, 900)$. (a) Streamline visualisation. (b) Comparison of the velocity (solide lines) along the $x = 0$ (blue) and $y = 0$ (red) lines with their two-dimensional counterparts (dashed lines).

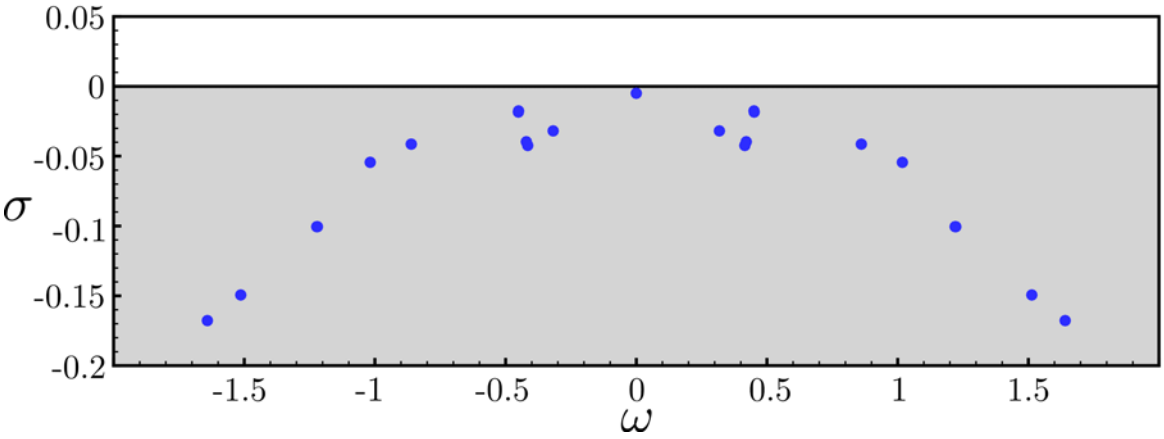

Figure A.2: Spectrum of the linearised Navier-Stokes operator for $(\Lambda, Re) = (6, 900)$.

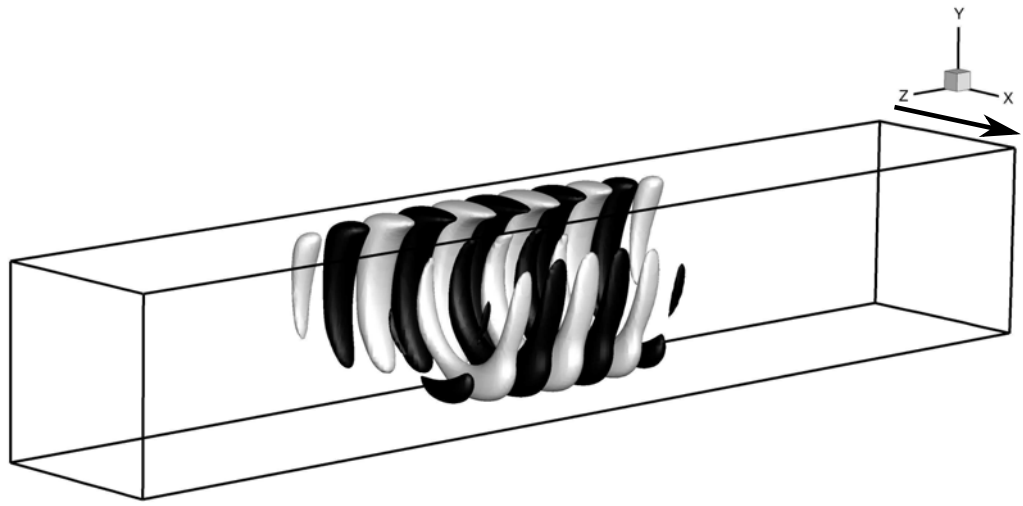

(a)

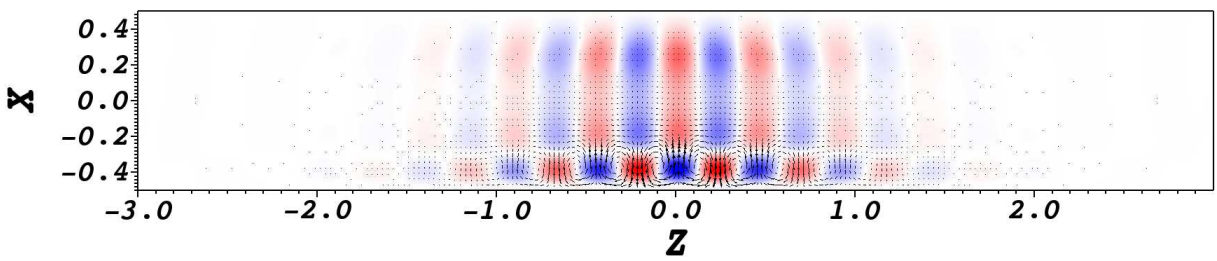

(b)

Figure A.3: (a) Vertical velocity component of the leading symmetric global mode's real part. Isosurfaces depict ±10% of the vertical velocity's maximum. (b) Motion it induces in the $y = -0.25$ plane. Vectors depict the in-plane motion whereas coloured contours shows the vertical motion.

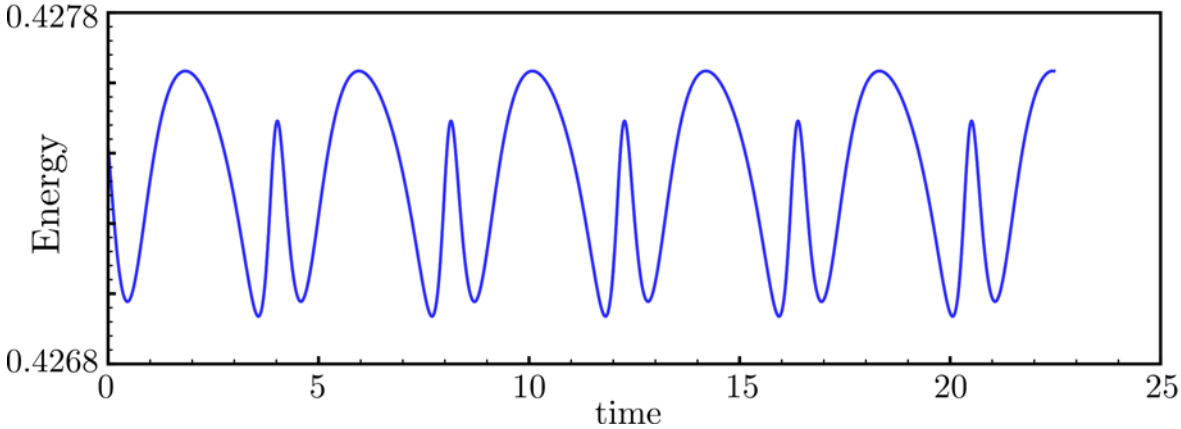

Figure A.4: Time evolution of the kinetic energy of the flow within a lid-driven cavity of spanwise aspect ratio $\Lambda = 6$ at $Re = 925$.

becomes unstable at a lower Reynolds number ($Re_c \simeq 900$). Moreover, the eigenspectrum of linearised Navier-Stokes operator is no more dominated by a complex conjugate pair of eigenvalues but a real-valued one indicating it might be related to the $S1$-branch observed in 2.5D lid-driven cavity flows [152]. It thus appears that the flow does not experience a Hopf bifurcation but either a transcritical or pitchfork one. Yet, the underlying linear instability mechanism remains unchanged: creation of Taylor-Görtler like vortices due to a centrifugal instability of the flow. Direct numerical simulation of the non-linearly saturated flow at $Re = 925$ has revealed that, despite the eigenspectrum of the linearised Navier-Stokes operator being dominated by a real eigenvalue, unsteadiness is observed in the preliminary DNS. This behaviour appears to be in contradiction with the observations made by Albensoeder & Kuhlmann [8**?**] on a $\Lambda = 6.55$ lid-driven cavity flow. Because of the preliminary character of the present study, the mechanism responsible for the emergence of this low frequency unsteadiness has not been investigated yet. A possible hypothesis however is that it might be related to the wavelength selection mechanism presented in [8]. Further calculations and in-depth analyses are however required to fully answer this question.

Appendix B

Influence of the shape on the roughness-induced transition

Contents

B.1 Introduction 174

B.2 Problem formulation 174

B.3 Results and discussion 175

B.4 Conclusion 177

The work presented in this appendix results from a joint collaboration between myself, Stefania Cherubini, Jean-Christophe Robinet and Emmanuel Leriche. It has been presented at the *Instability and Control of Massively Separated Flows* Conference held early September 2013 in Prato, Italy. It has morever been submitted and accepted for publication in Springer's *Fluid Mechanics and its applications* series. The pdf version of this short paper as well as the slides of the talk given at the conference can be found online[1].

Abstract

Global instability analysis of the three-dimensional flow past two roughness elements of different shape, namely a cylinder and a bump, is presented. In both cases, the eigenspectrum is made of modes characterised by a varicose symmetry and localised mostly in the zones of large base flow shear. The primary instability exhibited is the same in both cases and consists in an isolated unstable mode closely related to streaks local instability. For the cylinder however, a whole branch of modes is in addition destabilised as the Reynolds number is further increased.

[1]https://sites.google.com/site/loiseaujc/publications/conference-proceedings

B.1 Introduction

Delaying transition in spatially developing boundary layer flows has been a long time challenge. For small amplitude disturbances and supercritical Reynolds numbers, the linear stability theory predicts the slow transition process due to the generation, amplification and secondary instability of Tollmien-Schlichting (TS) waves. It has been shown recently in Ref.[67] that those TS waves can be stabilised by streamwise streaks. In this experimental work, sub-optimal streaks have been created using a periodic array of cylindrical roughness elements. Despite the stabilising effect of the streaks on the TS waves, the flow may undergo transition to turbulence right downstream the roughness elements provided the streaks are strong enough. This roughness-induced transition has been extensively investigated experimentally by different authors [44, 149, 159]. For cylindrical roughness elements, in the early 60's, most of the results available back then have been reviewed in Ref.[158] into one transition diagram, thus giving an empirical criterion for transition. However, fewer studies have been carried out on smooth roughness elements, and the influence of the shape of the roughness on the destabilisation process has not yet been investigated in detail. Though the mechanism responsible for transition to turbulence in the flow past a 3D roughness element is not yet fully understood, it is believed that it is due to an instability of the streaks induced by the roughness elements. Thus, in order to investigate the origin of unsteadiness, a global instability analysis on the three-dimensional flow past a sharp-edged and a smooth roughness element is performed.

B.2 Problem formulation

The aim of the present work is to investigate the influence of the shape of the roughness element on the streaks generation further downstream along with their possible global instability. Two different kinds of roughness elements having aspect ratio $d/k = 2$ (where d is the diameter and k is the maximum height of the roughness), both mounted on a flat plate, have thus been considered: a cylindrical roughness element, and a smoother one defined by a cubic cosine function, $h(r) = k\cos^3(\pi r/d)$, r being the distance from the centre of the bump on the $x - z$ plane.

The flow past these roughness elements is studied using the 3D incompressible Navier-Stokes (NS) equations, non-dimensionalised with respect to the maximum height k of the roughness and the free-stream velocity U_∞; therefore, the Reynolds number is defined as $Re = U_\infty k/\nu$, ν being the kinematic viscosity. The computational domain extends from $x = -15$ to $x = 90$ in the streamwise direction, has a spanwise extent of $L_z = 16$ and wall-normal dimension $L_y = 50$ such that the global stability results are almost independent of the domain size. The Blasius velocity profile prescribed at the inlet ($x = -15$) is chosen such that, in the absence of the roughness element, one would have a theoretical Blasius boundary layer thickness of $\delta_{99} = 2$ at $x = 0$.

The behaviour of an infinitesimal perturbation $\mathbf{q} = (\mathbf{u}, p)^T$ superposed to a 3D steady state $\mathbf{Q} = (\mathbf{U}, P)^T$ has been studied using a global stability analysis. The steady base flows have been computed using the selective frequency damping (SFD) approach introduced in Ref.[6]. The following boundary conditions have been applied: at the inlet, the

Blasius boundary layer velocity profile is imposed for the streamwise and wall-normal components of the velocity, whereas its spanwise component is set to zero. At the outlet, a standard outflow boundary condition is used. In the spanwise direction, periodic boundary conditions are imposed for the three components of the velocity. At the upper boundary, the streamwise component has been set equal to U_∞, and a Neumann condition on the wall-normal direction has been imposed for the wall-normal and spanwise components of the velocity. Finally, a no-slip condition is imposed on the flat plate and the roughness element's walls.

Once the base flow has been computed, the NS equations are linearised around such a steady state, leading to a problem of the following type:

$$\frac{\partial \mathbf{u}}{\partial t} = A\mathbf{u}, \tag{B.1}$$

which is subject to the same boundary conditions as previously except regarding the inflow and the upper boundaries where a zero-velocity condition is prescribed. To perform a global stability analysis, one has to compute the eigenvalues of the Jacobian matrix A, which is a hard computational task due to the large number of degrees of freedom involved. Thus, a time-stepper approach as introduced in Ref.[57] and Ref.[20] has been used, which avoids the explicit storage of A and direct computation of its eigenvalues.

All of the calculations were performed using the code Nek5000 [62]. Spatial discretisation is done by a spectral elements method with Lagrange polynomials of order $N = 8$. The convective terms are advanced in time using an extrapolation of order 3, whereas the viscous terms use a backward differentiation of order 3 as well.

B.3 Results and discussion

Figure B.1 shows base flows obtained at $Re = 1000$ for both roughness elements considered. An upstream and a downstream reversed flow region are shown in the right frames of figure B.1 by the $U = 0$ isosurface (blue). In the left frames, the streaks induced by the roughness elements, being defined as the deviation of the base flows from the Blasius velocity profile U_B as in Ref.[44], are plotted. These flows share similar features: five streaks can be observed, two positive (red) and three negative (green) ones. These are induced by the presence of strong horseshoe vortices wrapped around the roughness elements, whose legs transport the low and high-momentum flow upwards and downwards in the boundary layer. These counter-rotating vortices induce the two outer pairs of streaks, whereas the central low-speed one is due to the streamwise velocity deficit induced by the roughness element.

Though their main structure is similar, some differences are found between the two flow fields. Indeed, for the case of the bump: (i) the separation zone is smaller than for the cylinder; (ii) the horseshoe vortex wrapping around the roughness element is much more spanwise-localised, its legs being weaker and closer one to the other; (iii) the streaks are weaker and quickly fade away downstream of the roughness element, whereas for the cylinder they appear to sustain on a much longer streamwise extent.

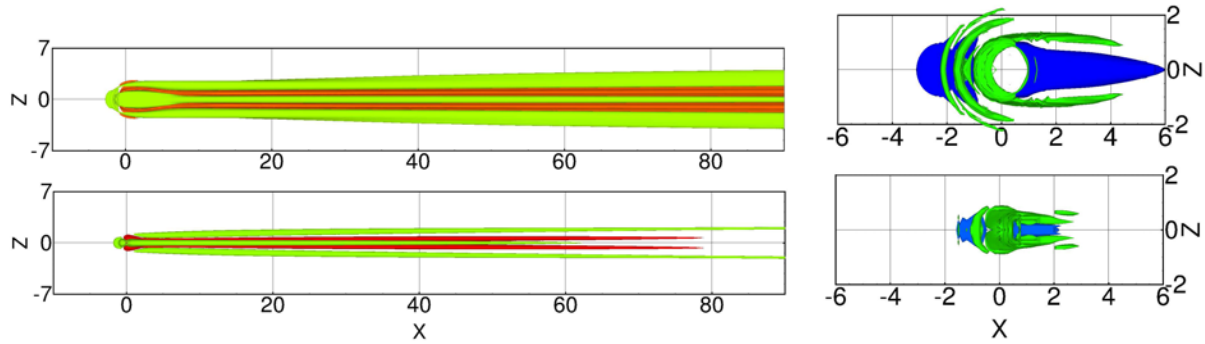

Figure B.1: Base flows computed at $Re = 1000$ in the presence of a cylinder (top) and a bump (bottom). The left frames show positive (red) and negative (green) surfaces of $U_{st} = U - U_B$, with $U_{st} = \pm 0.1$ (top) and $U_{st} = \pm 0.05$ (bottom); the right frames show isosurfaces of the $U = 0$ contour (blue), highlighting the separation zone, and the Q-criterion (green, for $Q = 0.1$).

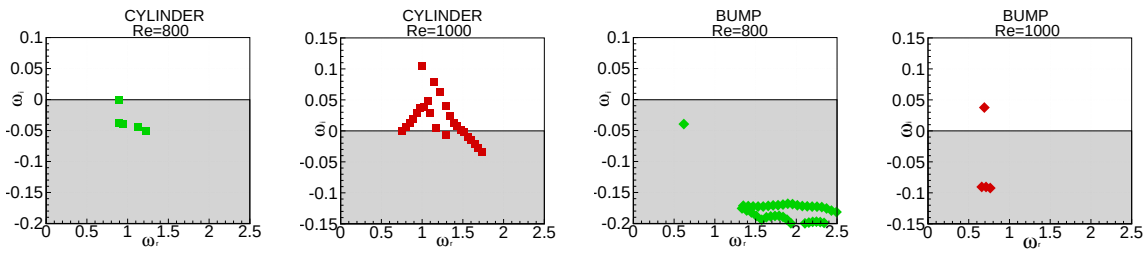

(a) (b) (c) (d)

Figure B.2: Eigenspectra obtained for the flow past a cylinder with $Re = 800$ (a) and $Re = 1000$ (b), and for the flow past a bump with $Re = 800$ (c) and $Re = 1000$ (d).

The eigenspectra obtained for the cylinder case at $Re = 800$ and $Re = 1000$ are provided in Figure B.2 (a) and (b), respectively. At $Re = 800$, one can observe a single isolated eigenvalue lying almost on the neutral axis. Slightly increasing the Reynolds number drives the most unstable mode to move towards the upper-half complex plane, so that the flow becomes globally unstable at $Re_{cr} \approx 805$. Further increasing the Reynolds number yields a whole branch of eigenvalues to move in the upper-half complex plane, as shown in Figure B.2 (b) for $Re = 1000$.

Regarding the bump, a similar behaviour has been found. Figure B.2 (c) shows the eigenspectrum obtained for $Re = 800$. As previously, a single isolated mode is observed within the lower-half complex plane. When the Reynolds number is increased this eigenvalue moves upwards, reaching the upper-half of the complex plane at $Re_{cr} \approx 891$ as shown on figure B.2 (d).

As to get some insights on the instability mechanisms, the shape of the two unstable global modes is closely looked at. Figure B.3 provides the streamwise component of the velocity for the most unstable eigenmode obtained at $Re = 1000$ for the cylinder case (left) and the bump one (right). These global modes are both characterised by streamwise alternated patches of positive/negative velocity developing mostly along the central low-

speed streak, showing a symmetry with respect to the $z = 0$ plane. For the cylindrical element, the wave packet is placed well downstream of the roughness element, in a region where the streaks are well-developed and quasi-parallel. On the other hand, in the bump case, the most unstable eigenmode is placed closer to the roughness element which is concordant with the weaker streaks and gradients induced by the bump as well as their smaller streamwise extent.

The location and structure of the spatial support of the most unstable modes with respect to the base flow streaks at $Re = 1000$ are shown in figure B.4 (a) and (b) for both cases, respectively. For the cylinder case, the streamwise velocity contours of the eigenvector (shaded contours) and of the base flow (solid lines) are provided in the $x = 25$ plane. The strong deformation of the $U = const$ contours indicates the large amplitude of the streaks. The zones of maximum amplitude of the eigenvector are localised on the flanks and the top of the streaks, where the spanwise and wall-normal shears are the largest. A similar behaviour is observed for the bump case, as shown in figure B.4 (b). As indicated by the deformation of the $U = const$ contours in the $x = 15$ plane, the streaks are weaker and much more localised in the spanwise direction. The spatial structure of the eigenvector is similar to the one recovered for the cylinder, showing a mushroom-shaped disturbance on top of the central low-speed streak, with maximum velocity values located in the zones of maximum base-flow shear. However, the spatial support of the mode is much more compact in the spanwise direction.

These locations seem to indicate that these unstable global modes might be linked to a streak instability similar to the one recovered for parallel optimal streaks in Ref.[13] and that the instability mechanism might be related to the transport of the base flow shear by the perturbation. It is noteworthy that, for parallel streaks, the primary instability is of sinuous type, whereas in the present case it is of varicose type. However, one must note that for thinner roughness elements (not presented here) similar sinuous instabilities have also been recovered. The present results also confirm that, for large roughness elements, varicose perturbations are the most dangerous ones, as also highlighted by a global transient growth analysis in Ref.[41].

B.4 Conclusion

The flows past two roughness elements, a cylindrical and a cubic-cosine one, have been investigated. The cylindrical roughness element induces strong streaks which appear to be well sustained in the streamwise direction, whereas in the bump case the streaks are weaker and eventually fade away. In both cases, a global stability analysis of the three-dimensional steady base flow has been carried out. In all of the cases considered, the spectra are composed by modes characterised by a varicose symmetry, mostly localised in the zones of large base flow shear and related to an instability of the quasi-parallel streaks. Finally, the critical Reynolds number being higher for the smooth bump than for the cylindrical roughness element might be related to the weaker amplitude of the induced streaks in the former case.

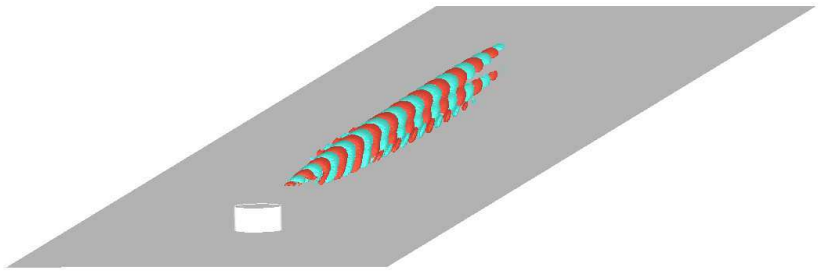

(a)

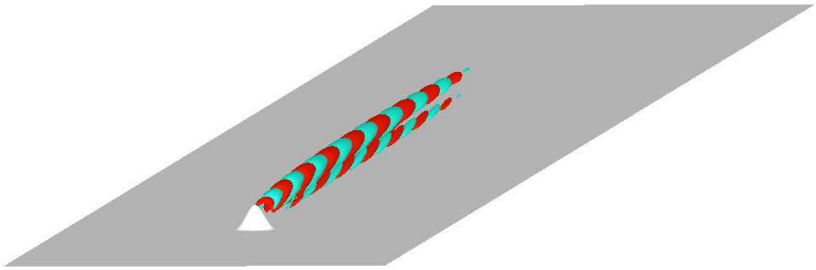

(b)

Figure B.3: Streamwise velocity component of the eigenvector of the most unstable mode obtained at $Re = 1000$ for the cylindrical roughness element (a) and the smooth one (b).

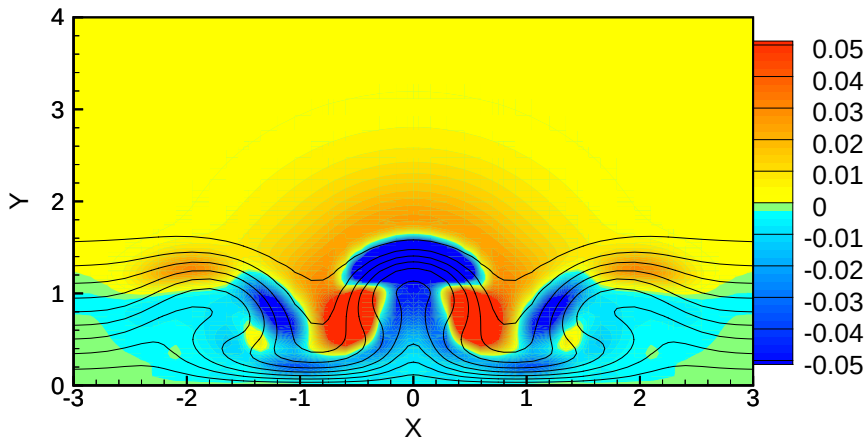

(a)

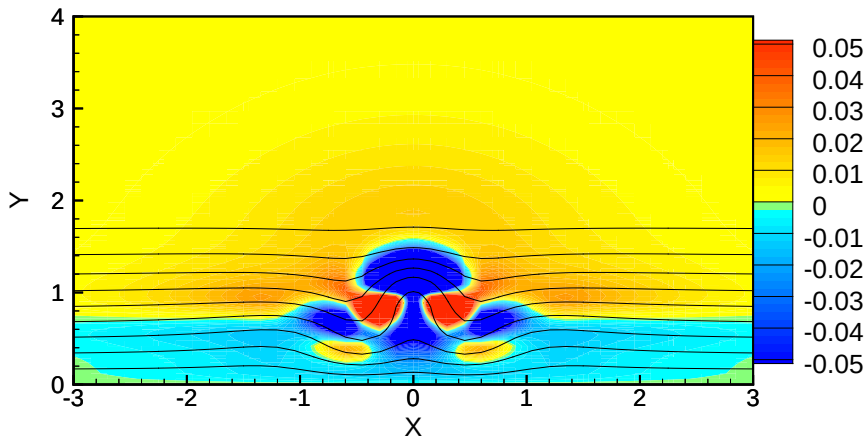

(b)

Figure B.4: Shaded contours of the streamwise component the most unstable mode for the cylindrical roughness element in the plane $x = 25$ (a) and the cubic-cosine-shaped one at $x = 15$ (b) with $Re = 1000$. The solid lines are the base-flow streamwise velocity contours in the range $[0.1, 0.9]$.

Bibliography

[1] Web page of depositphotos. http://depositphotos.com/5877843/stock-illustration-Ath

[2] Web page of webmd. http://www.webmd.com/heart-disease/atherosclerosis-19012.

[3] M. Acalar and C. Smith. A study of hairpin vortices in a laminar boundary layer: part 1, hairpin vortices generated by a hemisphere protuberance. *J. Fluid Mech.*, 175:1–41, 1987.

[4] S. A. Ahmed and D. P. Giddens. Velocity measurement n steady flow through axisymmetric stenoses at moderate reynolds numbers. *J. Biomech.*, 16:505–516, 1983.

[5] C.K. Aidun. Principles of hydrodynamic instability: Application in coating systems. part 2: Exemples of flow instability. *Tappi Journal*, 3:213–220, 1991.

[6] E. Akervik, L. Brandt, D. S. Henningson, J. Hoepffner, O. Marxen, and P. Schlatter. Steady solutions of the navier-stokes equations by selective frequency damping. *Physics of fluids*, 18, 2006.

[7] S. Albensoeder and H. C. Kuhlmann. Accurate three-dimensional lid-driven cavity flow. *J. Comput. Phys.*, 206:536–558, 2005.

[8] S. Albensoeder and H. C. Kuhlmann. Nonlinear three-dimensional flow in the lid-dirven square cavity. *J. Fluid Mech.*, 569:465–480, 2006.

[9] S. Albensoeder, H.C. Kuhlmann, and H.J. Rath. Three-dimensional centrifugal-flow instabilities in the lid-driven cavity problem. *Physics of fluids*, 12, 2001.

[10] F. Alizard, U. Rist, and J.-Ch. Robinet. Linear instability of streamwise corner flow. In *Advances in Turbulence XII*, volume 132, pages 67–70, 2009.

[11] C. Allery, J.-M. Cadou, A. Hamdouni, and D. Razafindralandy. Application of the asymptotic numerical method to the Coanda effect study. *Revue européenne des éléments finis*, ??:1–21, 2003.

[12] Amond and Patera. Numerical calculation of stable three-dimensional tertiary states in grooved-channel flow. *Phys. Fluids A 1*, 1989.

[13] P. Andersson, L. Brandt, A. Bottaro, and D.S. Henningson. On the breakdown of boundary layer streaks. *J. Fluid Mech.*, 428:29–60, 2001.

[14] A. C. Antoulas. *Approximation of large-scale dynamical systems.* Society for Industrial and Applied Mathematics (SIAM), 2005.

[15] D. Arnal, R. Houdeville, A. Séraudie, and O. Vermeersch. Overview of laminar-turbulent transition investigations at ONERA toulouse. In 41st *AIAA Fluid Fynamics Conference*, 2011.

[16] W.E. Arnoldi. The principle of minimized iterations in the solution of the matrix eigenvalue problem. *Quarterly of Applied Mathematics*, 9:1951, 1951.

[17] M. Asai, Y. Konishi, Y. Oizumi, and M. Nishioka. Growth and breakdown of low-speed streaks leading to wall turbulence. *J. Fluid Mech.*, 586:371–396, 2007.

[18] M. Asai, M. Minagawa, and M. Nishioka. The instability and breakdown of a near-wall low-speed streak. *J. Fluid Mech.*, 455:289–314, 2002.

[19] M. Avila, A. P. Willis, and B. Hof. On the transient nature of localized pipe flow turbulence. *J. Fluid Mech.*, 646:127–136, 2010.

[20] S. Bagheri, E. Akervik, L. Brandt, and D. S. Henningson. Matrix-free methods for the stability and control of boundary layers. *AIAA Journal*, 47, 2009.

[21] S. Bagheri, P. Schlatter, P.J. Schmid, and D.S. Henningson. Global stability of a jet in crossflow. *J. Fluid Mech.*, 624:33–44, 2009.

[22] C. J. Baker. The laminar horseshoe vortex. *J. Fluid Mech.*, 95:347–367, 1978.

[23] P. Balakumar and M. Kegerise. Roughness induced transition in a supersonic boundary layer. In 43rd *AIAA Fluid Dynamics Conference*, 2013.

[24] Barkley and Henderson. Floquet stability analysis of the periodic wake of a circular cylinder. *J. Fluid Mech.*, 1996.

[25] D. Barkley, H.M. Blackburn, and S.J. Sherwin. Direct optimal growth analysis for timesteppers. *International journal for numerical methods in fluids*, 57:1435–1458, 2008.

[26] D. Barkley, H.M. Blackburn, and S.J. Sherwin. Direct optimal growth analysis for timesteppers. *Int. J. Meth. Fluids*, 57:1435–1458, 2008.

[27] J.-Fr. Beaudoin. *Contrôle actif d'écoulement en aérodynamique automobile.* PhD thesis, Ecole des Mines de Paris, 2004.

[28] J.D. Benson and C.K. Aidun. Transition to unsteady nonperiodic state in a through-flow lid-driven cavity. *Phys. Fluids A*, 4:2316–2319, 1992.

[29] M. Bernardini, S. Pirozzoli, and P. Orlandi. Compressibility effects on roughness-induced boundary layer transition. *Int. J. Heat and Fluid Flow*, 35:45–51, 2012.

[30] F. P. Bertolotti, T. Herbert, and P. R. Spalart. Linear and nonlinear stability of the blasius boundary layer. *J. Fluid Mech.*, 242:441–474, 1992.

[31] H.M. Blackburn and S.J. Sherwin. Instability modes and transition of pulsatile stenotic flow: pulse-period dependence. *J. Fluid Mech.*, 573:57–88, 2007.

[32] H.M. Blackburn, S.J. Sherwin, and D. Barkley. Convective instability and transient growth in steady and pulsatile stenotic flows. *J. Fluid Mech.*, 607:267–277, 2008.

[33] O. Botella and R. Peyret. Benchmark spectral results on the lid-driven cavity flow. *Comp. Fluids*, 27(4):421–433, 1998.

[34] L. Brandt. Numerical studies of the instability and breakdown of a boundary-layer low-speed streak. *European Journal of Mechanics - B/Fluids*, 26(1):64–82, 2007.

[35] L. Brandt. Numerical studies of the instability and breakdown of a boundary layer low-speed streak. *European Journal of Mechanics B/Fluids*, 26:64–82, 2007.

[36] G. A. Brès and T. Colonius. Three-dimensional instabilities in compressible flow over open cavities. *J. Fluid Mech.*, 599:309–339, 2008.

[37] O. R. Burggraf. Analytical and numerical studies of the structure of steady separated flows. *J. Fluid Mech.*, 24:113–151, 1966.

[38] R. A. Cassanova and D. P. Giddens. Disorder distal to modified stenoses in steady and pulsatile flow. *J. Biomech.*, 11:441–453, 1978.

[39] F. Charru. *Instabilités hydrodynamiques.* EDP Sciences, ??

[40] K. K. Chen, J. H. Tu, and C. W. Rowley. Variants of dynamics mode decomposition: boundary condition, koopman and fourier analyses. *J. Nonlinear Science*, 22(6):887–915, 2012.

[41] S. Cherubini, M.D. De Tullio, P. De Palma, and G. Pascazio. Transient growth in the flow past a three-dimensional smooth roughness element. *J. Fluid Mech.*, 724:642–670, 2013.

[42] J. Chicheportiche, X. Merle, X. Gloerfelt, and J.-Ch. Robinet. Direct numerical simulation and global stability analysis of three-dimensional instabilities in a lid-driven cavity. *C.R. Mech.*, 2008.

[43] J. M. Chomaz. Global instabilities in spatially developing flows: non-normality and non linearity. *Annu. Rev. Fluid Mech*, 37:357–392, 2005.

[44] M. Choudhari and P. Fischer. Roughness-induced transient growth. *35th AIAA Fluid Dynamics Conference and Exhibit, Toronto, Ontario Canada*, AIAA-2005-4765, 2005.

[45] J. D. Cole. On a quasilinear parabolic equation occuring in aerodynamics. *Quart. Appl. Math.*, 9:225–236, 1951.

[46] C. Cossu and L. Brandt. On Tollmien-Schlichting-like waves in streaky boundary layers. *European Journal of Mechanics - B/Fluids*, 23(6):815–833, 2004.

[47] G.D. Davis and G.D. Mallinson. An evaluation of upwind and central difference approximations by a study of recirculating flow. *Comput. Fluids*, 4, 1976.

[48] N. de Tullio, P. Paredes, N.D. Sandham, and V. Theofilis. Laminar-turbulent transition induced by discrete roughness element in a supersonic boundary layer. *J. Fluid Mech.*, 735:613–646, 2013.

[49] N.A. Denissen and E.B. White. Roughness-induced bypass transition revisited. *AIAA Journal*, 46(7):1874–1877, 2008.

[50] N.A. Denissen and E.B. White. Continuous spectrum analysis of roughness-induced transient growth. *Phys. Fluids*, 21(114105), 2009.

[51] N.A. Denissen and E.B. White. Secondary instability of roughness-induced transient growth. *Phys. Fluids*, 25(114108), 2013.

[52] M.O. Deville, P.F. Fischer, and E.H. Mund. *High-Order methods for incompressible fluid flow.* Cambridge University Press, 2002.

[53] Y. Ding and M. Kawahara. Linear stability of incompressible fluid flow in a cavity using finite element method. *Int. J. Num. Meth. Fluids*, 27:139–157, 1998.

[54] P. G. Drazin. *Introduction to hydrodynamic instability.* Cambridge University Press, 2002.

[55] P. G. Drazin and W. H. Reid. *Hydrodynamic stability.* Cambridge University Press, 1981.

[56] A. Ducoin, J.-Ch. Robinet, and J.-Ch. Loiseau. The scenario of laminar to turbulent: Transition on a wing section - a numerical study. *Submitted for publication to J. Fluid Mech.*, 2014.

[57] W.S. Edwards, L.S. Tuckerman, R.A. Friesner, and D.C. Sorension. Krylov methods for the incompressible navier-stokes equations. *Journal of computational physics*, 110:82–102, 1994.

[58] U. Ehrenstein and F. Gallaire. Two-dimensional global low-frequency oscillations in a separating boundary layer flow. *J. Fluid Mech.*, 614:315–327, 2008.

[59] F. G. Ergin and E. B. White. Unsteady and transitional flows behind roughness elements. *AIAA Journal*, 44(11):2504–2514, 2006.

[60] Y. Feldman and A. Yu. Gelgat. Oscillatory instability of a three-dimensional lid-driven flow in a cube. *Physics of fluids*, 22, 2010.

[61] P. Fischer and M. Choudhari. Numerical simulation of roughness induced transient growth in a laminar boundary layer. In 34th *AIAA Fluid Dynamics Conference*, 2004.

[62] P. F. Fischer, J. W. Lottes, and S. G. Kerkemeier. nek5000 Web page. https://nek5000.mcs.anl.gov/index.php/Main_Page, 2008.

[63] P.F. Fischer, J.W. Lottes, and S.G. Kerkemeir. nek5000 Web pages, 2008. http://nek5000.mcs.anl.gov.

[64] A. Fortin, M. Jardak, J.J. Gervais, and R. Pierre. Localization of hopf bifurcations in fluid flow problems. *Int. J. Numer. Meth. Fluids*, 24:1185–1210, 1997.

[65] J.H.M. Fransson, L. Brandt, A. Talamelli, and C. Cossu. Experimental and theoretical investigation of the nonmodal growth of steady streaks in a flat plate boundary layer. *Physics of Fluids*, 10(3627), 2004.

[66] J.H.M. Fransson, L. Brandt, A. Talamelli, and C. Cossu. Experimental study of the stabilization of Tollmien–Schlichting waves by finite amplitude streaks . *Phys. Fluids*, 17(5):054110, 2005.

[67] J.H.M Fransson, A. Talamelli, L. Brandt, and C. Cossu. Delaying transition to turbulence by a passive mechanism. *Phys. Rev. Letters*, 96(064501), 2006.

[68] J.J. Gervais, D. Lemlin, and R. Pierre. Some experiments with stability analysis of discrete incompressible flows in the lid-driven cavity. *Int. J. Numer. Meth. Fluids*, 24:477–492, 1997.

[69] F. Giannetti and P. Luchini. Structural sensitivity of the first instability of the cylinder wake. *J. Fluid Mech.*, 581:167–197, 2007.

[70] Goldhirsch, Orszag, and Maulik. Aan efficient method for computing leading eigenvalues and eigenvectors of large asymmetric matrices. *J. Sci. Comp. 2*, 1987.

[71] F. Gómez, R. Gómez, and V. Theofilis. On three-dimensional global linear instability analysis of flows with standard aerodynamics codes. *Aerospace Science and Technology*, 2013.

[72] F. Gómez, P. Parades, R. Gómez, and V. Theofilis. Global stability of cubic and large aspect ratio three-dimensional lid-driven cavities. In *42nd AIAA Fluid Dynamics Conference and Exhibit*, 2012.

[73] N. Gregory and W.S. Walker. The effect of transition of isolated surface excrescences in the boundary layer. Technical Report R. & M 2779, Aeronautical research council, England, 1955.

[74] M. D. Griffith, T. Leweke, M. C. Thompson, and K. Hourigan. Effect of small asymmetries on axisymmetric stenotic flow. *J. Fluid Mech.*, 721.

[75] M. D. Griffith, T. Leweke, M. C. Thompson, and K. Hourigan. Steady inlet flow in stenotic geometries: convective and absolute instabilities. *Journal of fluid mechanics*, 616:11–133, 2008.

[76] M.D. Griffith, M.C. Thompson, T. Leweke, and K. Hourigan. Convective instability in steady stenotic flow: optimal transient growth and experimental observation. *J. Fluid Mech.*, 655:504–514, 2010.

[77] D. Hammond and L.G. Redekopp. Local and global instability properties of separation bubbles. *European Journal of Mechanics B/Fluids*, 17:145–164, 1998.

[78] P. Holmes, J. L. Lumley, and G. Berkooz. *Turbulence, Coherent Structures, Dynamical systems and Symmetry.* Cambridge University Press, 1996.

[79] E. Hopf. The partial differential equation $u_t + uu_x = \mu u_{xx}$. *Comm. Pure and Appl. Math.*, 3(3):201–230, 1950.

[80] P. Huerre. chapter Open Shear Flow Instabilities.

[81] P. Huerre and P.A. Monkewitz. Local and global instabilities in spatially developing flows. *Annu. Rev. Fluid Mech.*, 22:473–537, 1990.

[82] M. Ilak, P. Schlatter, S. Bagheri, and D.S. Henningson. Bifurcation and stability analysis of a jet in cross-flow: onset of global instability at a low velocity ratio. *J. Fluid Mech.*, 686:94–121, 2012.

[83] P. S. Iyer and K. Mahesh. High-speed boundary-layer transition induced by a discrete roughness element. *J. Fluid Mech.*, 729:524–562, 2013.

[84] J. Jeong and F. Hussain. On the identification of a vortex. *J. Fluid Mech.*, 285:69–94, 1995.

[85] R.D. Joslin and C.E. Grosch. Growth characterisitcs downstream of a shallow bump: computation and experiments. *Phys. Fluids*, 7:3042–3047, 1995.

[86] Kaiktsis, Karniadakis, and Orszag. Unsteadiness and convective instabilities in two-dimensional flow over a backward-facing step. *J. Fluid Mech*, 1996.

[87] G. Karniadakis and S. Sherwin. *Spectral/hp element methods for computational fluid dynamics.* Oxford science publications, 2005.

[88] A. M. A. Khalifa and D. P. Giddens. Charaterization and evolution of poststenotic disturbances. *J. Biomech.*, 14:279–296, 1981.

[89] P.S. Klebanoff and K.D. Tidstrom. Mechanism by which a two-dimensional roughness element induces boundary-layer transition. *Physics of fluids*, 15(1173), 1972.

[90] Y. Konishi and M. Asai. Experimental investigation of the instability of spanwise-periodic low-speed streaks. *Fluid Dyn. Res.*, 34(5):299, 2004.

[91] J. R. Koseff and R. L. Street. The lid-driven cavity flow: a synthesis of qualitative and quantitative observations. *J. Fluids Eng.*, 106:390–398, 1984.

[92] J. R. Koseff and R. L. Street. Visualization studies of a shear driven three-dimensional recirculating flow. *J. Fluids Eng.*, 106:21–29, 1984.

[93] J.R. Koseff and R.L. Street. On end walls effect in a lid-driven cavity flow. *J. Fluids Eng.*, 106:385–389, 1984.

[94] H. C. Kuhlmann and S. Albensoeder. Stability of the steady three-dimensional lid-driven flow in a cube and the supercritical flow dynamics. *Phys. Fluids*, 26(024104), 2014.

[95] O. Ladyzhenskaya. *The mathematical theory of viscous incompressible flows.* New York: Gordon and Breach, 1969.

[96] M. T. Landahl. A note on an algebraic instability of inviscid parallel shear flows . *J. Fluid Mech.*, 98:243–251, 1980.

[97] M.T. Landahl. Wave breakdown and turbulence. *SIAM J. Appl. Maths*, 28:735–756, 1975.

[98] M.T. Landahl. On sublayer streaks . *J. Fluid Mech.*, 212:593–614, 1990.

[99] D. Lanzerstorfer and H. Kuhlmann. Global stability of multiple solutions in plane sudden-expansion flow. *J. Fluid Mech.*, 702:378–402, 2012.

[100] R.B. Lechoucq and D.C. Sorensen. Deflation techniques for an Implicitely Restarted Arnoldi Iteration. *SIAM J. Matrix Anal. & Appl.*, 17(4):789–821, 1996.

[101] J. Leray. Sur le mouvement d'un liquide visqueux emplissant l'espace. *Acta Mathematica*, 63:193–248, 1934.

[102] E. Leriche. *Direct numerical simulation of a lid-driven cavity flow by a Chebyshev spectral method.* PhD thesis, Ecole Polytechnique Fédérale de Lausanne, Switzerland, 1999.

[103] E. Leriche. Direct numerical simulation in a lid-driven cubical cavity at high Reynolds number by a Chebyshev spectral method. *Journal of Scientific Computing*, 27(1–3), 2006.

[104] E. Leriche and S. Gavrilakis. Direct numerical simulation of the flow in a lid-driven cubical cavity. *Phys. Fluids*, 12:1363–1376, 2000.

[105] A. Liberzon, Yu. Feldman, and A. Yu. Gelfgat. Experimental observation of the steady-oscillatory transition in a cubic lid-driven cavity. *Physics of fluids*, 23, 2011.

[106] J.-Ch. Loiseau, S. Cherubini, J.-Ch. Robinet, and E. Leriche. Influence of the shape on the roughness-induced transition. In *Fluid Mechanics and its applications series*, volume ?? Springer, 2013.

[107] Q. long, X. Y. Xu, K. V. Ramnarine, and P. Hoskins. Numerical investigation of physiologically realistic pulstaile flow through arterial stenosis. *J. Biomech.*, 34:1229–1242, 2001.

[108] P. Luchini and A. Bottaro. Adjoint equations in stability analysis. *Annual Review of fluid mechanics*, 46:493–517, 2014.

[109] F. Mallinger and D. Drikakis. Instability in three-dimensional, unsteady, stenotic flows. *Intl. J. Heat Fluid Flow*, 23:657–663, 2002.

[110] Mamun and Tuckerman. Asymmetry and hopf bifurcation in spherical couette flow. *Phys. Fluids*, 1995.

[111] Marcus and Tuckerman. Simulation of flow between concentric rotating spheres. part 2. transitions. *J. Fluid Mech.*, 185, 1987.

[112] O. Marquet, D. Sipp, and L. Jacquin. Sensitivity analysis and passive control of cylinder flow. *J. Fluid Mech.*, 615:221–252, 2008.

[113] M. Marquillie and U. Ehrenstein. On the onset of nonlinear oscillations in a separating boundary-layer flow . *J. Fluid Mech.*, 490(169–188), 2003.

[114] A. Michalke. On the inviscid instability of the hyperboloc tangent velocity profile. *J. Fluid Mech.*, 19:543, 1964.

[115] A. Michalke. On spatially growing disturbances in an inviscid shear layer. *J. Fluid Mech.*, 23:521, 1965.

[116] A. Monokrousos, E. Akervik, L. Brandt, and D. S. Henningson. Global three-dimensional optimal disturbances in the Blasius boundary-layer flow using time-steppers . *J. Fluid Mech.*, 650:181–214, 2010.

[117] E. Non, R. Pierre, and J.-J. Gervais. Linear stability of the three-dimensional lid-driven cavity. *Phys. Fluids*, 18(084103), 2006.

[118] W. M. Orr. The stability or instability of the steady motions of a perfect liquid and of a viscous liquid. *Proc. R. Irish Acad. A*, 27:9–68, 1907.

[119] A. T. Patera. A spectral element method for fluid dynamics: laminar flow in a channel expansion. *Journal of computational physics*, 54:468–488, 1984.

[120] J. Peixinho and H. Besnard. Transition to turbulence in slowly divergent pipe flow. *Phys. Fluids*, 25(111702), 2013.

[121] J. Perraud, D. Arnal, A. Séraudie, and D. Tran. Laminar-turbulent transition on aerodynamics surfaces with imperfections. In *Prague, Czech Republic*, 2004.

[122] E. Piot, G. Casalis, and U. Rist. Stability of the laminar boundary layer flow encountering a row of roughness elements: Biglobal stability approach and dns. *European Journal of Mechanics - B/Fluids*, 27(6):684 – 706, 2008.

[123] R. E. Pitt, S. J. Sherwin, and V. Theofilis. BiGlobal stability analysis of steady flow in constricted channel geometries. *Int. Journal Num. Meth. Fluids*, 47:1229–1235, 2005.

[124] M. Poliashenko and C.K. Aidun. A direct method for computation of simple bifurcations. *J. Comput. Phys.*, 121:208–218, 1995.

[125] Y. Pomeau and P. Manneville. Intermittent transition to turbulence in dissipative dynamical systems. *Commun. Math. Phys.*, 74:189–197, 1980.

[126] N. Ramanan and G. M. Homsy. Linear stability of lid-driven cavity flow. *Phys. Fluids*, 6:2690–2701, 1994.

[127] S. C. Reddy and D. S. Henningson. Energy growth in viscous channel flows. *J. Fluid Mech.*, 252:209–238, 1993.

[128] O. Reynolds. An experimental investigation of the circumstances which determine whether the motion of water in parallel channels shall be direct or sinuous and of the law of resistance in parallel channels. *Phil. Trans. R. Soc. Lond.*, 174:935–982, 1883.

[129] J.-Ch. Robinet. Etude des instabilités dans des écoulements spatialement inhomogènes. Habilitation à diriger des recherches de l'Université Pierre et Marie Curie, 2007.

[130] J.-Ch. Robinet, X. Gloerfelt, and C. Corre. Dynamics of two-dimensional square lid-driven cavity at high reynolds number. In *3rd symposium on global flow instability and control*, Crete, 2005.

[131] C. W. Rowley, I. Mezić, S. Bagheri, P. Schlatter, and D. S. Henningson. Spectral analysis of nonlinear flows. *Journal of fluid mechanics*, 641:115–127, 2009.

[132] H. Sakamoto and M. Arie. Vortex shedding from a rectangular prism and a circular cylinder placed vertically in a turbulent boundary layer. *J. Fluid Mech.*, 126:147–165, 1983.

[133] E. Sanmiguel-Rojas and T. Mullin. Finite-amplitude solutions in the flow through a sudden expansion in a circular pipe. *J. Fluid Mech.*, 691:201–213, 2012.

[134] Schatz, Barkley, and Swinney. Instabilities in spatially periodic channel flow. *Phys. Fluids*, 1995.

[135] P. J. Schmid. Nonmodal stability theory. *Annual Review of fluid mechanics*, 2007.

[136] P. J. Schmid. Dynamic mode decomposition of numerical and experimental data. *Journal of fluid mechanics*, 656:5–28, 2010.

[137] P. J. Schmid and L. Brandt. Analysis of fluid systems: stability, receptivity, sensitivity. 2013.

[138] P. J. Schmid and D. S. Henningson. *Stability and transition in shear flows*. Springer, 2001.

[139] P.J. Schmid and J.L. Sesterhenn. Dynamic mode decomposition of experimental data. In *8th international sysmposium on particle image velocitymetry*, 2008.

[140] R. Sedney. A survey of the effects of small protuberanecs on boundary-layer flows. *AIAA Journal*, 11(6):782–792, 1972.

[141] P.N. Shankar and M.D. Deshpande. Fluid mechanics in the driven cavity. *Annu. Rev. Fluid Mech.*, 32:93–136, 2000.

[142] S.J. Sherwin and H.M. Blackburn. Three-dimensional instabilities and transition of steady and pulsatile axisymmetric stenotic flows. *J. Fluid Mech.*, 533:297–327, 2005.

[143] G. M. Shroff and H. B. Keller. Stabilization of unstable procedures: the recursive projection method. *SIAM J. Numer. Anal*, 30(4):1099–1120, 1993.

[144] I.J. Sobey and P. Drazin. Bifurcations of two-dimensional channel flows. *J. Fluid Mech.*, 171:263–287, 1986.

[145] A. Sommerfeld. Ein beitrag zur hydrodynamischen erklaerung er turbulenten fluessigkeitsbewegungen. *Atti del 4 Congresso Internazionale dei Matematici, Ser. I*, 3:116–124, 1908.

[146] H. B. Squire. On the stability of three-dimensional disturbances of viscous flow between parallel walls. *Proc. R. Soc. Lond. A*, 142:621–628, 1933.

[147] K.A. Stephani and D.B. Goldstein. DNS study of transient disturbance growth and bypass transition due to realistic roughness. In 47th *AIAA Aerospace Sciences Meeting Including the New Horizons Forum and Aerospace Exposition*, 2009.

[148] P. K. Subbareddy, M. D. Bartkowicz, and G. V. Candler. Direct numerical simulation of high-speed transition due to an isolated roughness element. *J. Fluid Mech.*, 748:848–878, 2014.

[149] I. Tani, H. Komoda, and Y. Komatsu. Boundary-layer transition by isolated roughness. Technical Report 375, Aeronautical Research Institute, University of Tokyo, 1962.

[150] Terence Tao. Finite time blowup for an averaged three-dimensional Navier-Stokes equation. 2014. arxiv: 1402-0290v2.

[151] T. Tatsumi and T. Yoshimura. Stability of the laminar flow in a rectangular duct. *J. Fluid Mech.*, 212:437–449, 1990.

[152] V. Theofilis, P.W. Duck, and J. Owen. Viscous linear stability analysis of rectangular duct and cavity flows. *J. Fluid Mech.*, 505:249–286, 2004.

[153] H.M. Tufo, P.F. Fischer, M.E. Papka, and K. Blom. Numerical simulation and immersive visualization of hairpin vortices. In *ACM/IEEE SC99 Conf. on High performances networking and computing*, 1999.

[154] A. Tumin and E. Reshotko. Receptivity of a boundary-layer flow to a three-dimensional hump at finite reynolds numbers. *Phys. Fluids*, 17(094101), 2005.

[155] S.S. Varghese, S.H. Frankel, and P.F. Fischer. Direct numerical simulation of stenotic flows. part 2: Pulsatile flow. *J. Fluid Mech.*, 582:281–318, 2007.

[156] S.S. Varghese, S.H. Frankel, and P.F. Fischer. Direct numerical simulation of the stenotic flows. part 1: Steady flow. *J. Fluid Mech.*, 582:253–280, 2007.

[157] O. Vermeersch. *Etude et modélisation du phénomène de croissance transition pour des couches limites incompressibles et compressibles.* PhD thesis, ISAE, Toulouse, 2009.

[158] A.E. von Doenhoff and A.L. Braslow. The effect of distributed roughness on laminar flow. In Lachmann, editor, *Boundary layer control*, volume 2. Pergamon, 1961.

[159] E. B. White. Transient growth of stationary disturbances in a flat plate boundary layer . *Phys. Fluids*, 14(12):4429, 2002.

[160] Z. Zhou, Z. Wang, and J. Fan. Direct numerical simulation of the transional boundary-layer flow induced by an isolated hemispherical roughness element. *Comput. Methods Appl. Mech. Engrg.*, 199:1573–1582, 2010.

Dynamics and global stability analyses of three-dimensional flows

RÉSUMÉ : Comprendre, prédire et finalement retarder la transition vers la turbulence dans les écoulements sont d'importants problèmes posés aux scientifiques . Ces questions ont été principalement adressées via la théorie des instabilités hydrodynamiques dans le cadre de laquelle la croissance ou décroissance au cours du temps de petites perturbations de l'écoulement sont analysées. Jusqu'à récemment, ces analyses de stabilité portaient sur des écoulements relativement simples (parallèles ou bidimensionnels). L'objectif de la présente thèse est d'étendre ces analyses à des écoulements tridimensionnels réalistes tels que l'écoulement à l'intérieur d'une cavité entraînée, celui dans un tuyau servant de modèle à l'écoulement sanguin au sein d'une artère atteinte de sténose, ou encore celui se développant au voisinage d'une petite rugosité sur une plaque plane.

Mots clés : Couche limite, Instabilité, transition à la turbulence, rugosité, cavité entraînée, sténose

Dynamics and global stability analyses of three-dimensional flows

ABSTRACT : Understanding, predicting and eventually delaying transition to turbulence in fluid flows have been challenging issues for scientists. These problems have mostly been addressed using the hydrodynamic linear stability theory. In this framework, the stability of the flow is assessed from the time evolution of infinitesimal perturbations. Until recently, these analyses were essentially done for relatively simple flows (parallel or two-dimensional). The aim of the present thesis is thus to extend these analyses to realistic three-dimensional flows among which the flow within a cuboid lid-driven cavity, the flow in a stenotic pipe and finally the boundary layer flow over a roughness element mounted on a flat plate.

Keywords : Boundary layer, instability, transition to turbulence, roughness, lid-driven cavity, stenotic pipe flow.

ARTS ET MÉTIERS

ParisTech